LEGIBILITY NOTICE

A major purpose of the Technical Information Center is to provide the broadest dissemination possible of information contained in DOE's Research and Development Reports to business, industry, the academic community, and federal, state and local governments.

Although a small portion of this report is not reproducible, it is being made available to expedite the availability of information on the research discussed herein.

ANL/APS-TM--5

DE90 010201

Proceedings of the Impedance and Bunch Instability Workshop

October 31 - November 1, 1989

Organized by

Argonne National Laboratory
Advanced Photon Source
Accelerator Systems Division
9700 South Cass Avenue
Argonne, Illinois 60439

April 1990

Table of Contents

LIST OF WORKSHOP PARTICIPANTS

Karl Bane	SLAC
S.H. Be	RIKEN
Alex Bogacz	FNAL
Daniel Brandt	CERN
Dominic Chan	LANL
Yong Ho Chin	LBL
Dick Cooper	LANL
Laurent Farvacque	ESRF
Robert Gluckstern	University of Maryland
M. Hara	RIKEN
Frady A. Harfoush	FNAL
Bill K.Y. Ng	FNAL
Keith Symon	University of Wisconsin
Jiunn-Ming Wang	BNL
Bruno Zotter	CERN

ANL/APS PARTICIPANTS

Hana Bizek
Yanglai Cho
Weiren Chou
Youngjoo Chung
Joseph M. Cook
Edwin A. Crosbie
Steven L. Kramer
Robert L. Kustom
Alireza Nassiri
Lee C. Teng
Larry R. Turner

1/2

Introductory Remarks

L.C. Teng

ANL/APS

Argonne National Laboratory
Advanced Photon Source
Impedance and Bunch Instability Workshop
October 31 - November 1, 1989

IMPEDANCE AND BUNCH INSTABILITY WORKSHOP

Introductory Remarks

The accepted interpretation of the physical process limiting single beam-bunch current in an electron storage ring is simple and straightforward. As the maximum local current along the bunch exceeds the longitudinal microwave (turbulence) instability threshold, the bunch will lengthen and widen until the current falls below the rising instability threshold. One can continue to pump electrons into the bunch and the bunch continues to lengthen following the threshold value until the transverse fast head-tail (mode coupling) instability threshold is reached and acts to limit further increase in the bunch current. Thus, one would like the transverse threshold to be higher than the longitudinal threshold, at least for the un-lengthened bunch. In this short introductory talk, I will give only a tabulated list of the various facets of the problem to serve as orientation to the Workshop.

Types of Instability Problems

- Single Bunch -- Instability is controlled mainly by the high frequency end of the broad-band impedance of the beam enclosure. This is difficult to calculate and hard to control, and is, hence, more troublesome.

- Coupled Bunch -- Instability is caused mainly by high-impedance narrow-band resonances in localized beam enclosure structures. The source of the resonance

can, in principle, be located and corrected. The narrow-band nature of this instability also makes feedback damping devices simple and effective.

Computations

- Electromagnetics -- With given beam bunch and enclosure configurations, calculate the induced field or impedance. This can be done in either the time or the frequency domain. (In more than one degree-of-freedom instead of time and frequency domains, we really have the coordinates-domain and the modes-domain, but I will continue to use the words time and frequency for this qualitative discussion.) These cases of calculation can be tabulated as:

	Bunch expansion basis functions	EM quantity computed
Time Domain	δ-function $\delta(t)$	Wake potential $W(t)$
Frequency Domain	Harmonic component $e^{-i\omega t}$	Coupling impedance $Z(\omega)$

The computation is usually performed separately for each beam enclosure element and the results are summed.

For enclosure elements with simple geometries, analytical solutions are possible; but for most elements one has to resort to computer codes such as TBCI, MAFIA, etc.

The computer codes can handle only physically realistic beam bunches. But for instability computations, we need the electromagnetics of the basis functions in

which to expand the arbitrary beam bunch. Thus, in the t-domain one has to fake the results for a δ-function bunch; and in the f-domain, one has to engage some model to extend to high harmonic frequencies. (The high frequency behavior of the traditional broad-band resonator impedance model is not correct!)

- Dynamics -- One can either solve the Vlasov equation in the modes-domain using computer codes BBI, ZAP, etc., or do straightforward particle tracking in the coordinates-domain using SIMTRAC. Aside from the usual concerns of precision, convergence, etc., there does not seem to be any problem with these codes.

Measurements

- On operating machines, one can measure the single bunch lengthening threshold; hence, the longitudinal coupling impedance. The measured impedance is sometimes at variance with the computed value. The measured transverse impedances are, however, generally in fair agreement with computation.

For coupled bunches, since the instability is caused by specific high impedance resonances, the measurements are used more for the "detect instability → seek responsible resonance → eliminate resonance" procedure rather than for the verification of some computational results.

- For off-line measurement on individual beam enclosure element, one can use either a linac beam or a microwave carrying wire. Either measurement has questionable accuracy and, hence, questionable utility. The difficulty is evident when one remembers that the stored beam senses the wakefield or coupling impedance effect in some 10^5 passages through the impedance elements (assuming an average

element spacing of ~ 30 m and an instability growth time of ~10 ms) and we are trying to measure the effect after a single passage.

Thus, while the general understanding of the beam instability problem is undoubtedly correct, we are far from being able to predict or even to describe the phenomena quantitatively. If the Workshop can make some progress or generate some new approaches for these problems, it will have made a great contribution. At the minimum, the Workshop will provide an opportunity for the very useful and essential communication and interchange.

Thank you all for coming.

Impedance and Bunch Lengthening in the APS*

W. Chou and H. Bizek

ANL/APS

Argonne National Laboratory
Advanced Photon Source
Impedance and Bunch Instability Workshop
October 31 - November 1, 1989

---

*This research was supported by the U.S. Department of Energy, Office of Basic Energy Sciences, under Contract W-31-109-ENG-38.

Contents

1 Introduction

- Goal: Single bunch current limit 5 mA.
- Methods:
  1. Establishing impedance budget;
  2. Studying single bunch instabilities:
     - Longitudinal bunch lengthening;
     - Transverse threshold current.
- Controversial results from two different approaches:
  - Broad-band resonator model with $Q = 1$:
    $\longrightarrow$ Large bunch lengthening;
  - Pseudo-Green function:
    $\longrightarrow$ Little bunch lengthening.

  Question: Which one should we believe?

2 Impedance budget

2.1 Code calculations

2-D — TBCI, ABCI, URMEL.
3-D — MAFIA (T3).

Components	Number	Code
RF cavities	15	2D
Transitions from chamber to insertion device (ID) section	34	2D, 3D
Transitions from chamber to RF section	3	2D, 3D
Shielded bellows	160	2D, 3D
Shielded transitions	80	2D, 3D
Flange full-penetration weldments	480	2D
Elliptical tube weldments	80	2D
Shielded end conflats	80	2D
Valves	80	2D, 3D
Crotch absorbers	80	3D
Transitions from chamber without antechamber to that with antechamber	120	3D
Scrapers	2	3D

Some examples of these components are show in Fig. 1.

2.2 Analytic formulae

Analytical formulae are available for the following cases: [1]

- Space charge;
- Resistive wall;
- Synchrotron radiation; [1]
- Button-type beam position monitors. (A total of 360)

2.3 Data scaled from existing machines

The impedances of the following components are scaled from the PEP.

Components	Number
Ion/NEG pump ports (screened)	200
Injection bumpers	4
Abort kickers	2
Diagonostic instruments:	
current transformers	2
horizontal hf pickup electrodes	2
vertical hf pickup electrodes	2
horizontal pingers	2
vertical pingers	2

2.4 Budget

Based on the results obtained from the above, the budget is established.

Longitudinal	$\mid Z/n \mid_{\parallel}$	$1 \sim 2\ \Omega$
Transverse	$Z_{\perp}$	$0.7\ \ M\Omega/m$

In this budget, the following components are not included.

Components	Number
Injection thin pulse septum	1
Abort Lambertson septum	1
Injection thin dc septum	1
Injection thick dc septum	1
Photon beam ports	many
Injection Y beam port	1
Extraction Y beam port	1
Bent chamber in dipole sections	80

[1] It is controversial whether or not this part of impedance has any effects on beam instabilities.

3 Code calculations

3.1 Time-domain approach

The computer codes TBCI (2-D), ABCI (2-D) and MAFIA (3-D) are employed to calculate the following quantities for various components listed in the previous section.[2]

- Wake potential $W(\tau)$;
- Loss factor $k(\sigma)$ (integration of $W(\tau)$);
- Impedance $Z(\omega)$ (Fourier transform of $W(\tau)$).

3.2 Testing of codes

A series of tests have been performed in order to know the validity of the results obtained from the code calculations.

3.2.1 Comparison with field-matching method

Two types of simple geometries are chosen for this comparison.

1. Small pillbox with beam tubes (*H. Henke*). (Fig. 2(a))
2. Single steps (*S. A. Kheifets*).

The impedance spectra obtained from the field-matching method are compared with that from $TBCI + FFT$. The agreement are fairly good, except that the latter gives double or triple peaks, which are not completely understood and are under further investigation. As an example, Figs. 2(b)-(c) illustrate the results for geometry 1. The results for geometry 2 can be found in [1].

3.2.2 Comparison with boundary perturbation method

When the perturbation is small and the geometry is suitable for TBCI computing, the agreement is excellent. This work is underway and will be reported in [3].

3.2.3 Accuracy and convergence tests

1. Single precision (32-*bit*) *vs.* double precision (64-*bit*):
   The former is performed on a VAX, while the latter on a CRAY X-MP. The agreement is surprisingly good for TBCI as well as for MAFIA(T3). Fig. 3 shows some results of this comparison. The difference between the VAX and the CRAY output is negligible.

[2] An alternative is the frequency-domain approach, [2] which we have not adopted.

2. Convergence tests – $k(\sigma)$ *vs.* mesh size:

   (a) The geometry of transitions from chamber to ID section:

   - This geometry is important. Because it is the major contributor to the transverse impedances, and because it is difficult to calculate.
   - The convergence of TBCI output is slow, see Fig. 3.
     A possible explanation: When the tapered angle θ is small ($\sim 5°$) and the tapered part is long ($20cm$), the matching between the real and the TBCI-approximated boundary is poor, and it varies as the mesh size changes.
   - Another code, ABCI, allows δz different from δr. But numerical instabilities arise due to the violation of the *Courant criterion* when we try to let $\delta z > \delta r$ in order to match the real boundary. [4] This problem remains to be resolved.
   - Incorrect output of TBCI (and ABCI) is observed in certain cases, namely, near the bunch head, W_{transv} becomes negative and W_{longi} and W_{azimu} become positive, see Fig. 4(a). These results are unphysical. [3] These incorrect results can be corrected by either increasing the ratio of $\sigma/\delta z$ or taking certain error-correction procedures. (Fig. 4(b))

   (b) Other geometries: No convergence problem. Fig. 5 shows the transverse loss curves of an RF cavity calculated using two different mesh sizes.

3.2.4 3-D MAFIA(T3) *vs.* 2-D TBCI

1. For geometries with rotational symmetry:
   2-D and 3-D outputs are in general agreement. An example is given in Fig. 8.

2. For geometries with elliptic cross-sections:
   The situation is more complicated. One example is the transition from chamber to ID section. MAFIA is used to calculate for the real 3-D geometry, while TBCI for the 2-D approximation with the radius equal to the dimension of the minor semi-axis of the ellipse.

   (a) Restrictions in choosing the mesh sizes in MAFIA(T3). [4]

   - Maximum ratio of mesh sizes ≤ 3;
   - The longitudinal mesh size δz should be uniform and the smallest one compared with the others.

   Violation may lead to strange results. (Fig. 6)

[3] According to T. Weiland, these incorrect output reflects the limitation of the first order approximation on which TBCI is based.

[4] R. Klatt, private communication.

(b) The 3-D result of the dipole component of the vertical loss, k_y, is much larger than its 2-D counterpart. The cause is not clear. For $\sigma = 1.75cm$,

	TBCI (circular approx.)	MAFIA
$k_y(m=1)\ (V/pC \cdot m)$	34	190

3.3 Some Results of general interest

3.3.1 Negative transverse impedance

In 3-D calculations, many structures, in which the horizontal dimension is substantially larger than the vertical one, exhibit negative transverse impedances. Two examples are given below.

1. SPS adaptors: (Fig. 7) [5]
   The first peak of the horizontal wake potential, $W_h^{(peak)}$, and the horizontal loss, k_h, are shown in Fig. 8. When the horizontal dimension of the structure increases while keeping all the other parameters fixed, a smooth transition from positive to negative values is observed for $W_h^{(peak)}$ as well as for k_h.
   Fig. 9 gives more information about how the negative horizontal wake force, F_h, is generated. Fig. 9(a) shows that the dipole component of F_h is positive, whereas the higher order multipole components give a negative F_h as shown in Fig. 9(b). And the sum is negative as seen in Fig. 9(c).

2. Transitions from chamber to ID section:
   Similar phenomenon is observed. For a bunch length of $1.75cm$,

	Dipole	Higher order multipoles	Total
$k_x\ (V/pC \cdot m)$	38	-40.3	-2.3

3.3.2 Composition rule

When the separation between two successive discontinuities is large enough, one may decompose a complicated structure into simple components and compose these components to form new structures and obatain the same value of the impedance. The new structures should be easier to compute. Figs. 10 and 11, and Tables 1-3, illustrate two examples as the applications of this rule. [6]

4 Broad-band resonator (BBR) model

4.1 Loss factors of various components

Figs. 12 and 13 exhibit, respectively, the longitudinal loss, $k_{\|}$, and the transverse one, $k_{\perp}$, of various components and the sums.

- Longitudinal: Main contributors are the RF cavities.
- Transverse: The transitions from chamber ID section are dominant.
  - We have compared the $k_\perp$ of three different transition shapes. No significant improvement is seen, as shown in Fig. 14.
  - When the radius of the tube in the ID section is increased from $0.4cm$ (current design) to $0.6cm$, $k_\perp$ will be reduced by about half, as expected.

4.2 Loss factors of a BBR

These are given in Fig. 15.

4.3 Fitting techniques and results

The following two techniques are employed to get the parameters (R, Q and f_r) of a BBR.

1. Least-squares fit: for both logintudinal and transverse.
2. Zotter's technique: for transverse only. [7]

The results are as follows:

- Transverse: Both techniques work well. Fig. 16 is an example.
- Longitudinal: The fitted value of Q is extremely small. (Fig. 17) BBR is not an adequate model in this case.

5 Pseudo-Green function

5.1 TBCI calculations

TBCI is used to compute the logitudinal wake potentials $W_\parallel(\tau)$ of various types of components for a very short bunch ($\sigma = 1.5\ mm$). [5] The total wake of the APS storage ring is obtained using the formula

$$W_\parallel^{(total)} = \sum_i W_\parallel^{(i)} \cdot N^{(i)},$$

in which $N^{(i)}$ is the number of each component. (Fig. 18(a))

5.2 Manipulation of TBCI results

In order to get the pseudo-Green function from the TBCI results, the following procedure is adopted.

1. At time 0, the pseudo-Green function should take its maximum value. Assume time 0 occurs when $W_\parallel^{(total)}$ takes its peak value.

[5] The natural r.m.s. bunch length of the APS storage ring is $5.3mm$.

2. Reflect $W_{\|}^{(total)}$ about the time 0 axis from the left to the right in order to preserve the area, and multiply it by a factor of 2 as a conservative measure. The new curve is taken as the pseudo-Green function, see Fig. 18(b).

3. Other possible choices of time 0 have also been tried.

   - At (peak of $W_{\|}^{(total)}$) $\pm$ 1 mesh; (Fig. 18(c) and (d))
   - At (peak of $W_{\|}^{(total)}$) $\pm$ 2 meshes.

6 Bunch lengthening in the APS

6.1 BBR model approach

Because the small Q value of a BBR model does not make any physical sense, we keep $Q = 1$ and use BBR as the input of the following three codes to perform the bunch instability calculations. The results are comparable to each other.

1. BBI; (Fig. 19)
2. ZAP;
3. SIMTRAC.

6.2 Pseudo-Green function approach

We also employ the pseudo-Green function obtained in Sec. 5 as the input of SIMTRAC to do the same kind of calculations. In this approach, we have tried

- Five different choices of time 0 of $W_{\|}^{(total)}$; (Sec. 5.2)
- Different number of superparticles (up to 4,000);
- Different number of turns (up to 5,000, which is about 4 times the synchrotron damping time).

The results are self-consistent, see Fig. 20.

6.3 Contraversial results

The bunch lengths obtained from the two different approches are very different.

	Zero current	$I = 5\ mA$
BBR model ($Q = 1$)	$0.53cm$	$\sim 2.7cm$
Pseudo-Green function	$0.53cm$	$\sim 0.7cm$

The reason for this discrepancy is simple – The Green function calculated from a BBR with $Q = 1$ is *very* different from the pseudo-Green function. (Fig. 21)

As another comparison, we also calculate the bunch lengthening of a hyperthetic machine. It consists of thousands of small pill-boxes, of which the Green function is known analytically. [8] The results are close to that obtained from the pseudo-Green function approach. (Fig. 20(a))

On the other hand, if we allow the BBR have a very small Q value as obtained from the fitting procedure (Sec. 4.3), then the resulting bunch length is also very small ($\sim 0.7cm$).

7 Conclusions

1. It is inappropriate for the APS to use the broad-band resonator as a model to study the longitudinal bunch instabilities. Because it may result in very small Q values which are apparently unphysical. Furthermore, the bunch lengths calculated from a BBR with $Q = 1$ may be misleading.

2. More work is needed in order to convince ourselves that the bunch lengths obtained from the pseudo-Green function approach are believable.

References

[1] W. Chou and Y. Jin, *Impedance Studies - Part 4: APS Impedance Budget*, ANL Light Source Note LS-115 (April 1988).

[2] R. H. Siemann, *Computer Models of Instabilities in Electron Storage Rings*, AIP Conference Proceedings No. 127, p. 388 (1985).

[3] W. Chou, *Impedance Calculations Using Boundary Perturbation Method*, submitted to the Spring Meeting of the American Physical Society, Division of Physics of Beams, Washington, D.C., April 16-19, 1990.

[4] E. Isaacson and H. B. Keller, *Analysis of Numerical Methods*, John Wiley & Sons, Inc. (1966).

[5] W. Chou, *Negative Transverse Impedance*, ANL Light Source Note LS-140 (June 1989).

[6] W. Chou and Y. Jin, *Impedance Studies - Part 1: A Composition Rule*, ANL Light Source Note LS-112 (April 1988).

[7] B. Zotter, CERN LEP-TH/87-34 (1987).

[8] G. Dôme, 1985 Particle Accelerator Conference, IEEE Transactions on Nuclear Science, Vol. NS-32, p.2531 (October, 1985).

Table 1

MAFIA Output for the

Loss Factors of a Periodic Structure*

Component/Structure	Longitudinal, $k_\parallel$ (V/pC)
Expansion	486.6×10^{-3}
Pinch	-484.6×10^{-3}
Cavity	1.956×10^{-3}
Scraper	2.064×10^{-3}
2-period	3.913×10^{-3}

Table 2

TBCI Output for the Loss Factors of a Periodic Structure*

Component/Structure	Longitudinal, $k_\parallel$ (V/pC)	Transverse, $k_\perp$ (V/pC/m)
Expansion	46299.0×10^{-5}	551.1
Pinch	-46294.4×10^{-5}	-501.94
Cavity	3.561×10^{-5}	54.41
Scraper	3.715×10^{-5}	43.95
2-period	7.117×10^{-5}	108.8

Table 3

TBCI Output for the Loss Factors of a

Combined RF Cavity - Transition Structure*

Component/Structure	Longitudinal, $k_\parallel$ (V/pC)	Transverse, $k_\perp$ (V/pC/m)
RF Cavity	0.3199	2.235
Transition	0.0123	5.561
Whole structure	0.3424	7.995

*RMS bunch length σ = 1.75 cm.

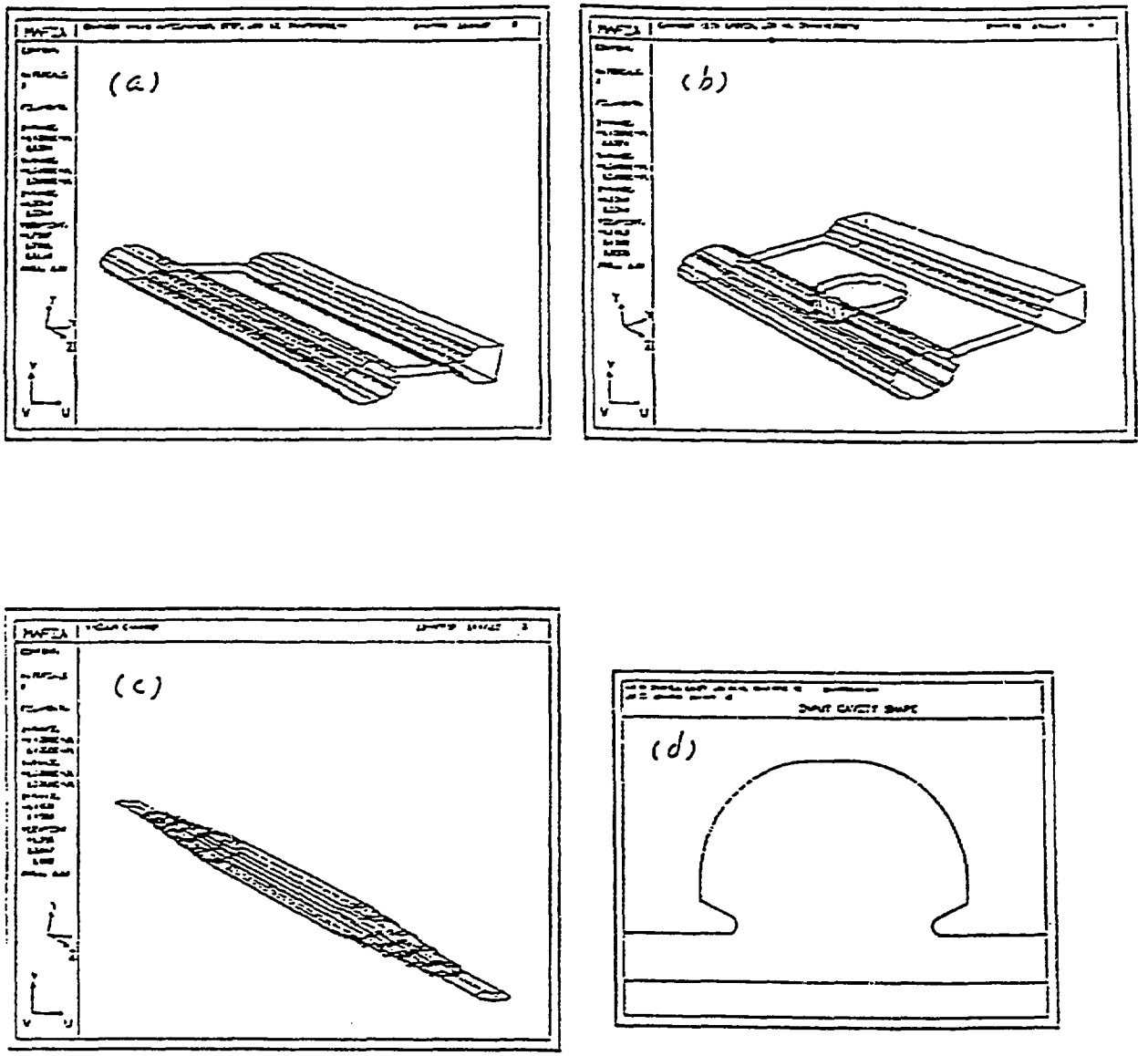

Fig. 1. Examples of the components used in the code calculations. (a) A transition between the chamber with and without an antechamber. (b) A chamber with an antechamber and a crotch absorber. (c) A transition between the chamber and ID section, both with an elliptic cross section. (d) An RF cavity.

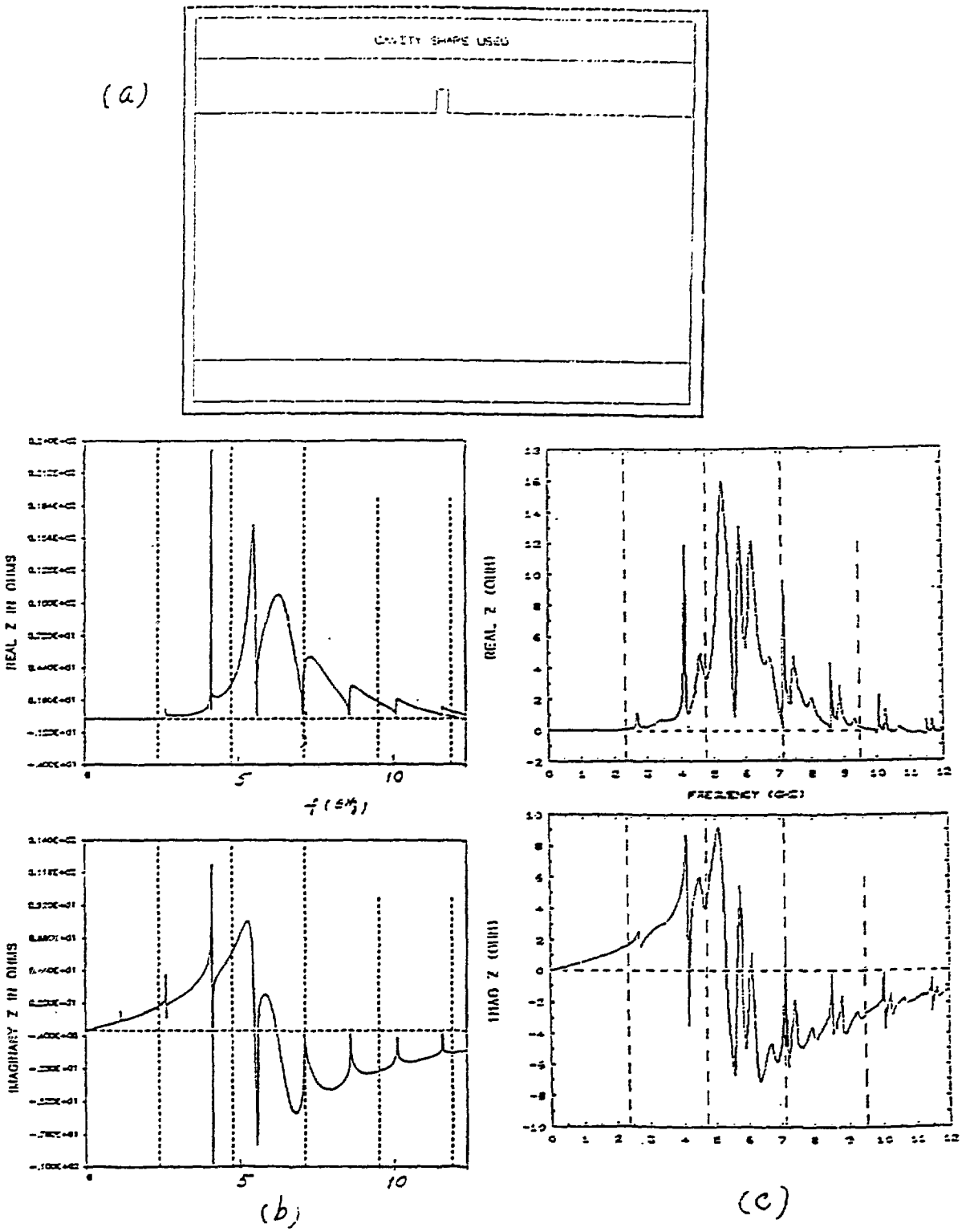

Fig. 2. (a) A small pillbox with beam tubes. (b) *Henke*'s results of the impedance spectra of the geometry shown in (a), using field-matching method. (c) Our results for the same geometry, obtained from $TBCI + FFT$. Note that some peaks in (b) split into two or three.

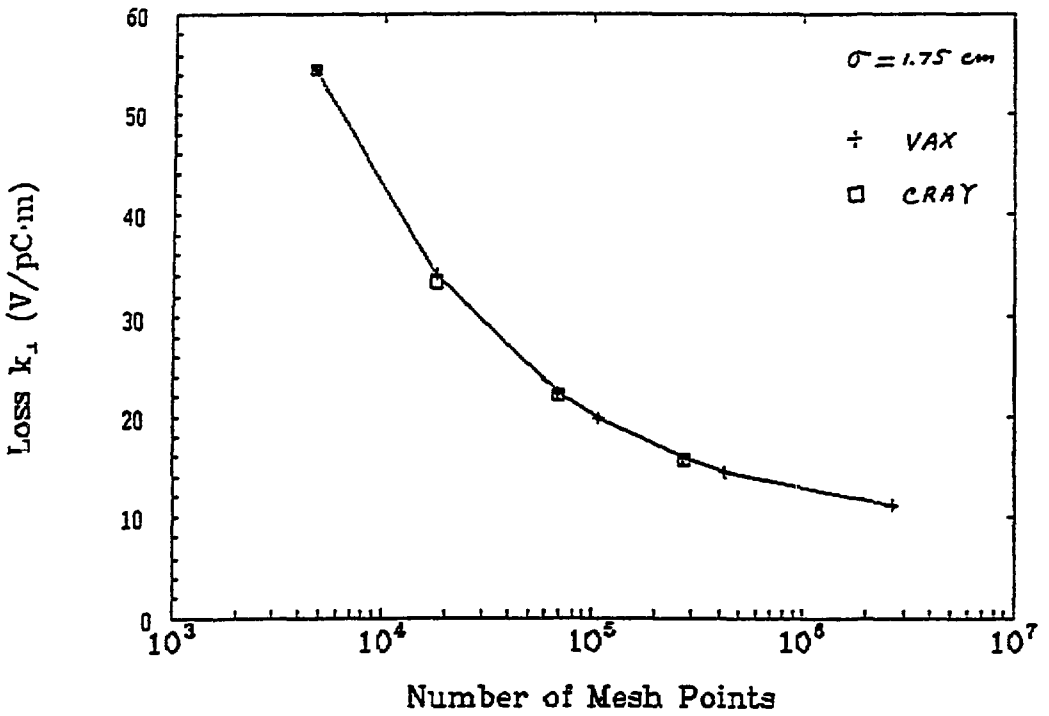

Fig. 3. Accuracy and convergence test of TBCI output for a transition from chamber to ID section.

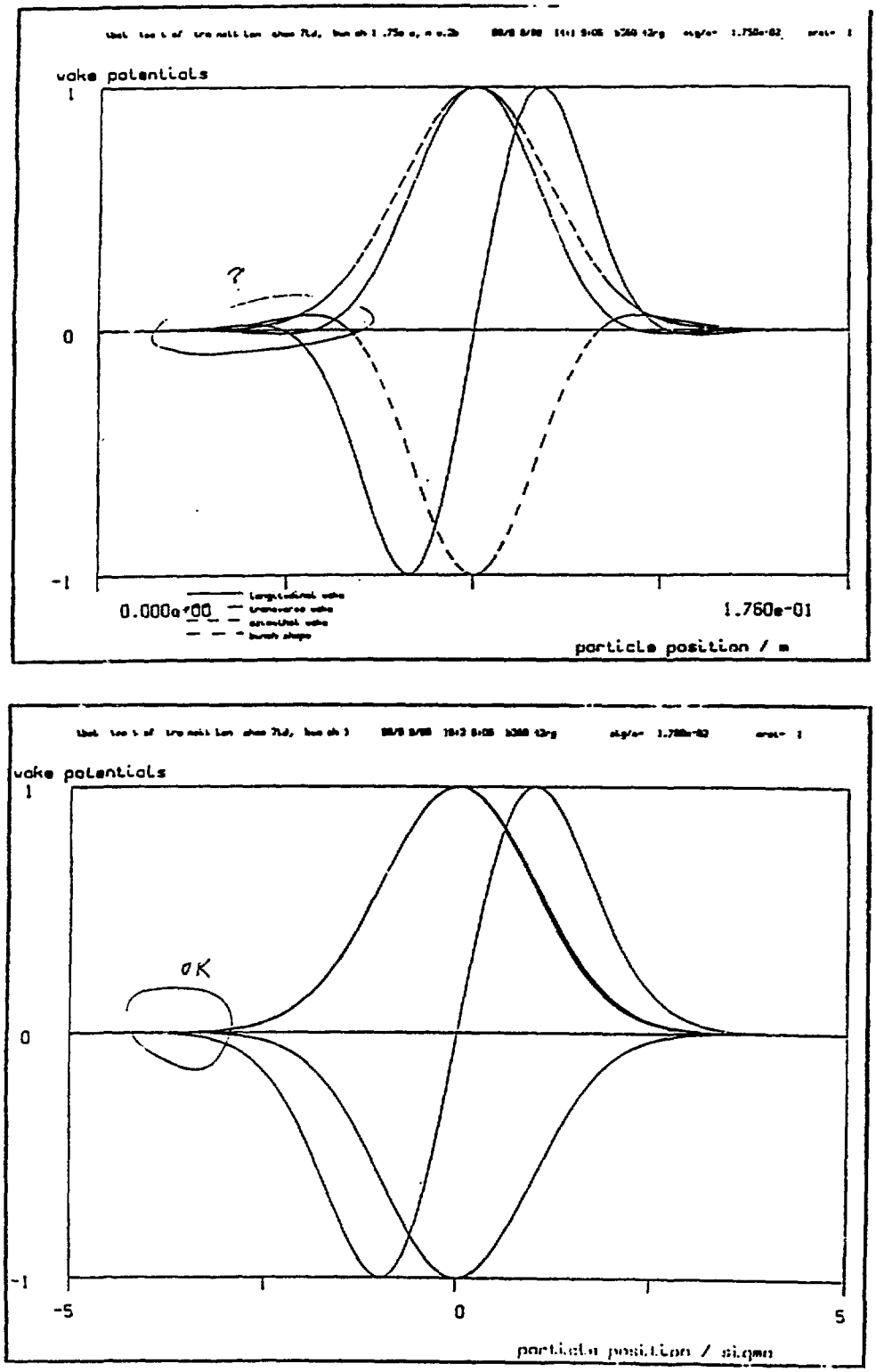

Fig. 4. (a) The wake potentials obtained from TBCI for a transition from chamber to ID section. Note the humps near the bunch head, which are incorrect. (b) The corrected wake potentials.

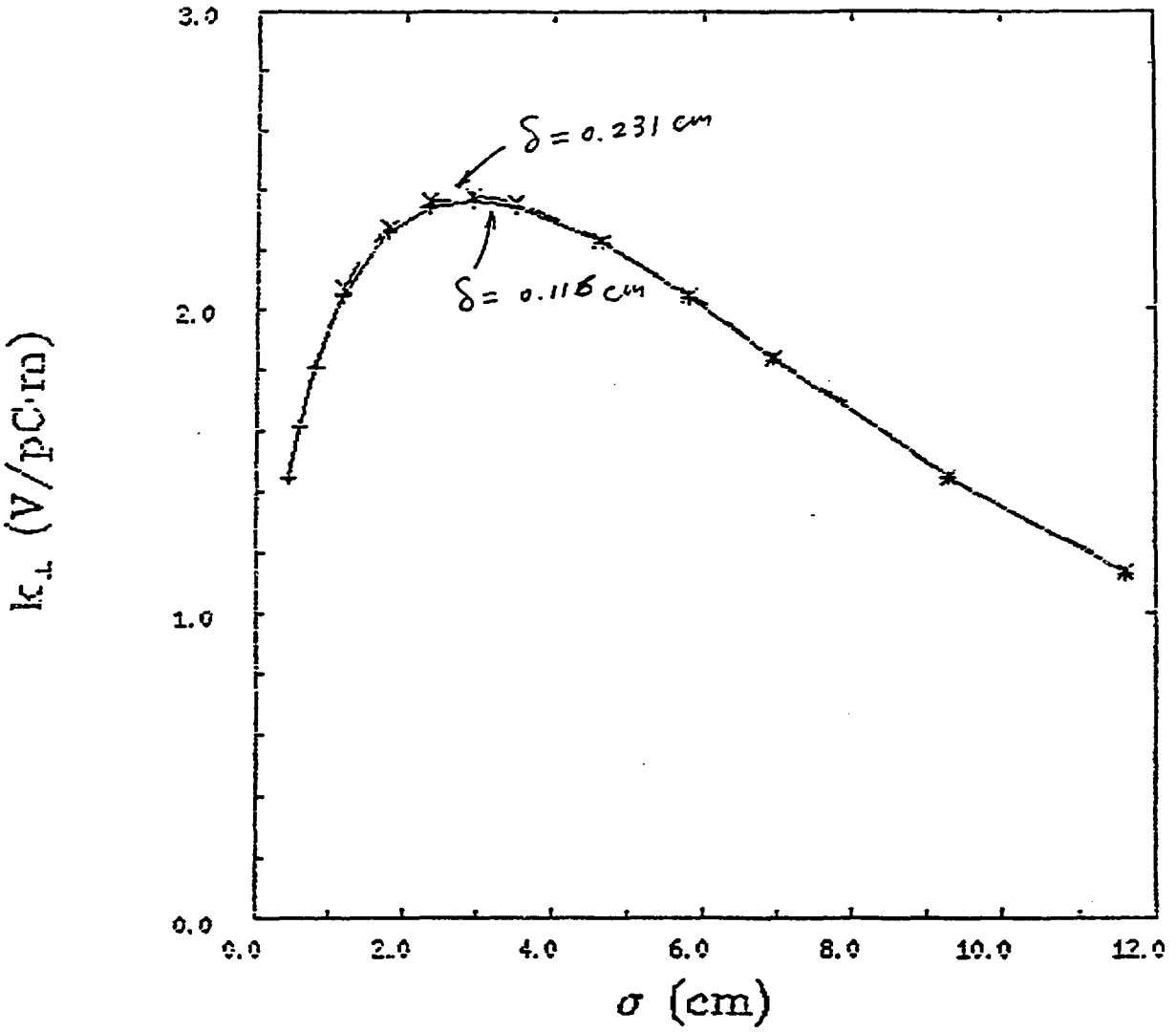

Fig. 5. Convergence test of TBCI output for an RF cavity.

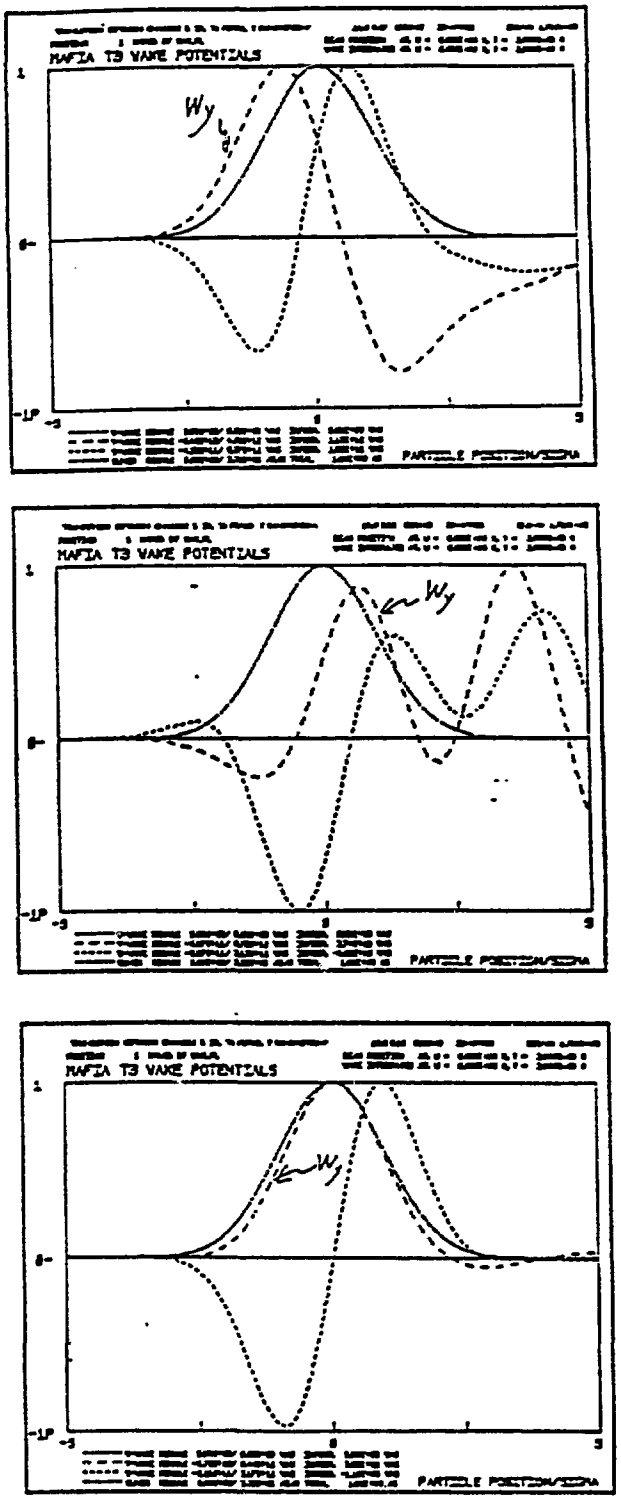

Fig. 6. The wake potentials calculated by MAFIA(T3) for a transition from chamber to ID section, using different mesh sizes. Note that the shapes of the wakes differ drastically from each other. This is due to the improper choices of mesh sizes (see text).

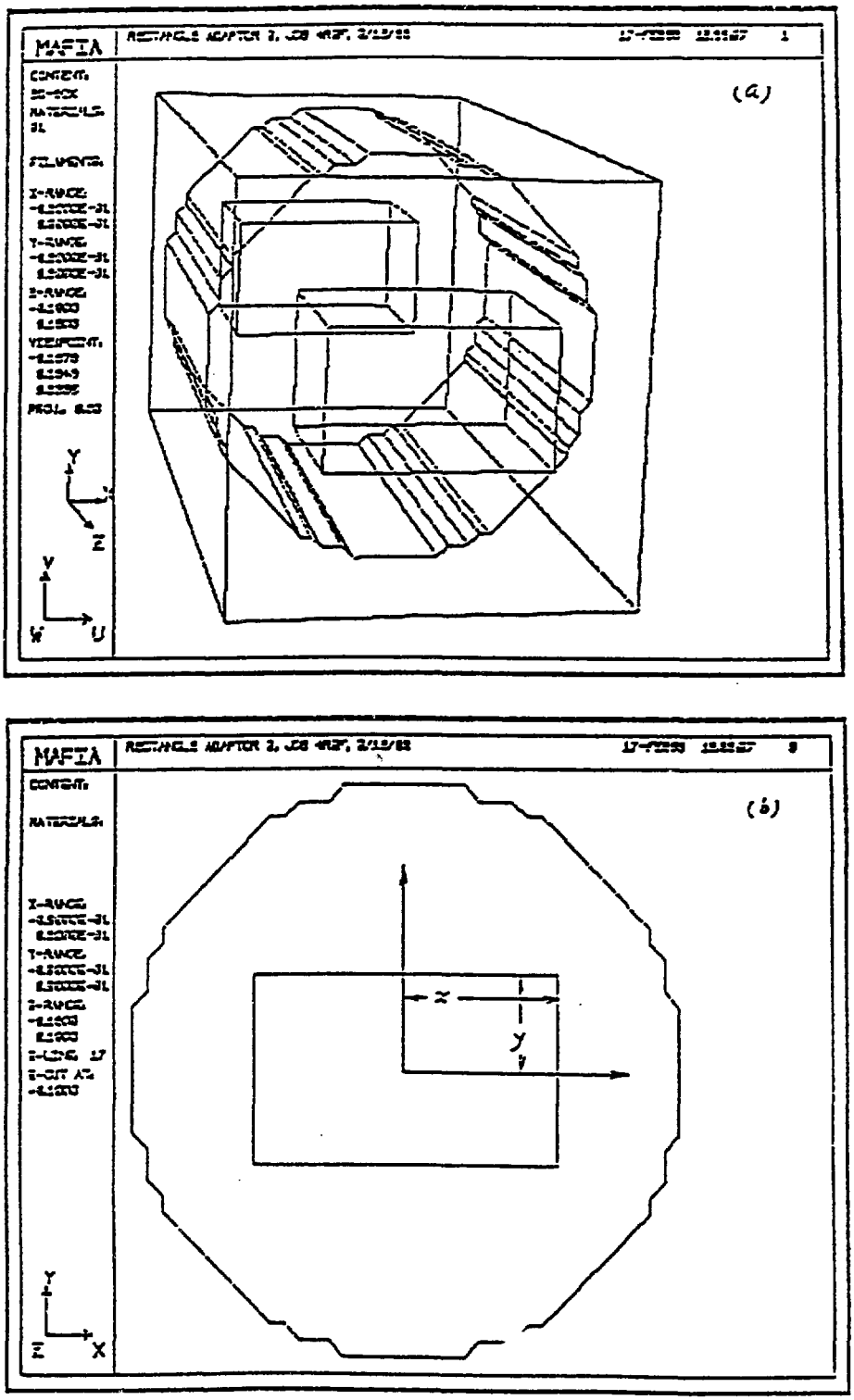

Fig. 7. The geometry used in the 3-D simulation of an SPS adaptor. (a) 3-D view and (b) Front view.

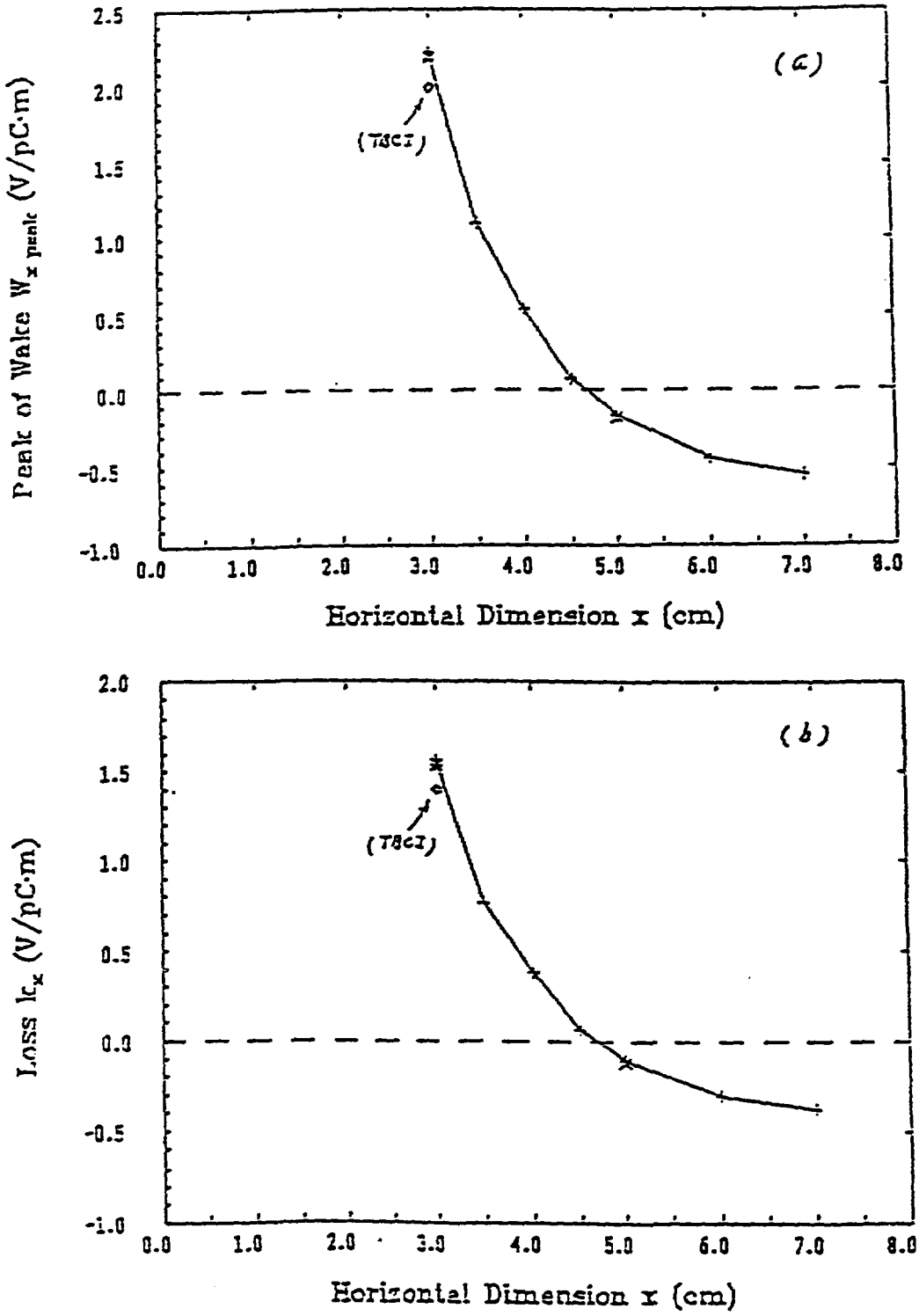

Fig. 8. The first peak of the horizontal wake potential *vs.* x, the half-width of the horizontal side of the rectangular cross section of beam tubes. (see Fig. 7) (b) The horizontal loss factor *vs.* x. The 2-D TBCI results for a circular cross section are also plotted, which are close to the 3-D MAFIA results.

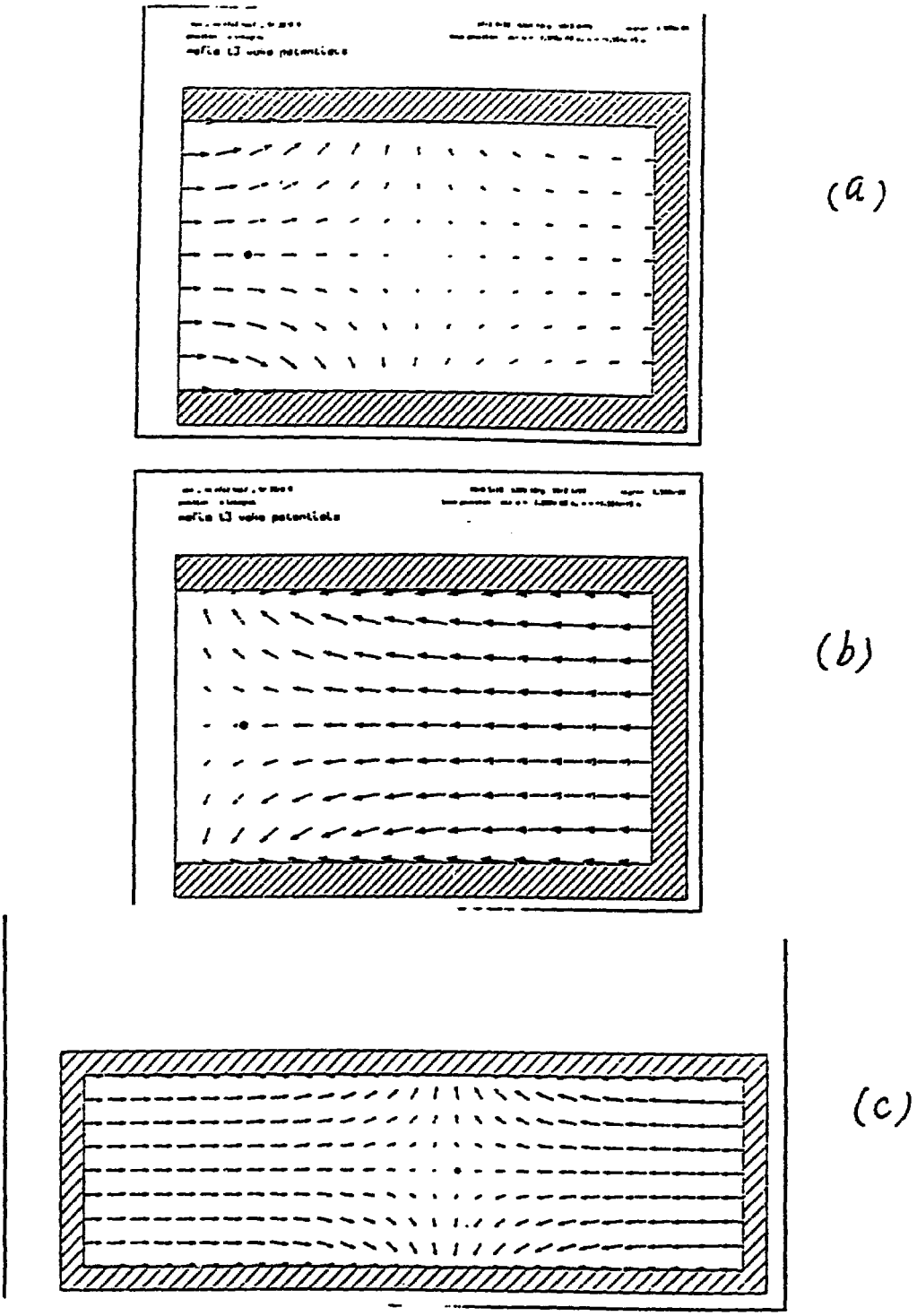

Fig. 9. (a) The dipole component of the horizontal forces. The dot is the location of the beam. The left side line is the vertical axis. (b) The higher order multipoles of the horizontal forces. (c) The total horizontal forces, which tend to kick the horizontally displaced beam back to the center.

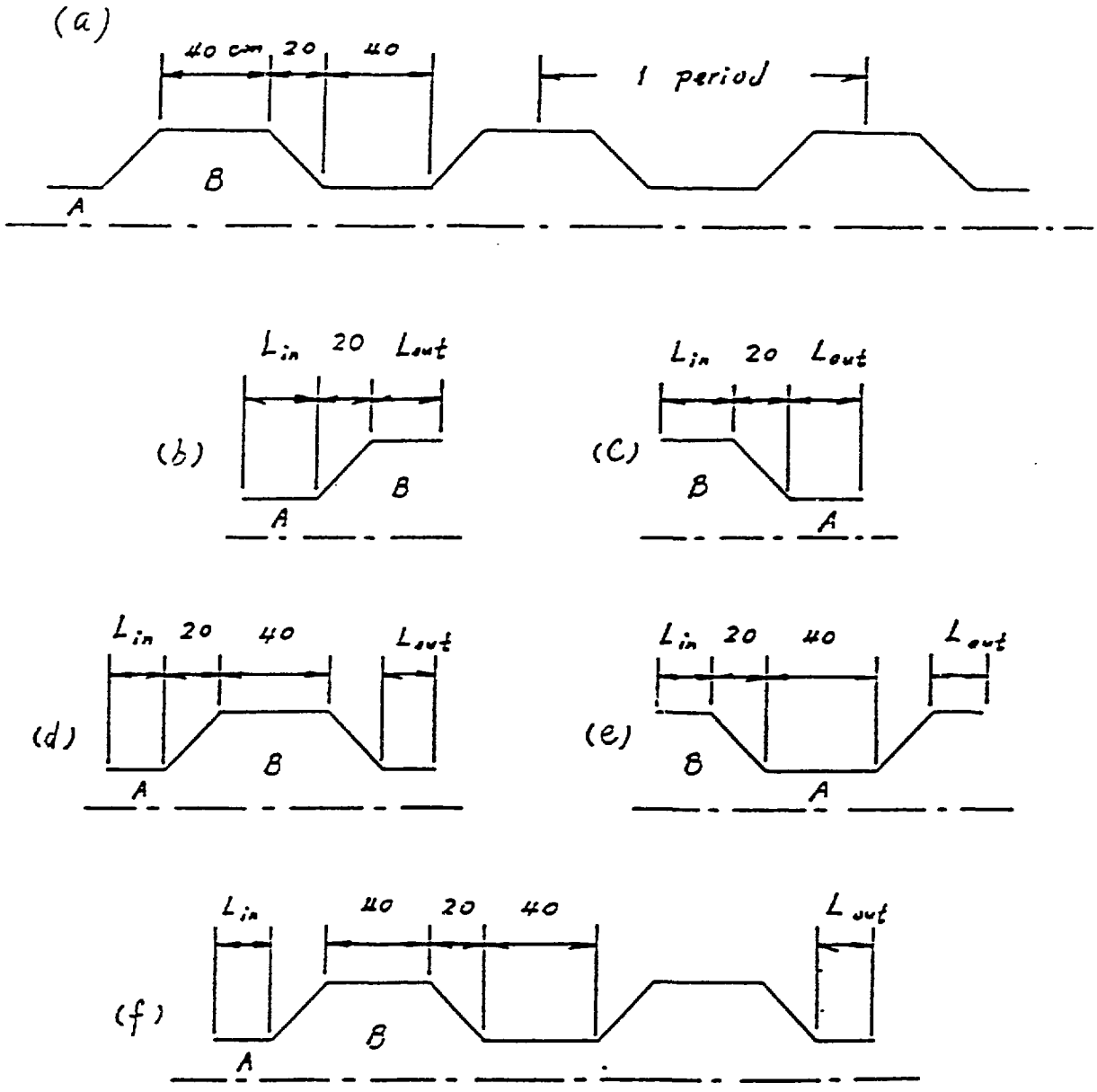

Fig. 10. (a) A periodic structure consists of a series transitions from chmaber to ID section. It is decomposed to (b) *expansion* components and, (c) *pinch* components. These components are then recomposed to form different types of new structures: (d) cavities, (e) scrapers and, (f) 2-period. According to the composition rule, (d) and (e) have the same loss, which is the sum of (b) and (c) and is also equal to half of that of (f). See Table 1 and 2.

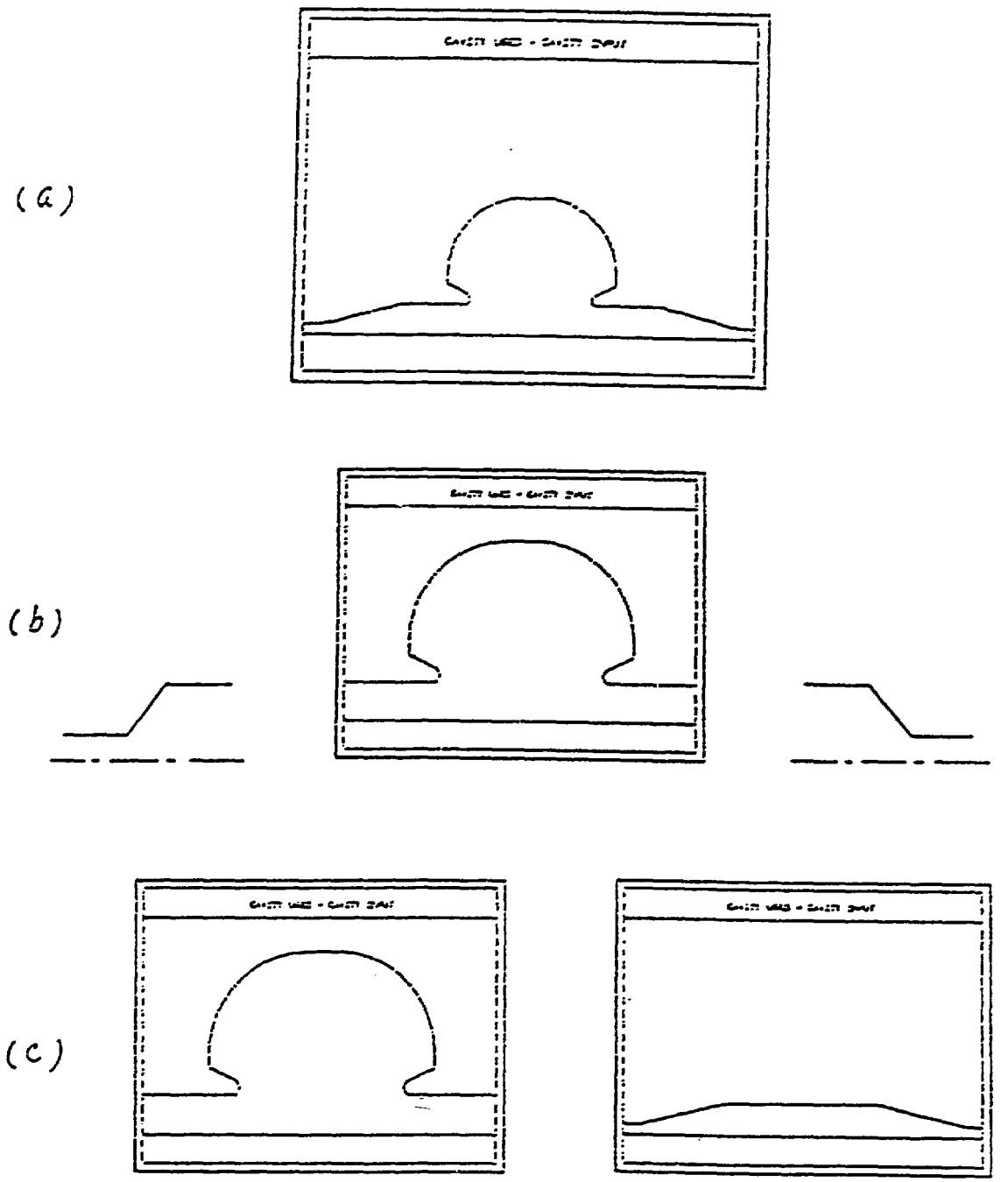

Fig. 11. (a) A complex structure consists of an RF cavity and two tapered parts. (b) This structure is decomposed to three components. (c) These components are then recomposed to form two new structures. Both (a) and (c) give the same loss, (see Table 3) while (c) is easier to compute.

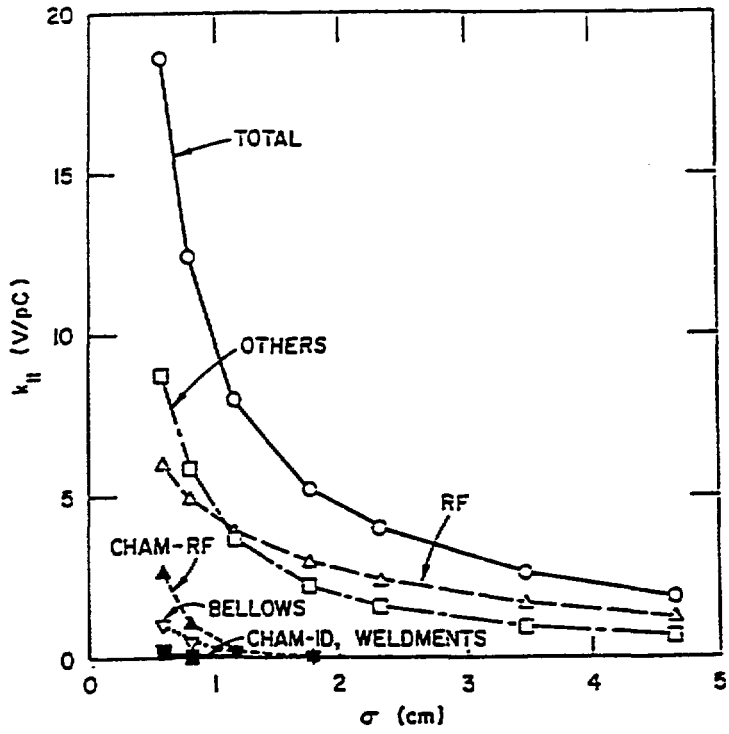

Fig. 12. The logitudinal loss factors of various components of the APS storage ring, and their sum.

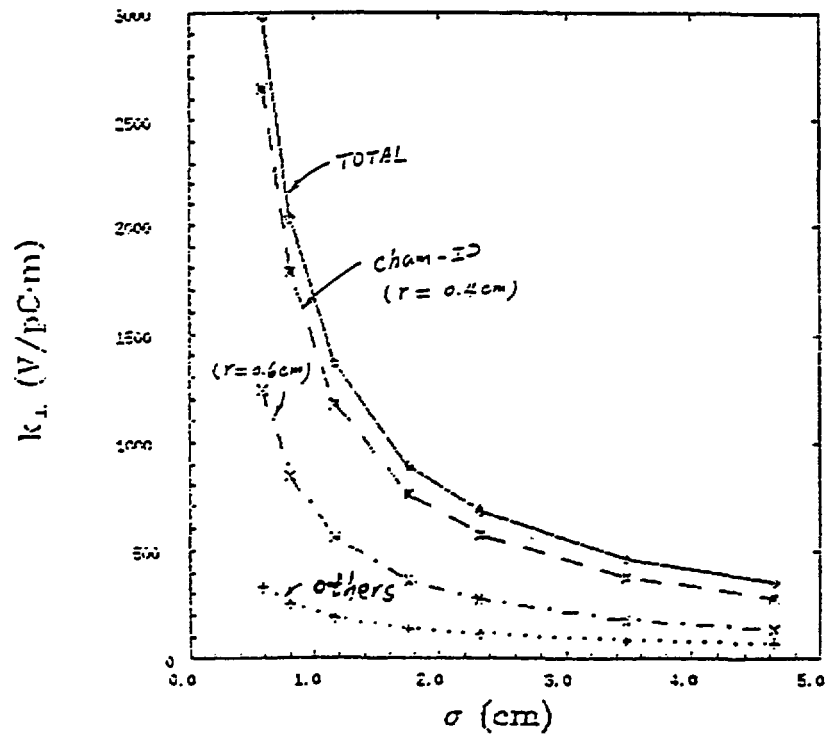

Fig. 13. The transverse loss factors of the APS storage ring. The transitions from chamber to ID section is a dominant contributor.

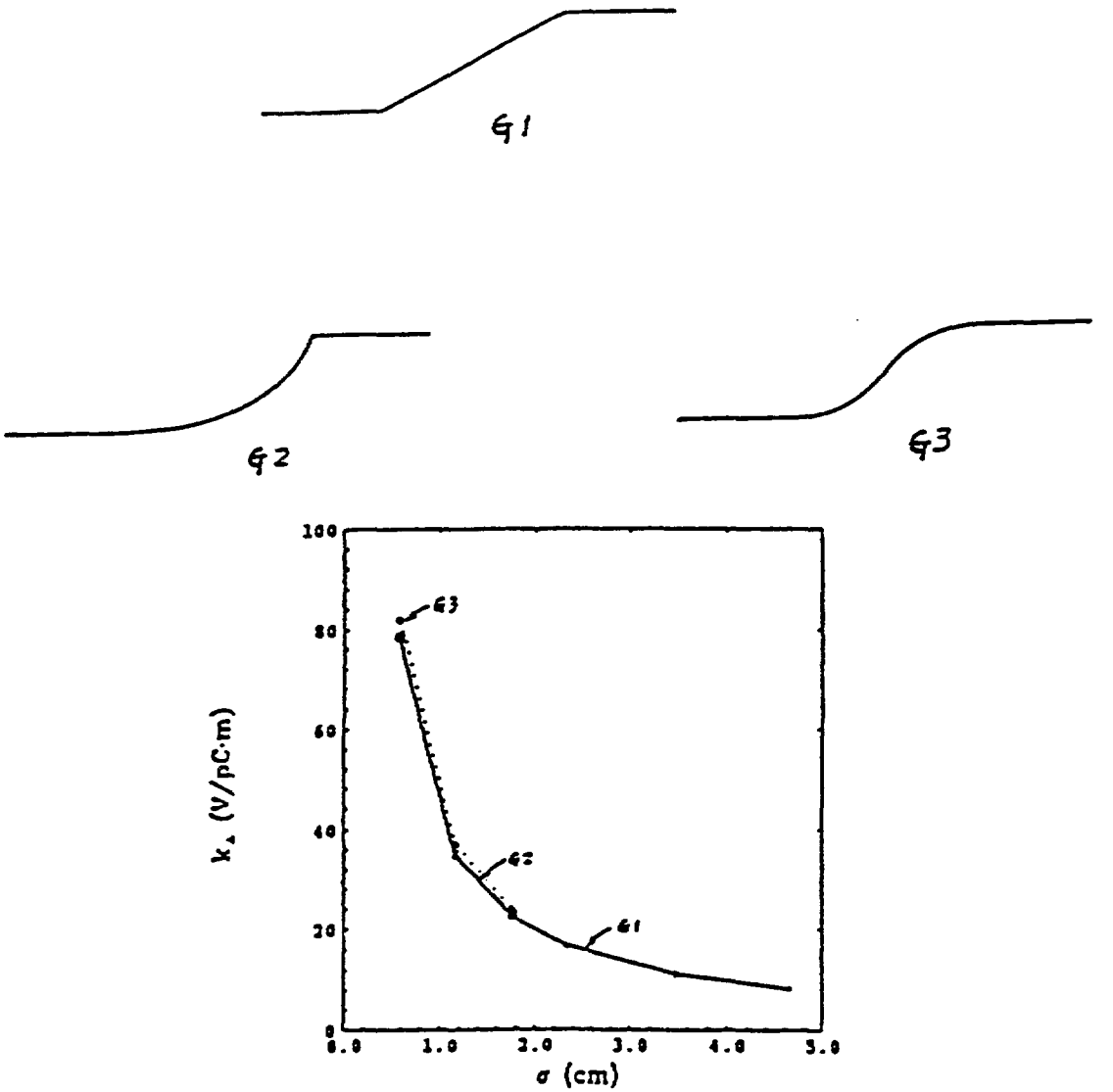

Fig. 14. Three different transition shapes and the corresponding transverse losses.

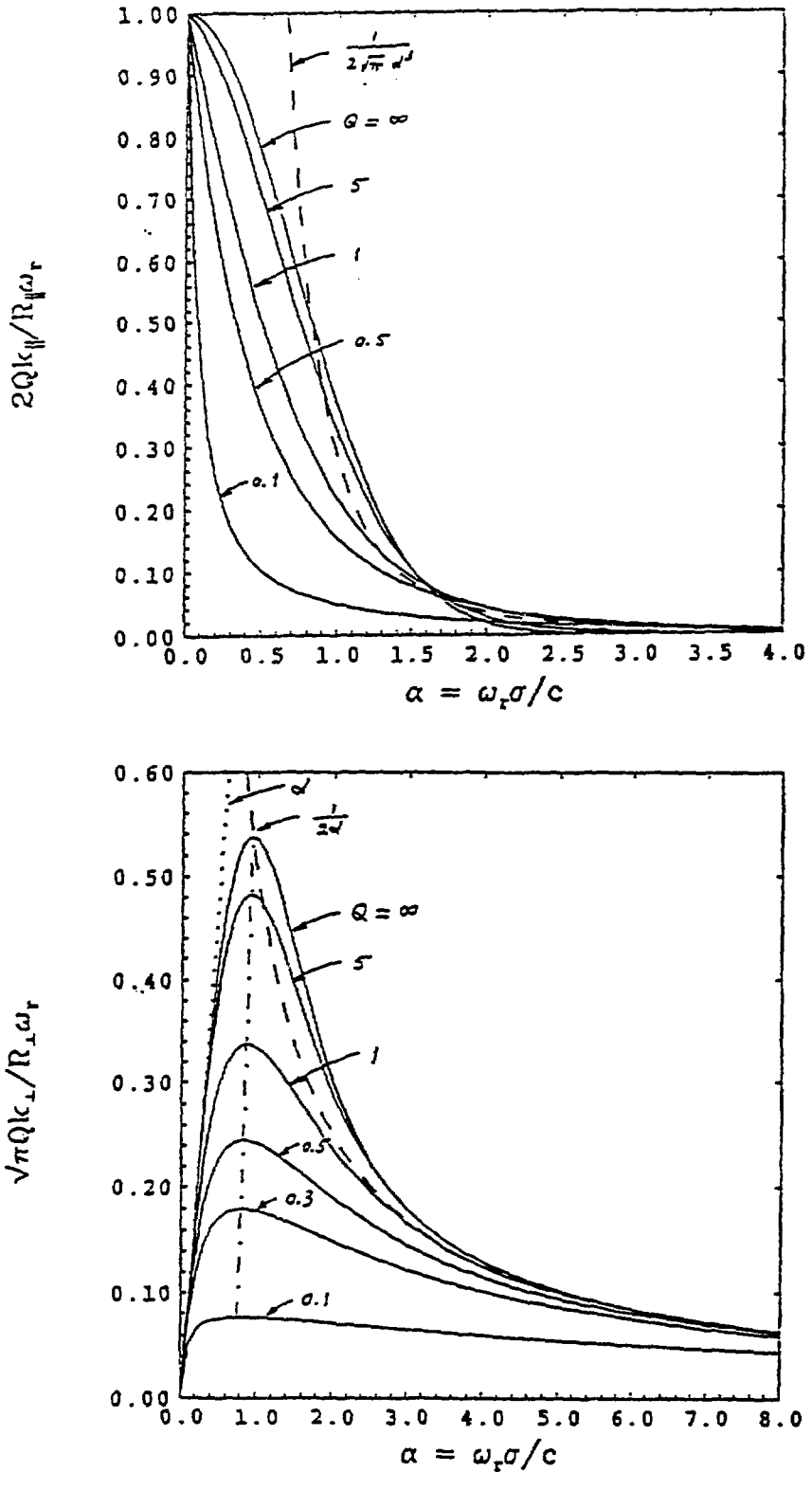

Fig. 15. The normalized loss factors of a broad-band resonator: (a) longitudinal and, (b) transverse.

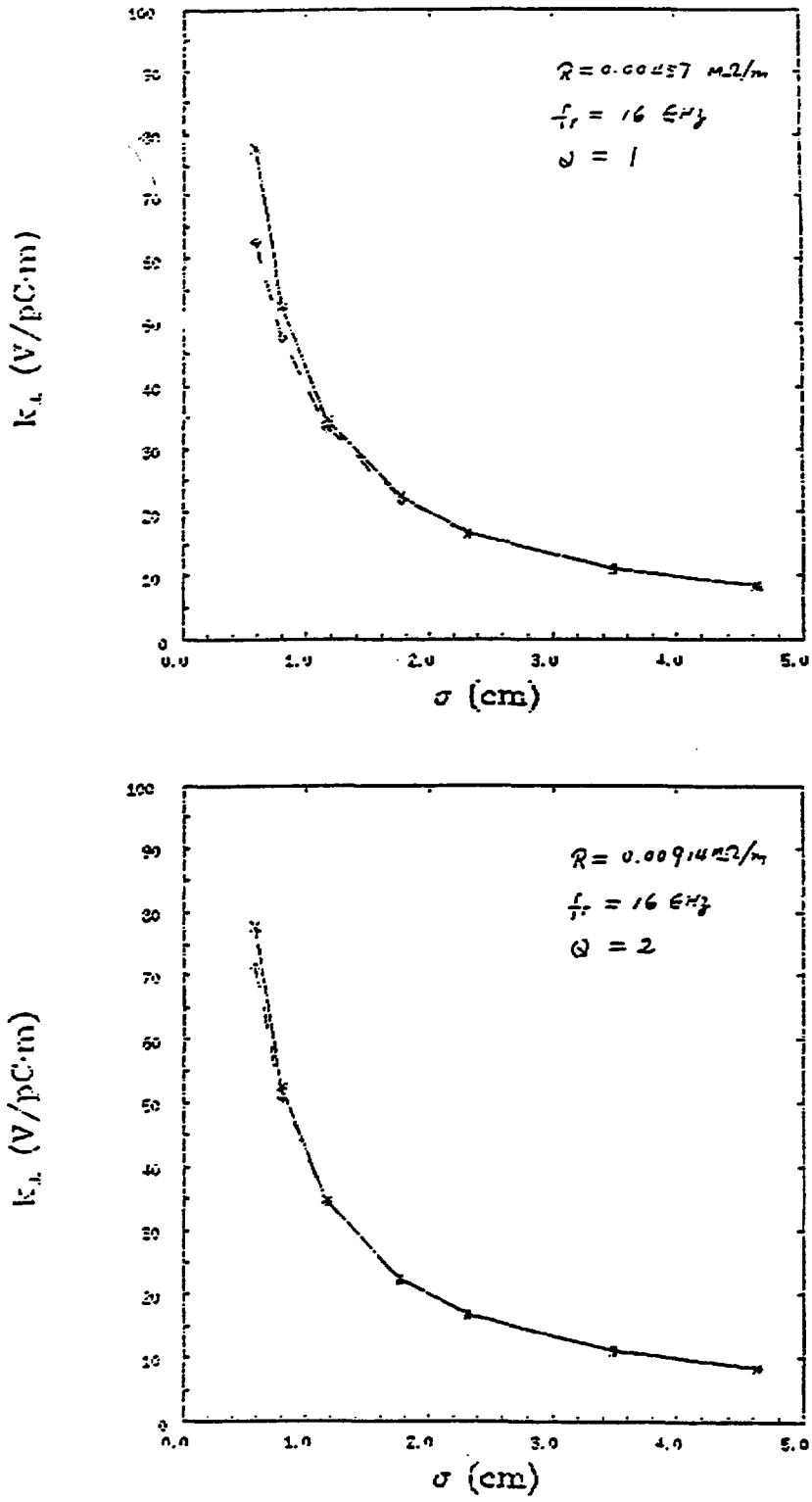

Fig. 16. The transverse losses of a transition from chamber to ID section, and the least-squares fit to a broad-band resonator.

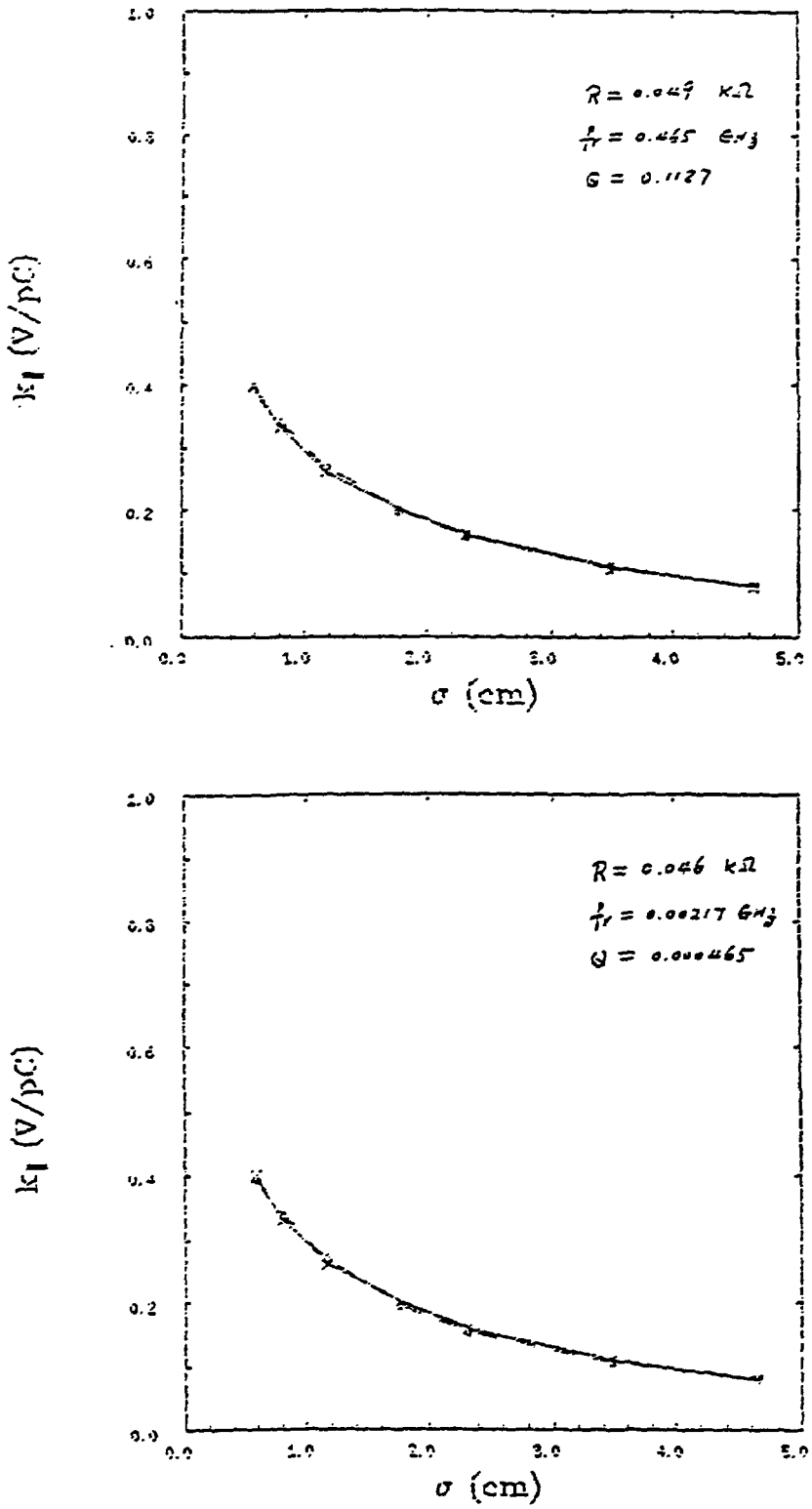

Fig. 17. The longitudinal losses of an RF cavity, and the least-squares fit to a broad-band resonator, using two different weights. The fitted parameters are unphysical.

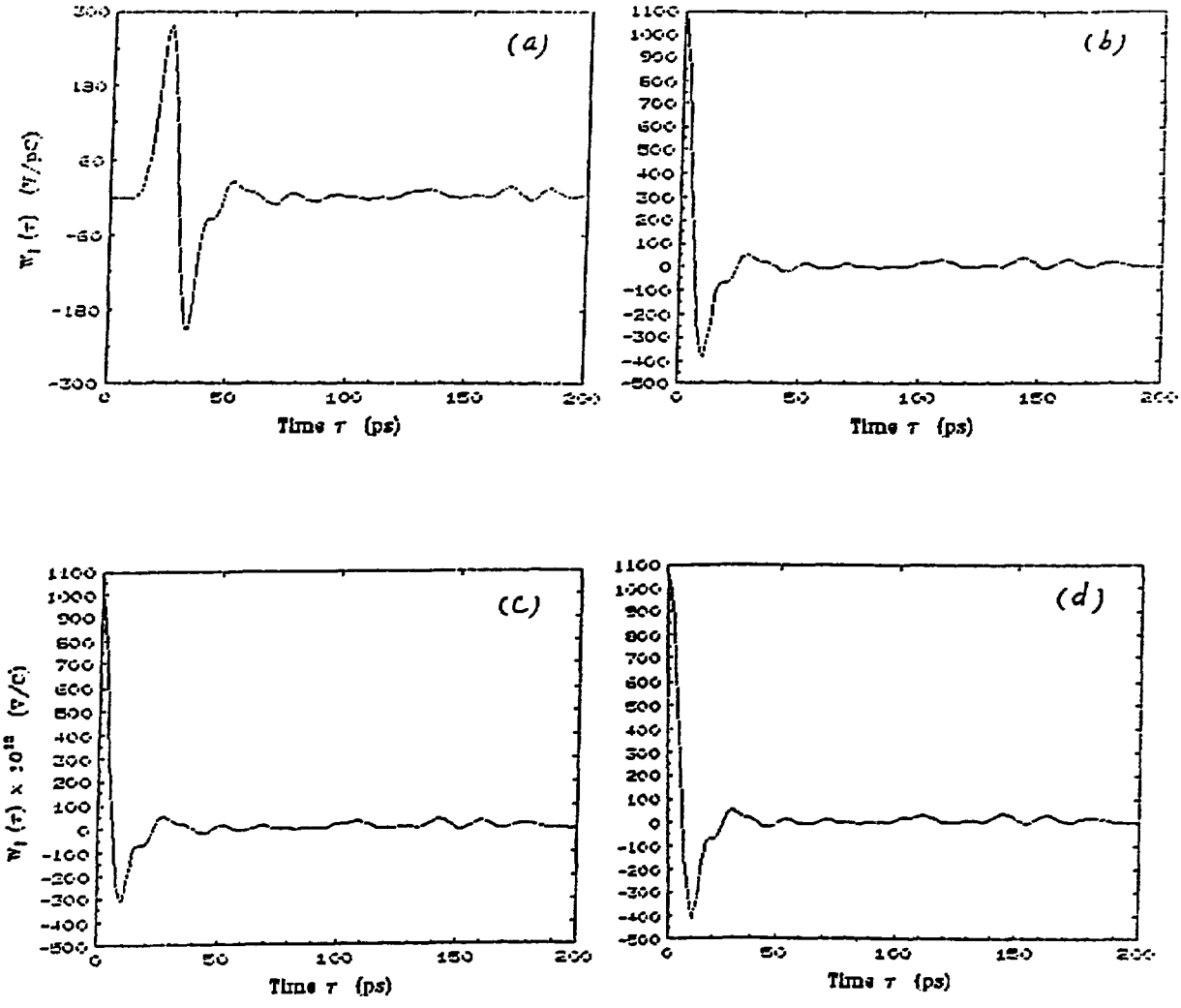

Fig: 18. (a) The longitudinal wake potential, $W_{\|}^{(total)}$, of the APS storage ring, calculated by TBCI for a bunch of $\sigma = 1.5mm$. (b) The longitudinal pseudo-Green function obtained from reflection about the axis at the peak of $W_{\|}^{(total)}$. (c) The longitudinal pseudo-Green function obtained from reflection about the axis at (peak of $W_{\|}^{(total)}$) + 1 mesh. (b) The longitudinal pseudo-Green function obtained from reflection about the axis at (peak of $W_{\|}^{(total)}$) - 1 mesh.

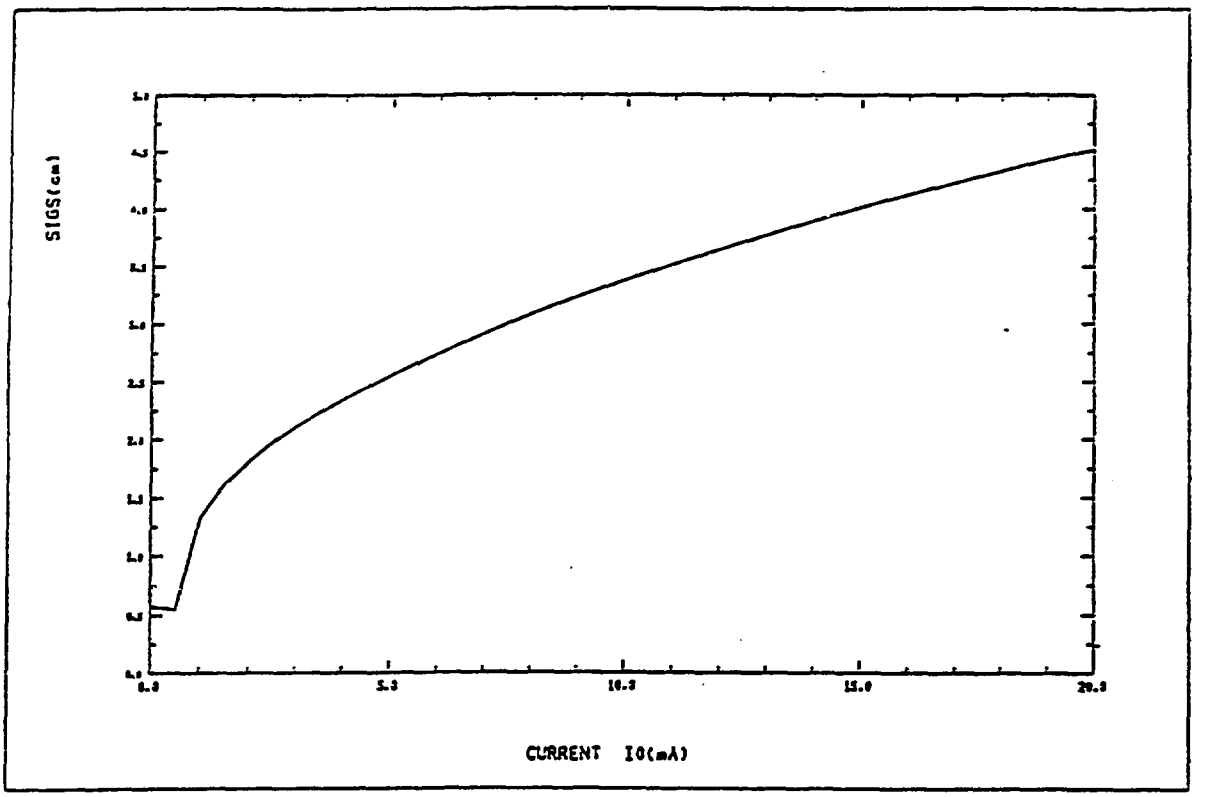

Fig. 19. Bunch lengthening in the APS, calculated by BBI using a broad-band resonator model with $Q = 1$ (turbulence and potential well effects).

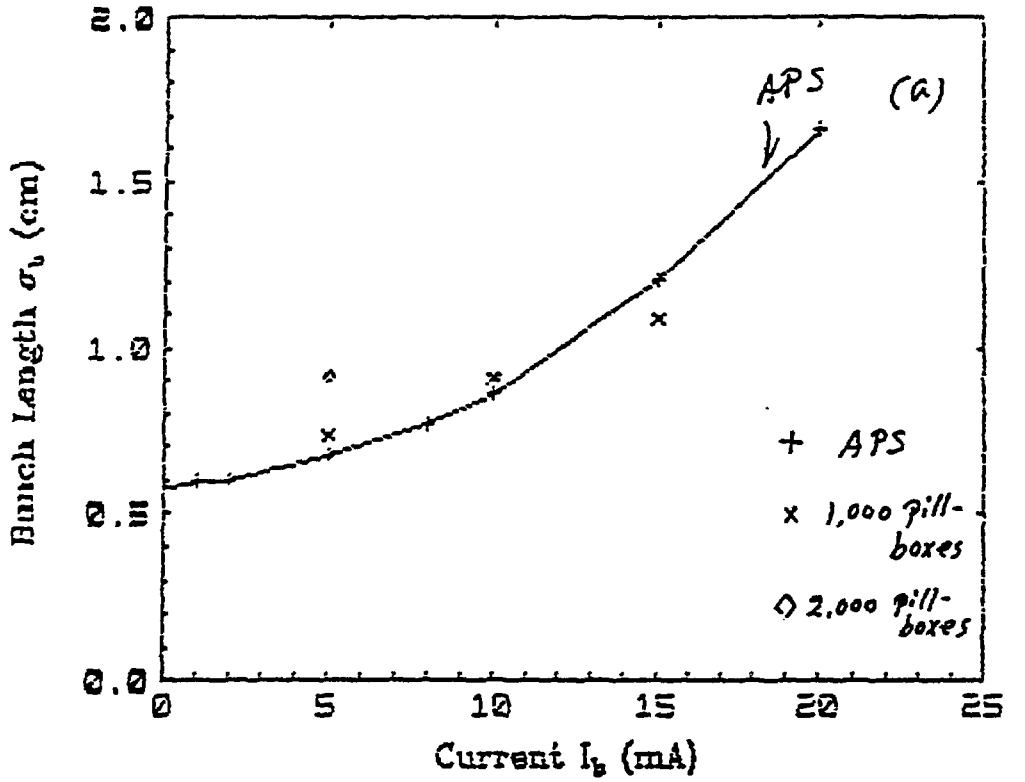

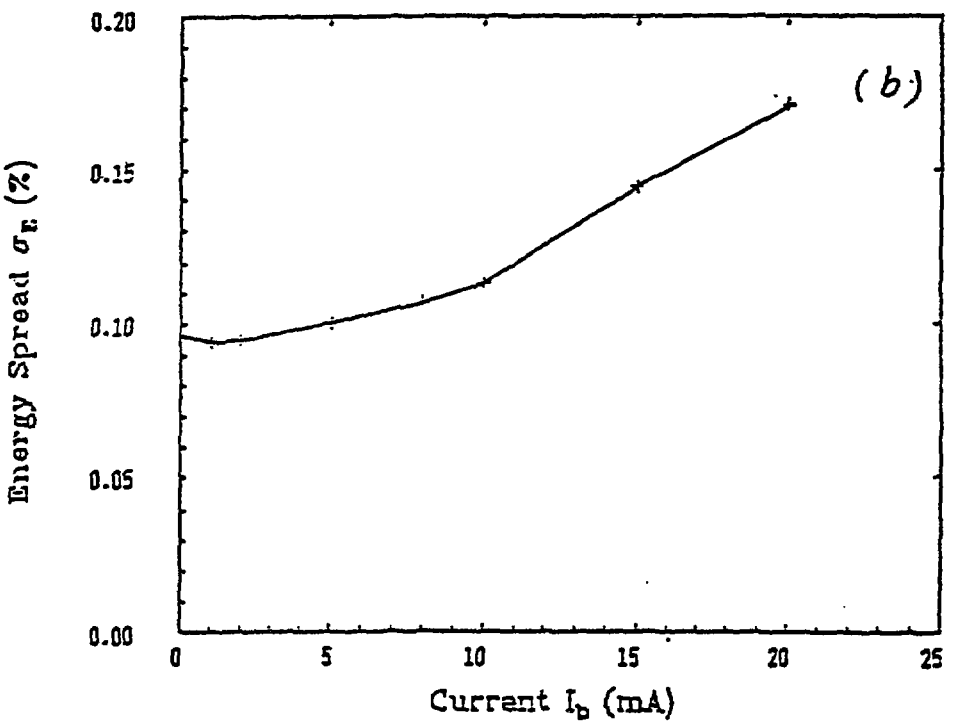

Fig. 20. SIMTRAC calculations using a pseudo-Green function. (a) Bunch lengthening in the APS. The results for a hyperthetic machine consists of thousands of small pill-boxes are also shown. (b) Energy spread in the APS.

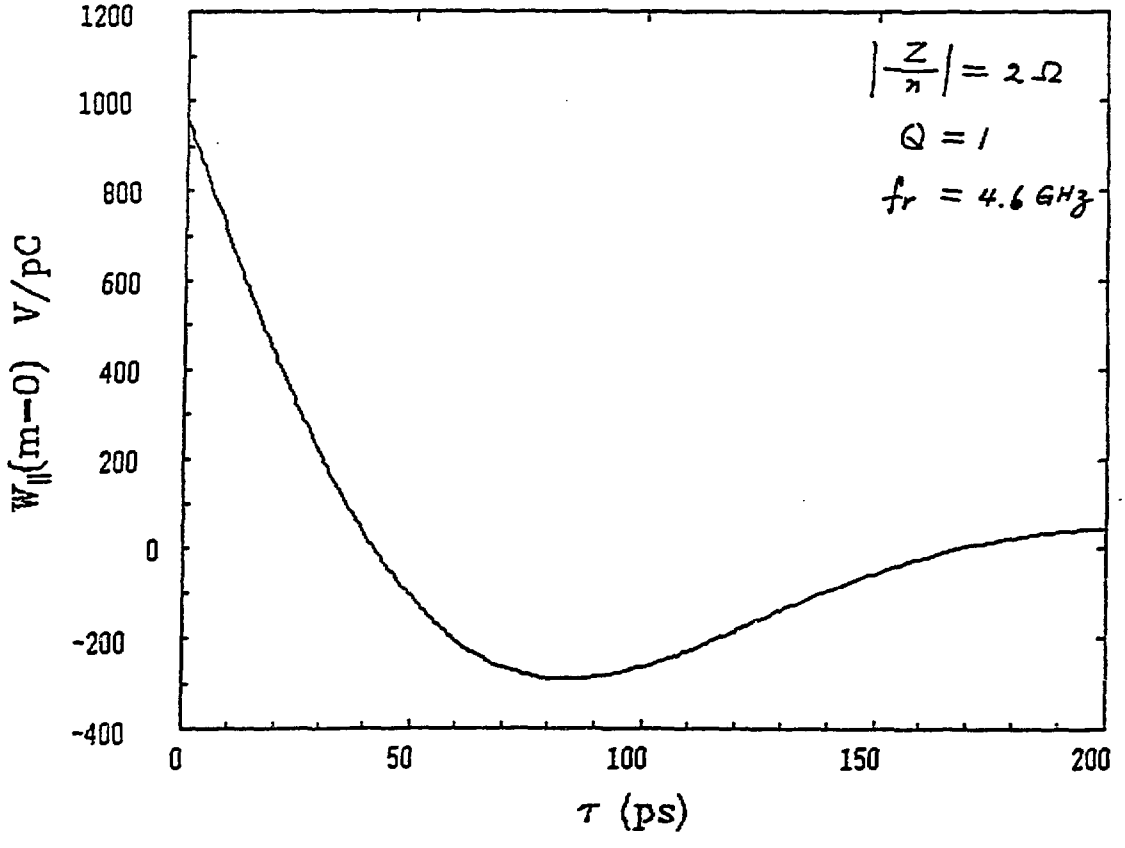

Fig. 21. The longitudinal Green funtion of a broad-band resonator with $Q = 1$, which is very different from the pseudo-Green function (Fig. 18(b)).

Single Bunch Stability in the ESRF

L. Farvacque

ESRF

Argonne National Laboratory
Advanced Photon Source
Impedance and Bunch Instability Workshop
October 31 - November 1, 1989

SINGLE BUNCH STABILITY IN THE ESRF

L. Farvacque

1. Longitudinal wake potential / impedance

   - numerical study of elementary contributions
   - measurements
   - summation of wake potentials
   - broadband model

2. Bunch lengthening / stability

   - potential well distortion (G. Besnier)
   - tracking (M.P. Level)

NUMERICAL SIMULATIONS

time domain analysis performed with TBCI

A cylindrical approximation of individual components of the vacuum chamber has been studied :

- flanges
- transitions between standard cross-section and undulator chamber or RF cavity
- RF cavity

Results are :

- wake potential $W(\tau)$
- loss parameters $k(\sigma_l)$

Limitations of the method are :

- cylindrical symmetry
- size of the problem (mesh limitation)
- minimum bunch length
- computation time

Several bunch lengths have been studied between 5 mm and 20 mm .

EXAMPLE OF RESULTS

" capacitive" impedance : RF cavity

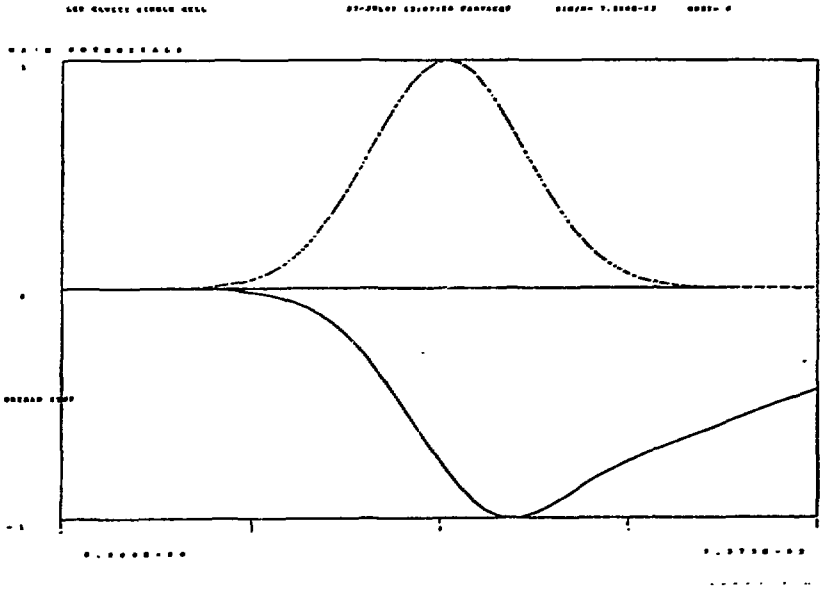

"inductive" impedance : tapered transition

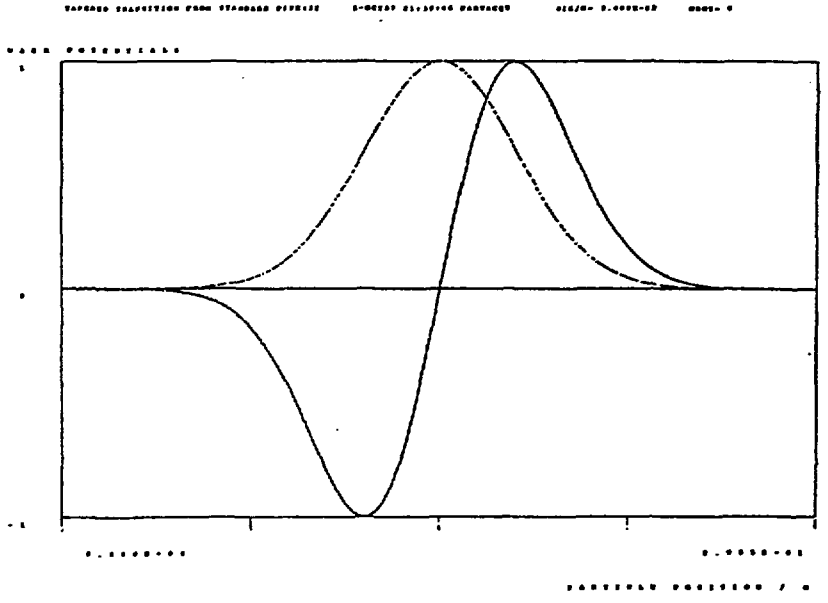

MEASUREMENTS

Measurements are necessary when the cylindrical approximation is not realistic. The coaxial wire method which is used gives a wake potential that can be substitued to the computed wake in the analysis (or added to other components).

1st measurement campaign (september 1988) :

measurements have been performed at CERN, in the time domain (pulse generator + sampling scope).

tested devices consisted in :

- simple geometries to be checked / 2D computations (unshielded bellow ...)
- very crude approximations of 3D elements (slot, crotches...)

Future in-house measurements:

A measurement bench is presently being tested at ESRF, working in the frequency domain (synthesized pulse). First results using the devices already measured at CERN are in excellent agreement.

In both cases, the influence of the axial conducting wire can give significant differences with the real wake potential created in an empty pipe.

COMPARISON WITH TBCI

bellow, l= 102 mm, Ø=102 mm

MEASUREMENT

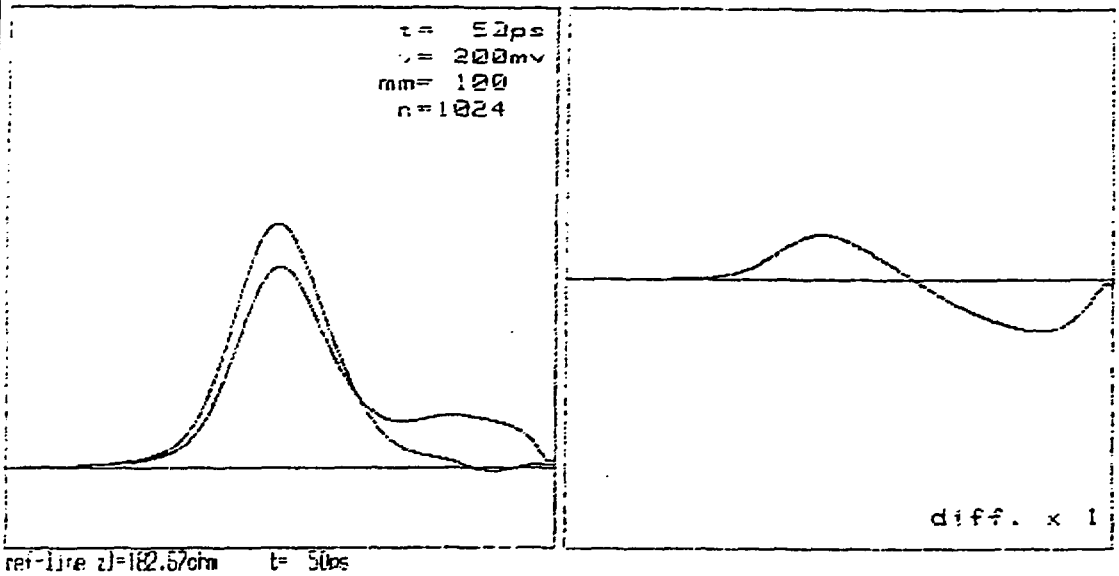

pulse **wake potential**

COMPUTATION

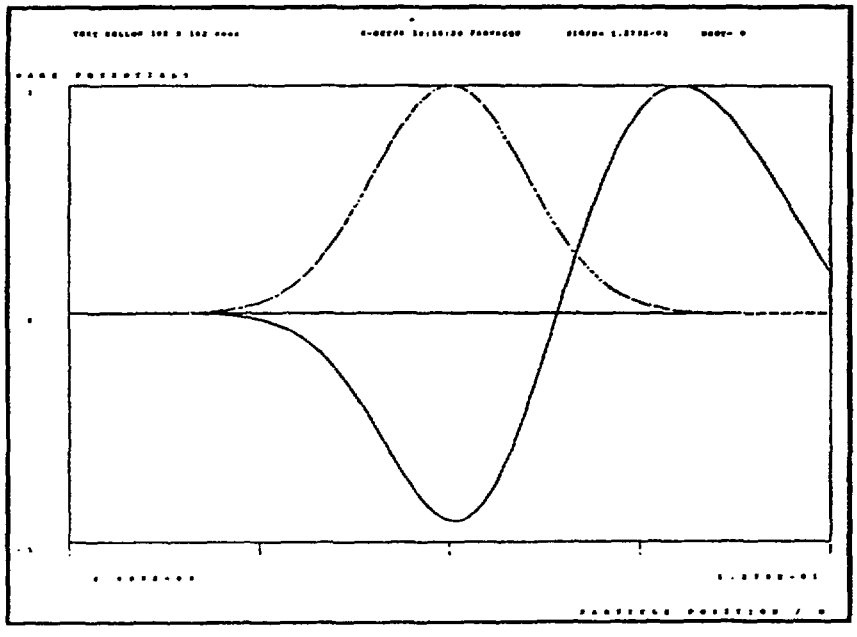

$k_{\parallel}$ = 0.341 V/pC

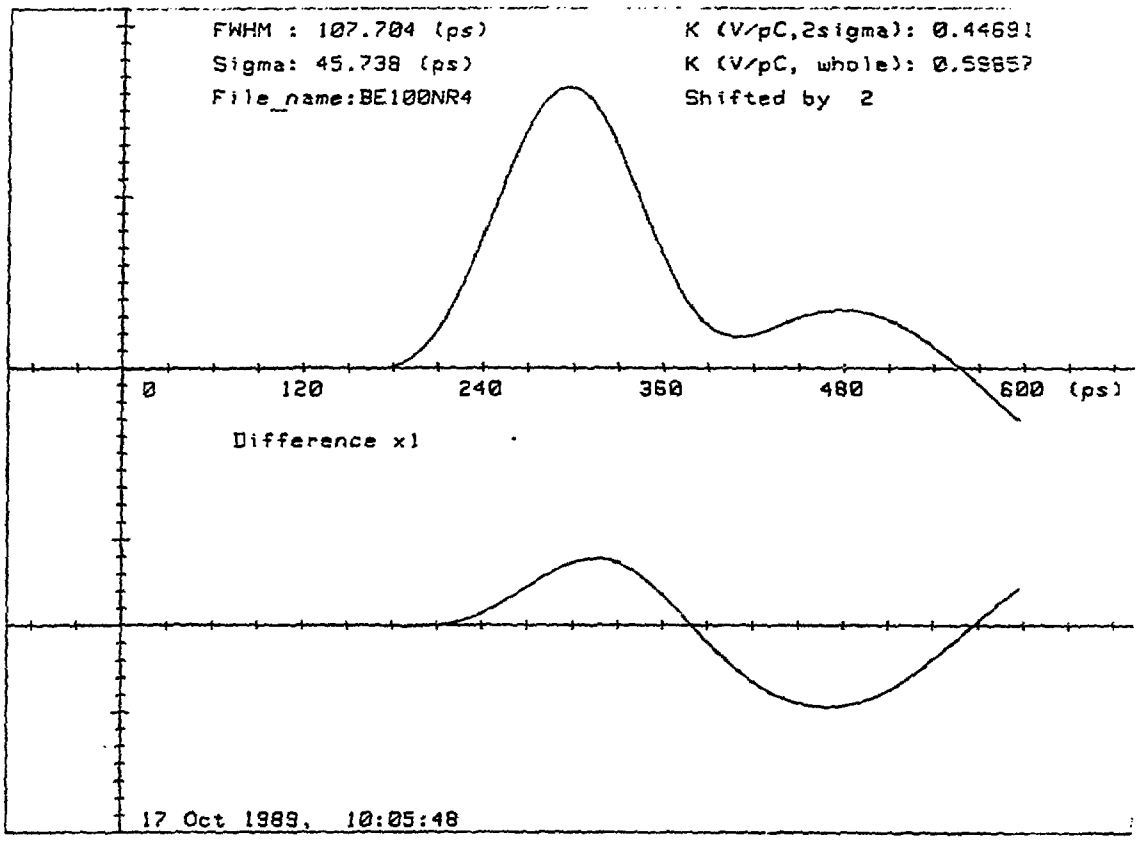
FWHM : 107.704 (ps)
Sigma: 45.738 (ps)
File_name:BE100NR4
K (V/pC,2sigma): 0.44691
K (V/pC, whole): 0.59857
Shifted by 2
0
120
240
360
480
600 (ps)
Difference x1
17 Oct 1989, 10:05:48

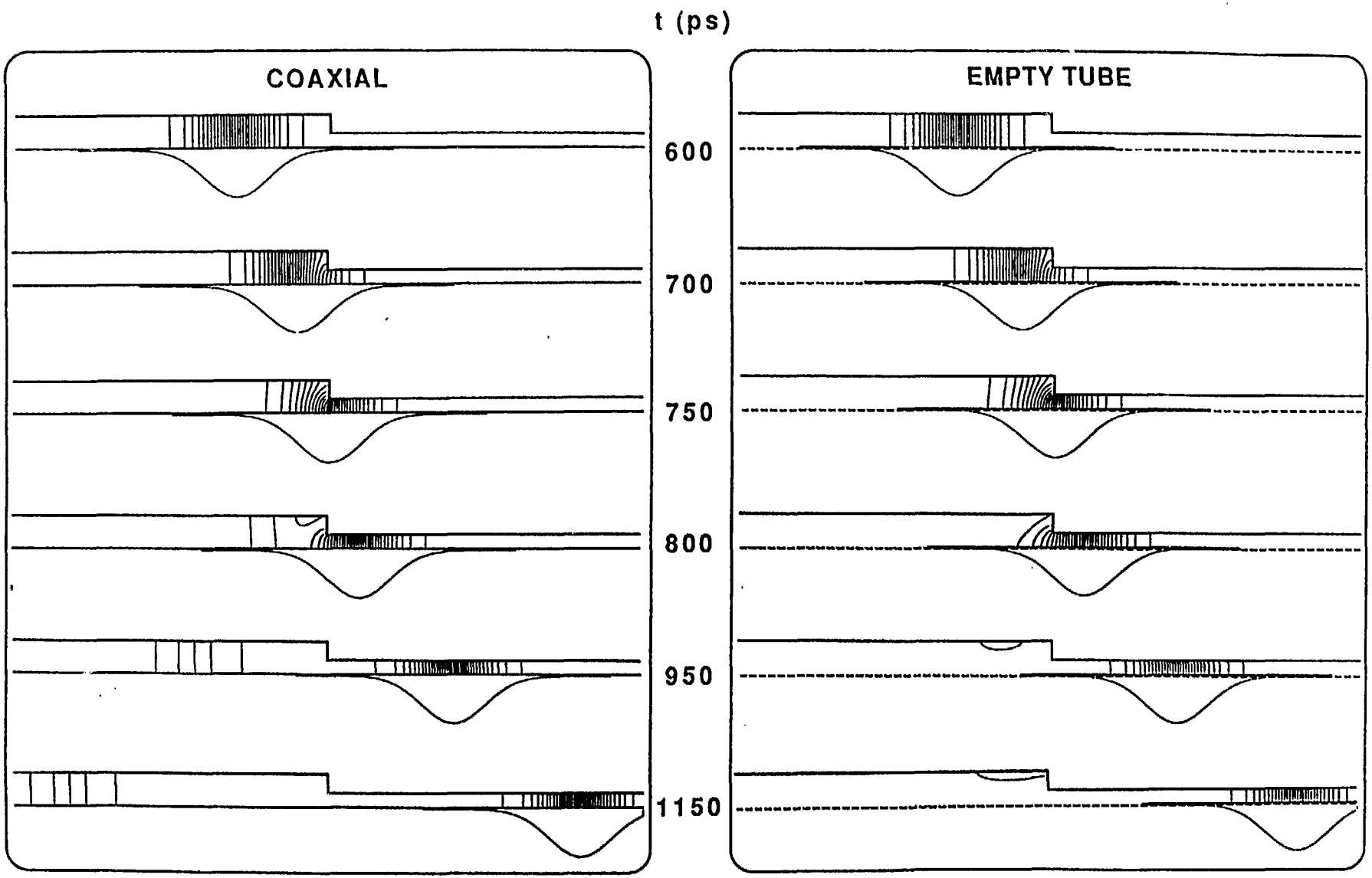

TBCI results

SUMMATION OF WAKE POTENTIALS

Wake potentials (computed or measured) are added before any modelling or approximation is made. Until now, only the main computed wake potentials have been used. This includes :

- tapered transitions to undulator chambers
- transitions to RF cavities
- flanges
- RF cavities

The result for the ESRF vacuum chamber is mainly resistive :

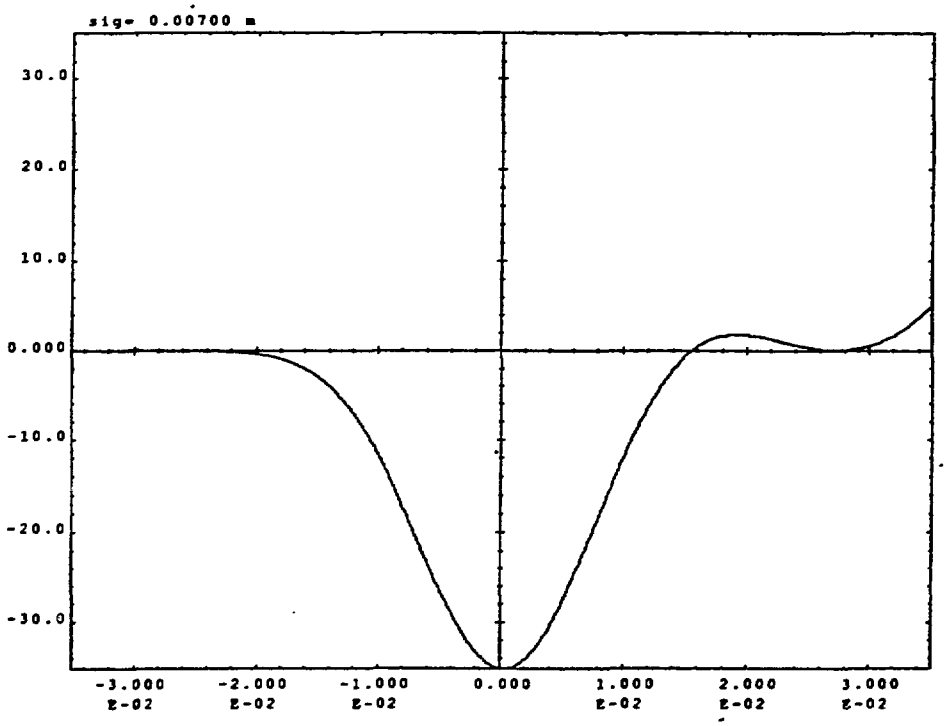

LOSS PARAMETERS

K longitudinal

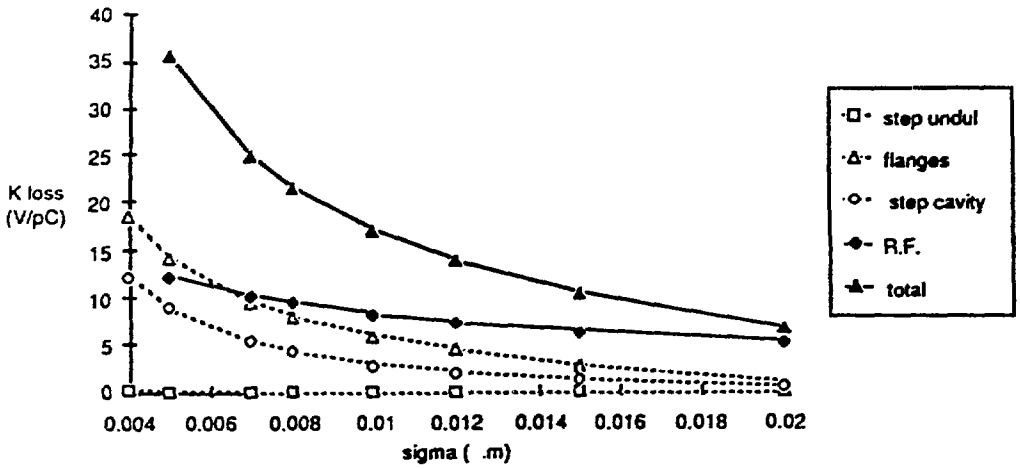

K transverse

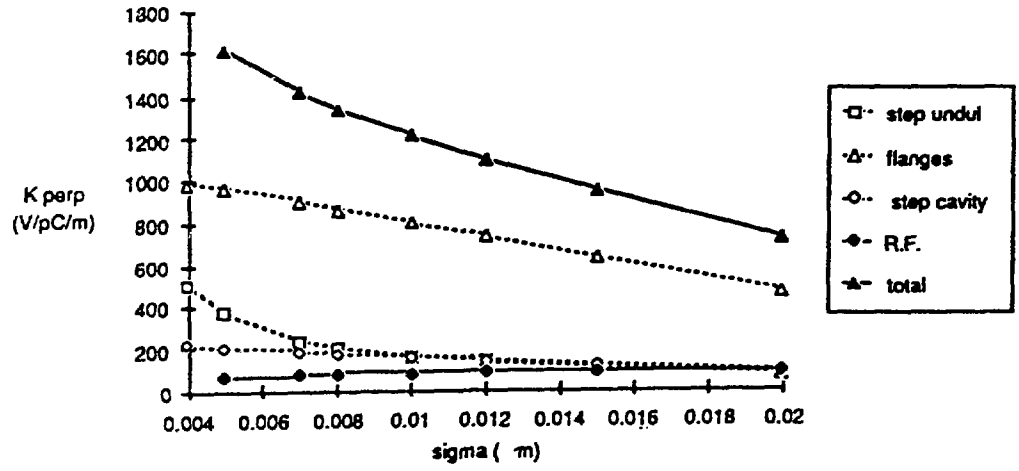

IMPEDANCE MODEL

Broadband resonator model :

$$Z_{//}(\omega) = R_s \frac{1 + j\,Q\left(\frac{\omega_r}{\omega} - \frac{\omega}{\omega_r}\right)}{1 + Q^2\left(\frac{\omega_r}{\omega} - \frac{\omega}{\omega_r}\right)^2}$$

different methods can be used to fit the 3 parameters R_s, ω_r, Q :

1. adjustment of loss parameters:

R_s, ω_r, Q are adjusted so that the loss parameters for bunch lengths between 5 and 20 mm match the estimated values.

Q determination is very approximate

For a given bunch length, the wake potential of the adjusted broad-band resonator is rather different from the desired one.

BROAD-BAND MODEL

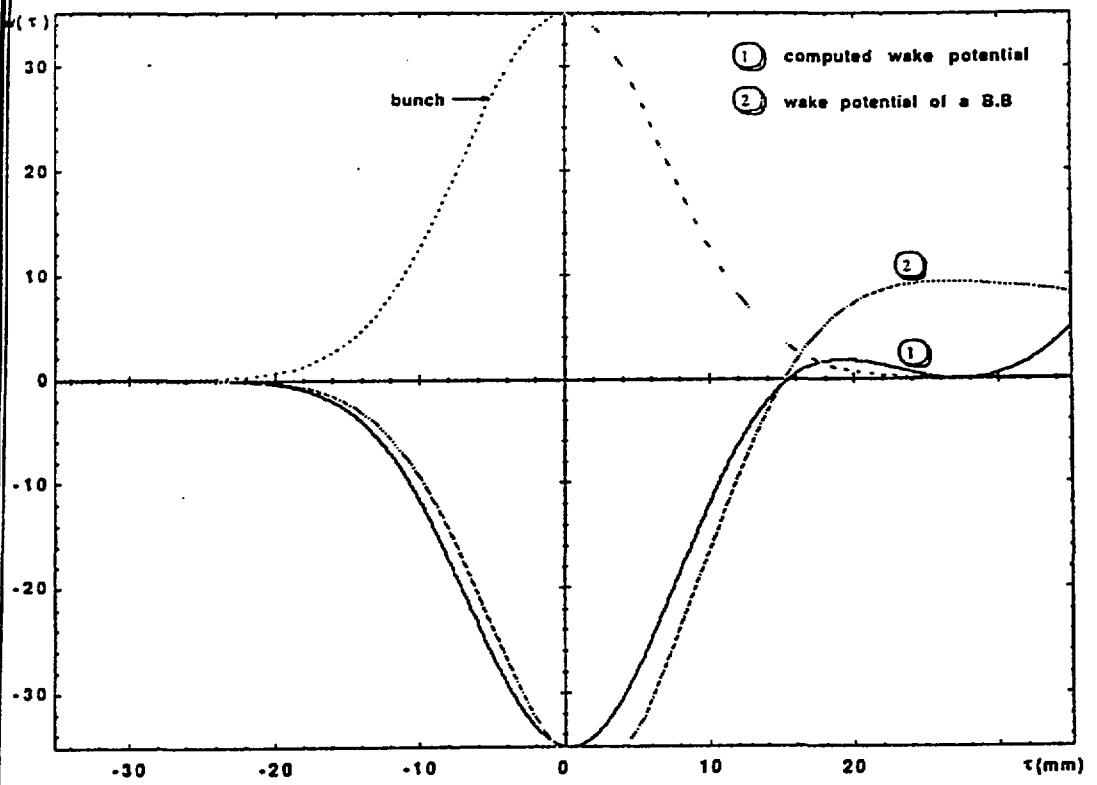

2. Wake potential method:

Parameters of the resonator are adjusted so that the wake potential a bunch (with a gaussian line density $\lambda(\tau)$) is the best approximation of the computed curve:

$$W(\tau) = \frac{1}{2\pi} \int_{-\infty}^{+\infty} \lambda(\omega).\, Z(\omega).\, \exp(j\,\omega\tau).\, d\omega$$

Advantage : very good agreement for the wake potential within the bunch: all short range effects should be correctly represented by the model.

Drawback : the approximation is valid in the vicinity of the choosen bunch length (5 mm to 10 mm in our case) . For a different bunch length (20 mm) we must use a different model.

	f_r (GHz)	R_s (kΩ)	Q
5 mm ≤ σ_l ≤ 10 mm	4.68	2.16	0.055
20 mm ≤ σ_l	4.11	2.91	0.254

Any other impedance model could be fitted with this method (no attempt until now).

BROAD-BAND MODEL

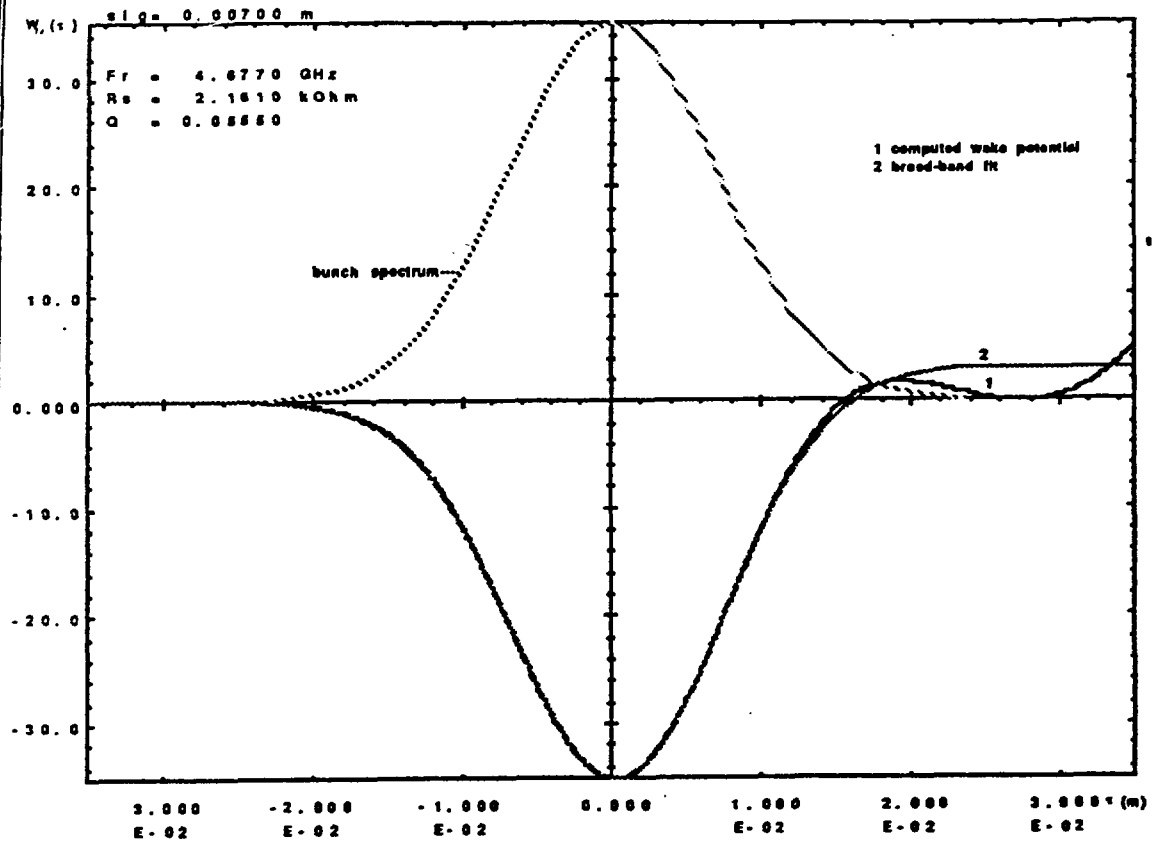

LONGITUDINAL POTENTIAL WELL

Basic equations:

τ time delay

$\lambda_0(\tau)$, $\tilde{\lambda}_0$ (p ω_0) line density of the bunch

$\varepsilon = \dfrac{I}{h\omega_0 \widehat{V_{rf}} \left|\cos\varphi_{s0}\right|}$ intensity parameter

synchrotron motion :

$$\ddot{\tau} = -\omega_{s0}^2 \left(\tau + \varepsilon \frac{2\pi}{\omega_0} W_\lambda(\tau) \right)$$

or in frequency domain

$$\ddot{\tau} = -\omega_{s0}^2 \left(\tau + \varepsilon \sum_p Z_{//p} \widetilde{\lambda_{0p}} e^{jp\omega_0\tau} \right)$$

Hamiltonian :

$$H_0(\tau, \dot{\tau}) = \dot{\tau}^2/2 + U_{eff}$$

where the potential U_{eff} includes contribution from rf potential and wake potential of the bunch :

$$U_{eff}(\tau) = \omega_{s0}^2 \left(\tau^2/2 + \varepsilon \frac{2\pi}{\omega_0} S_\lambda(\tau) \right)$$

S_λ is the "step function response", such that

$$W_\lambda(\tau) = \frac{dS_\lambda}{d\tau}$$

Vlasov equation for $f_0(\tau,\dot{\tau})$ longit. distribution function :

$$\dot{\tau}\frac{\partial f_0}{\partial \tau}+\ddot{\tau}\frac{\partial f_0}{\partial \dot{\tau}}=0$$

a gaussian distribution of momentum expressed as:

$$f_0(\tau,\dot{\tau})=\lambda_0(\tau)\frac{\exp\left(-\dot{\tau}^2/2\sigma_{\dot{\tau}}^2\right)}{\sqrt{2\pi}\,\sigma_{\dot{\tau}}}, \qquad \sigma_{\dot{\tau}}=\omega_{s0}\sigma_{\tau 0}=\text{constant}$$

leads to :

$$\frac{\partial \lambda_0}{\partial \tau}=-\lambda_0(\tau)\frac{1}{\sigma_{\tau 0}^2}\left(\tau+\varepsilon\frac{2\pi}{\omega_0}W_\lambda(\tau)\right)$$

and after integration

$$\lambda_0(\tau)=C\exp\left\{-\left(\frac{\tau^2}{2}+\varepsilon\frac{2\pi}{\omega_0}S_\lambda(\tau)\right)/\sigma_{\tau 0}^2\right\}$$

(Haissinski equation)

S_λ depends on the unknown function λ_0 :

analytical solutions have been derived for

pure inductance	(B. Zotter)
pure resistance	(A.G. Ruggiero)

a numerical solution is used in the ESRF case with the broad-band resonator model

BUNCH LENGTHENING

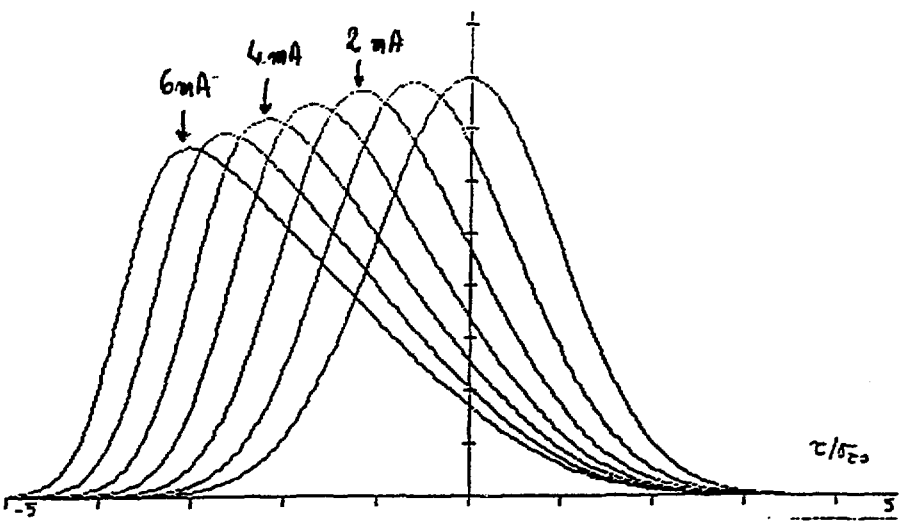

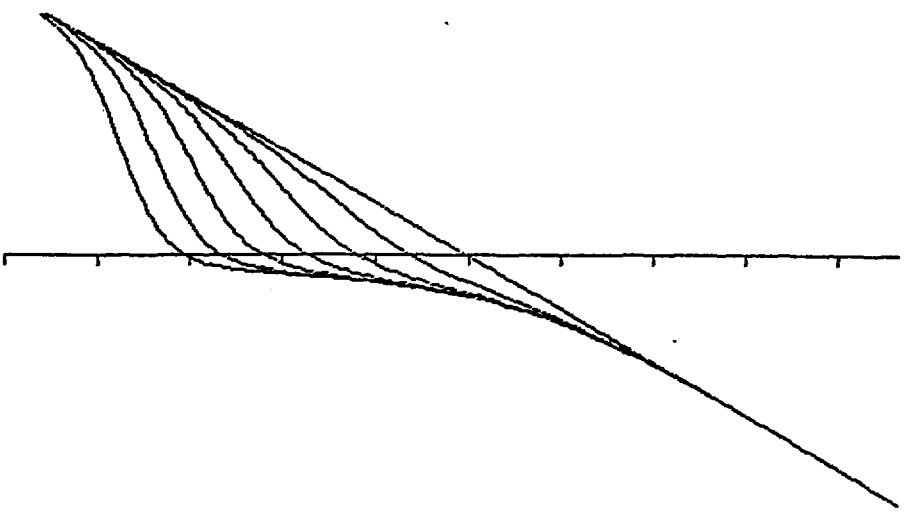

pure resistive impedance R_s = 2.16 kΩ

NUMERICAL SOLUTION

$$\lambda_0^{(n)}(\tau) = C^{(n)} \exp\left\{ -\left(\frac{\tau^2}{2} + \varepsilon^{(n)} \frac{2\pi}{\omega_0} S_\lambda^{(n-1)}(\tau) \right) / \sigma_{\tau 0}^2 \right\}$$

λ_0 is initialized with a gaussian ($\varepsilon^{(0)} = 0$).
iterative $\varepsilon^{(n)}$ increase + relaxation

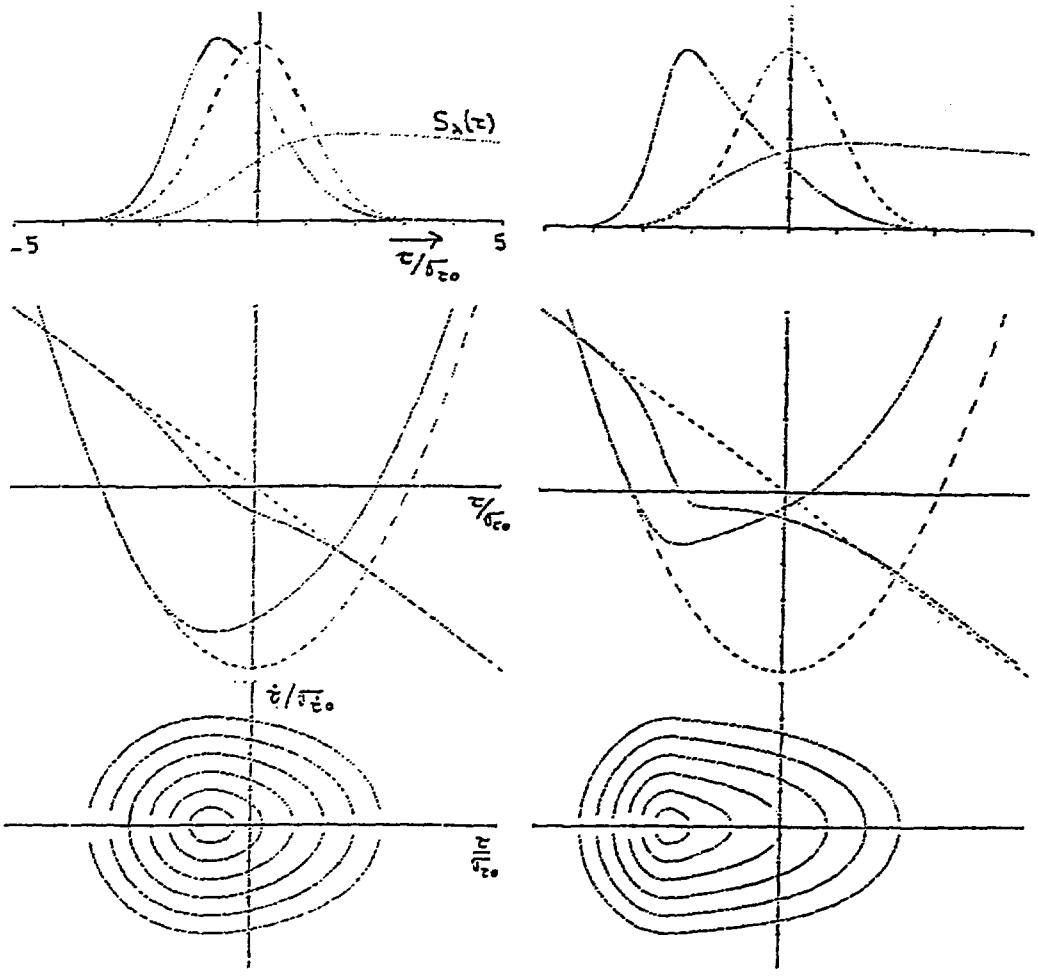

I = 3 mA

I = 7.5 mA

BUNCH LENGTHENING

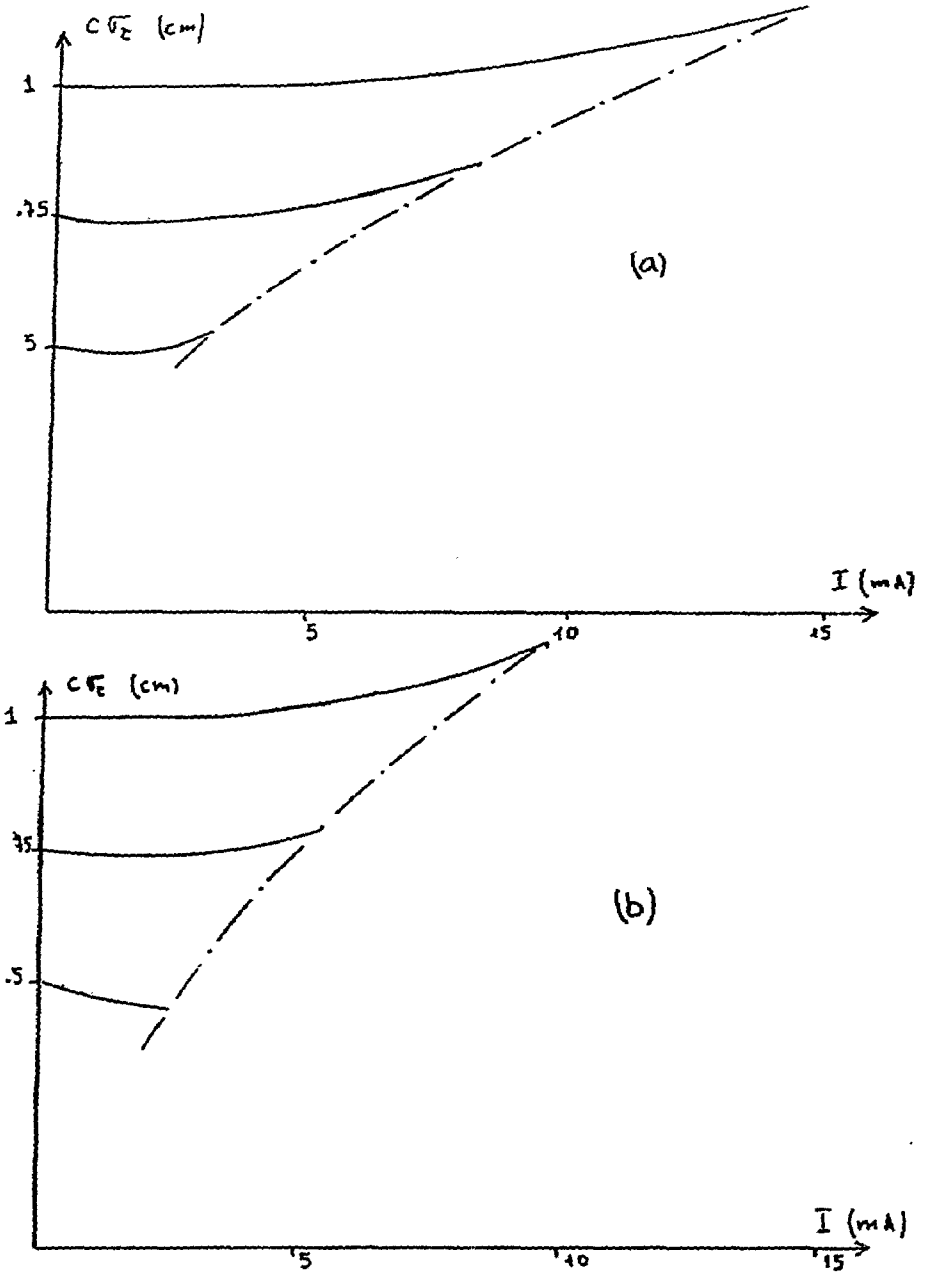

(a) Resonator 1 (5 mm ≤ σ_l ≤ 10 mm)

(b) Resonator 2 (20 mm ≤ σ_l)

MOMENTS OF THE LINE DENSITY

the bunch shape can be estimated knowing the first moments of the line density function :

barycentre $\quad \bar{\tau} = m_1 = \int \tau . \lambda_0(\tau) . d\tau$

rms length $\quad \sigma_\tau^2 = m_2 = \int \left(\tau - \bar{\tau}\right)^2 . \lambda_0(\tau) . d\tau$

skewness $\quad s = \dfrac{m_3}{\sigma_\tau^3} = \int \left(\tau - \bar{\tau}\right)^3 . \lambda_0(\tau) . d\tau$

approximation :

$$\frac{\partial \lambda_0}{\partial \tau} + \frac{\tau}{\sigma_{\tau 0}^2} \lambda_0(\tau) = -\frac{\varepsilon}{\sigma_{\tau 0}^2} \lambda_0(\tau) \sum_p Z_{//p} \widetilde{\lambda_{0p}} e^{jp\omega_0 \tau}$$

$\widetilde{\lambda_{0p}}$ is approximated by the spectrum of a gaussian with rms σ_τ . Coefficients are developped to 1st order in ε :

$$\bar{\tau} = -\varepsilon \sum_p \mathrm{Re}\left(Z_{//p}\right) \widetilde{\lambda_{0p}}^2$$

$$\frac{\sigma_\tau^2}{\sigma_{\tau 0}^2} = 1 + \frac{\varepsilon}{\omega_0 \sigma_{\tau 0}^2} \sum_p \mathrm{Im}\left(\frac{Z_{//p}}{p}\right) \left(p\, \omega_0 \sigma_\tau\right)^2 \widetilde{\lambda_{0p}}^2$$

$$s = \frac{\varepsilon}{\omega_0 \sigma_{\tau 0}^2} \sum_p \mathrm{Re}\left(\frac{Z_{//p}}{p}\right) \left(p\, \omega_0 \sigma_\tau\right)^3 \widetilde{\lambda_{0p}}^2$$

LONGITUDINAL STABILITY

Mode coupling cannot explain the turbulent instability threshold :

$m = \pm 1 : \omega_c^2 = \omega_{s0}^2$: the coherent shift is exactly balanced by the incoherent shift

$m = 1,2$: the two modes are decoupled

The threshold has then to be estimated by crude assumptions on potential well or bunch shape distortions. It is related to the appearance of a null rf slope.

In the ESRF case, this threshold corresponds to a value of the asymetry $s_{th} \approx 0.6$. Above the threshold, the bunch lengthens with this constant asymetry value.

TRACKING

Simulation has been performed with SIMTRAC (D. Brandt). Longitudinal and transverse motion of N super particles is studied with damping and wakefields.

Wakefields are concentrated in RF-stations. They are calculated from a broad-band resonator model.

Parameters :

Energy	6 GeV
revolution time	2.833 μs
Circumference	849.39 m
rms energy spread	6.18 MeV
Damping time τ_E	3.7 ms
τ_z	7.4 ms
Vertical tune	11.2
Vertical emittance	$6.2\ 10^{-10}$ m.rad
Averaged β_z	12 m
Harmonic number	992
RF Voltage	9.9 MV
Radiation losses	7.48 Mev
Momentum compaction	$2.82\ 10^{-4}$
Bunch length	5.3 mm
Synchrotron frequency	$6.68\ 10^{-3}$

TRACKING PARAMETERS :

500 Particles. 5000 Turns ~ 3.8 τ_E

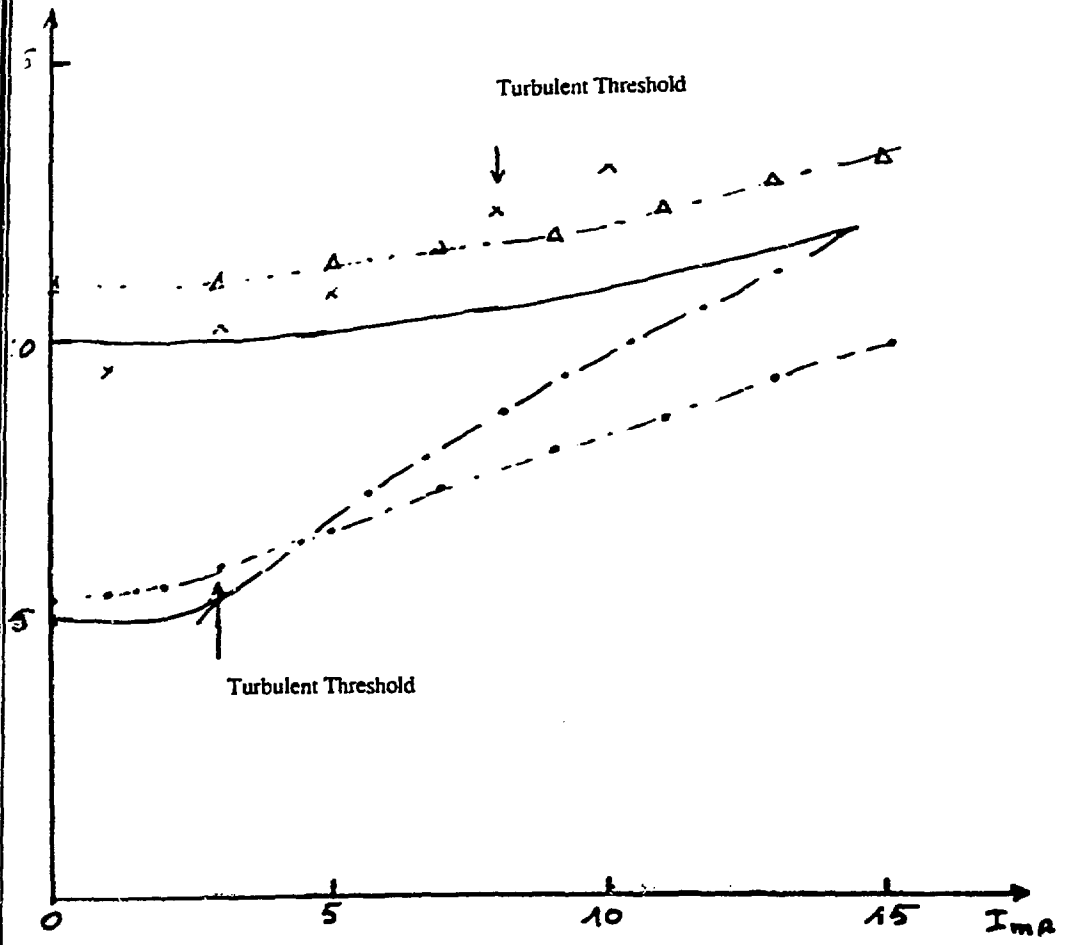

Bunch lengthening 1st Resonator

— Besnier results

⊼ SIMTRAC results

•	$\alpha = 2.64\ 10^{-4}$	V = 9.9 Mv	$\gamma_S = 6.7\ 10^{-3}$
Δ	$\alpha = 10.4\ 10^{-4}$	V = 9.9 Mv	$\gamma_S = 1.33\ 10^{-2}$
×	$\alpha = 4.5\ 10^{-4}$	V = 8.4 Mv	$\gamma_S = 6.7\ 10^{-3}$

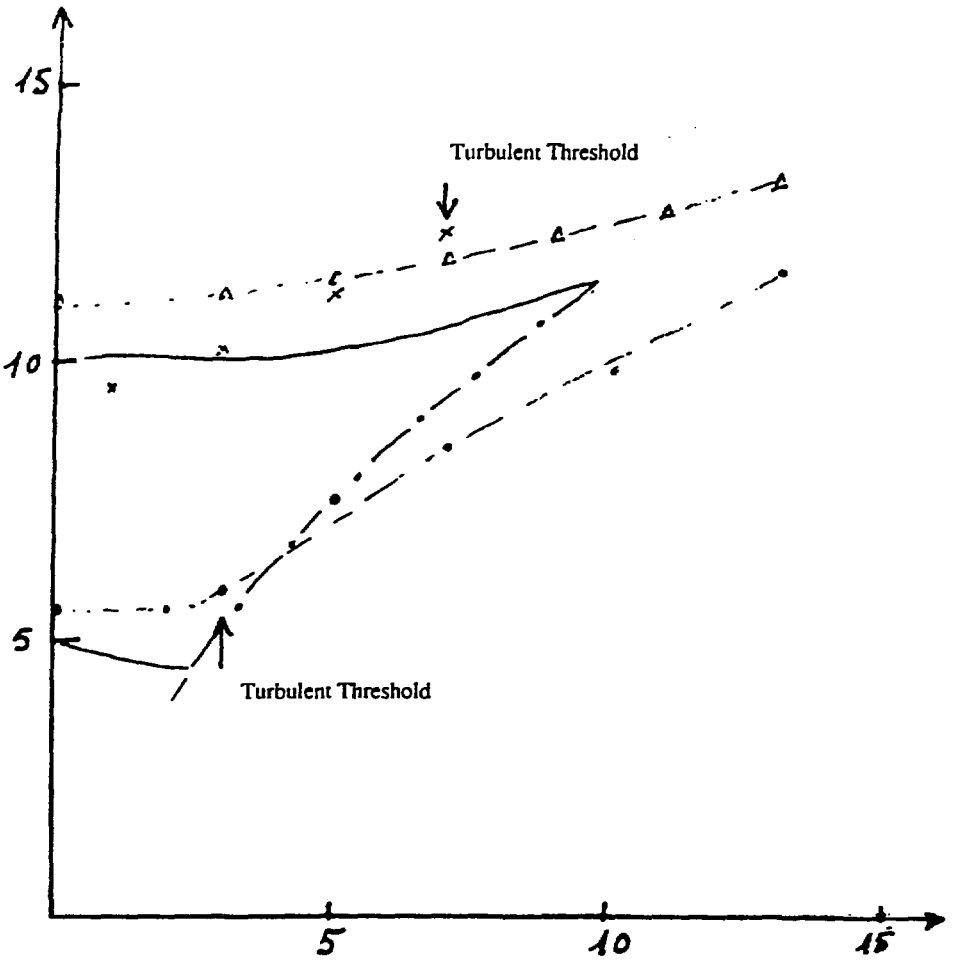

Bunch lengthening 2nd Resonator

— Besnier calculation

× SIMTRAC calculation

•	$\alpha = 2.6\ 10^{-4}$	V = 9.9 Mv	$\gamma_s = 6.7\ 10^{-3}$
Δ	$\alpha = 10.4\ 10^{-4}$	V = 9.9 Mv	$\gamma_s = 1.33\ 10^{-2}$
×	$\alpha = 4.5\ 10^{-4}$	V = 8.4 Mv	$\gamma_s = 6.7\ 10^{-3}$

A Longitudinal Mode-Coupling Instability Model for Bunch Lengthening*

Y.H. Chin

Lawrence Berkeley Laboratory

Argonne National Laboratory
Advanced Photon Source
Impedance and Bunch Instability Workshop
October 31 - November 1, 1989

---

*The full-length paper is published in Particle Accelerators, Vol. 13, pp 179-198 (1983).

INTRODUCTION

There are not many theories to explain a normal bunch lengthening from first principles.

Widely used is the analogy from Laslett-Neil-Sessler criterion for coasting beams, e.g., A. Hofmann, LEP-70174.

He derives the scaling law for SPEAR II from LNS criterion:

$$\sigma_z\,(\mathrm{cm}) = 4.4 \times 10^{-2} \left[\frac{I_o\,(\mathrm{mA})\,\alpha}{\nu_s^2\,E\ (\mathrm{GeV})} \right]^{\frac{1}{1.32}}$$

which is in good agreement with the experimental result

$$\sigma_z\,(\mathrm{cm}) = 5.6 \times 10^{-2} \left[\frac{I_o\,(\mathrm{mA})\,\alpha}{\nu_s^2\,E\ (\mathrm{GeV})} \right]^{\frac{1}{1.32}}$$

Wilson

8. Z(ω) for SPEAR

From data on bunch lengthening (next lecture), the SPEAR impedance function at high frequencies was determined to have the form:

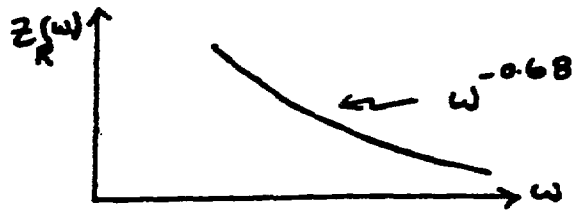

2. At low frequencies, the impedance must fall to zero as $\omega \to 0$. In this region, $Z_R(\omega)$ was arbitrarily chosen as linear: $Z_R(\omega) \sim \omega$

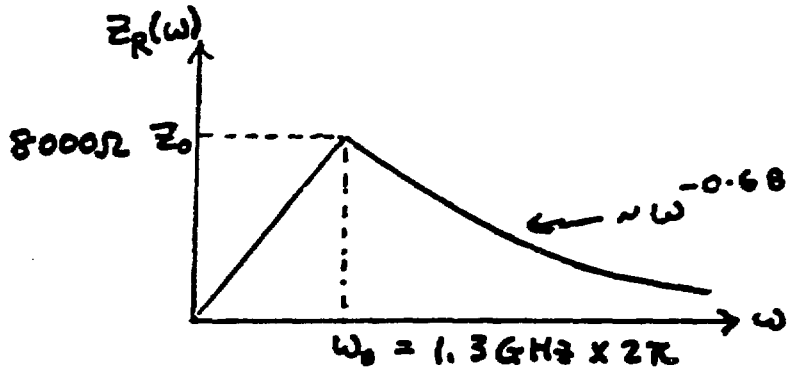

3. The parameters Z_0 and ω_0 were determined by using

$$k(\sigma) = \frac{1}{\pi}\int_0^\infty Z_R(\omega)\, e^{-\omega^2\sigma^2}\, d\omega$$

to fit the measured loss data:

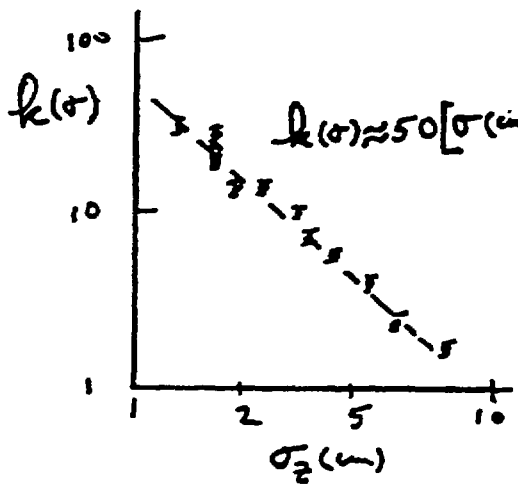

$Z_0 = 8000\ \Omega$

$\omega_0 = 2\pi \times 1.2$ GHz

The measurements are reported in SLAC-PUB-1894 (copies will be distributed next lecture). The fitting procedure is descirbed in PEP-233.

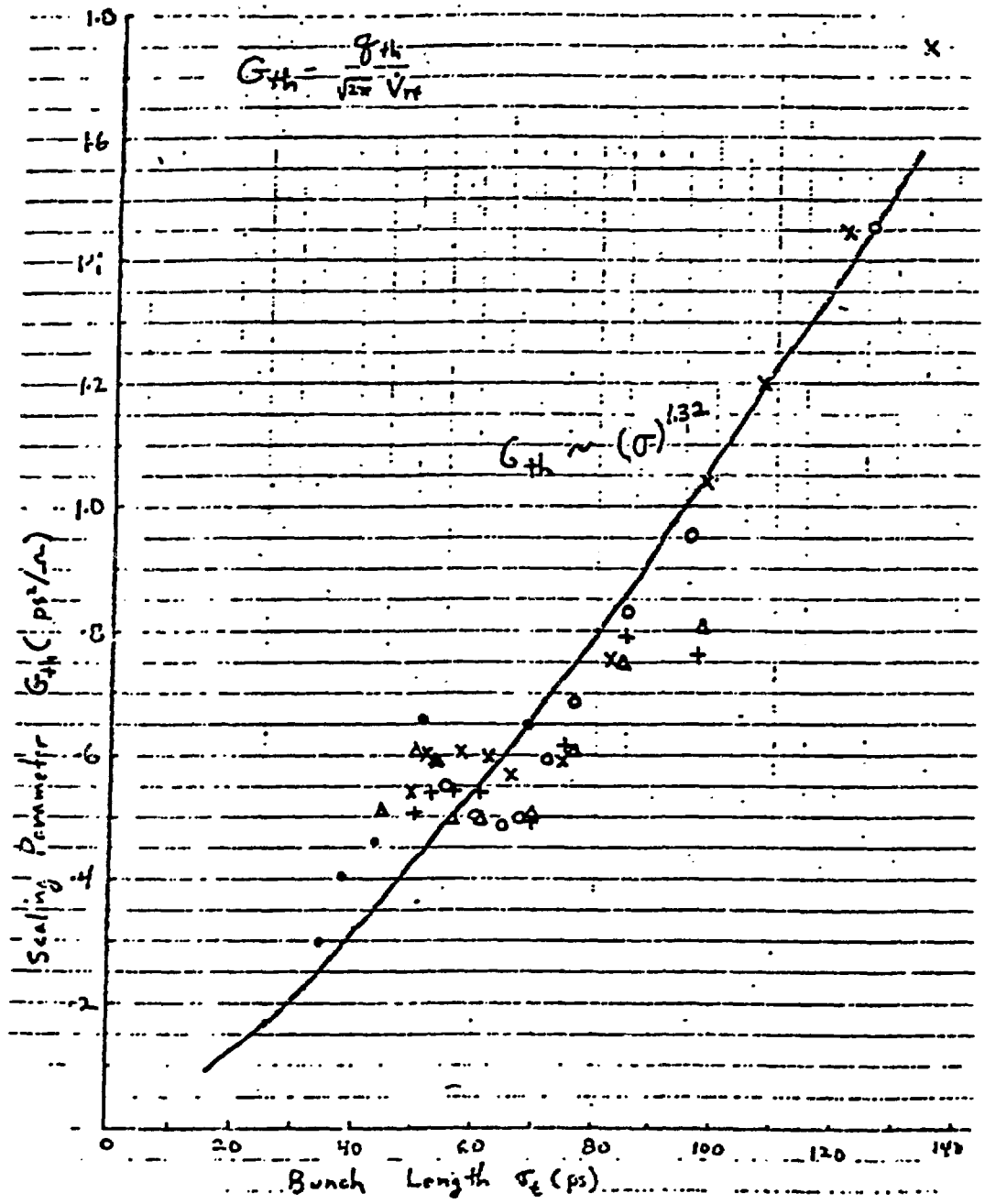

Threshold for Onset of Bunch Oscillations vs. Bunch Length in SPEAR.

We need a source of mechanism for bunch lengthening:

1) Single bunch instability

2) Fast growth rate

3) Broad band impendance

Sacharer proposed a mode-coupling instability model (CERN/PS/ER/77-5).

Since then,

Chao and Gareyte: Water bag model

Chin, Satoh and Suzuki: Gaussian distribution

BUNCH LENGTHENING AND MICROWAVE INSTABILITY

F.J. Sacherer
CERN, Geneva, Switzerland

Introduction and Summary

A single-bunch instability that leads to blow-up of bunch area and microwave signals (100 MHz to 3 GHz) has been observed in the PS[1] and the ISR[2]. A similar instability may cause bunch lengthening in electron storage rings. Attempts to explain this as a high-frequency coasting-beam instability require e-folding rates faster than a synchrotron period, and wavelengths shorter than a bunch length. In this case, the usual Keil-Schnell coasting-beam criterion[3] is used, but with local values of bunch current and momentum spread, as suggested by Boussard[4]. This yields $|Z/n| = 13\ \Omega$ for the ISR, and values about five to ten times larger for the PS. The restrictions mentioned above, however, are not fulfilled near threshold, or for frequencies as low as 100 MHz.

A direct approach, without coasting-beam approximations, is presented in this paper. The basic idea is that the usual bunched-beam modes*), dipole, quadrupole, sextupole, etc., become unstable at intensities sufficiently high for their coherent frequencies to cross, as indicated in Fig. 1. If $Z(\omega)$ is known, the frequency shifts can be computed, and surprisingly, one finds thresholds near the coasting beam values, but with fewer assumptions.

The lowest thresholds occur for wakefields that decay in about a bunch length. In general, lowering Q-values does not help, since the threshold depends on the area under the resonance curve. For very rapidly decaying wakes, the bunch is stable, in agreement with a conjecture of Hereward[5]. Only one wavelength along the bunch is sufficient for instability.

The main results are presented here (Part 1), while the derivations are given elsewhere[6] (Part 2). For other approaches, see references 7 to 10.

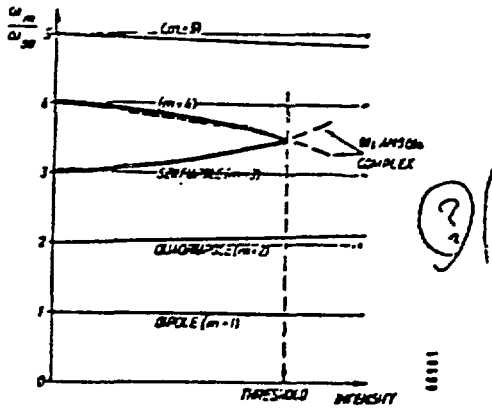

Fig. 1 Coherent frequencies ω_m versus intensity

Modes of Oscillation

For low intensities, a bunch can oscillate in the usual dipole, quadrupole and higher modes (Fig. 2) with frequencies near harmonics of the synchrotron frequency, $\omega_m \approx m\omega_s$. The oscillating part of the line density $\lambda_m(t)$ is approximately sinusoidal, and a little thought

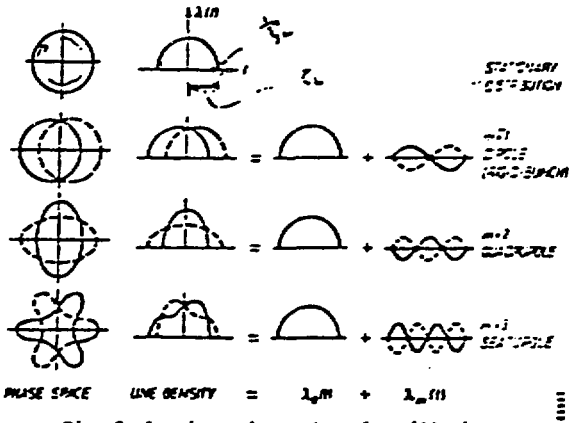

Fig. 2 Low-intensity modes of oscillation

shows it to be a standing wave with fixed nodes, so there is no instability if the wakefield decays before the next bunch arrives*). However, at sufficiently high intensities for two coherent frequencies to merge as indicated in Fig. 1, the two standing waves add to give travelling waves, one moving forward and one backward along the bunch, one of which is stable and the other unstable. This is the connection with the coasting-beam travelling-wave modes.

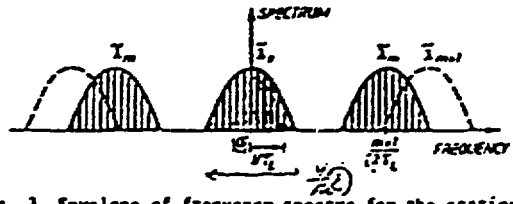

Fig. 3 Envelope of frequency spectra for the stationary distribution and for modes m and m+1

The spectra for the low intensity modes are shown in Fig. 3. Mode m is peaked near the frequency $(m+1)/2\tau_l$ of the sine wave $\lambda_m(t)$, and extends $\pm 1/\tau_l$ Hz corresponding to the bunch-length τ_l sec. For example, mode m = 5 for a 1 msec bunch is centred at 3 GHz, and lies mostly above the pipe cut-off.

The actual spectrum is a line spectrum within the envelopes of Fig. 3. For one bunch, the frequencies

$$f_p = pf_0 + mf_s\ , \qquad -\infty < p < \infty \qquad (1)$$

occur, where f_s is the synchrotron frequency and f_0 is the revolution frequency in Hz. For M equally spaced bunches, only every M^{th} line occurs,

$$f_p = (q + pM)f_0 + mf_s\ , \qquad -\infty < p < \infty \qquad (2)$$

(q: mode number)

*) A longitudinal chromaticity due to the dependence of the synchrotron frequency on momentum deviation would lead to a head-tail instability analogous to the transverse case, but this effect has been estimated to be very small[11].

OUTLINE OF THEORY

Vlasov equation for particle distribution $\psi(\theta_L, \theta, \epsilon)$

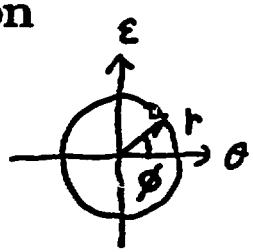

$$\frac{\partial \psi}{\partial \theta_L} + \theta' \frac{\partial \psi}{\partial \theta} + \epsilon' \frac{\partial \psi}{\partial \epsilon} = 0$$

plug in

$$\psi = \psi_o(r) + \exp\left(-i\frac{\Omega}{\omega_o}\theta_L\right) \sum_{m=-\infty}^{\infty} R_m(r) \exp(im\phi$$

↑ Gaussian distribution

and solve the first-order equation for $R_m(r)$. The result converges to the eigenvalue eq.

for $\lambda = \frac{\Omega}{\nu_s}$:

$$\det\left((\lambda^2 - m^2) I - M \right) = 0$$

The stability condition is $\lambda^2 \geq 0$. and λ = real.

CALCULATION RESULTS FOR SPEAR II

Two scaling parameters:

$$G = \frac{eT^2}{(2\pi)^{5/2}} \xi$$

$$\xi = \frac{\alpha I}{\nu_s^2 E}$$

Using SPEAR II impedance of Wilson et al., the calculated threshold values of G are 4 - 5 times larger than the experimental data.

The best fit of the experimental data with the resonator model

$$Z(\omega) = \frac{R_s}{1 - iQ\left(\frac{\omega}{\omega_r} - \frac{\omega_r}{\omega}\right)}$$

is obtained when $R_s = 4 \times 10^4$ ohm, $Q = 0.6$ and $\omega_r/2\pi = 1.3$ GHZ.

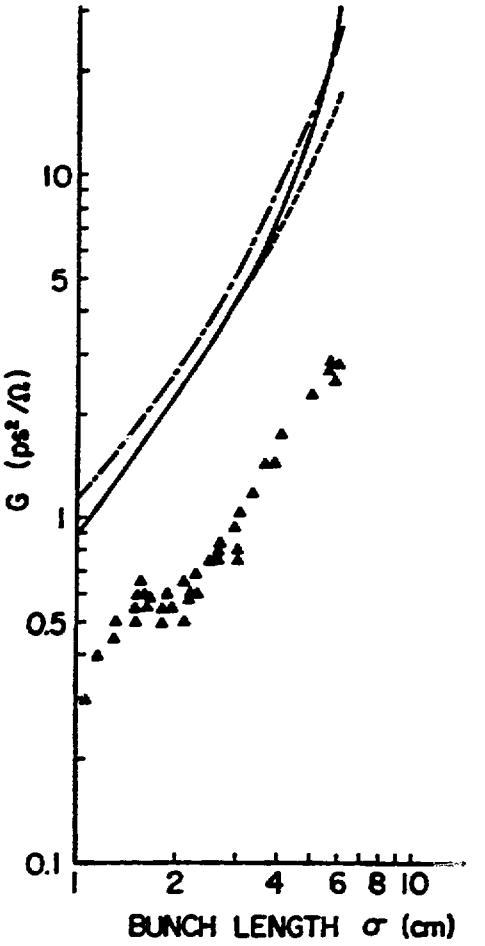

FIGURE 1(a) Scaling parameter G as a function of bunch length σ. The solid curve shows a case where four azimuthal and five radial modes are included. The dashed curve shows a case where two azimuthal and five radial modes are included. The dot-dash curve shows a case where two azimuthal modes and only one radial mode for each azimuthal mode are included. The triangles show the experimental data. The coupling impedance of Wilson et al.[14] is used.

We have also calculated the potential-well bunch lengthening using the coupling impedance of Wilson et al. The bunch lengthening $\Delta\sigma/\sigma$ due to potential-well distortion is given by[15]

$$\frac{\Delta\sigma}{\sigma} = -\frac{\xi e}{2\pi}\sum_{p=1}^{n} \operatorname{Im} Z(p\omega_0)p \exp(-p^2\sigma^2/2), \tag{3.3}$$

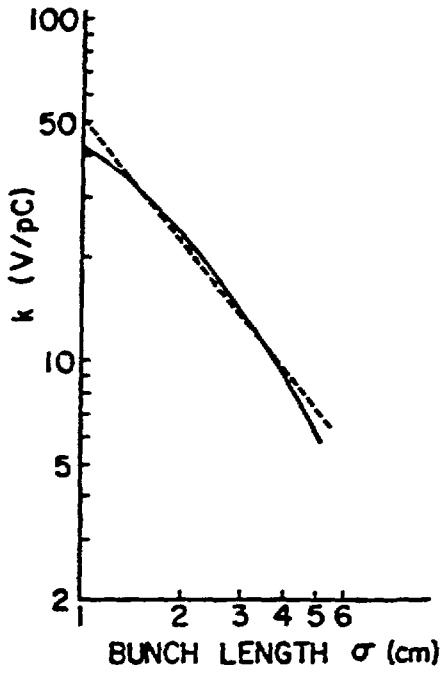

FIGURE 1(b) Loss parameter k as a function of bunch length σ. The solid curve shows the calculation when the same coupling impedance as in Fig. 1(a) is used. The dashed curve represents the experimental data.

where ξ is given by Eq. (2.49). The numerical results are $\Delta\sigma/\sigma = -3.2 \times 10^{-2}$/mA at $\sigma = 1.76$ cm, $\nu_s = 0.033$ and $E = 1.55$ GeV, $\Delta\sigma/\sigma = -6.9 \times 10^{-3}$/mA at $\sigma = 2.51$ cm, $\nu_s = 0.033$ and $E = 2.21$ GeV and $\Delta\sigma/\sigma = -2.4 \times 10^{-3}$/mA at $\sigma = 2.68$ cm, $\nu_s = 0.042$ and $E = 3.0$ GeV. The results are consistent with the experimental data.[14]

Resonator Model

Other parametrizations have been tried and fitted to the experimental data. The simplest parametrization is a broadband resonator model given by

$$Z(\omega) = \frac{R_s}{1 - iQ\left(\frac{\omega}{\omega_r} - \frac{\omega_r}{\omega}\right)}. \tag{3.4}$$

With this parametrization, the threshold current is fitted. The result is shown in Fig. 2(a). The parameters are $R_s = 4 \times 10^4$ ohm, $Q = 0.6$ and $\omega_r/2\pi = 1.3$ GHz. The calculated curve fits qualitatively well with the experimental data. The wiggle observed at about $\sigma = 1.5$ cm is also reproduced. To see the details of the mode coupling, the

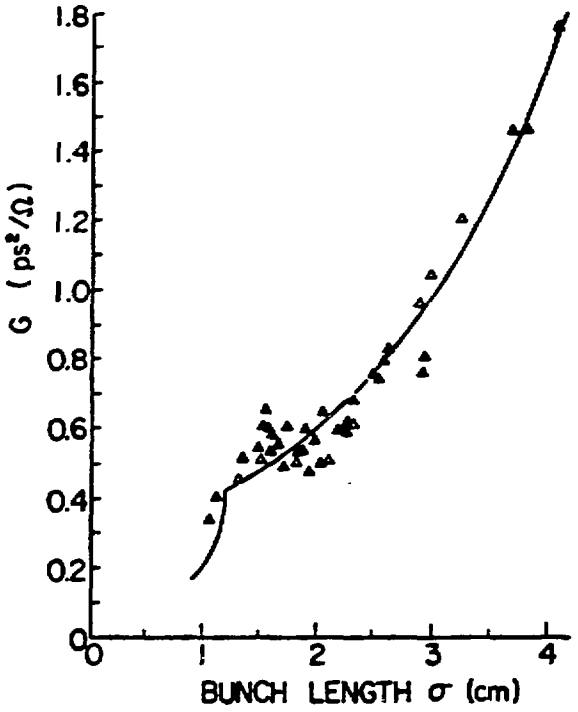

FIGURE 2(a) Scaling parameter G as a function of bunch length σ. The solid curve shows the calculation when a resonator impedance of $R_s = 4 \times 10^6$ ohm, $Q = 0.6$ and $\omega_r/2\pi = 1.3$ GHz is used. The triangles show the experimental data.

real and imaginary parts of the coherent oscillation frequency λ in units of synchrotron frequency are shown in Figs. 3(a) and 3(b) for $\sigma = 0.9$ cm (30 ps) and in Figs. 4(a) and 4(b) for $\sigma = 1.8$ cm (60 ps). For simplicity, two radial modes are shown in the figures. We see that at $\sigma = 0.9$ cm, mode coupling between $m = 1$ and $m = -1$ modes occurs while at $\sigma = 1.8$ cm, mode coupling between $m = 1$ and $m = 2$ modes occurs. We thus see that the wiggle at about $\sigma = 1.5$ cm is explained by the change of the combinations of azimuthal modes in this range of bunch length. The loss parameter k is calculated by using the same impedance as described above and plotted by a solid curve in Fig. 2(b). The fit to the experimental data of Eq. (3.2) is also shown by a dotted curve. The calculated values are larger than the experimental values by factor of about three. Thus the absolute value prediction of theory is not so good, although it explains the qualitative behavior of threshold currents fairly well.

A Further Parametrization of Coupling Impedance

A low-Q resonator model is frequently used to parametrize a broadband impedance. However, in this model, Re $Z(\omega)$ behaves as $1/\omega^2$ and Im $Z(\omega)$ behaves as $1/\omega$ as ω

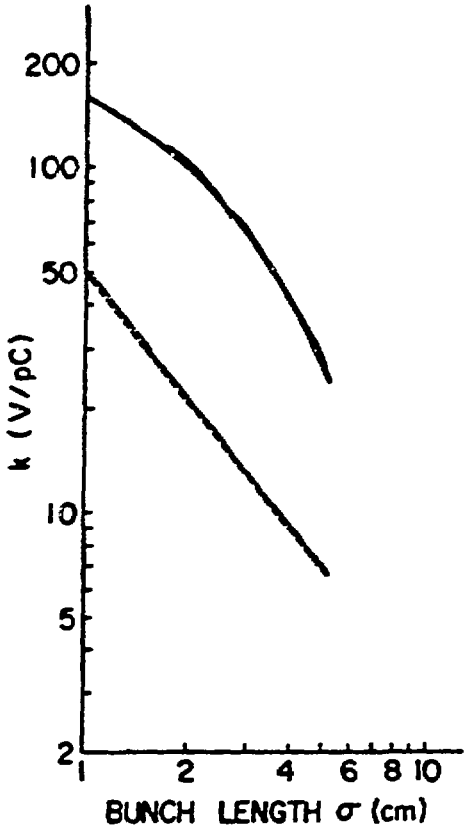

FIGURE 2(b) Loss parameter k as a function of bunch length σ. The solid curve shows the calculation when the same coupling impedance as in Fig. 2(a) is used. The dashed curve represents the experimental data.

becomes large. On the other hand, the scaling law of Chao and Gareyte requires an asymptotic form that Re $Z(\omega)$ and Im $Z(\omega)$ behave as $\omega^{-0.65}$. A simple extension of the resonator model, which has a causal property is given by formula 2.3.2 of *Ref.* 19.

$$\int_{-\infty}^{\infty} (a - ix)^{-\nu} e^{-ixy}\, dx = \begin{cases} 2\pi y^{\nu-1} e^{-ay}/\Gamma(\nu) & y > 0 \\ 0 & y < 0 \end{cases}$$
$$(\mathrm{Re}\, a > 0,\ \mathrm{Re}\, \nu > 0). \tag{3.5}$$

With the formula (3.5) we parametrize the coupling impedance as

$$Z(\omega) = \frac{R}{Q}\frac{\omega_r}{2\omega_r} I^{\nu} \left\{ \frac{\omega_1 \omega_r^{\nu-1}}{(\omega - \omega_1)^{\nu}} - \frac{\omega_2 \omega_r^{\nu-1}}{(\omega - \omega_2)^{\nu}} \right\}, \tag{3.6}$$

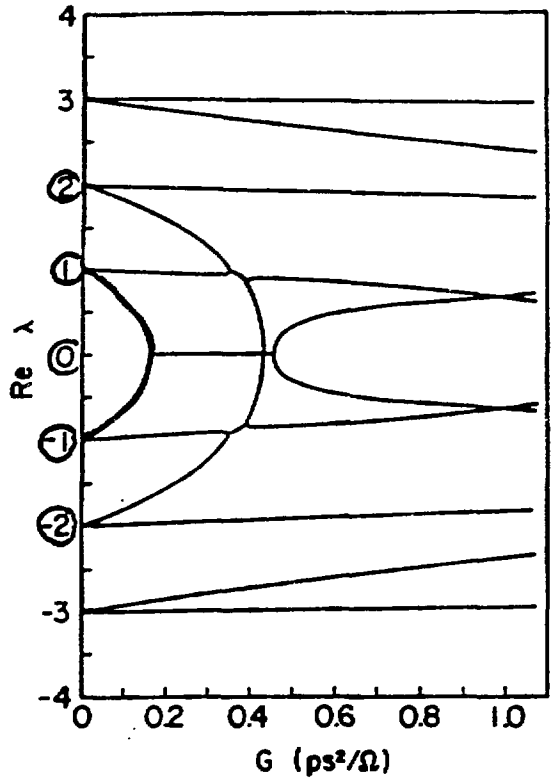

FIGURE 3(a) The real part of the coherent frequency λ in unit of synchrotron frequency as a function of the scaling parameter G. The bunch length is 0.9 cm.

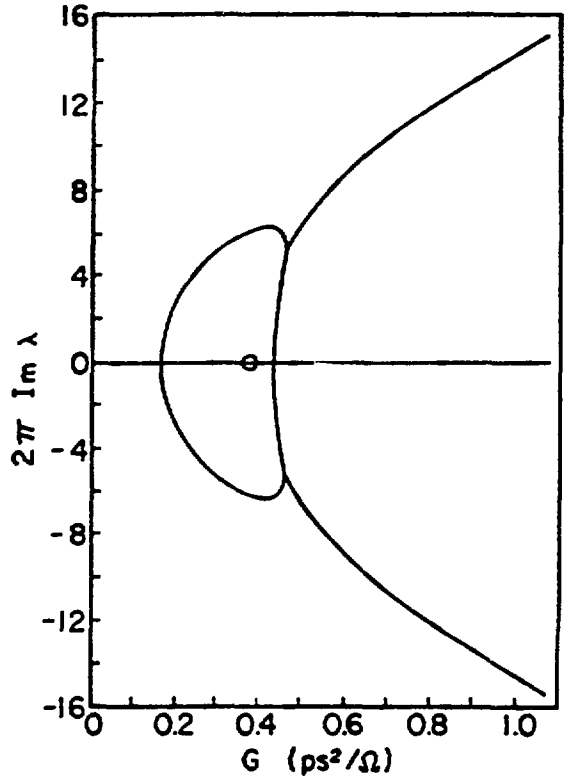

FIGURE 3(b) The imaginary part of 2π times the coherent frequency λ in unit of synchrotron frequency as a function of the scaling parameter G. The bunch length is 0.9 cm.

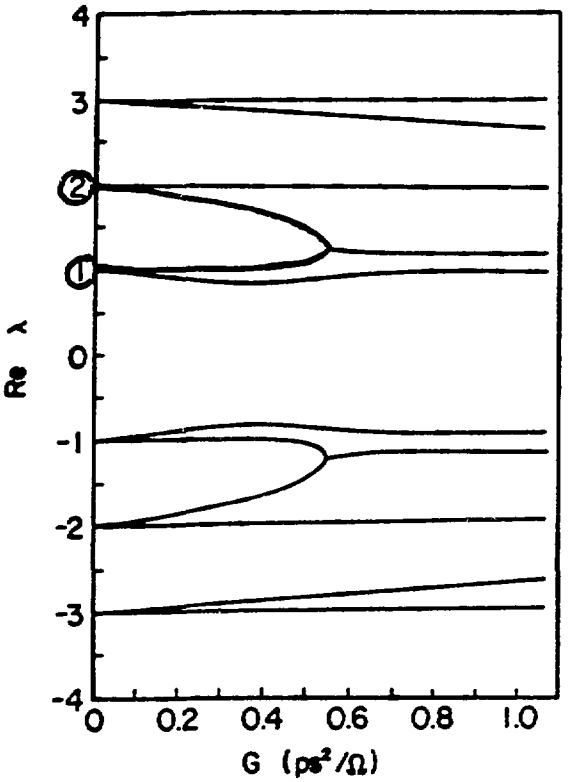

FIGURE 4(a) The real part of the coherent frequency λ in unit of synchrotron frequency as a function of the scaling parameter G. The bunch length is 1.8 cm.

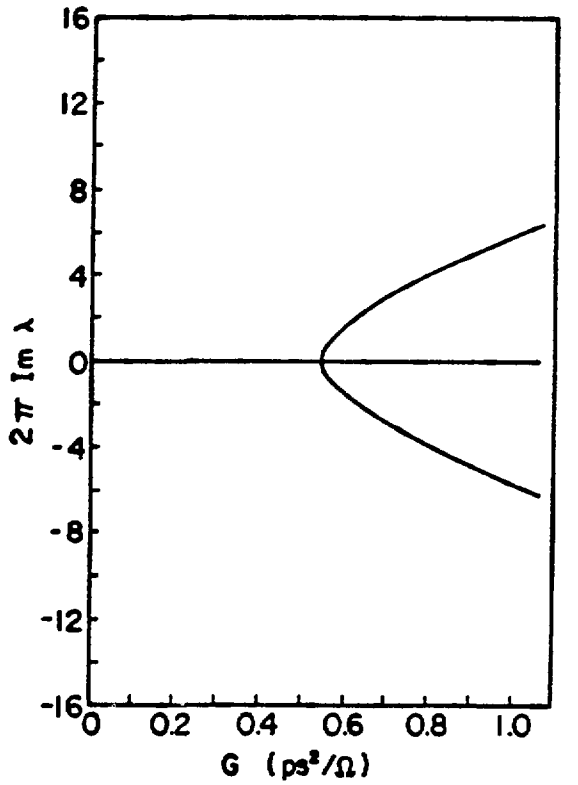

FIGURE 4(b) The imaginary part of the circular coherent frequency 2πλ in unit of synchrotron frequency

Note that the wiggle around σ_z = 1.5 cm is reproduced

change of mode - coupling pair

CONCLUSIONS

1. If the estimate of SPEAR II impedance is ok, the mode-coupling model gives too large threshold current.

   We need another mechanism of instability

2. If the reproduction of the wiggle by the mode-coupling model is not coincidence, we should reconsider the estimate of impedance or the impedance model.

High-Frequency Behavior of Longitudinal Coupling Impedance*

Robert L. Gluckstern, Rui Li, and
Filippo Neri

University of Maryland

Argonne National Laboratory
Advanced Photon Source
Impedance and Bunch Instability Workshop
October 31 - November 1, 1989

---

*Work supported by the Department of Energy.

This contribution to the impedance/bunch lengthening workshop is a summary of recent results regarding the longitudinal coupling impedance and its behavior at frequencies above the cutoff of the beam pipe. Numerical computations are based on a program written by F. Neri[1] which uses a modification of SUPERFISH to compute the longitudinal coupling impedance for an azimuthally symmetric obstacle of arbitrary r,z cross section and on a program developed by R. Li and F. Neri[2] for N pillboxes based on an expansion in TM modes in each cavity and beam pipe section.

A general analysis has been developed[3], leading to an integral equation for the axial electric field at the beam pipe radius within the obstacle. The solution of this equation for a small obstacle (small kg) for the admittance is[4]

$$Z_o Y(k) \cong 2\pi ka\left[\frac{-j}{kg\ \tanh(b-a)} + \sum_{s=1}^{\infty} \frac{e^{-jb_s g/a}}{b_s} + \frac{j}{\pi}\ell n\ 4\right], \qquad (1)$$

where

$$b_s = \left(k^2a^2 - j_s^2\right)^{1/2}, \quad b_s = -j\beta_s, \quad \beta_s = \left(j_s^2 - k^2a^2\right)^{1/2}. \qquad (2)$$

Here j_s are the zeroes of $J_o(x)$. The result in Eq. (1) is in close agreement with numerical results, as discussed in Reference 4, for g/a = .05, b/a = 1.1.

The kernel of the integral equation was approximated for high frequency[3], leading to the prediction for the (local) average (over frequency) impedance for a single cavity

$$\frac{Z(k)}{Z_o} \cong \frac{(1 - j)}{2\pi}\sqrt{\frac{g}{\pi a}}\,\frac{1}{\sqrt{ka}} \quad , \quad ka \gg 1 \, , \tag{3}$$

independent of the shape of the cavity. This result is in agreement with the predictions of others (J. Lawson, G. Dôme, S.A. Heifets and S.A. Kheifets; citations included in Reference 3). Numerical results for a pillbox cavity with $g/a = \pi/4$, $b/a = 1.5$ are shown in Figs. 1(a) and 1(b). The average is in approximate (10%) agreement with Eq. (3) for $ka > 25$, but there appear to be oscillations with ka of magnitude comparable with the average. An analytic description of these oscillations has not yet been developed.

An analytic approximation has been obtained[5] for the coupling impedance per pillbox of N pillboxes at high frequency. The form for the admittance per pillbox (valid for $N = 1$ and for $N \gg 1$) is

$$NZ_oY(k) \cong (1 + j)\,\pi\sqrt{\frac{\pi a}{g}}\,\sqrt{ka} + \alpha\sqrt{N - 1}\,\tan^{-1}\left(\frac{\alpha}{2\sqrt{N}}\right) \tag{4}$$

where

$$\alpha = (1 + j)\,\frac{\sqrt{\pi ka}}{\sqrt{L/a}} \tag{5}$$

and where L is the center to center separation of the pillboxes.

For $N \to \infty$ ($NL/a \gg ka$) this reduces to

$$NZ_oY(k) \cong (1 + j)\,\pi\sqrt{\frac{\pi a}{g}}\,\sqrt{ka} + j\pi\,\frac{ka^2}{L} \tag{6}$$

for a periodic structure. It is easy to show, for large ka, that the imaginary part of the impedance decreases as k^{-1} and the real part as $k^{-3/2}$. Moreover the real and imaginary parts are connected by causality, leading to the sum rule

$$\int_0^\infty dk\ R(k) = \frac{L}{2a^2} NZ_0 , \tag{7}$$

where $Z(k) = R(k) + j\ X(k)$.

For large but finite N, the $k \to \infty$ limit ($ka \gg NL/a$) is

$$\frac{Z_N(k)}{Z_0} \cong \frac{(1 - j)}{2\pi} \sqrt{\frac{g}{\pi a}} \frac{1}{\sqrt{ka}} \left[\frac{N}{1 + \frac{1}{2}\sqrt{\frac{Ng}{L}}} \right] . \tag{8}$$

When $Ng \gg L$, the impedance varies as $N^{1/2}$ as suggested by R.B. Palmer.[6]

Figures 2(a) and 2(b) show a preliminary comparison of the predictions of Eq. (4) with numerical results for the impedance averaged over intervals $\Delta k = \pi/g$ for N = 10 and 20, with $g/a = \pi/8$, $L/a = \pi/6$. The correction factor in the brackets in Eq. (8) is approximately confirmed. A final point, raised in the workshop, is that this "shadowing" effect will be reduced if the propagating modes are significantly attenuated between pillboxes.

The analysis can be extended[7] to the case of a pulse (TEM mode) on a wire of radius r_0 along the axis of the beam pipe and obstacle, a simulation technique[8] used to measure the impedance. The kernel in the integral equation is modified primarily by the shift of j_s to $\tilde{j}_s$, the zeroes of

$$J_o(x) - \frac{J_o(kr_o)}{Y_o(kr_o)} Y_o(x) \quad . \tag{9}$$

It is easy to show that the shift is of order $[\ell n\ (a/r_o j_s)]^{-1}$. The numerical program was modified[7] to apply to the pulse on the wire and the quantity

$$\frac{Z(k)}{Z_o} = \frac{\ell n(a/r_o)}{\pi} [1 - T(k)] \tag{10}$$

was computed for $r_o/a = .1$ and $.01$. Here T(k) is the transmission coefficient for the coaxial (TEM) mode on the wire. Results for a small pillbox showed the shift in structure corresponding to the new values $\tilde{j}_s$, but the average behavior was essentially unchanged. The results for high frequency, which depend on the sum of contributions for many values of s, were almost identical to those calculated for the impedance without the wire.

References

[1]R.L. Gluckstern and F. Neri, Computation of Coupling Impedance Using Cavity Codes, Proceedings of the 13th International Conference on High Energy Accelerators, Novisibirsk, USSR, p. 170 (1986); Characteristics of the Broad Resonance in the Longitudinal Coupling Impedance, Proceedings of the Particle Accelerator Conference, Washington, DC, p. 1069 (1987).

[2]Private communication.

[3]R.L. Gluckstern, Phys. Rev. D, 39, 2773 (1989)

[4]R.L. Gluckstern and F. Neri, Longitudinal Coupling Impedance of a Small Obstacle, Proceedings of the Particle Accelerator Conference, Chicago, IL, March 1989, copy included as Appendix A.

[5]R.L. Gluckstern, High Frequency Dependence of the Coupling Impedance for a Large Number of Obstacles, Proceedings of the Particle Accelerator Conference, Chicago, IL, March 1989, copy included as Appendix B.

[6]R.B. Palmer, A Qualitative Study of Wake Fields for Very Short Bunches, SLAC Report SLAC-PUB-4433, October 1987.

[7]R.L. Gluckstern and R. Li, Analysis of Coaxial Wire Measurement of Longitudinal Coupling Impedance, Proceedings of the 14th International Conference on High Energy Accelerators, Tsukuba, Japan, August 1989, copy included as Appendix C.

[8]See, for example, H. Hahn and F. Pederson, On Coaxial Wire Measurements of the Longitudinal Coupling Impedcance, BNL Report No. 50870 (1978).

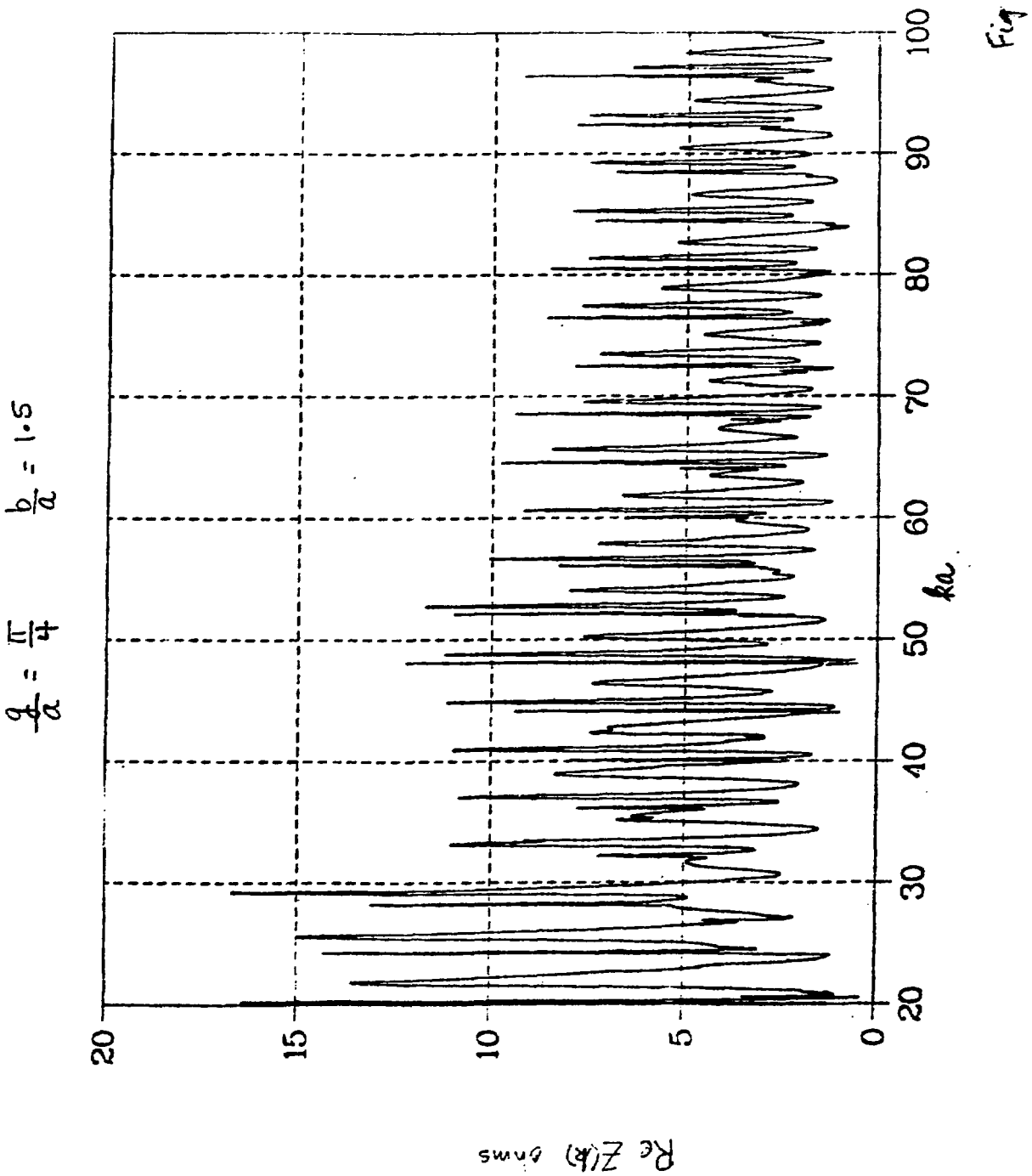
$\frac{\phi}{\alpha} = \frac{\pi}{4}$
$\frac{b}{a} = 1.5$
Re Z(k) ohms
20
15
10
5
0
20
30
40
50
60
70
80
90
100
ka

Fig 1(a)

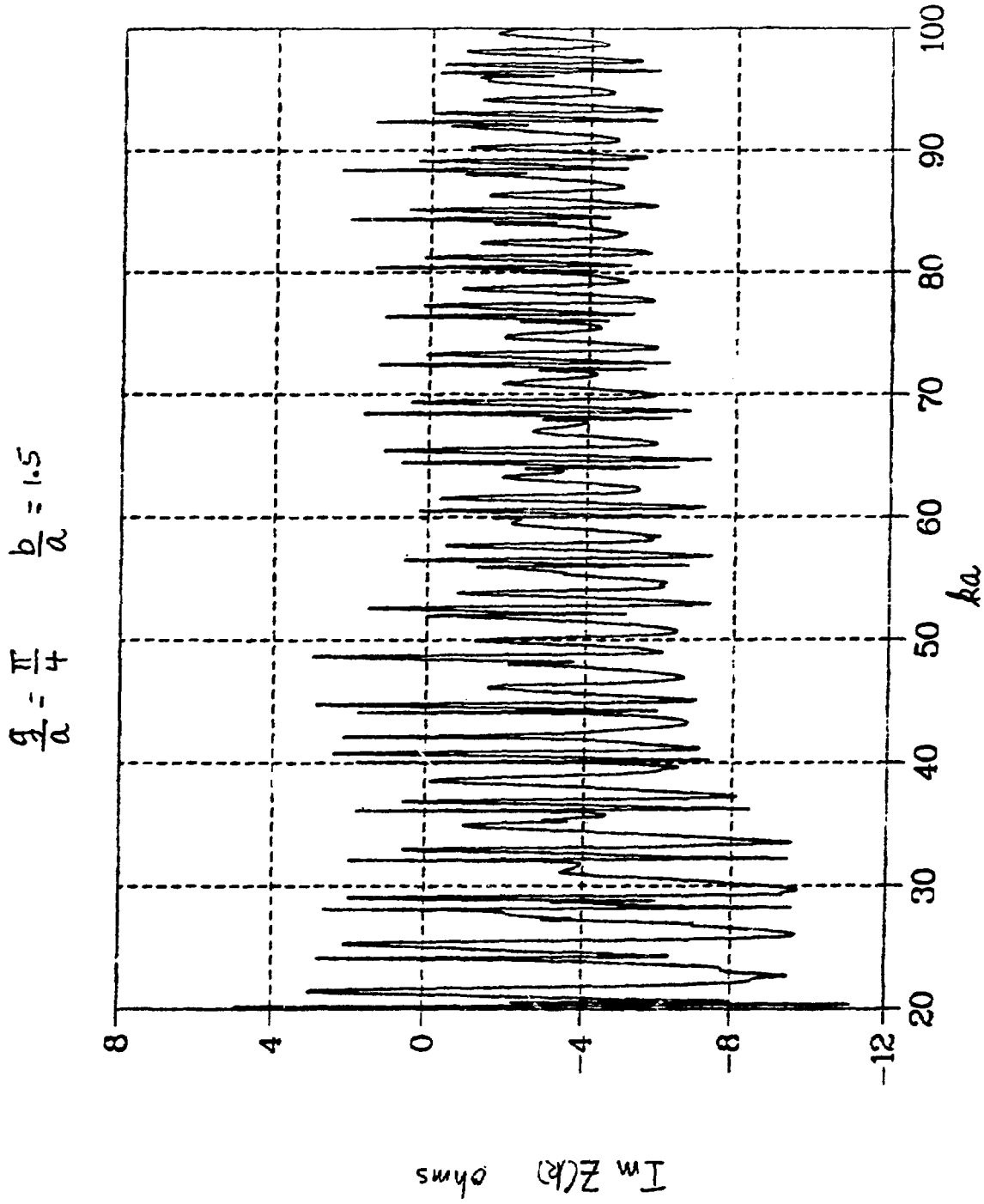
$\frac{\theta}{\alpha} = \frac{\pi}{4}$
$\frac{b}{a} = 1.5$
8
4
0
-4
-8
-12
20
30
40
50
60
70
80
90
100
ka
Im Z(k) ohms

Fig. 1(b)

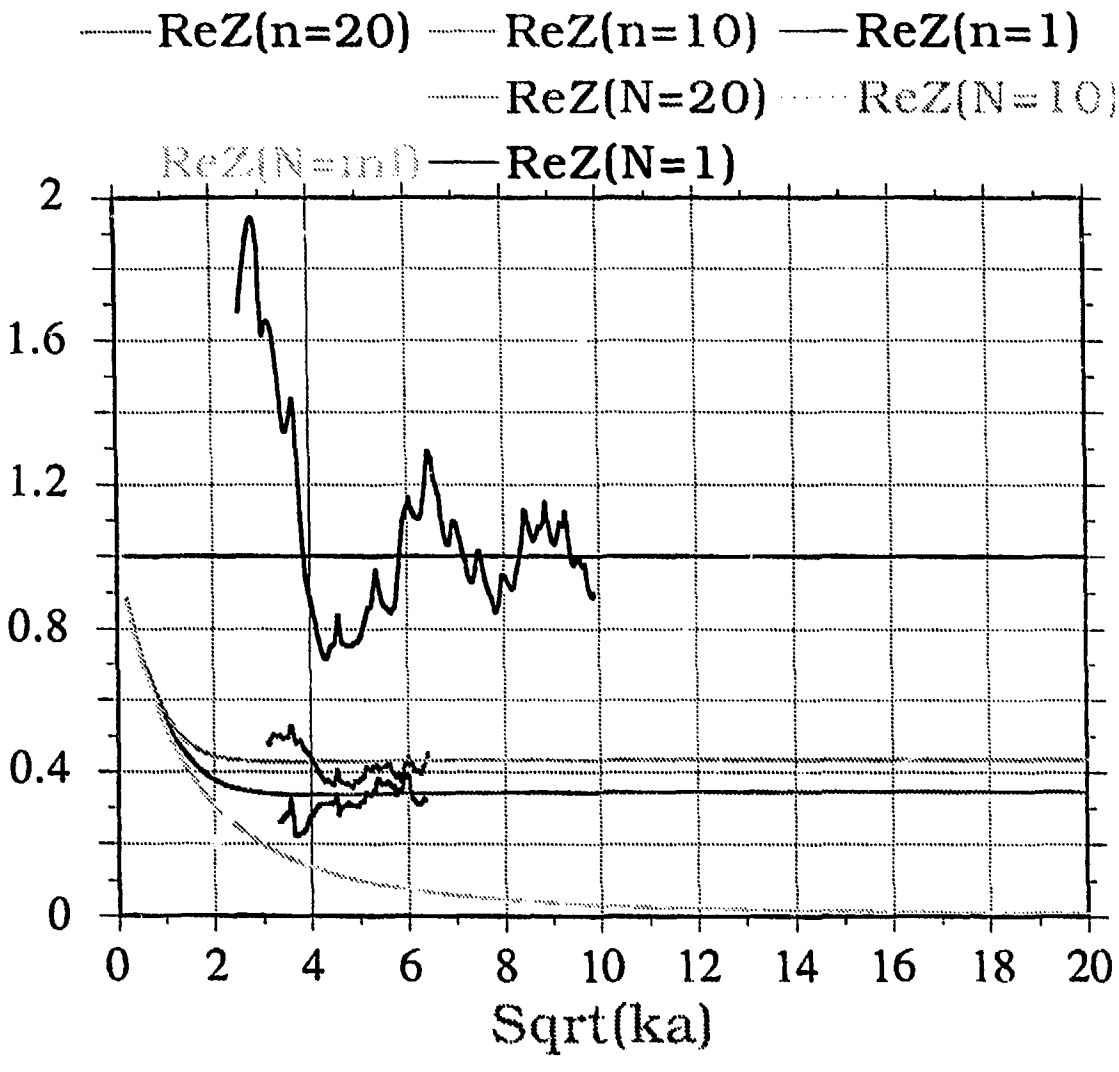

$\frac{a}{d} = \frac{\pi}{8}$ $\frac{l}{a} = \frac{\pi}{6}$ $\frac{b}{a} = 1.2$

Fig. 2(a)

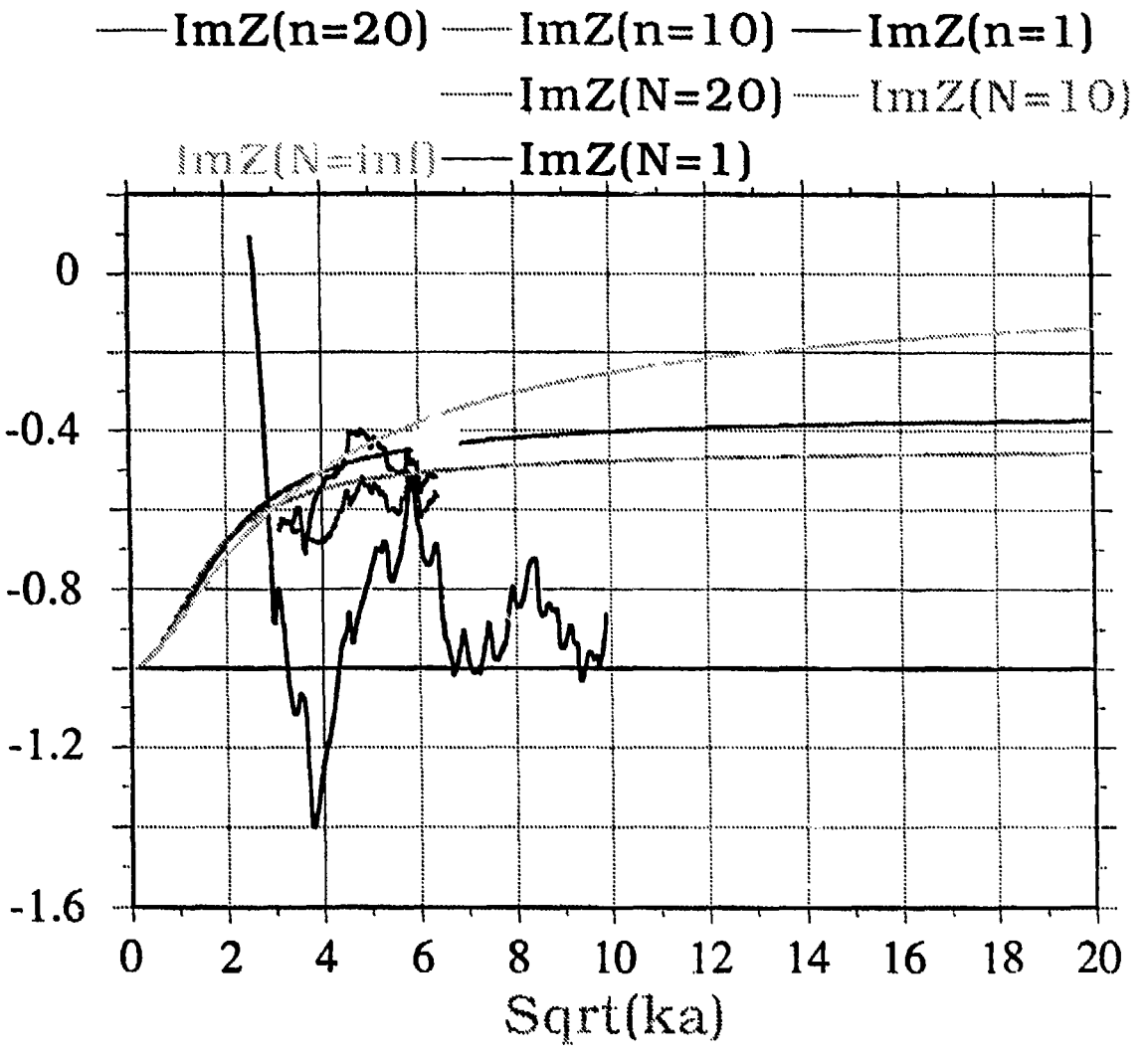

$\frac{g}{a} = \frac{\pi}{8}$ $\frac{l}{a} = \frac{\pi}{6}$ $\frac{b}{a} = 1.2$

Fig. 3(b)

Presented at the Particle Accelerator Conference, March 1989

Longitudinal Coupling Impedance of a Small Obstacle[1]

Appendix A

R.L. Gluckstern and F. Neri
Physics Department, University of Maryland, College Park, MD 20742

I. Introduction

In a recent paper[2], the longitudinal impedance for a narrow pill-box with beam pipes was investigated analytically and numerically, in order to understand the structure of the impedance as a function of frequency in the region above the cutoff of the beam pipe. The field matching procedure described by Henke[3] was used in the limit of a narrow pill-box and the impedance was expressed as sum which required a cutoff for convergence. In the present paper we start with the integral equation for the field at the pipe radius[4,5] and solve this equation rigorously in the case of a small obstacle of general shape. In this way we obtain a more accurate representation of the important broad resonance[2] which dominates the behavior in the frequency range above the cutoff of the beam pipe.

II. Analysis

The starting point for the analysis is the integral equation obtained for the electric field in the obstacle at the pipe radius.[5] Specifically, we have

$$\int_0^g dz'\, F(z') \left[K_p\,(|z'-z|) + K_c(z',z)\right] = j\, e^{-jkz} \tag{2.1}$$

and

$$\frac{Z(k)}{Z_0} = \frac{1}{ka^2}\int_0^g dz\, F(z)\, e^{jkz} \quad . \tag{2.2}$$

Here $kc/2\pi$ is the frequency, a is the pipe radius, $Z_o = 120\pi$ ohms is the impedance of free space, and the azimuthally symmetric cavity, of general shape in the r,z plane, extends axially from $z = 0$, to $z = g$ at the pipe radius $r = a$. Apart from a constant, $F(z)$ is the axial electric field for $r = a$ and $0 < z < g$. The component of the kernel from the pipe field is

$$K_p(|u|) = \frac{2\pi j}{a} \sum_{s=1}^{\infty} \frac{e^{-jb_s|u|/a}}{b_s} \quad , \tag{2.3}$$

where

$$b_s = \sqrt{k^2a^2 - j_s^2} \quad , \quad \beta_s = \sqrt{j_s^2 - k^2a^2} \quad . \tag{2.4}$$

Here j_s is the <u>sth</u> zero of the Bessel function $J_o(x)$ and b_s is to be replaced by $-j\beta_s$ when $j_s > ka$. The component of the kernel from the "cavity fields" is

$$K_c(z,z') = 4\pi^2 \sum_{\ell} \frac{h_\ell(z)\, h_\ell(z')}{k^2 - k_\ell^2} \quad , \tag{2.5}$$

where the orthonormal (azimuthally symmetric) modes of the cavity (with an imaginary metal wall at $r = a$) are defined by

$$\nabla \times \vec{e}_\ell = k_\ell \vec{h}_\ell \quad , \quad \nabla \times \vec{h}_\ell = k_\ell \vec{e}_\ell \quad , \tag{2.6}$$

and where $h_\ell(z) \equiv \left[h_\ell(a,z)\right]_\varphi$ is the azimuthal component of the normalized magnetic field at $r = a$.

III. Small Obstacle Solutions

The "cavity kernel" in Eq. (2.5) requires a sum over the modes in the cavity. For a small cavity, this sum is dominated by the lowest mode for which the solution for the magnetic field is the constant field

$$h_o(z) = \frac{1}{\sqrt{2\pi a\,\Delta}} \quad , \tag{3.1}$$

normalized so that $\int h_o^2(z)\,dv = 1$ over the annular cavity of length $2\pi a$ and cross sectional area Δ. The frequency of this mode corresponds to $k_o = 0$, so that

$$K_c(z',z) \cong \frac{2\pi}{k^2 a\Delta} \quad . \tag{3.2}$$

The "pipe kernel" in Eq. (2.3) is more difficult to evaluate for a small obstacle, since the sum in Eq. (2.3) does not converge if $|u| = |z' - z|$ is set equal to zero. To proceed we add and subtract $K_p(g)$, which is independent of z' and z, to obtain

$$K_p(|u|) = K_p(g) + \frac{2\pi j}{a} \sum_{s=1}^{\infty} \frac{e^{-jb_s|u|/a} - e^{-jb_s g/a}}{b_s} \quad . \tag{3.3}$$

Since $|u|/a$ and g/a are very small, the major contributions to the sum in Eq. (3.3) occur for large s, in which case we obtain

$$\sum_{s=1}^{\infty} \frac{e^{-jb_s|u|/a} - e^{-jb_s g/a}}{b_s} \cong \frac{j}{\pi} \int_0^{\infty} d\beta\, \frac{(e^{-\beta|u|/a} - e^{-\beta g/a})}{\beta}$$

$$= \frac{j}{\pi} \ln \frac{g}{|u|} \quad . \tag{3.4}$$

The integral equation for $F(z')$ in Eq. (2.1) therefore becomes

$$\int_0^1 dx' \, f(x') \left[K - \frac{2j}{\pi} \ln |x' - x| \right] = 1 \quad , \tag{3.5}$$

where

$$x' = z'/g \quad , \quad x = z/g \quad , \quad \pi g F(z') = a f(x') \tag{3.6}$$

and

$$K = - \frac{2j}{k^2 \Delta} + 2 \sum_{s=1}^{\infty} \frac{e^{-jb_s g/a}}{b_s} \quad . \tag{3.7}$$

The solution of Eq. (3.5) can be expressed in terms of the solution of

$$\int_0^1 dx' \, L(x') \ln|x' - x| = 1 \quad , \quad 0 < x < 1 \quad . \tag{3.8}$$

Specifically we find

$$f(x') = \frac{L(x')}{K/J - 2j\pi} \quad , \tag{3.9}$$

where

$$J = \left[\int_0^1 dx \, L(x) \right]^{-1} \quad . \tag{3.10}$$

We then obtain the admittance from Eq. (2.2) as

$$Z_o\, Y(k) = 2\pi\, ka\left[-\frac{j}{k^2\Delta} + \sum_{s=1}^{\infty} \frac{e^{-jb_s g/a}}{b_s} + j\,\frac{2\ell n2}{\pi}\right], \qquad (3.11)$$

where we have used the solution of Eq. (3.8) in the form[6]

$$L(x) = -\frac{x^{-1/2}(1-x)^{-1/2}}{2\pi\,\ell n2}\,, \quad J = -2\ell n2\,. \qquad (3.12)$$

IV. Numerical Results and Discussion

We have used Eq. (3.11) to calculate the real and imaginary parts of the admittance, shown as the solid lines in Figs. 1(a) and 1(b) for a small pillbox with b/a = 1.1 and g/a = .05. The dots correspond to the results of the computer program developed to calculate the longitudinal impedance of an azimuthally symmetric cavity of general shape in a beam pipe.[2] The agreement between the two confirms the validity of Eq. (3.11). Furthermore, the "sawtooth" structure of that part of the admittance involving the zeroes of $J_o(x)$ depends primarily on the parameter ka (and only logarithmically on kg) while the primary dependence on the pillbox size (b,g) is contained only in the smooth part of the susceptance, which is most important for small values of $k^2\Delta$.

If one smooths the "sawtooth" structure, equivalent to averaging over k for values of ka above the cutoff of the beam pipe, one finds the features of the broad resonance discussed in depth in an earlier paper.[2]

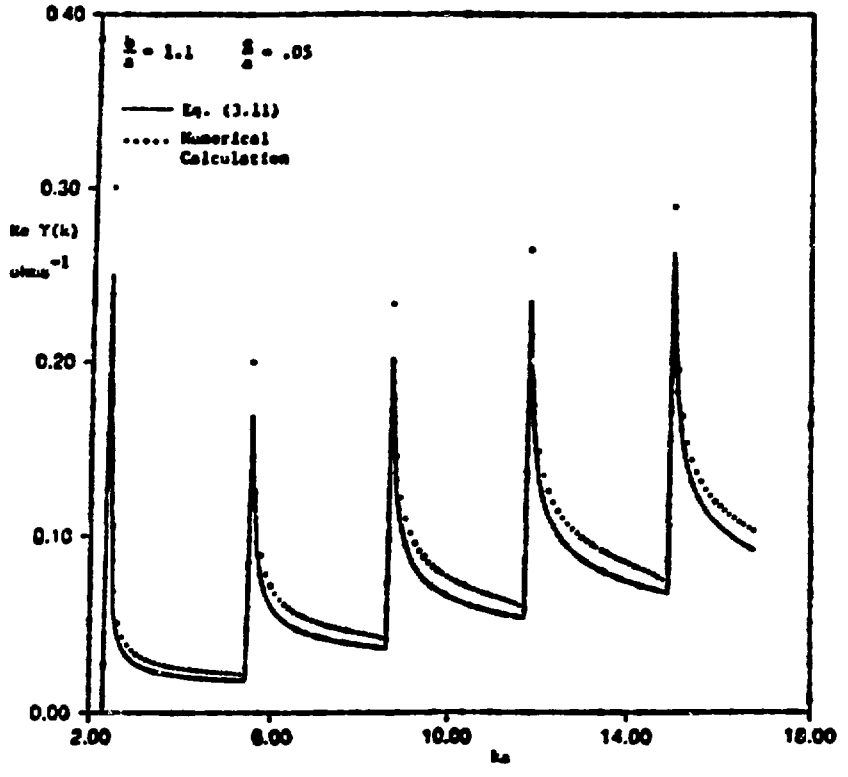

Figure 1(a) Real Part of Admittance as a Function of Frequency

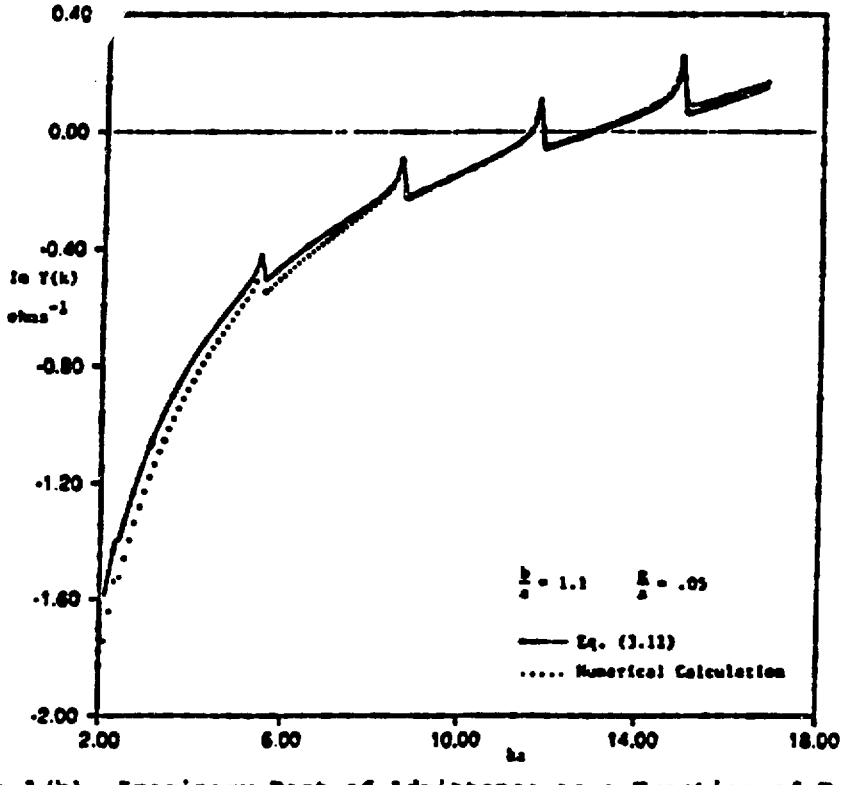

Figure 1(b) Imaginary Part of Admittance as a Function of Frequency

V. References

1. Work supported by the Department of Energy.

2. R.L. Gluckstern and F. Neri, Proceedings of the Particle Accelerator Conference, Washington, D.C., March 1987, p. 1069.

3. H. Henke, Point Charge Passing a Resonator with Beam Tubes, CERN-LEP-RF/85-41.

4. R.L. Gluckstern, High Frequency Behavior of the Longitudinal Impedance for a Cavity of General Shape, submitted for publication.

5. R.L. Gluckstern and B. Zotter, Coupling Impedance for Asymmetric Cavities, CERN-LEP-613, July 1988.

6. See Appendix A.

Appendix A

In order to demonstrate that

$$L(x) = -\frac{x^{-1/2}\,(1-x)^{-1/2}}{2\pi\,\ell n\,2} \tag{A.1}$$

is a solution of Eq. (3.8), we make the substitutions

$$x' = \frac{1+\cos\theta'}{2}\ , \quad x = \frac{1+\cos\theta}{2}\ , \tag{A.2}$$

from which we obtain

$$Q \equiv \int_0^1 \frac{dx'}{\sqrt{x'(1-x')}}\,\ell n\,|x'-x| = \frac{1}{2}\,\mathrm{Re}\int_{-\pi}^{\pi} d\theta'\,\ell n\left(\frac{\cos\theta-\cos\theta'}{2}\right)\ . \tag{A.3}$$

Use of the exponential forms for cos θ, cos θ′ leads to

$$Q = \frac{1}{2}\,\mathrm{Re}\int_{-\pi}^{\pi} d\theta'\,\left[\ell n\,e^{i\theta} + \ell n(1-e^{-i(\theta'+\theta)}) + \ell n\,(1-e^{i(\theta'-\theta)}) - \ell n\,4\right]$$

$$= -\pi\,\ell n\,2 + \int_0^{\pi} d\psi\,\ell n(1-\cos\psi)\ , \tag{A.4}$$

where $\psi = \theta' \pm \theta$, and where the last form of Q is clearly independent of θ, as required by Eq. (3.8).

A power series expansion of the integrand in Eq. (A.3) leads to

$$Q = -\pi\,\ell n\,2 + \frac{\pi}{2}\sum_{m=1}^{\infty}\frac{\Gamma(m+\frac{1}{2})}{m\,\Gamma(\frac{1}{2})\,m!}\ . \tag{A.5}$$

The sum over m in Eq. (A.5) can be shown to be equivalent to the sum obtained from the power series expansion of the integrand in

$$Q = -\pi \ln 2 + \frac{\pi}{2}\int_0^1 \frac{du}{u\sqrt{1-u}}\left(1 - \sqrt{1-u}\right) \quad , \tag{A.6}$$

which is readily evaluated as

$$Q = -\pi \ln 2 + \pi \ln \left(1 + \sqrt{1-u}\right)\Big|_0^1 = -2\pi \ln 2 \ . \tag{A.7}$$

Thus

$$\int_0^1 L(x') \ln |x' - x| \, dx' = -\frac{Q}{2\pi \ln 2} = 1 \quad , \tag{A.8}$$

as required in Eq. (3.8), and

$$J = \left[\int_0^1 dx \, L(x)\right]^{-1} = -2 \ln 2 \quad , \tag{A.9}$$

as stated in Eq. (3.12).

Presented at the Particle Accelerator Conference, March 1989

High Frequency Dependence of the Coupling Impedance for a Large Number of Obstacles[1]

Appendix B

R.L. Gluckstern
Physics Department, University of Maryland, College Park, MD 20742

I. Introduction

We have recently derived[2,3] an integral equation for the axial electric field at the pipe radius in the presence of an azimuthally symmetric cavity of arbitrary shape in a beam pipe of circular cross section. We have further shown that the local average of the coupling impedance over frequency decreases as $k^{-1/2}$ for high frequency, essentially independent of the cavity shape. In another paper[4], we extend the derivation to several cavities and obtain the high frequency behavior for a periodic cavity. In this case the real part of the impedance per cell is shown to vary as $k^{-3/2}$, in agreement with Heifets and Kheifets[5], and the imaginary part varies as k^{-1}, as required by causality.

In the present paper we analyze the case of N cavities and explore the high frequency behavior for large N, in an effort to understand the transition to a periodic structure. Not unexpectedly, the result depends critically on which of the limits ($k \to \infty$ or $N \to \infty$) is taken first.

II. Analysis

The starting point for the analysis is the integral equation obtained for the axial electric field in a single obstacle at the beam pipe radius.[2,3] Specifically we have

$$\int_0^g dz'\ G(z')\left[\hat{K}_p(z-z') + \hat{K}_c(z',z)\right] = j \qquad (2.1)$$

and

$$\frac{Z(k)}{Z_o} = \frac{1}{ka^2}\int_o^g dz\, G(z) \quad . \tag{2.2}$$

Here $kc/2\pi$ is the frequency, a is the pipe radius, $Z_o = 120\pi$ ohms is the impedance of free space, and the azimuthally symmetric obstacle, of general shape in the r,z plane, extends axially from z = 0 to z = g at the pipe radius r = a. Apart from a constant and the factor exp(jkz), G(z) is the axial electric field for r = a and 0 < z < g.

The modified "pipe" kernel, $\hat{K}_p(u)$, has the form[2]

$$\hat{K}_p(u) = \frac{2\pi j}{a}\sum_{s=1}^{\infty}\frac{e^{jku - j\,b_s\,|u|/a}}{b_s} \cong \frac{2\pi j}{ka^2}\left\{\begin{matrix} 0 & ,u<0 \\ \sum_{s=1}^{\infty} e^{juj_s^2/2ka^2} & ,u>0 \end{matrix}\right\} \quad . \tag{2.3}$$

where $u = z - z'$, $b_s^2 = k^2a^2 - j_s^2$, and where the last form in Eq. (2.3) is obtained by averaging over frequency, with the dominant contributuion coming from $1 \ll j_s \ll ka$. For $|u| \ll ka^2$, the sum over s can be converted to an integral, leading to

$$\hat{K}_p(u) \cong \left\{\begin{matrix} 0 & ,u<0 \\ \dfrac{(j-1)\sqrt{\pi}}{a\sqrt{ku}} & ,u>0 \end{matrix}\right\} \quad . \tag{2.4}$$

A similar analysis[2] for the "smoothed" high frequency limit of $\hat{K}_c(z',z)$ also leads to the same result, namely

$$K_c(z',z) \cong \left\{\begin{matrix} 0 & ,z'>z \\ \dfrac{(j-1)\sqrt{\pi}}{a\sqrt{k(z-z')}} & ,z'<z \end{matrix}\right\} \quad . \tag{2.5}$$

The solution of Eq. (2.1) with the kernels in Eqs. (2.4) and (2.5) then yields the "smoothed" high frequency limit for the impedance for a single obstacle:

$$\frac{Z_o}{Z(k)} = Z_o Y(k) = F_o(k), \quad F_o(k) = \frac{(1 + j)\, \pi a \sqrt{\pi k}}{\sqrt{g}} . \tag{2.6}$$

For several obstacles, it is easy to see that Eq. (2.1) can be generalized to

$$\sum_m \int_m dz'_m\, G(z'_m) \left[\hat{K}_p(z_n - z'_m) + \delta_{mn} \hat{K}_c(z'_m, z_n)\right] = j , \tag{2.7}$$

where z'_m and z_n denote the variables z' and z within cavities m and n, and $\int_m dz'_m$ is over cavity m. The coupling between different cavities occurs through the pipe kernels, whereas the cavity kernels are diagonal. If we now use the high frequency kernels in Eqs. (2.4) and (2.5) for the diagonal terms and Eq. (2.3) for the pipe kernel in the coupling terms, it is clear that the only surviving contributions to the sum over m will be those for $z'_m < z_n$, that is $m \leq n$. Specifically we obtain

$$\frac{2(1 + j)\sqrt{\pi}}{a\sqrt{k}} \int_o^t \frac{dt'\, G_n(t')}{\sqrt{t - t'}} + \frac{2\pi}{ka^2} \sum_{s=1} \sum_{m=1}^{n-1} \exp\left[\frac{j(n - m)L j_s^2}{2ka^2}\right] \int_o^g dt'\, G_m(t') = 1 , \tag{2.8}$$

where $z'_m = mL + t'$, $z_n = nL + t$, and where we assume that we hav N identical cavities whose centers are spaced a distance L apart. We have also approximated $z_n - z'_m$ by $(n - m)L$ in the non-diagonal terms,

corresponding to the assumption NL >> g. The impedance is then

$$\frac{Z(k)}{Z_o} = \frac{1}{ka^2} \sum_{m=1}^{N} \int_o^g dt\, G_m(t) \quad . \tag{2.9}$$

Equation (2.8) can be simplified by writing

$$G_n(t') = \frac{(1 - j)\, a \sqrt{k}}{4\pi \sqrt{\pi}\, \sqrt{t'}}\, y_n \quad , \tag{2.10}$$

leading to

$$y_n + \frac{(1 - j)\, \sqrt{g}}{a \sqrt{\pi k}} \sum_{s=1}^{\infty} \sum_{m=1}^{n-1} y_m \exp\left[\frac{j(n - m) L j_s^2}{2ka^2}\right] = 1 \tag{2.11}$$

and

$$\frac{Z(k)}{Z_o} = \frac{(1 - j)\, \sqrt{g}}{2\pi a \sqrt{\pi k}} \sum_{n=1}^{N} y_n \quad . \tag{2.12}$$

Our task is to solve Eq. (2.11) for y_n and then use Eq. (2.12) to obtain the impedance. This can be facilitated by constructing the transform $w(h) = \sum_{n=1}^{\infty} h^n y_n$, in which case use of the convolution theorem leads to the solution

$$w(h) = \frac{h}{1 - h} \left[1 + \frac{(1 - j)\, \sqrt{g}}{2\pi a \sqrt{\pi k}}\, p(h)\right]^{-1} \quad , \tag{2.13}$$

where

$$p(h) = \sum_{s=1}^{\infty} \sum_{\ell=1}^{\infty} h^{\ell} e^{\frac{\ell L j_s^2}{j 2ka^2}} \cong \sum_{s=1}^{\infty} \frac{h}{1 - h - j \frac{L j_s^2}{2ka^2}} . \tag{2.14}$$

The last form of Eq. (2.14) holds in the range $ka^2 >> Lj_s^2$.

A simple approximation to $Z(k)$ in Eq. (2.12) for large N can be obtained by evaluating

$$w[\exp(-1/N)] = \sum_{n=1}^{\infty} y_n e^{-n/N} , \tag{2.15}$$

where the exponential cut-off simulates the sum from n = 1 to N in Eq. (2.12). For $h \cong 1 - 1/N$, we find

$$w\left(1 - \frac{1}{N}\right) \cong N\left[1 + \frac{(1 - j)\sqrt{g}}{\sqrt{\pi ka^2}} \sum_{s=1}^{\infty} \frac{1}{\frac{1}{N} - j \frac{L j_s^2}{2ka^2}}\right]^{-1} . \tag{2.16}$$

Let us first consider the limit $N \to \infty$. In this case we can use $\sum_{s=1}^{\infty} j_s^{-2} = 1/4$ to evaluate the sum over s, to obtain

$$N Z_o Y(k) \cong \frac{(1 + j)\pi a \sqrt{\pi k}}{\sqrt{g}} + \frac{j\pi ka^2}{L} , \text{ large } N , \tag{2.17}$$

the result obtained earlier[4] for a periodic structure. If instead, we

assume that $1 << N << ka^2/L$, the sum over s can be converted to an integral over j_s from 0 to ∞ to give

$$N Z_o Y(k) \cong \frac{(1 + j)\ \pi a \sqrt{\pi k}}{\sqrt{g}} \left[1 + \frac{\sqrt{gN}}{\sqrt{\pi L}}\right] . \tag{2.18}$$

This limit corresponds to converting the sum over s to an integral in Eq. (2.11), leading to

$$y_n + \frac{1}{\pi}\frac{\sqrt{g}}{\sqrt{L}} \sum_{m=1}^{n-1} \frac{y_m}{\sqrt{n - m}} = 1 . \tag{2.19}$$

For large n, it is easy to show from Eq. (2.19) that the asymptotic form of y_n is

$$y_n \to \frac{\sqrt{L}}{\sqrt{gn}} , \tag{2.20}$$

leading to

$$N Z_o Y(k) \cong \frac{(1 + j)\ \pi a \sqrt{\pi N k}}{2\sqrt{L}} . \tag{2.21}$$

This result, which is more accurate than Eq. (2.18) for large N because it uses $\sum_{n=1}^{N} y_n$ rather than $\sum_{n=1}^{\infty} y_n e^{-n/N}$, suggests that Eq. (2.18) can be made more accurate by replacing the factor $gN/\pi L$ by $gN/4L$ to obtain

$$N Z_o Y(k) \cong \frac{(1 + j)\ \pi a \sqrt{\pi k}}{\sqrt{g}} \left[1 + \frac{\sqrt{gN}}{2\sqrt{L}}\right], \text{ large } ka. \tag{2.22}$$

This surprising result predicts that the impedance will vary as $N^{1/2}$ once $N > L/g$, and that the transition to the periodic result in Eq. (2.17) takes place when $N > ka^2/L$.

Finally, we can obtain a reusIt which properly contains both limits by converting the sum over s in Eq. (2.16) to an integral over j_s with a lower limit on j_s chosen to retain the relation $\sum_{s=1}^{\infty} j_s^{-2} = 1/4$. In this way we obtain the relation

$$N Z_o Y(k) \cong F_o(k) + \alpha \sqrt{N-1} \tan^{-1} \frac{\alpha}{2\sqrt{N}} , \qquad (2.23)$$

with

$$\alpha = \frac{(1 + j)\, a \sqrt{\pi k}}{\sqrt{L}} , \qquad (2.24)$$

which can easily be seen to give the limit in Eq. (2.17) as $N >> ka^2/L$ and the limit in Eq. (2.22) for $1 << N << ka^2/L$. The change to N-1 in Eq. (2.23) is made to give the correct limit when N=1.

We have repeated the analysis for a small obstacle, that is where $kg \sim 1$ even though $kL >> 1$. The entire analysis and final result in Eq. (2.23) are unchanged, except that $F_o(k)$ is now the <u>actual</u> single obstacle admittance. In the case $kg << 1$, Gluckstern and Neri[6] have shown that

$$F_o(k) \cong 2\pi ka \left[-\frac{j}{k^2 \Delta} + \sum_{s=1}^{\infty} \frac{e^{-jb_s g/a}}{b_s} + j \frac{2\ell n 2}{\pi} \right] , \qquad (2.25)$$

where Δ is the cross sectional area of the (small) pillbox.

III. Discussion

Equation (2.23) gives a result for the average impedance (admittance) for N equally spaced identical cavities at high frequency. The transition to the periodic result shows clearly when $NL >> ka^2$. In addition, Eq. (2.23) predicts that, for $ka^2 >> NL$ the impedance will return to a $k^{-1/2}$ dependence at high frequency, but with a coefficient which varies as $N^{1/2}$ for large N, as given in Eq. (2.22). This has important implications where there are a large number of obstacles, and where conventional wisdom has up to now been to add impedances. We have checked this result by evaluating y_n numerically from Eq. (2.19). In addition, we have allowed g/L and L to be different for each cavity and confirm numerically that the $N^{1/2}$ result does not depend on delicate phase cancellations. Moreover, we expect that the analysis for the transverse coupling impedance will be parallel, and therefore believe that our conclusions are correct at high frequency for multiple obstacles of any shape in a beam pipe of any cross section.

IV. Acknowledgment

I would like to thank Filippo Neri for several helpful conversations, and John Diamond for performing the numerical calculations.

V. References

1. Work supported by the Department of Energy.
2. R.L. Gluckstern, High Frequency Behavior of the Longitudinal Coupling Impedance for a Cavity of Arbitrary Shape, to be published in Physical

Review D.

3. R.L. Gluckstern and B. Zotter, The Coupling Impedance of Asymmetric Cavities, CERN-LEP-613, July 1988.

4. R.L. Gluckstern, Longitudinal Impedance of a Periodic Structure at High Frequency, to be published in Physical Review D.

5. S.A. Heifets and S.A. Kheifets, High Frequency Limit of the Longitudinal Impedance of an Array of Cavities, SLAC-PUB-4625 (1988).

6. R.L. Gluckstern and F. Neri, Longitudinal Coupling Impedance of a Small Obstacle, companion paper, this Conference; see also R.L. Gluckstern, Longitudinal Coupling Impedance for Several Small Pillboxes, CERN Report LEP-TH/88-39, June 1988.

TO BE PRESENTED AT THE 14th INTERNATIONAL CONFERENCE ON HIGH ENERGY ACCELERATORS, KEK, JAPAN

Appendix C

ANALYSIS OF COAXIAL WIRE MEASUREMENT OF LONGITUDINAL COUPLING IMPEDANCE[1]

R.L. GLUCKSTERN AND R. LI
Physics Department, University of Maryland, College Park, MD, USA

I. INTRODUCTION

In recent work[2], a method has been developed to calculate the longitudinal impedance for an azimuthally symmetric obstacle in a beam pipe of circular cross section. The method has been applied to a small obstacle[3], to an obstacle of general shape at high frequency[2], and to several obstacles, including a periodic structure[4,5] at high frequency.

Coupling impedances are difficult to measure directly. Instead, the reflection and transmission coefficients for a pulse carried through the obstacle on a thin coaxial wire are measured and the results approximate the longitudinal coupling impedance.[6]

In the present paper, an analysis is carried out including the coaxial wire and new boundary conditions for the fields at the surface of the wire. We then estimate the validity of the coaxial wire measurement for a variety of frequencies and geometries. Finally, several numerical calculations are carried out for both the beam and the wire pulse. The results confirm the predictions of the analysis.

II. ANALYSIS FOR A BEAM

Let us consider a beam pipe of radius a which enters and leaves an azimuthally symmetric cavity of general shape. The longitudinal impedance can be obtained by field matching at r = a. The source fields in the ultrarelativistic limit are

$$E_z^{(s)} = 0 \ , \ Z_o H_\varphi^{(s)} = - \frac{Z_o I_o}{2\pi r} e^{-jkz} = -E_r^{(s)} \ . \tag{2.1}$$

Adding the pipe fields, we find

$$E_z = \int_{-\infty}^{\infty} dq \ A(q) \ e^{-jqz} \ \frac{J_o(Kr)}{J_o(Ka)} \ , \tag{2.2}$$

$$Z_o H_\phi = - \frac{Z_o I_o}{2\pi r} e^{-jkz} - jk \int_{-\infty}^{\infty} dq\ A(q)\ e^{-jqz} \frac{J_o'(Kr)}{K J_o(Ka)} . \qquad (2.3)$$

Here $k = \omega/c$, the suppressed time dependence is $\exp(j\omega t)$, $Z_o = 120\pi$ ohms, and I_o is the driving current. We have defined $K = \sqrt{k^2 - q^2}$ and take the contour in the q plane below the poles on the negative real axis and above the poles on the positive real axis so that we have only outgoing waves for the pipe fields as $z \to \pm\infty$. Defining $E_z(a,z) \equiv f(z)$, we have

$$f(z) = \int_{-\infty}^{\infty} dq\ A(q)\ e^{-jqz} , \quad A(q) = \frac{1}{2\pi} \int_o^g dz\ f(z)\ e^{jqz} , \qquad (2.4)$$

where $f(z)$ vanishes for $z < 0$, $z > g$.

The fields in the annular cavity region for $r \geq a$ are expanded into an orthonormal set of cavity modes[3] which satisfy metallic boundary conditions on the outer wall of the cavity as well as at $r = a$. Matching the magnetic field in the pipe and cavity regions leads to

$$\int_o^g dz'\ F(z') \left[K_p(z' - z) + K_c(z,z') \right] = j\ e^{-jkz} , \qquad (2.5)$$

where the pipe and cavity kernels are

$$K_p(u) = \int_{-\infty}^{\infty} dq\ e^{-jqu}\ \hat{J}(q) , \quad K_c(z,z') = 4\pi^2 \sum_\ell \frac{h_\ell(z)\ h_\ell(z')}{k^2 - k_\ell^2} . \qquad (2.6)$$

Here $h_\ell(z)$ is the normalized magnetic field in mode ℓ at $r = a$, $f(z) = F(z)\ Z_o I_o / ka^2$, and $\hat{J}(q)$ is defined in Eq. (2.7). The sum in Eq. (2.6) is over all azimuthally symmetric modes in the annular cavity.

We can obtain a more explicit form for $K_p(u)$ in Eq. (2.6) by using the identity

$$\hat{J}(q) \equiv \frac{J_o'(Ka)}{Ka\ J_o(Ka)} = - 2 \sum_{s=1}^{\infty} \frac{1}{q^2a^2 - b_s^2} . \qquad (2.7)$$

where j_s are the zeroes of $J_o(x)$, and where $b_s^2 = k^2a^2 - j_s^2 = -\beta_s^2$. For positive u, the contour in Eq. (2.6) can be closed in the lower half plane, en-

closing the poles at $qa = b_s$ and $qa = -j\beta_s$. For negative u, the contour encloses the poles at $qa = -b_s$ and $qa = j\beta_s$. The result for $K_p(u)$ is then

$$K_p(u) = \frac{2\pi j}{a} \sum_{s=1}^{\infty} \frac{e^{-jb_s|u|/a}}{b_s} \tag{2.8}$$

where $b_s \to -j\beta_s$ when $j_s > ka$.

The longitudinal impedance of the cavity can be written as

$$\frac{Z(k)}{Z_o} = \frac{1}{Z_o I_o} \int_{-\infty}^{\infty} dz\, e^{jkz} E_z(0,z) = \frac{2\pi A(k)}{Z_o I_o} = \frac{1}{ka^2} \int_o^g dz\, F(z)\, e^{jkz} . \tag{2.9}$$

The solution of Eq. (2.5) for $F(z')$ can then be used to obtain the impedance by means of Eq. (2.9).

III. ANALYSIS FOR A COAXIAL WIRE

We now start with a TEM mode in the beam pipe including a coaxial wire of radius r_o, described by

$$\tilde{E}_z = 0 , \quad Z_o \tilde{H}_\phi = - \frac{Z_o I_o}{2\pi r} e^{-jkz} = -\tilde{E}_r , \tag{3.1}$$

where ~ stands for the coaxial wire case and where we have normalized to make Eq. (3.1) identical to Eq. (2.1). Adding the pipe fields, we find

$$\tilde{E}_z = \int_{-\infty}^{\infty} dq\, \tilde{A}(q) e^{-jqz} \frac{F_o(Kr)}{F_o(Ka)} , \tag{3.2}$$

$$Z_o \tilde{H}_\phi(r,z) = - \frac{Z_o I_o}{2\pi r} e^{-jkz} + jk \int_{-\infty}^{\infty} dq\, \tilde{A}(q)\, e^{-jqz} \frac{F_1(Kr)}{K\, F_o(Ka)} , \tag{3.3}$$

where the linear combinations

$$F_o(x) = Y_o(x) - \mu\, J_o(x) , \quad F_1(x) = Y_1(x) - \mu\, J_1(x) , \tag{3.4}$$

with $\mu = Y_o(Kr_o)/J_o(Kr_o)$, are chosen to satisfy the boundary condition on the surface of the wire. The contour in the q plane is as before in order that we only have outgoing waves for the pipe fields.

The analysis continues as in Section II. The only difference is that $\hat{J}(q)$ in Eq. (2.7) is now

$$\tilde{J}(q) = -\frac{1}{Ka}\left[\frac{Y_1(Ka) - \mu J_1(Kr_o)}{Y_o(Ka) - \mu J_1(Kr_o)}\right] . \tag{3.5}$$

The function $\tilde{J}(q)$ is analytic in q or K, except for a second order pole at K=0 (first order poles at q=±k), and first order poles at the zeros of the denominator of Eq. (3.5). We can then write $\tilde{J}(q)$ as a sum over these poles by finding the appropriate residues, obtaining finally

$$\tilde{J}(q) = -2\sum_{s=0}^{\infty}\frac{\alpha_s}{q^2a^2 - \tilde{b}_s^2} , \tag{3.6}$$

where $\tilde{b}_s^2 = k^2a^2 - i_s^2 = -\tilde{\beta}_s^2$, and where

$$\alpha_s = \frac{J_o^2(r_o i_s/a)}{J_o^2(r_o i_s/a) - J_o^2(i_s)} , \; s \geq 1 , \; \alpha_o = \frac{1}{2\,\ell n(a/r_o)} . \tag{3.7}$$

Here i_s is the value of Ka at the zeroes of $F_o(Ka)$, with $i_o \equiv 0$. The pipe kernel is therefore

$$\tilde{K}_p(u) = \frac{2\pi j}{a}\sum_{s=0}^{\infty}\frac{\alpha_s}{\tilde{b}_s}\, e^{-j\tilde{b}_s|u|/a} . \tag{3.8}$$

The expression for the magnetic field in the cavity region is identical to that for the case of a beam on axis, since the boundary conditions are not affected by the presence of the wire. The integral equation for the axial electric field at the beam pipe is therefore

$$\int_o^g dz'\, \tilde{F}(z')\left[\tilde{K}_p(|z'-z|) + K_c(z,z')\right] = j\, e^{-jkz} , \tag{3.9}$$

with $\tilde{K}_p$ being given by Eq. (3.8) and K_c by Eq. (2.6).

In order to obtain the transmission and reflection coefficients, it is simplest to examine Eq. (3.3) for large positive and negative z. The TEM

(coaxial) modes correspond to the poles at $q = \pm k$. Specifically one obtains

$$Z_o \tilde{H}_\phi^{TEM} = - \frac{Z_o I_o}{2\pi r} + \frac{2\pi\, \alpha_o A(\pm k)\, e^{\mp jkz}}{r} , \qquad (3.10)$$

where the $\pm$ is for the pipe region with $z \gtrless 0$. Using Eq. (2.4), we obtain for the reflection and transmission coefficients

$$1 - T(k) = \frac{2\pi\alpha_o}{ka^2} \int_o^g dz\, \tilde{F}(z)\, e^{jkz} , \quad R(k) = \frac{2\pi\alpha_o}{ka^2} \int_o^g dz\, \tilde{F}(z)\, e^{-jkz} , \qquad (3.11)$$

where we have again used $\tilde{f}(z) = \tilde{F}(z)\, Z_o I_o / ka^2$.

Comparison of Eq. (3.11) with Eq. (2.9) shows why the impedance corresponds more closely to the transmission coefficient rather than the reflection coefficient, particularly at frequencies for which $kg \geq 1$. In fact the correspondence is

$$1 - T(k) \rightarrow \frac{\pi}{\ell n(a/r_o)} \frac{Z(k)}{Z_o} . \qquad (3.12)$$

IV. COMPARISON OF 1-T(k) AND $2\pi\alpha_o Z(k)/Z_o$

The difference between the coupling impedance and $1 - T(k)$ for the pulse on the wire is <u>totally</u> contained in the modified pipe kernel in Eq. (3.8). Specifically we have an additional term proportional to $[\ell n(a/r_o)]^{-1}$, a shift of the zeroes from j_s to i_s, and the modified coefficients α_s. For $r_o/a \ll 1$, it is easy to show that

$$i_s \cong j_s + \pi/2L_s , \quad s \geq 1 , \quad L_s = \ell n(2a/r_o j_s) - \gamma , \qquad (4.1)$$

where $\gamma = .577$ is Euler's constant. Also $\alpha_s^{-1} \cong 1 - \pi/2 j_s L_s^2$ for $s \geq 1$. Thus all changes are proportional to $[\ell n(a/r_o)]^{-1}$ or smaller, suggesting that there may be differences of order 20%, even for r_o/a as small as .01.

The result for a small obstacle of cross sectional area Δ may be taken directly from earlier work.[3] Specifically we can write

$$\frac{2\pi\, \alpha_o}{1 - T(k)} = 2\pi ka \left[- \frac{j}{k^2 \Delta} + \sum_{s=0}^{\infty} \frac{\alpha_s e^{-j\tilde{b}_s g/a}}{\tilde{b}_s} + j \frac{2\ell n 2}{\pi} \right] . \qquad (4.2)$$

We therefore expect that the primary difference for a small obstacle will be a shift in the frequency at which the singular behavior occurs from $ka = j_s$ to i_s. This is confirmed in Figs. 1a and 1b where we plot the real and imaginary parts of $Y(k)$ and $2\pi\alpha_o[1 - T(k)]^{-1}/Z_o$ for a pill box of length $g = .05a$ and width $b-a = .1a$ for $r_o/a = .01$. The corresponding results for $r_o/a = .1$ are shown in Figs. 2a and 2b. The numerical results are obtained with programs which expand the fields in the pipe region and the cavity plus pipe region into traveling axial waves. The figures clearly show that the details of the two results differ, but that the average over the sawtooth behavior is essentially unmodified.[7]

The result at high frequency is similarly easy to predict. In earlier work, we showed[2] that the average behavior of the impedance at high frequency is obtained by converting the sum over s in the pipe kernel to an integral over s, and that the main contributions come from s of order $(ka^2/g)^{1/2}$. Since the spacing of the zeroes is essentially unmodified, we expect no significant difference in the average behavior at high frequency. This is confirmed in Figs. 3a and 3b for the real and imaginary parts of $Z(k)$ and $Z_o[1 - T(k)]/2\pi\alpha_o$ for $g/a = \pi/4$, $b/a = 1.5$, $r_o/a = .1$. What is remarkable is that the complicated oscillatory behavior is duplicated as well.

V. SUMMARY

We have derived the integral equation for the transmission coefficient of the coaxial mode for a pulse along a wire on the axis of a beam pipe and cavity. The only difference between this equation and the one for the longitudinal coupling impedance is in the pipe kernel and is of order $[\ell n(a/r_o)]^{-1}$ or less. Specific predictions are made for the comparison between $Z(k)/Z_o$ and $[1 - T(k)]/2\pi\alpha_o$ for both a small obstacle, and for a larger obstacle at high frequency, and these are confirmed by numerical calculations. Our conclusion is that measurement of $Z_o[1 - T(k)]/2\pi\alpha_o$ corresponds remarkably well to the actual longitudinal coupling impedance.

VI. ACKNOWLEDGMENT

The authors would like to express their appreciation to Filippo Neri for helpful conversations.

VII. REFERENCES

1. Work supported by the Department of Energy.
2. R.L. Gluckstern, Phys. Rev. D, 39, 2732 (1989).
3. R.L. Gluckstern and F. Neri, Longitudinal Coupling Impedance of a Small Obstacle, Proceedings of the Particle Accelerator Conference, Chicago,

IL, March 1989.
4. R.L. Gluckstern, High Frequency Behavior of the Coupling Impedance for a Large Number of Obstacles, Proceedings of the Particle Accelerator Conference, Chicago, IL, March 1989.
5. R.L. Gluckstern, Phys. Rev. D, 39, 2780 (1989).
6. See, for example, H. Hahn and F. Pederson, On Coaxial Wire Measurements of the Longitudinal Coupling Impedance, BNL Report No. 50870 (1978).
7. The erratic nature of a few of the singularities is due to the cut off in mode number and the frequency step used in the numerical calculation.

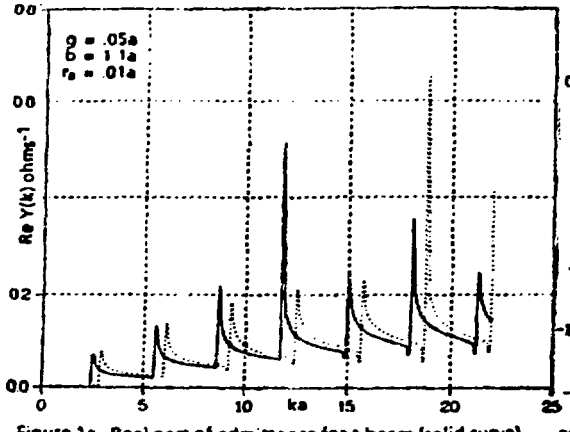

Figure 1a. Real part of admittance for a beam (solid curve) and a coaxial wire of radius r_0 = .01a (dashed curve).

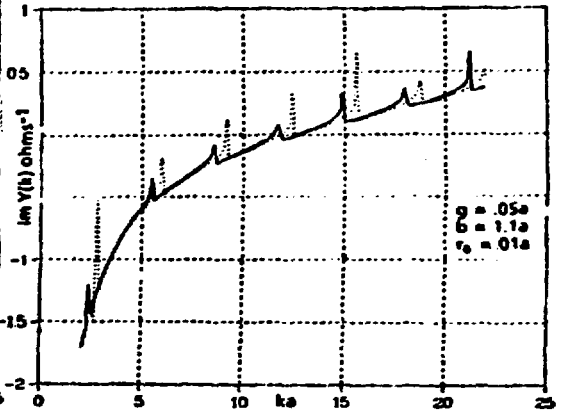

Figure 1b. Imaginary part of admittance for a beam (solid curve) and a coaxial wire of radius r_0 = .01a (dashed curve).

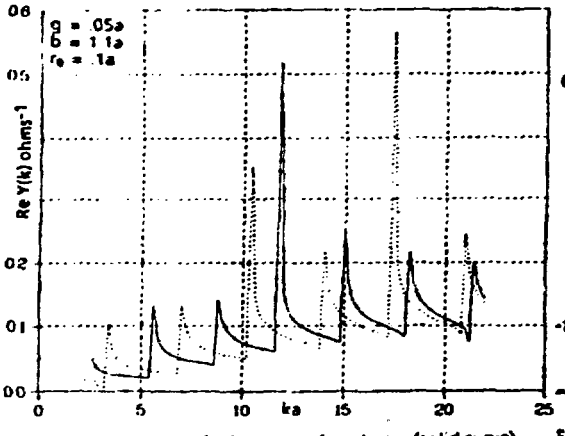

Figure 2a. Real part of admittance for a beam (solid curve) and a coaxial wire of radius r_0 = .1a (dashed curve).

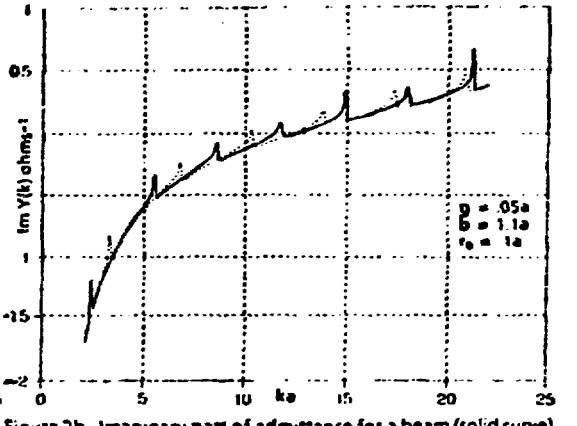

Figure 2b. Imaginary part of admittance for a beam (solid curve) and a coaxial wire of radius r_0 = .1a (dashed curve).

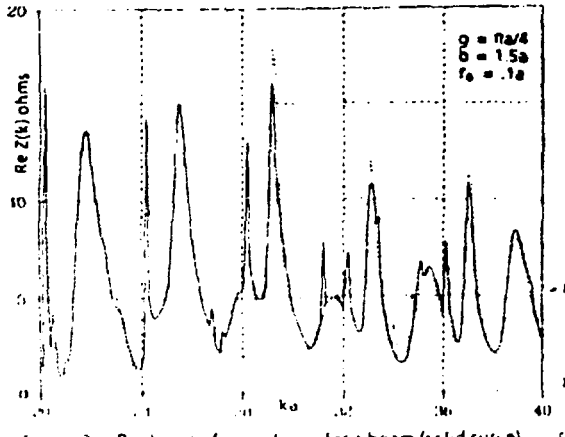

Figure 3a. Real part of impedance for a beam (solid curve)

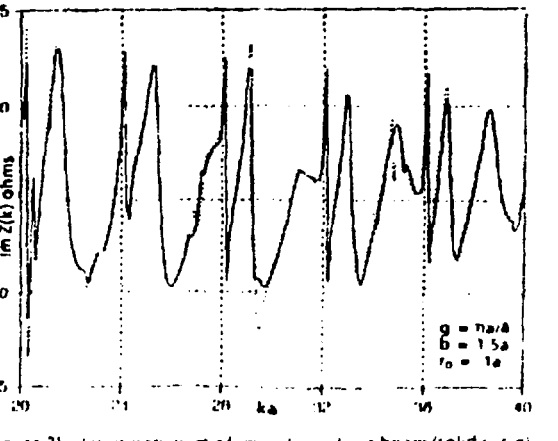

Figure 3b. Imaginary part of impedance for a beam (solid curve)

Beam-Induced Energy Spreads at Beam-Pipe Transitions*

K.C.D. Chan

Los Alamos National Laboratory

Argonne National Laboratory
Advanced Photon Source
Impedance and Bunch Instability Workshop
October 31 - November 1, 1989

---

*Work supported by the Department of Energy.

BEAM-INDUCED ENERGY SPREADS AT BEAM-PIPE TRANSITIONS*

K. C. D. Chan
Los Alamos National Laboratory, Los Alamos, NM 87545

Introduction

Wakefields are induced when a beam bunch traverses a transition along the beam pipe. A transition can be a change of beam-pipe cross section either in shape or in size. These wakefields will, in turn, modify the kinetic energy of the beam bunch resulting in an energy spread in the beam. This paper will describe a simple picture for understanding these wakefields and the applications of this understanding to the design of beam-pipe transitions with minimized energy spread. Only longitudinal wakefields are considered in this paper.

A Simple Physical Picture

A simple picture based on energy conservation can be used to describe the physics at a beam-pipe transition. Figure 1 shows a bunch of electrons passing through a transition. This is a step-down transition where a circular beam pipe reduces its radius. The figure shows a time sequence of pictures of the electric field lines. The first and the last of these pictures represent two states when the electric field lines are straight. At these states, the static electromagnetic field energy (referred to as static energy hereafter) of the beam bunch is in equilibrium. The difference of the static energies between these two equilibrium states depends only on the two beam-pipe radii and is given by the following formula:

$$\Delta W = \frac{q^2}{4\pi^{3/2}\epsilon_0\sigma_{\rm rms}} ln\left(\frac{b}{a}\right) \ ,$$

where

b is the radius of the larger beam pipe
a is the radius of the smaller beam pipe
$\sigma_{\rm rms}$ is the rms half-width of the beam bunch
q is the charge of the beam bunch.

Static energy is lost during the transition. By conservation of energy, this amount of lost static energy is shared between the energy of a backward-going scattered wave and the kinetic energy gain of the bunch. One can put more of the static energy into the kinetic energy gain by using a tapered transition to decrease the amount of backward

* Work supported by Los Alamos National Laboratory Institutional Supporting Research, under the auspices of the United States Department of Energy.

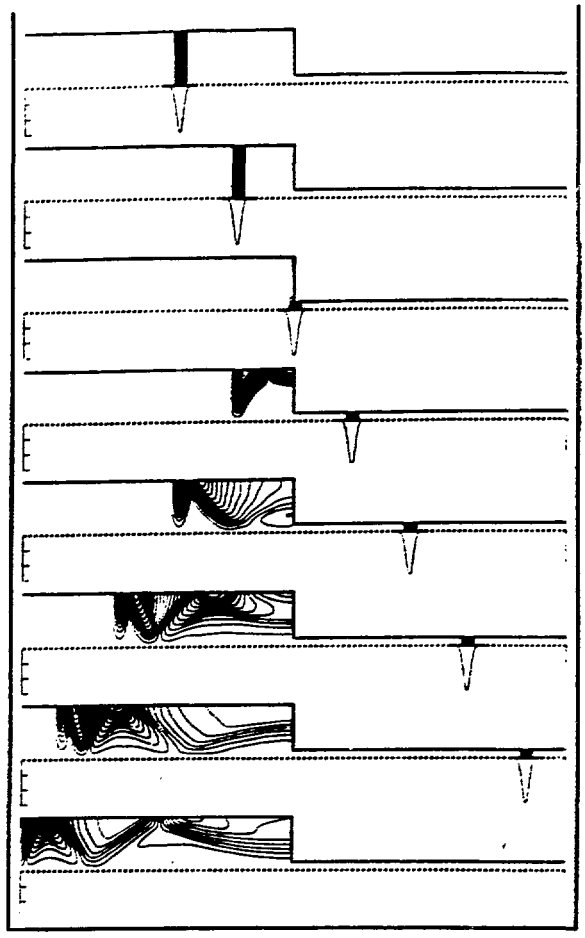

Fig. 1. A picture sequence showing the electric field lines when a bunch passes a step-down transition. The density of the field lines represents the electric field strength.

wave generated. Figure 2 shows the wake functions of a beam bunch traversing a tapered transition. The wake function is proportional to the kinetic energy gain of the beam bunch. The curves show, as expected, an increase of the kinetic energy for the decreasing taper angle.

Figure 3 shows a similar picture sequence for a step-up transition. Both the increase of the static energy and the energy of the forward-going scattered wave have to come from a loss in the kinetic energy of the beam bunch. Figure 4 shows the wake functions for a tapered step-up transition with the wake functions becoming more negative with the increasing taper angle because more intense scattered waves are generated.

The simple picture described in this section shows that the static energy and the kinetic energy of the beam bunch are re- distributed at a beam-pipe transition. Changes in kinetic energy of a beam bunch resulting from wakefields can only happen by an energy exchange with the static energy and by an energy transfer to the scattered waves. A more quantitative account can be found in Ref. 1.

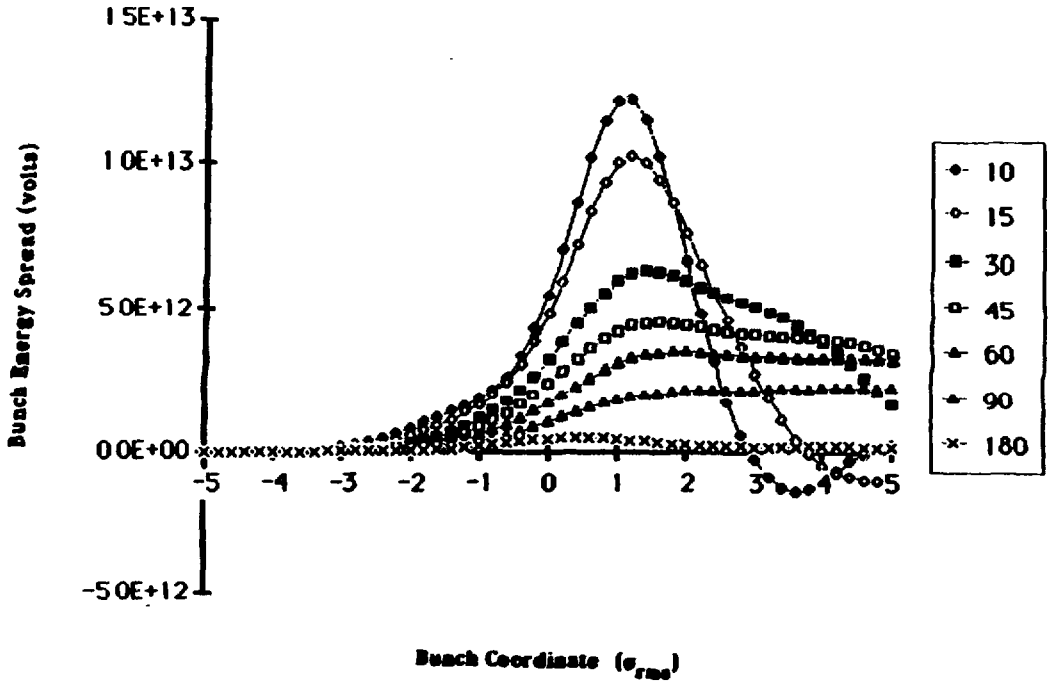

Fig. 2. Wake function of step-down transitions of different taper angles. Negative bunch coordinates correspond to the front of the bunch.

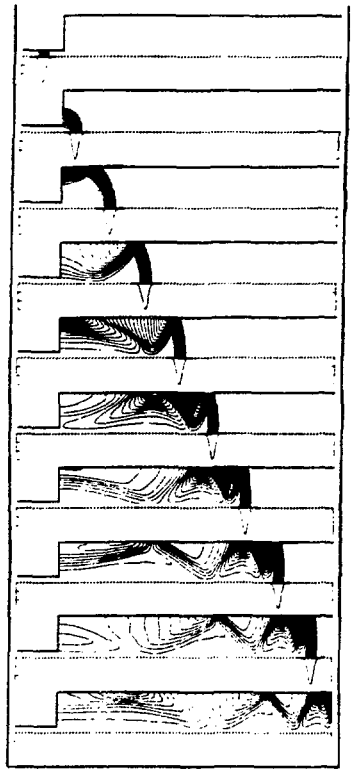

Fig. 3. A picture sequence showing the electric field lines when a bunch passes a step-up transition. The density of the field lines represents the electric field strength.

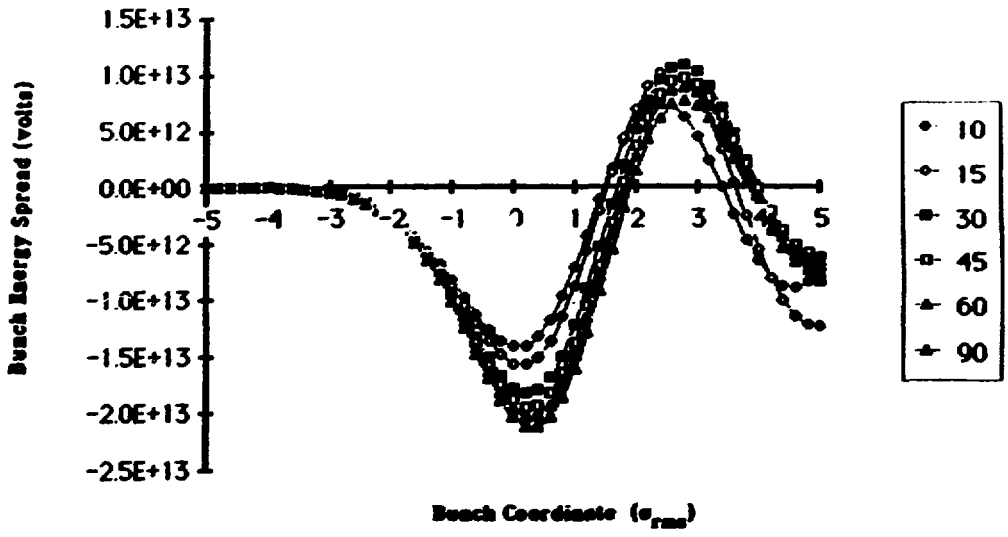

Fig. 4. Wake function of step-up transitions of different taper angles. Negative bunch coordinates correspond to the front of the bunch.

Applications

At various times it is necessary to design a beam pipe transition. The knowledge learned from the previous section can be applied in designing such a transition with reduced wakefields. One 2D and one 3D example are described here.

The 2D example is a design of a step-down transition as shown in Fig. 5. The larger beam pipe is extended over the smaller beam pipe. The extra static energy in the larger beam pipe, which is the source of beam energy change, is diverted into the coaxial portion of the transition. Without the extra static energy, there is no wakefield-induced energy spread. The wake function for this design is shown in Fig. 2 (wake function assigned taper angle of 180°).

The 3D example is a design of a transition from a circular to an elliptic beam pipe. In this case, the two causes of kinetic energy changes of a beam bunch are respectively minimized. First, scattered waves are minimized by tapering the transition. A slow (adiabatic) transition eliminates practically all scattered waves. Second, an exchange between the kinetic energy and static energy is minimized by choosing the proper cross section at the tapered section such that the static energy remains constant along the tapered transition. To 'match' the static energy, one transverse dimension is increased while the other is decreased, giving an ellipse with semiaxes of a and b. The pairs of a and b used along the taper are pairs that give the same static energy as the circular pipe.

A transition matching a circular beam pipe (radius 1.2 cm) to an elliptical beam pipe has been so designed. A 30-cm taper section of elliptical cross section is used. The major semiaxis a of the ellipse is increased gradually from 1.2 to 2.4 cm while the semi minor axis b is decreased from 1.2 to 1.0 cm. Figure 6 shows a comparison of wakefield effects with

and without this 'matched tapered section' as calculated using T3 (Ref. 2). By minimizing the two causes of kinetic energy changes, the wake function is reduced by over a factor of 10.

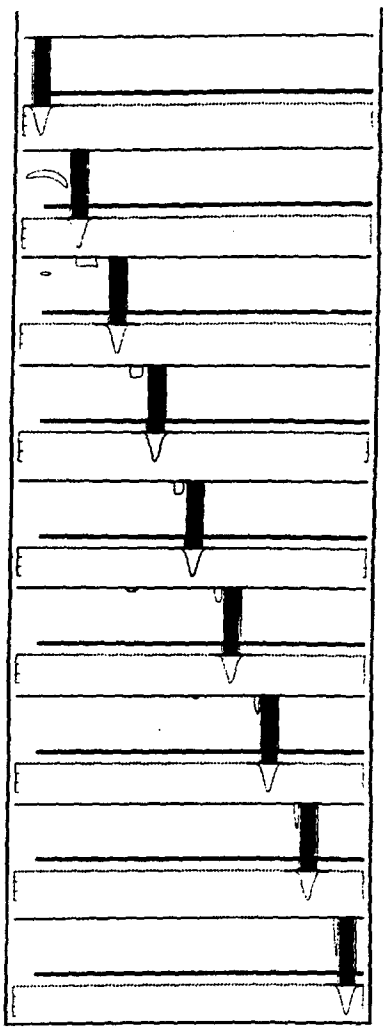

Fig. 5. A picture sequence showing the electric field lines when a bunch passes a step-down transition designed with minimized energy spread. The density of the field lines represents the electric field strength.

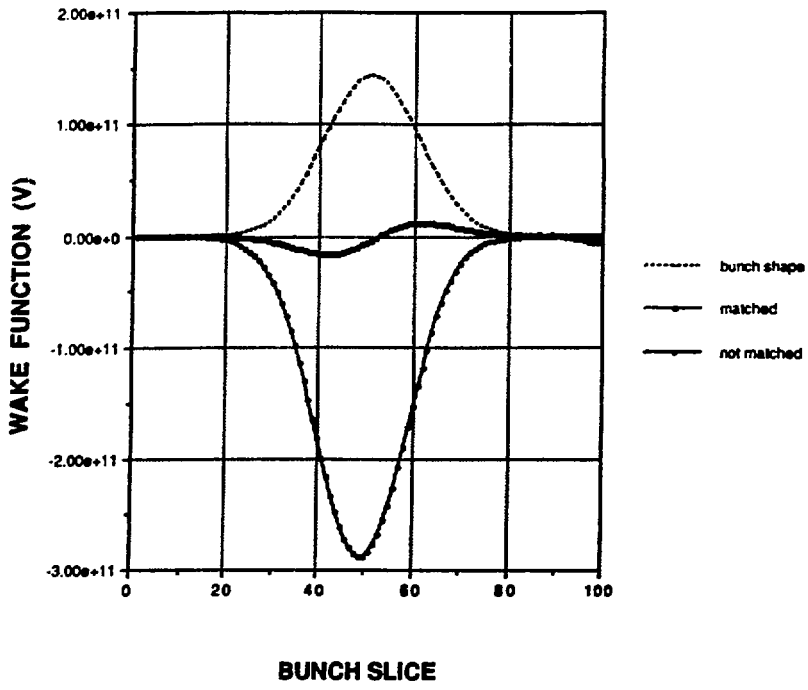

Fig. 6. Wake functions for a beam bunch traversing a transition between a beam pipe of circular and elliptical cross section, showing the reduction of the wake function by using a matched tapered transition.

Conclusion

Energy spread induced by wakefield effects at a beam-pipe transition can be understood and reduced by a simple physical picture based on energy considerations.

References

1. K. C. D. Chan, "Short-Range Wakefield Effects in Rf-Based Free-Electron Laser" (Los Alamos National Laboratory report LA-UR 88-2120), Free Electron Lasers (Proceedings of the Beijing FEL Seminar), August 11-23, 1988, Peking University, Beijing, People's Republic of China, Beijing Institute of Modern Physics Series, published by World Scientific, Singapore (1989).

2. R. Klatt, F. Krawczyk, W. R. Novender, C. Palm, T. Weiland, B. Steffen, T. Barts, M. J. Browman, R. Cooper, C. T. Mottershead, G. Rodenz, and S. G. Wipf, "MAFIA — A Three-Dimensional Electromagnetic CAD System for Magnets, RF Structures and Transient Wake-Field Calculation," Proc. 1986 Linear Accelerator Conf., Stanford Linear Accelerator Center report SLAC-303, 276-278 (1986).

On the Calculation of Wake Functions Using MAFIA-T3 Code

F.A. Harfoush and K.Y. Ng

of

Fermi National Accelerator Laboratory
Batavia, Illinois

Argonne National Laboratory
Advanced Photon Source
Impedance and Bunch Instability Workshop
October 31 - November 1, 1989

FN-521

ON THE CALCULATION OF WAKE FUNCTIONS USING MAFIA-T3 CODE

Fady A. Harfoush and King-Yuen Ng

Fermi National Accelerator Laboratory
Batavia, IL 60510

October, 1989
(Revised December 1989)

1 Wake Functions

A test charge at (r, θ, z) trailing a point source at (a, θ_0, z_o) experiences a wake force. This wake force can have both a longitudinal component and a transverse one. From Refs. [1] and [2] , the general form of the wake force components are given as:

$$F_z(s) = -\sum_{m=0}^{\infty} eI_m W'_m(s) r^m \cos m(\theta - \theta_0) \ , \tag{1}$$

$$F_\perp(s) = \sum_{m=1}^{\infty} eI_m W_m(s) m r^{m-1} [\hat{r} \cos m(\theta - \theta_0) - \hat{\theta} \sin m(\theta - \theta_0)] + F_\perp^0(s) \ , \tag{2}$$

where e is the charge of the test particle, $s = z_o - z$ is the longitudinal distance the test particle is lagging behind. The multipole coefficients of the point source are $I_m = qa^m$, where q is the charge of the source. Here, the wake force components have been integrated across the structure of the vacuum chamber; i.e., $F_z(s)$ and $F_\perp(s)$ have dimension [force*length]. The function $W_m(s)$ is called the transverse wake function or wake potential in the m-multipole and W'_m is the corresponding longitudinal wake function. The axis of the cylindrical coordinate is chosen as the path of be particle beam, along which coupling impedances are to be evaluated. With respect to this

axis the structure being studied may not have cylindrical symmetry. Under this situation, strictly speaking Eqs. (1) and (2) are not valid. However, we expect Eqs. (1) and (2) to hold when the offsets r and a of the test particle and source particle are sufficiently small, and this is actually what we need in the computation of impedances. For structures with no axial symmetry, the $m = 0$ component represented by $F_\perp^0(s)$ in Eq. (2) is in general nonzero.

In the case of cylindrical symmetry, TBCI computes each multipole m of the wake functions separately by setting $r = a =$ pipe radius to eliminate numerical noise. The transverse wake potential $W_m(s)$ is obtained by integrating $W'_m(s)$.

The 3-D MAFIA-T3 code [3], without any assumption of cylindrical symmetry, computes the total wake force separately for both the transverse and longitudinal components. It is clear from Eq. (1) that the lowest harmonic of the longitudinal wake function, $W_0(s)$, can be computed without offsetting the beam. For the transverse wake function, however, one must offset the beam by a. In accordance with TBCI, the transverse forces are computed at $r = a$ and $\theta = \theta_0$. The form of Eqs (1) and (2) become:

$$F_z(s) = -\sum_{m=0}^{\infty} eqW'_m(s)a^{2m} , \tag{3}$$

$$F_\perp(s) = \sum_{m=1}^{\infty} eqW_m(s)ma^{2m-1} + F_\perp^0(s) . \tag{4}$$

The dipole transverse wake is therefore given by:

$$W_1(s) \approx \frac{F_\perp(s) - F_\perp^0(s)}{eqa} , \tag{5}$$

provided that the higher multipoles do not contribute appreciably when a small a is chosen.

Since TBCI is so much different from MAFIA-T3, a comparison has to be made. For this purpose we select a cylindrically symmetrical smooth pillbox cavity. Results from the two codes for both the monopole and dipole of the longitudinal wake potentials and the dipole component of the transverse wake potential are compared. Similar calculations are made for an asymmetrical cavity using MAFIA-T3 only.

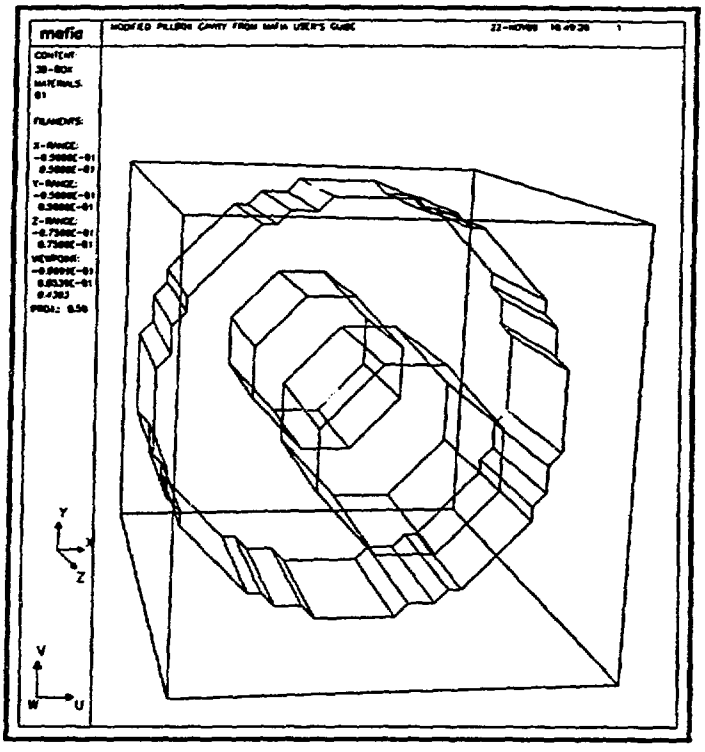

Figure 1: Problem geometry used in TBCI and MAFIA

2 The Symmetric Pillbox Cavity

The problem geometry is shown in Fig. 1. It consists of a cylindrical cavity of radius 5 cm and a length equal to 5 cm. The beam pipe is of radius 2 cm extruding 5 cm at each side. This geometry is modeled using both MAFIA and TBCI. In both cases, the source bunch is a gaussian truncated at $\pm 5\sigma$, where $\sigma = 5$ cm is the standard deviation.

2.1 Longitudinal Wakes

The longitudinal wake as obtained by MAFIA T3, for three different mesh sizes and offsets, are given in Fig. 2. This graph shows little dependence of the

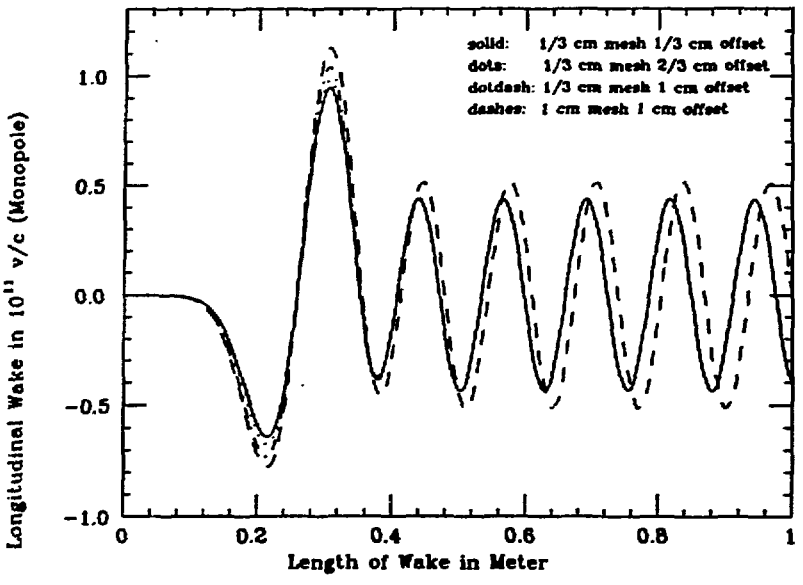

Figure 2: T3 longitudinal wake potentials for different mesh sizes and offset

potential on the offset implying that the dominant term in the longitudinal wake is the monopole term, not sensitive to the beam displacement. Also a decrease in the mesh size has little effect on both the peak values and frequency of oscillations. Fig. 3 is a pure longitudinal monopole obtained from MAFIA with $a = 0$ for two different mesh sizes. This plot should be compared with the longitudinal monopole wake potential as obtained by TBCI and shown in Fig. 4. Here the peaks for T3 vary from -0.644 to 0.980 ($\times 10^{11}$) v/c, and the peaks for TBCI vary from -0.619 to 0.922 ($\times 10^{11}$) v/c. The two results are in good agreement. The solid curve in Fig. 3 is the closest to the TBCI result both in peaks and frequency of oscillations. This curve corresponds to a smaller mesh size. A further decrease in mesh size in T3 had no effect on these results.

The dipole components for T3 and TBCI are shown in Figs. 5 and 6 respectively. The T3 dipole component is obtained by subtracting the longitudinal wake at no offset from the longitudinal wake with a beam offset. Such a subtraction can lead to some noise error as observed in the tail of Fig. 5.

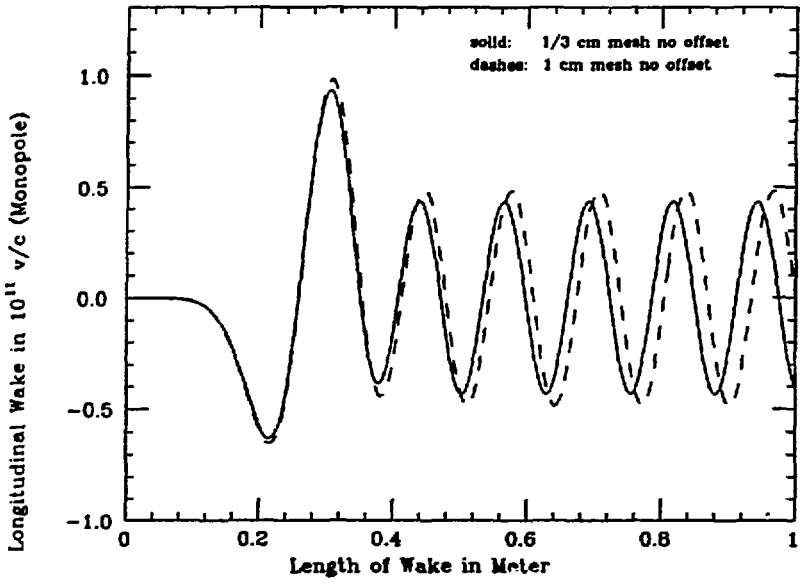

Figure 3: T3 longitudinal monopole wake potential with zero offset

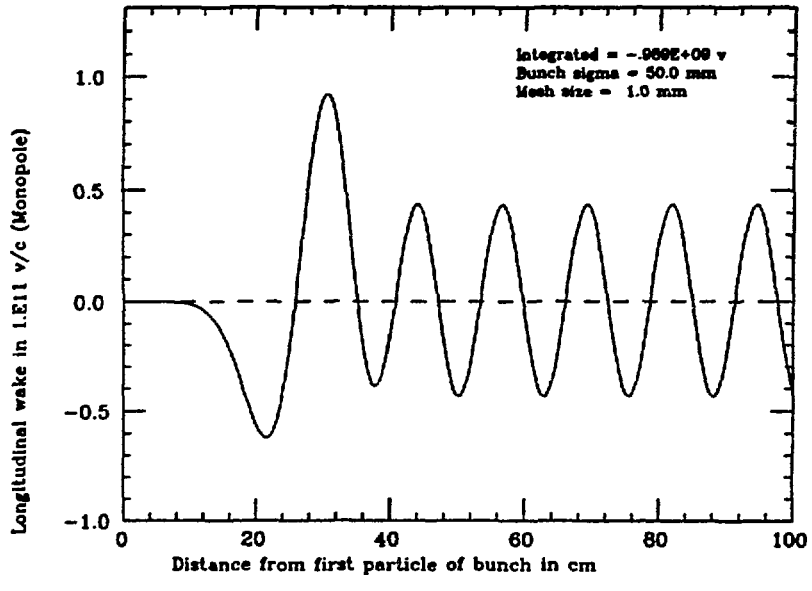

Figure 4: TBCI longitudinal monopole wake potential

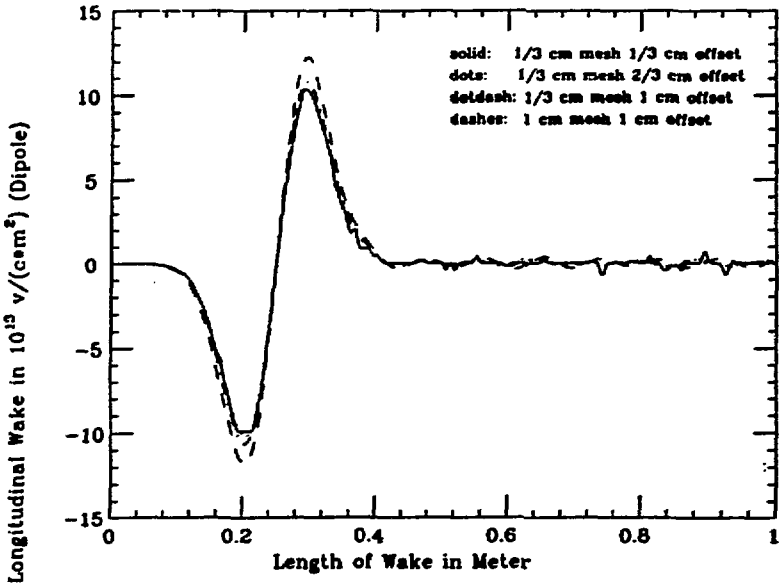

Figure 5: T3 longitudinal dipole wake potentials for different offsets and mesh sizes

From Eq. (3) the longitudinal dipole wake potential is obtained from:

$$W_1'(s) \approx \frac{F_z(s;a) - F_z(s;0)}{eqa^2} . \tag{6}$$

The subtraction noise error is of the order a^2. For this reason the result of the subtraction error is worse for $a = 1/3$ cm. Again the amplitudes obtained using TBCI, from -9.535 to 9.790 ($\times 10^{13} v/(cm^2)$), compare very closely to the solid curve results obtained from MAFIA. In calculating the dipole component of the longitudinal wake we have assumed that the contribution from higher order terms is negligible, something that was verified in Fig. 2.

The dipole component of the longitudinal wake can be calculated in a more straightforward manner. This is possible by considering the solution of the longitudinal wake at the beam location with half the cavity.

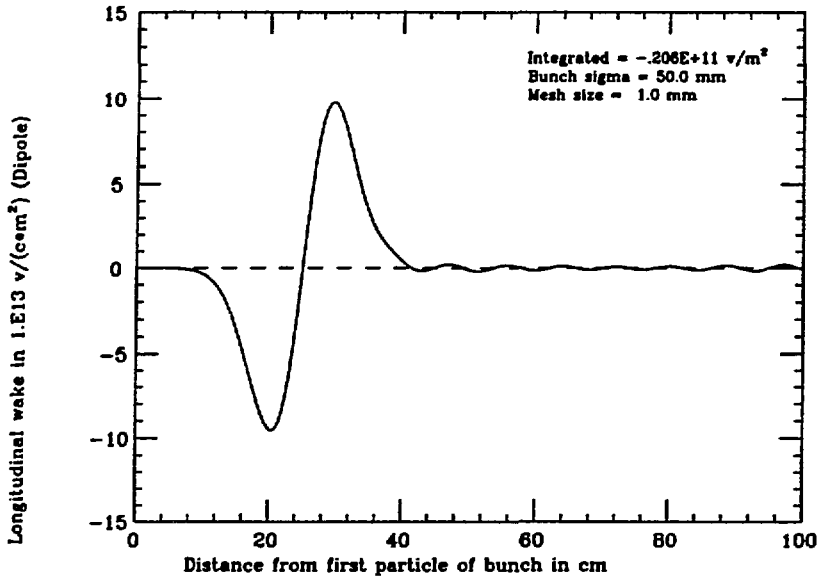

Figure 6: TBCI longitudinal dipole wake potential

2.2 Transverse Wakes

Since T3 does not compute each term separately, we need to first verify whether the dominant term in the summation of Eq. (2) is the dipole term. Figure 7 shows the transverse wake for different mesh sizes and offsets as obtained by MAFIA. The transverse wake potential is computed from the transverse wake force by dividing by a. The $W_1(z)$ peak decreases significantly as the mesh size and the offset decrease. However, a further decrease in mesh size has little effect on the result implying the presence of a dominant dipole term. The TBCI result is shown in Fig. 8. Both TBCI and MAFIA predicts almost the same result, 0.744 and 0.786 respectively. The oscillations in the tail of the wake disappear at one point in T3 raising some doubts on their validity.

3 The Asymmetric Cavity

This is a reproduction of the example given in the MAFIA manual [4]. The problem geometry is shown in Fig. 9. Because of the lack of cylindrical symmetry, this model can only be run with T3.

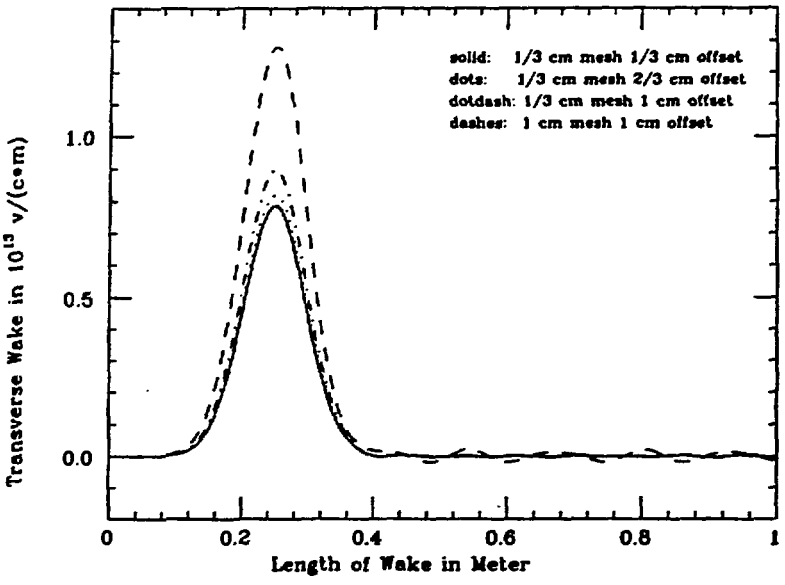

Figure 7: T3 transverse dipole wake potential for different offsets and mesh sizes

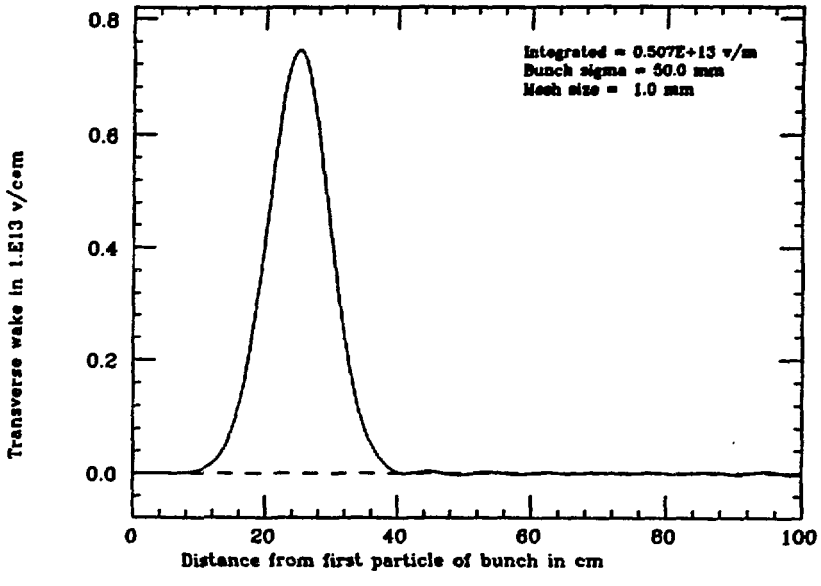

Figure 8: TBCI transverse dipole wake potential

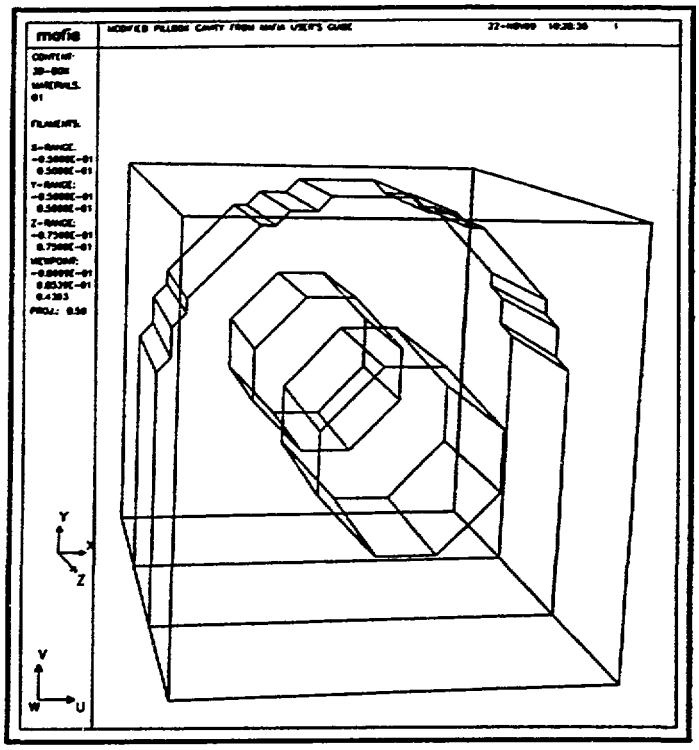

Figure 9: Asymmetric Cavity

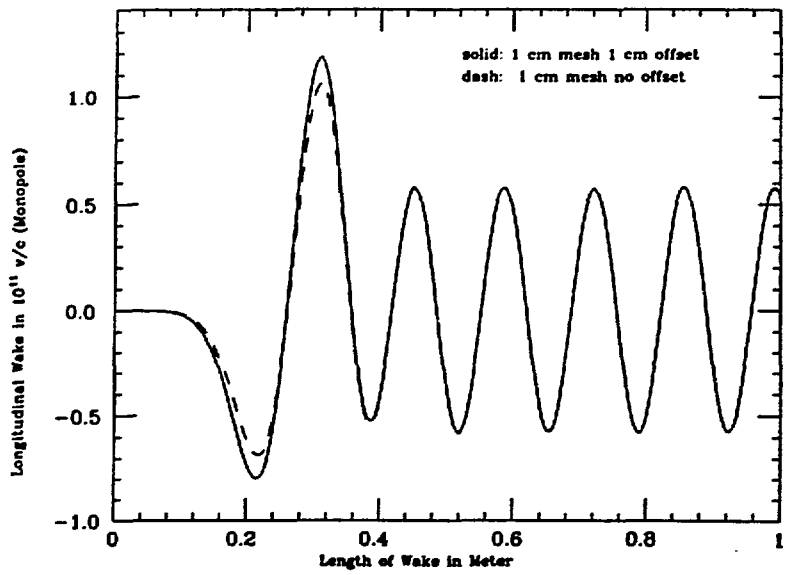

Figure 10: T3 longitudinal wake potential with and without displacement

3.1 Longitudinal Wakes

Figure 10 shows the longitudinal potential with and without beam displacement. One sees negligible difference in two cases. This is expected because the contribution is mainly the monopole contribution. The peak in amplitude corresponds to what is given in the MAFIA manual [4].

The longitudinal dipole wake is given in Fig. 11 for two mesh sizes and offsets. To see why the solid curve is not smooth we refer to the plot shown in Fig. 7. Again the result of subtraction with $a = 1/3$ cm leads to more noise error than the one with $a = 1$ cm, for the reason mentioned in section 2.1.

3.2 Transverse Wakes

The transverse wake, mainly dipole, is illustrated in Fig. 12 for two mesh sizes and offsets. Similar to previous results, the transverse wake decreases and converges to some value as the mesh size and offset decrease.

The wakes for this asymmetric cavity are in fact not much different from

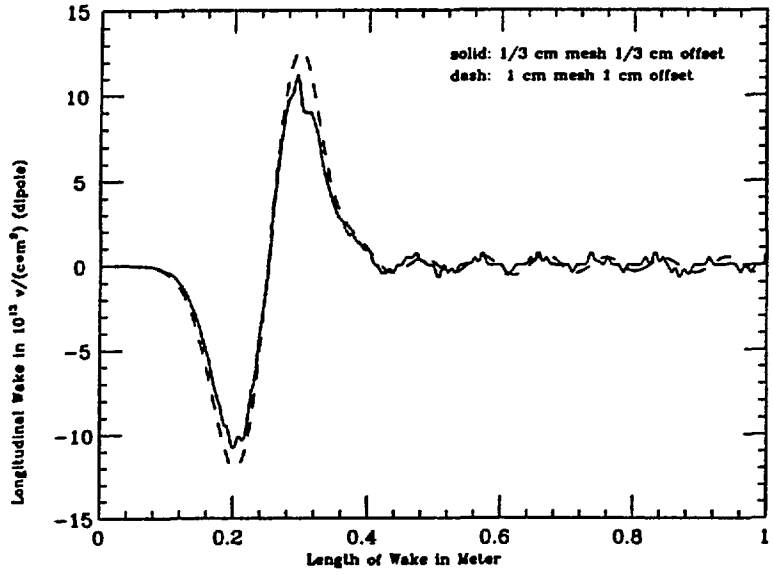

Figure 11: T3 longitudinal dipole wake potential for two different mesh sizes and offsets

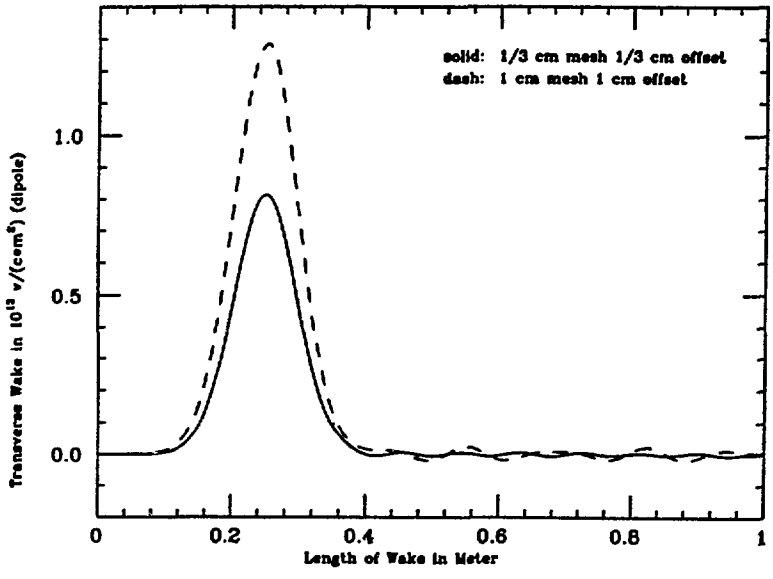

Figure 12: T3 transverse dipole wake potential

those of the symmetric pillbox. For this reason, in many cases it is quite good to approximate the asymmetric discontinuity by a symmetric continuity and use TBCI instead.

4 Summary and Conclusion

This is our first comparison of MAFIA T3 results against TBCI. Our results show a very good agreement both in peak amplitudes of the wake potential and the general shape of the wake functions. The oscillations in the tail of the functions obtained from T3 are not reliable. The spectrum of the wake, necessary for impedance calculations, depends very much on how sufficiently long the wake is to avoid truncation errors. This type of impedance calculations may not be very accurate in time domain and a better solution would be a 3-D eigen-modes solver like MAFIA-E31. We also conclude from these results that, although a small offset will reduce the contribution of higher multipoles, this will increase the computation error in subtractions and divisions. One should therefore be aware of the trade offs in selecting the amount of offset.

The calculations in this paper were done using the TBCI and MAFIA codes available at Fermi.

References

[1] Alexander W. Chao, SLAC-PUB-2946, June 1982.

[2] T. Weiland, Nucl. Inst. Meth., **216**, 31 (1983)

[3] T. Weiland, Particle Accelerators, **15**, 245 (1984).

[4] Mafia User Guide, DESY, LANL and KFA, May 3, 1988.

Preliminary Measurements of the Bunch Length and the Impedance of LEP

D. Brandt and B. Zotter

CERN

Argonne National Laboratory
Advanced Photon Source
Impedance and Bunch Instability Workshop
October 31 - November 1, 1989

Preliminary Measurements of the Bunch Length and the Impedance of LEP

D.Brandt, B.Zotter

11 January 1990

Abstract

Measurements of the bunch length as function of current with a pick-up button yield data which seem to violate Robinson's sum rule for the damping partition numbers, even when the corrections for cable length and risetime of the sampling scope are applied. Measuring the bunch length as function of RF voltage gives an estimate of the total correction, including the response of the pick-ups and the feedthroughs.

Simultaneous measurements of the bunch length and the horizontal emittance as functions of the RF frequency yield the variations of the damping partition numbers and hence the damping aperture. This can be used to estimate the RF frequency for which the orbit passes through the centers of the quadrupoles, and hence permits an absolute energy calibration of LEP.

The threshold current for turbulent bunch lengthening yields an effective impedance of only 20 mOhms for the short bunches below threshold. Assuming a broad-band resonator with a resonant frequency of 2 GHz, this corresponds to a low frequency inductance Z/n of about 1/4 Ohm. First measurements of the shift of the longitudinal quadrupole mode with current agree quite well with these values.

The transverse impedance has been obtained from the tune shift with current. Comparing horizontal and vertical shifts, the contributions of RF cavities and bellows can be separated. Although the threshold for transverse mode-coupling could not been measured yet, it is still expected to be near 3 mA in 4 (lengthened) bunches.

1 Introduction

Preliminary measurements of the impedance of LEP have been reported in Commissioning Notes 6 [1] and 21[2]. The conversion of the measured quantities to both longitudinal or transverse impedances relies on the knowledge of the bunch length, which therefore has to be measured first. Unfortunately, at the start-up of LEP the instrumentation was not complete: Bunch length measurements are foreseen to be done with a variety of diagnostic tools, such as fast diodes, auto-correlation techniques, and a streak camera. In the absence of these, a sampling oscilloscope had been connected to the pick-up buttons by a short cable, and we had to discover how to interpret the signals from this temporary set-up.

2 Bunch Length Measurement

2.1 Bunch Length Versus Current

The "raw data" for the bunch length at the injection energy of 20 GeV are shown in Fig.1. They were obtained with the signal from a pick-up button connected by a short cable to a sampling scope in the tunnel. The actual signal is shown in Fig.2, and can be seen to have an oscillation of about 6 GHz behind the bunch. Additional slower oscillations can be observed on a longer time scale. Since the exact transfer function of the pickups in the region of many GHz is not known we had to approximate its response. Using an equivalent Gaussian (with standard deviation σ_{corr}) has the advantage that the correction can be applied simply by quadratic addition

$$\sigma^2_{meas} = \sigma^2_{true} + \sigma^2_{corr} \tag{1}$$

Below the turbulent threshold, the measured bunch length for an RF voltage of $V_{RF} = 84\ MV$ was found to be approximately constant with a standard deviation of $\sigma_\tau = 32\ ps$, much larger than the expected zero current value of $\sigma_{\tau_0} = 18\ ps$ for this voltage. Without correction to the bunch length, this would correspond to a very small energy damping partition number $J_E = 2\ (\sigma_{\tau_0}/\sigma_\tau)^2$ of only 0.6 instead of the natural value of two.

Previously, the horizontal emittance of LEP at injection energy had been measured with a wire scanner, and found to be almost twice the expected value[3]. The corresponding damping partition number J_x was also only about 0.6, again smaller than the natural value of one. In a flat machine like LEP (for which $J_y = 1$), Robinson's sum rule [4] for the damping partition numbers requires $J_E + J_x = 3$, while this sum would be only 1.2 with the values found above. And we consider this rule inviolable!

Corrections of the raw data due to the cable length and the finite rise-time of the oscilloscope were estimated to be only $\sigma_{corr} \approx 14ps$[5], which would still lead to a strong violation of the sum rule. If we assume that the measurements of the horizontal emittance can be trusted, the corrections to the bunch length must be much larger. A value of σ_{corr} = 27 ps would be required to bring the low-current bunch length to the slightly shortened value of 16 ps, where the energy damping partition number becomes 2.4 and thus the correct sum of partition numbers is obtained.

The increased correction could be explained by the large physical size of the pick-up buttons (32 mm diameter) compared to the bunch lengths measured. However, rather than relying on this indirect reasoning, we attempted to measure the correction in LEP itself as described below.

2.2 Bunch Length versus RF Voltage

In LEP the bunches are short compared to the RF period, and the machine is operated at a synchronous phase angle near π at injection energy. Thus the usual linear approximation to the RF voltage is excellent. In this approximation, the product of bunch length and synchrotron tune is proportional to the energy spread $\sigma_s Q_s = \alpha R \delta_E$. For bunch currents

below the "turbulent threshold" ($I_b < I_{thr}$) the energy spread does not change with current. Assuming quadratic correction of the bunch length, we get

$$\sigma^2_{meas} - \sigma^2_{corr} = \left(\frac{\alpha\delta_E}{2\pi f_s}\right)^2 \tag{2}$$

We can make the RHS zero by extrapolating the measured values to $f_s \to \infty$. In Fig.3 we see that the values of the squared bunch length (full width at half maximum) fall nicely on a straight line, which intercepts the vertical axis near 5000 ps^2, i.e. $(FWHM)_{corr} = 70.7ps$. Assuming a Gaussian distribution, this value must be divided by 2.35 to obtain the standard deviation $\sigma_{corr} = 30ps$.

This 'measured' correction is somewhat larger than the 27 ps estimated earlier. The difference may be due to the Gaussian approximation used for the correction. Then σ_{corr} may not be independent of the true bunch length: e.g. for very short bunches, resonant oscillations appear to shorten the signal. The exact determination of the bunch length thus has to be postponed until instruments with a better resolution (e.g. the streak camera) become available.

2.3 Variation of Bunch Length with RF frequency

A change of the RF frequency shifts the particle orbit, which alters the magnetic field seen by the particles in the quadrupoles (and higher multipoles), and hence the amount of synchrotron radiation emitted. This fact is usually expressed as a change of the "damping partition numbers" J_E and J_x. In particular, J_x will become zero at some frequency below the nominal one - where the beam passes through the center of the lenses - and J_E vanishes at a frequency above it. The machine is stable over the (frequency) range where both J_x and J_E are positive, which is usually called the "damping aperture".

Fig. 4 shows the damping partition numbers at injection energy as function of the last 3 digits of the RF frequency (add 352 254 000 Hz). They were computed from the measured (and corrected) values of the bunch length and emittance with the expressions

$$J_E = 2\left(\frac{\sigma_{\tau o}}{\sigma_\tau}\right)^2 \qquad J_x = \frac{E_{xo}}{E_x} \tag{3}$$

The theoretical values are $\sigma_{\tau o} = 18ps$ for $V_{RF} = 84MV$, and $E_{xo} = 6.7nm$. The damping aperture is thus found to be about 560 Hz, in good agreement with computations. However, a number of inconsistencies appear in this plot:

i) for the previously determined bunch length correction of 30 ps, the points for J_E lie on a straight line, but this line exceeds the expected maximum of 3 (and even 4): This is in contradiction to Robinson's sum rule.

ii) the correction can be adjusted so that J_E remains below 3 by choosing $\sigma_{corr} = 27ps$. While this is quite acceptable in itself, it makes the line strongly curved - in contradiction to analytical estimates that its slope should not change by more than about 1 %.

iii) at injection energy, the horizontal damping partition number appear to be too small by a factor of about 2, and J_x reaches only about 1.6 at the upper limit of the damping aperture[3].

The "central frequency", i.e. where the orbits pass through the centers of the quadrupoles (as well as sextupoles and higher multipoles), can be determined by intersecting the curve for the damping partition number J_E with the nominal value. This should be 2 in a separate function machine, but only about 1.95 in LEP due to a small contribution of combined function quadrupoles caused by a thin layer of magnetic nickel on the vacuum chamber in the dipoles, which was needed for bonding the lead shielding to the aluminum chambers. We see from Fig.4 that this value is reached at about 140 Hz if we use the straight line connecting $J_E = 3$ on the lower edge of the damping aperture with $J_E = 0$ at the upper one, in quite good agreement with other measurements of this value (about 160 Hz) [6].

A possible explanation of the difficulties with the damping partition number J_x could be a blow-up of the horizontal beam size by synchro-betatron resonances. However, one cannot exclude measurement errors with the wire scanner as well as with the synchrotron light monitor. Recent measurement with a beam scraper at 45 GeV gave a much smaller emittance than the one obtained with synchrotron light, which had agreed reasonably well with the wire scanner in the past[7].

The difficulties with the energy damping partition number could be resolved if the natural bunch length was shorter than calculated, e.g. due to bunch shortening at low currents. In some models of bunch lengthening this is expected to occur for short bunches seeing a capacitive impedance[8], but no clear observation of shortening has been made in LEP. A more likely explanation is the inaccuracy of the measurement with a button pickup which is much larger than the bunch length. This problem should be solved when the streak camera will become operational in the near future.

3 Longitudinal Impedance

3.1 Turbulent Threshold

Calculation of the longitudinal impedance from the measured threshold current and bunch length can be obtained using the stability criterion for bunched beams[1]

$$\left|\frac{Z}{n}\right| = \frac{F h V_{\mathrm{RF}} \cos\phi_s}{\sqrt{2\pi} I_{\mathrm{thr}} (\omega_o \sigma_{thr})^3} \tag{4}$$

where the form factor $F = 1$ for a capacitive impedance (expected for short bunches), and about 1.4 for resistive impedances. Substituting the parameters of LEP yields the extremely low impedance of about $22m\Omega$ (for F=1). However, one has to specify that this is the "effective impedance" acting on a very short bunch, and *not* the usually quoted low frequency limit Z/n. Assuming a resonator impedance with resonant frequency ω_r, the effective impedance of short bunches $\sigma < 1/\omega_r$ is strongly reduced due to the overlap of the bunch spectrum with both the positive low-frequency inductance, and the negative high-frequency capacitance. The result is given approximately by

$$\left(\frac{Z}{n}\right)_{eff} = 2\,(\omega_r \sigma_\tau)^2 \quad \left|\frac{Z}{n}\right| \tag{5}$$

for short bunches ($\omega_r\sigma_t < 1$), whereas for longer ones ($\omega_r\sigma_t \geq 1$)

$$\left(\frac{Z}{n}\right)_{eff} = \left|\frac{Z}{n}\right| \tag{6}$$

applies.

In LEP, the major part of the longitudinal impedance is expected to come from the RF cavities, for which a broad-band resonator frequency of about 2 GHz has been estimated [9]. For a bunch length $\sigma_\tau = 16ps$ we find $\omega_r\sigma_t \sim 0.21$, and we have to use the short bunch expression to get the correction factor for the effective impedance of $2(\omega_r\sigma_t)^2 \sim .09$. Therefore, the low-frequency limit of the impedance then becomes

$$\left|\frac{Z}{n}\right| = 0.25\Omega \tag{7}$$

Since this result depends both on the form factor and on the assumed resonator frequency it could be larger if $F > 1$ or ω_r smaller than the resonant frequency assumed.

3.2 Longitudinal Quadrupole Mode

A few measurements of the shift of the longitudinal quadrupole mode could be made so far. For currents above about 80 μA, the second (and even higher) modes were visible without external excitation on a spectrum analyzer. The shift of the difference frequency $\Delta f_{s2} = f_{s2} - 2f_{s0}$ was found to be about 450 Hz/mA; see Fig. 5. Assuming that the quadrupole shift is half that of incoherent synchrotron frequency one gets an approximate expression for the longitudinal impedance

$$Im\left(\frac{Z}{n}\right) = \frac{4\pi^2 h V_{RF} cos\phi_s}{f_{s0}} \frac{\Delta f_{s2}}{\Delta I_b} \left(\frac{\sigma}{R}\right)^3 \tag{8}$$

With 820 Hz for the synchrotron frequency at the RF voltage of 55 MV, the effective longitudinal impedance is found to be $40m\Omega$, in quite good agreement with the value found from bunch lengthening. Since these measurements consist so far only of 3 points, they clearly have to be repeated before they can be trusted.

For azimuthally uniform impedances, such as a circular cylindric vacuum chamber wall, there exists a relation between the lowest longitudinal ($m = 0$) and the lowest transverse ($m = 1$) mode

$$Z_T = \frac{2R}{b^2}\left|\frac{Z}{n}\right| \tag{9}$$

where b is the chamber radius, and $n = \omega/\omega_0$ the mode-number. For localized impedances, such as RF cavities, this relation is only approximate. This is usually taken account of by replacing the actual radius by an "effective" one b_{eff}. The chamber half-height is used in place of the radius for the vertical impedance of elliptical vacuum chambers.

In LEP, the chamber radius in the RF cavities is 50 mm, while the chamber half-height in the bellows is only about 35 mm. Using a transverse impedance of 2.3 $M\Omega/m$ found below, we would need an effective radius of about 35 mm to get a longitudinal impedance in agreement with other measurements.

3.3 Higher Order Mode Loss

Measurements of the phase shift of a strong bunch relative to RF or to a small witness bunch allow determination of the higher order mode loss and hence of the longitudinal impedance. Unfortunately, these measurements need a rather high accuracy in the phase measurement, and have not yielded consistent results so far.

3.4 BBI Results

We have computed the bunch length as function of current with the program BBI, using the Hofmann-Maidment model[8] which is one of its options. The results for an impedance of 0.25 Ohm and an energy spread of 3.6 10^{-4} corresponding to the damping partition number $J_E = 2.4$ are shown in Fig.1, together with the measured values. The dependence of the bunch length on current for various values of the energy spread or the RF voltage is shown in Figs. 6 and 7. The real and imaginary part of the frequency shift of the lowest synchrotron sidebands have been computed with BBI for a transverse impedance of 2 $M\Omega/m$ with $Q = 1$ and a resonant frequency of 2.05 GHz. They are plotted in Fig.8, showing a threshold for the transverse mode-coupling instability near 0.75 μA per bunch, or 3 mA per beam of 4 bunches.

4 Transverse Impedance

The transverse impedance can be obtained from measurements of the betatron tune shifts with current. With a single bunch at injection energy a vertical tune shift of -0.13/mA and about -.07/mA in the horizontal plane[1] were found (see Figs.9 and 10).

The tune shift caused by N impedances can be written

$$\frac{\Delta Q}{\Delta I} = \frac{F_T\, R}{2\pi\sigma E/e} \sum_{i=1}^{N} \langle\beta\rangle_i Z_{Ti}^{eff} \tag{10}$$

where $\langle\beta\rangle_i$ is the average beta function at the i-th transverse impedance Z_{Ti}. The effective transverse impedance for a Gaussian in a resonator can be expressed as

$$Z_T^{eff} = Z_T F(\omega_r \sigma_t) \tag{11}$$

where the form factor can be approximated by $F(x) \approx 2x^2$ for $x < 1$ (bunches short compared to the resonant wavelength), and by $F(x) = 1$ for $x \geq 1$ (long bunches or high resonant frequency).

Since the RF cavities have circular beam holes, their contributions to the horizontal and the vertical shift must be equal, i.e. somewhat less than the smaller of the two shifts. Since the resonant frequency of the RF cavities is estimated at about 2 GHz, the "short bunch" expression applies when the bunches have only $\sigma_\tau = 18ps$. Thus a strong reduction of the effective impedance by a factor of almost 10 will occur. The average beta function in the RF cavity region has been reduced to less than 40 m in the design of LEP [10] in order to maximize the threshold of the transverse mode-coupling instability.

Much effort has been spent on shielding the vacuum chamber bellows, of which there are almost 3000 in LEP. They have a chamber height slightly above half their width. Since the transverse impedance varies with the second to third power of the radius, we expect their effect on the vertical tune shift to be about 5 times larger than on the horizontal one. The broad band resonant frequency of the bellows has been estimated to be larger than 8 GHz[9], and hence their effective impedance will be equal to the actual one even for the rather short 18 ps bunches. Furthermore, the average beta function at the bellows is about 75 m in both planes, almost twice the value at the RF cavities.

Substituting these conditions into the above expressions, we find two equations with two unknowns for the (vertical) transverse impedances of the RF cavities and the bellows, which we expect to be the two main contributors in LEP:

$$\begin{aligned} \frac{-\Delta Q_H}{\Delta I} &= \frac{R}{2\pi\sigma E/e}\left[2(\omega_r\sigma_t)^2 Z_T^{cav}\langle\beta\rangle_{cav} + 0.2 Z_T^{bel}\langle\beta\rangle_{bel}\right] \\ \frac{-\Delta Q_V}{\Delta I} &= \frac{R}{2\pi\sigma E/e}\left[2(\omega_r\sigma_t)^2 Z_T^{cav}\langle\beta\rangle_{cav} + Z_T^{bel}\langle\beta\rangle_{bel}\right] \end{aligned} \tag{12}$$

The measured frequency shifts per mA at LEP were[1]

$$\frac{\Delta Q_H}{\Delta I} = -0.070, \quad \frac{\Delta Q_V}{\Delta I} = -0.125, \tag{13}$$

The factor in front of the brackets (Eqs.12) for LEP is approximately 5.684 10^{-4} for a bunch length of 18 ps at injection energy. Thus the solution of these equations yields

$$\begin{aligned} Z_T^{cav} &\approx 2.23 M\Omega/m \\ Z_T^{bel} &\approx 0.16 M\Omega/m \end{aligned} \tag{14}$$

In spite of the seemingly much smaller value for the bellows, their contribution to the vertical tune shift for the short natural bunch length is just as large as that of the RF cavities due to the different form factors. The total transverse loss factor is only slightly higher than the original estimate of about 2 $M\Omega/m$, hence we expect that the threshold for transverse mode-coupling instability will be near the originally estimated values of 3/4 mA/bunch, or 3 mA per beam, if the bunches are lengthened to $\sigma = 4$ cm, e.g. with the wigglers which are already installed in LEP (see Fig.8 for BBI results).

5 Conclusions

The bunch length in LEP can be measured only with limited accuracy since it is usually well below the diameter of the button pickups used presently. The corrections which have to be applied to the "raw data" are often larger than the measurements themselves. This situation should improve when the streak camera will become operational.

The longitudinal impedance depends on the third power of the bunch length, and is thus particularly sensitive to measurement errors. Nevertheless, we can obtain a reasonable estimate of the broad band impedance by using the machine itself for calibration. We thus

find the value of approximately 1/4 Ohm for the low frequency limit of Z/n, while the effective impedance seen by a short bunch at injection energy is only about 20 mOhm.

In the transverse plane, the total impedance is found by separating the contributions of the RF cavities and of the bellows. For the assumptions made, the transverse impedance of the cavities appears to be slightly higher than computed, while the bellows impedance comes out slightly lower. Nevertheless, the contribution of the bellows to the vertical tune-shift is actually larger than that of the RF cavities for the short bunches at injection. The total transverse impedance thus is only slightly larger than has been estimated during the design. Thus the threshold for the transverse mode-coupling instability is still expected near 3 mA per beam (4 bunches, lengthened to $\sigma \approx 4cm$).

References

[1] D. Brandt et al, LEP Commissioning Note 6 (0ct.1989)

[2] D. Brandt et al, LEP Commissioning Note 21 (Dec.1989)

[3] J.P. Koutchouk, Commissioning Note 10 (1989)

[4] K. Robinson, Phys.Rev. 1959

[5] M. Placidi, private communication

[6] A. Hofmann et al, Commissioning Note 12 (1989)

[7] J.P. Koutchouk, private communication

[8] A. Hofmann, J. Maidment, LEP Note 168 (1979)

[9] B. Zotter, CERN LEP Divisional report TH/87-34 (1987)

[10] B. Zotter, LEP Note 448 (1983)

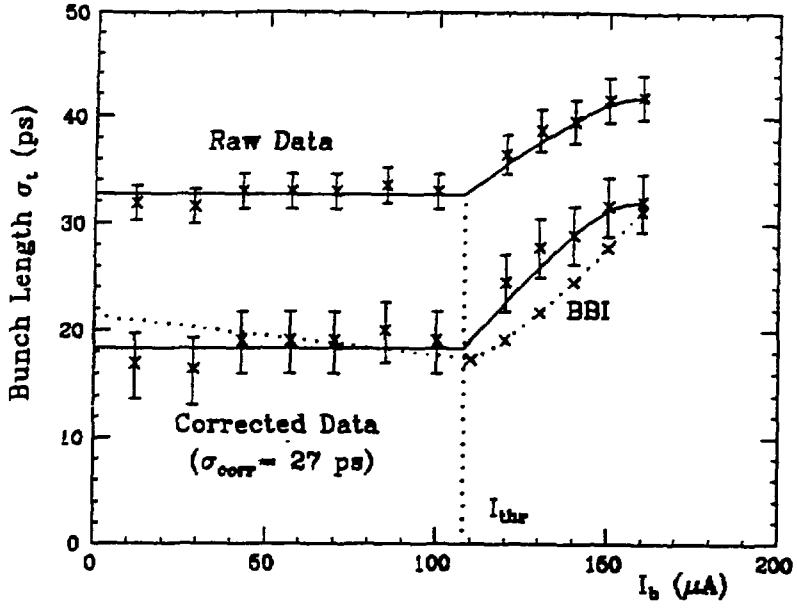

Figure 1: Variation of bunch length with current in a single bunch: raw data, corrected values, and results from BBI.

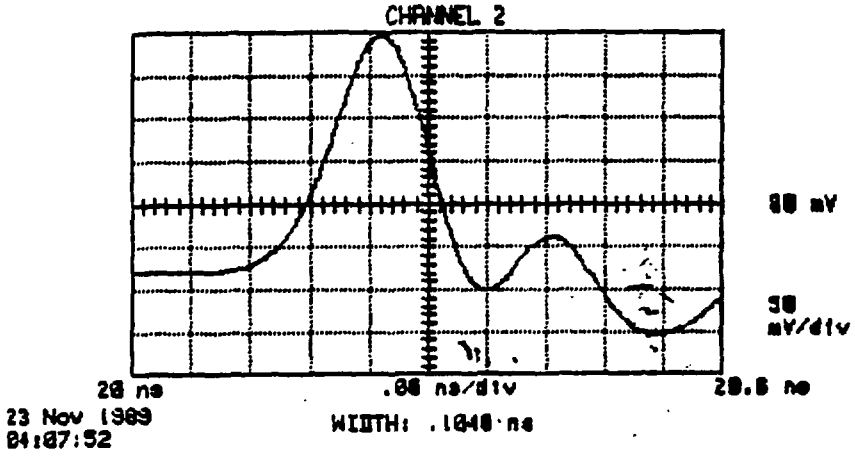

Figure 2: Signal from sampling oscilloscope connected to pickup for short bunch length: the horizontal scale is 50 ps/div.

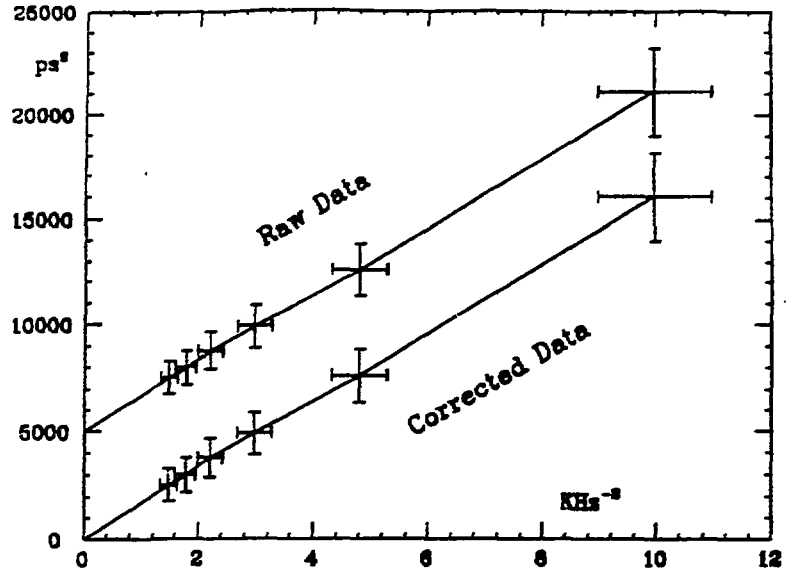

Figure 3: Variation of (squared FWHM) bunchlength with (inverse squared) synchrotron frequency: the upper curve shows "raw data", the lower one corrected values.

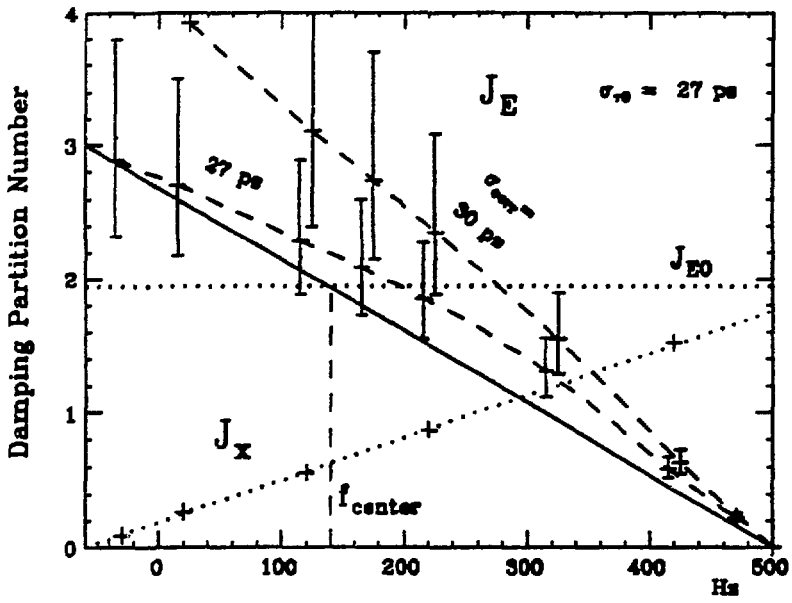

Figure 4: Variation of damping partition number J_E with RF frequency at 20 GeV for two different corrections of raw data: upper line - 30 ps, lower - 27 ps, solid - theoretical. For comparison we also show the measured damping partition number J_x (dotted line).

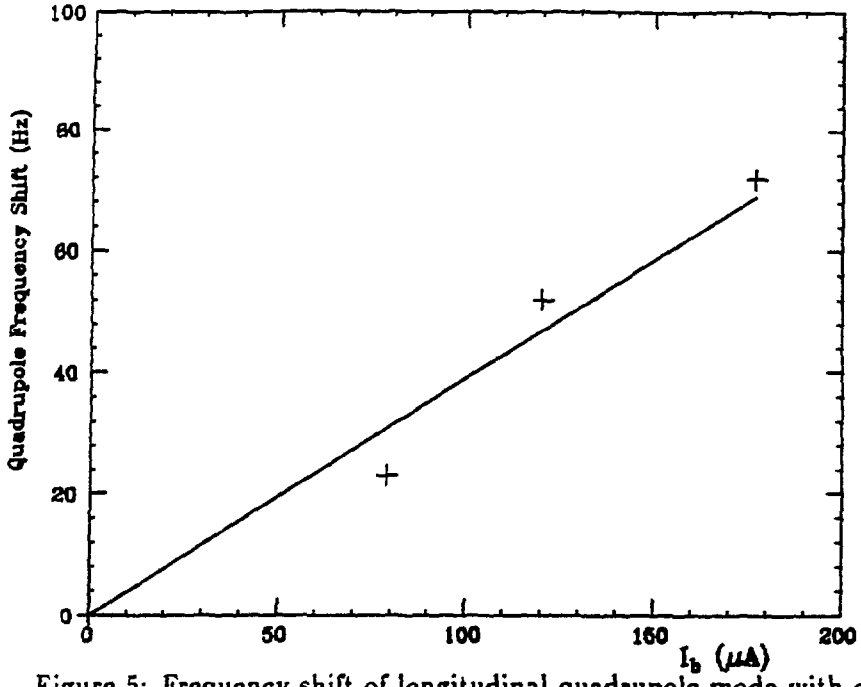

Figure 5: Frequency shift of longitudinal quadrupole mode with current.

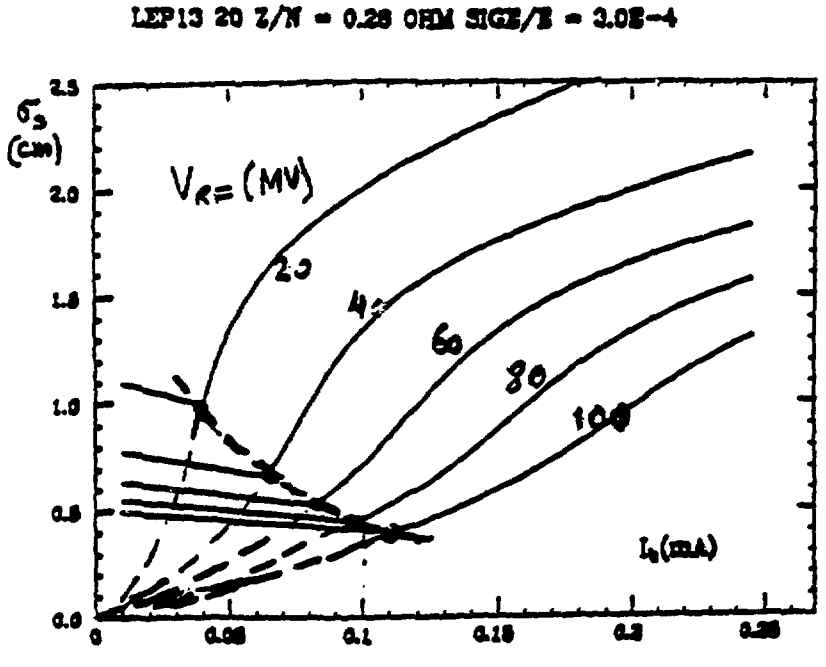

Figure 6: Bunchlength versus current for varying RF voltage - BBI

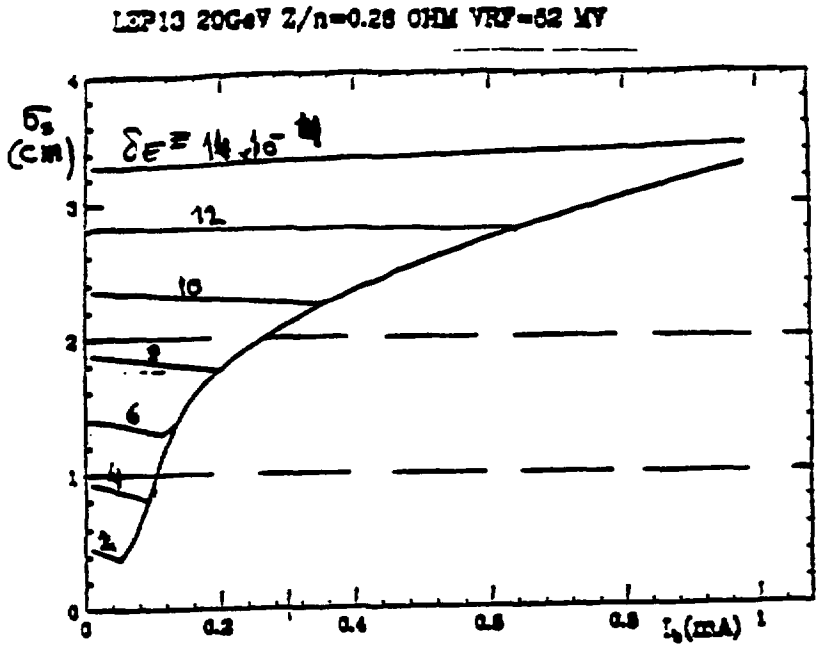

Figure 7: Bunchlength versus current for varying energy spread - BBI

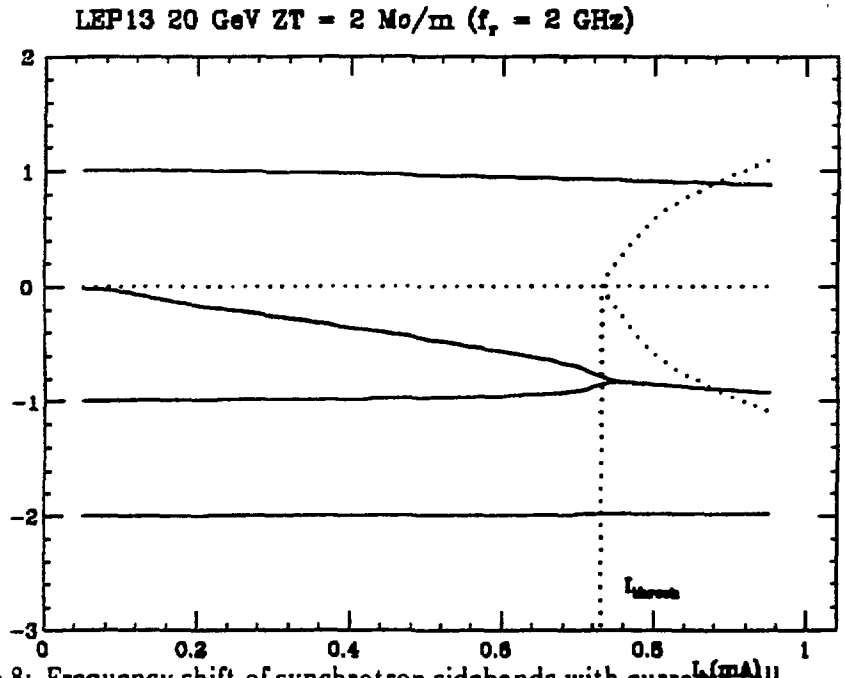

Figure 8: Frequency shift of synchrotron sidebands with current: full lines - real, dotted lines - imaginary part; Threshold for transverse mode coupling (BBI)

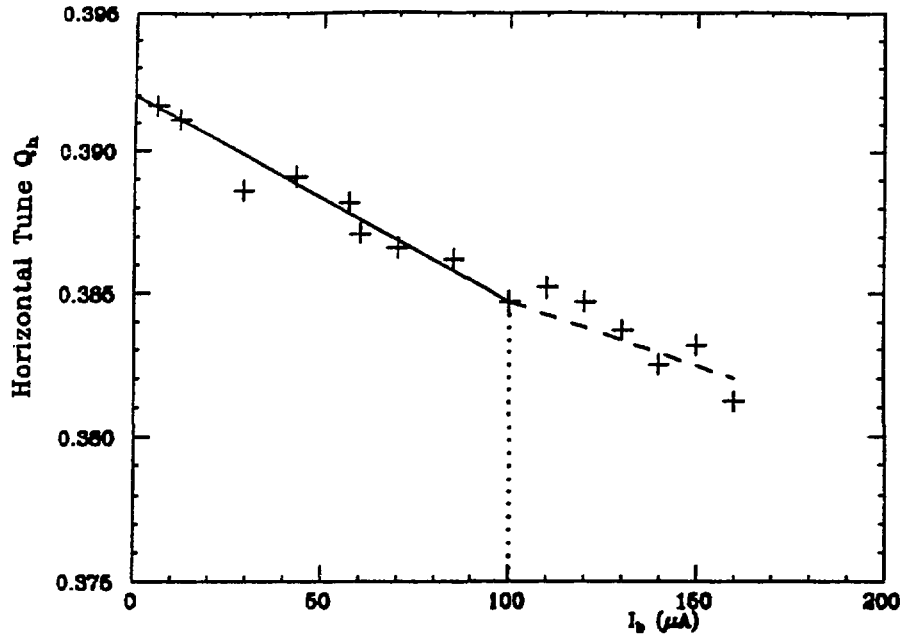

Figure 9: Variation of horizontal tune with current per bunch.

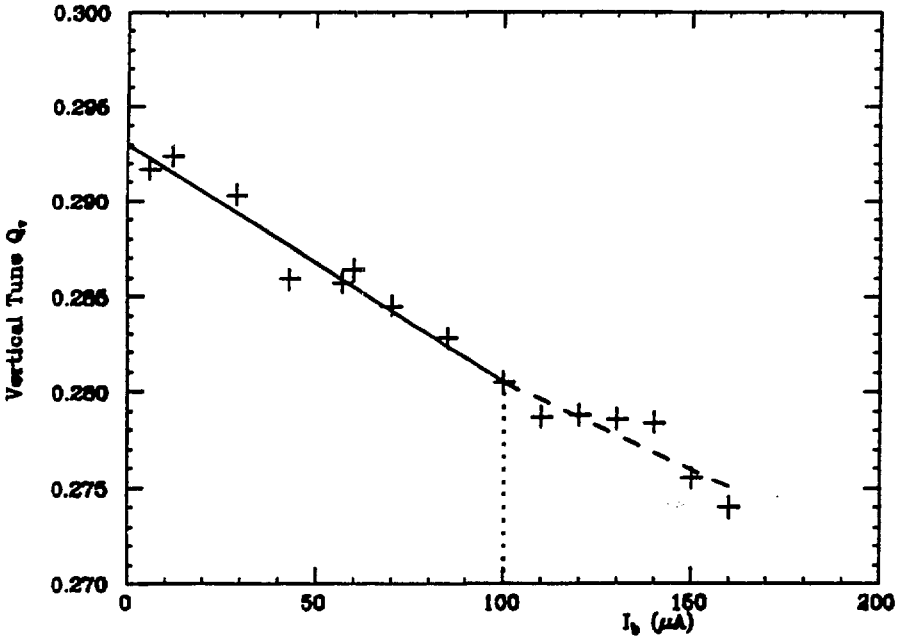

Figure 10: Variation of vertical tune with current per bunch.

Measurements and Simulations of Collective Effects in the CERN SPS

D. Brandt

CERN

Argonne National Laboratory
Advanced Photon Source
Impedance and Bunch Instability Workshop
October 31 - November 1, 1989

Measurements and Simulations of Collective Effects in the CERN SPS

D. Brandt

Abstract

Starting from experimental observations of both longitudinal and transverse instabilities of lepton bunches in the SPS, one uses a simulation program to fit an impedance model such as to best reproduce the measured data. In a first step this model is compared with measurements previously performed with protons and then it is used in the code to simulate the dynamical behaviour of the beam along the whole SPS cycle. As far as the behaviour of the beam parameters and the predicted instability thresholds are concerned, the simulations are in fair agreement with the subsequent experimental observations and clearly demonstrate that a broad band resonator is an adequate model for the description of the SPS coupling impedance.

1. Introduction

The aim of this paper is to present an interesting comparison between experimental and simulation results obtained for the CERN SPS machine, when the latter is operated with leptons. Starting from the experimental observation of instabilities, one uses a simulation program in order to fit an impedance model such as to best reproduce the measured data. This fitted broad band resonator model is then compared with measurements of the SPS transverse impedance previously obtained with protons. After having made sure of the good agreement between these two sets of results, it is possible to simulate the behaviour of the beam along the whole cycle and check to what extent it should be possible to increase the observed thresholds by modifying the injection conditions. The final step evidently consists in comparing the predicted thresholds with those measured in the machine under the same conditions.

2. Experimental observation of instabilities

When used as an injector for leptons, the SPS is an ideal tool for the study of collective effects. As a matter of fact, it then allows for injection both below and well above the thresholds for instabilities.

With these parameters, the best fit is obtained for:

$$(R/Q)_T = 23\ M\Omega/m$$
$$Q = 1.0 \qquad (1)$$
$$fr = 1.35\ GHz$$

As can be seen from Fig. 2, there is a fair agreement between the simulation results and the measured data. In addition to this, it has been recently suggested [2] that a better fit to the actual SPS impedance could be a broad band resonator model with a quality factor Q = 6.0. In this particular case, the measured data would then be best reproduced with:

$$(R/Q)_T = 17\ \ M\Omega/m$$
$$Q = 6.0 \qquad (2)$$
$$fr = 1.35\ GHz$$

For both cases, the simulations predict a threshold for transverse instability lying around 10^{10} part./bunch, which is therefore in good agreement with the observed threshold.

3. Simulated tune shifts of the fundamental (m = 0) mode

Although the two impedance models defined by Eqs. (1) and (2) yield the same instability threshold, they exhibit quite a different behaviour when considering the detuning as a function of the current. Indeed depending on the model considered, the simulated coherent tune shift of the m = 0 mode (tune) at threshold is

$$\begin{aligned} &\Delta Qc = 1.5\ Q_S \text{ for} \\ &23\ M\Omega/m \text{ and } Q = 1.0 \\ &\Delta Qc = 0.7\ Q_S \text{ for } 17\ M\Omega/m \text{ and } Q = 6.0 \end{aligned} \qquad (3)$$

Actually, these results deserve some comments, especially when considering that the measured tune shifts are very often used for the determination of parameters related to collective effects (e.g. the impedance).

As a matter of fact, the tune shift simulated with the Q = 6.0 resonator could be misleading since it would correspond to the behaviour expected for short bunches, and certainly not for the long bunches we have in the machine.

Indeed, in the short bunch regime, the spectrum of the m = 0 mode extends in the GHz range, where the resistive component of the coupling impedance is large, and it is therefore likely that the modes m = 0 and m = -1 couple first and determine the threshold. In such a case one would therefore expect:

$$(\Delta Q_c)_{th} \leq Q_s \tag{4}$$

On the contrary, for the long bunches in the SPS, the spectrum of the m = 0 mode extends only up to 500 MHz, where the coupling impedance is mainly inductive (produce a tune shift but a negligible coupling). In this case, it is the modes m = -2 and m = -3 which mainly overlap with the resistive component of the coupling impedance and therefore determine the threshold. In this case, at threshold, one would expect:

$$(\Delta Q_c)_{th} > Q_s \tag{5}$$

Actually, this behaviour has been experimentally verified both in the CERN EPA machine and in the DCI machine at Orsay.

Consequently, the apparent discrepancy between the simulated tune shifts quoted in Eq (3) can be completely explained by the inherent difference of the two impedance models. As can be seen from Fig. 3, the inductive part of the Q = 6.0 model is only one sixth of the shunt value so that one has to expect a reduced detuning. Although this example might appear trivial, it is essentially meant to be a warning against the ambiguities hidden in the Q = 1.0 broad band resonator model usually considered, namely:

a) To describe correctly the longitudinal behaviour of the bunch the relevant parameter is not Z/n, but much more the resistive peak value.

b) The threshold for transverse stability is not uniquely related to the measured tune shift (inductive part) but is influenced by the value of the resistive peak.

4. Longitudinal vs. transverse instability signals

The energy spread of the bunches delivered from the CERN CPS varied between 0.06 and 0.1%. This relatively small variation has significant implications for the observation of the instabilities. Remembering that the threshold for the longitudinal microwave instability scales with the square of the energy spread, one observes that for;

$$\Delta p/p = 6.10^{-4} \Rightarrow N_{th} = 0.4\ 10^{10}\ \text{part./bunch}$$
$$\Delta p/p = 1.10^{-3} \Rightarrow N_{th} = 1.2\ 10^{10}\ \text{part./bunch} \qquad (6)$$

These analytical results are fully consistent with our observations since they explain why, depending on the injection conditions, we observe either a longitudinal or a transverse instability first. Actually, it should be mentioned that this behaviour is also fairly well reproduced by the simulation.

5. Measurement of the SPS impedance with protons

In the SPS, both the longitudinal and the transverse impedances have been measured on several occasions in the past. Unfortunately, due to the very different conditions for the measurements (energy, bunch lengths, intensities,..) the results do exhibit a rather large spread among each other, namely:

$$7.5 \leq Z/n\ (\Omega) \leq 20.0$$

and
$$13.0 \leq Z_T\ (M\Omega/m) \leq 48.0 \qquad (7)$$

with a resonant frequency lying around 1.3 GHz. Because it was felt that these results might have been influenced by very different effects like space charge and nonlinearities, it was decided to repeat these measurements with protons for two distinct energies. We measured the tune shifts as a function of the intensity at both 26 GeV (Fig. 4) and 315 GeV (Fig. 5). With these two sets of results it is possible to estimate the effective transverse impedance according to:

$$Z_T = - C\ E/e\ \sigma_s\ \frac{\Delta Q}{\Delta N} \qquad (8)$$

The corresponding results for the two transverse planes are listed in Table 2.

E(GeV)	Z_T^V (MΩ/m)	Z_T^H (MΩ/m)
315	26.8	- 16.9
26	33.2	- 9.9

Table 2
Transverse impedances from measured tune shifts with protons.

These results mainly call for two remarks:

a) They confirm that the horizontal and vertical impedances of the SPS have opposite signs.

b) The results in the horizontal plane seem to indicate that at 26 GeV, there does indeed exist an additional detuning acting on top of that from the impedance, e.g. detuning due to space charge.

This last statement is not straightforward since it is usually accepted that the direct space charge is a purely incoherent effect, and should therefore not contribute to our measurement. Strictly speaking, this argument only holds when the beam is kicked as a rigid ensemble (e.g. for a purely rectangular distribution). In the present situation, due to its distribution, the beam is not kicked rigidly so that it is conceivable that the direct space charge effect contributes to the tune shifts. Fortunately, space charge and impedance effects do behave quite differently as a function of the energy: the space charge varies with $1/\gamma^3$, whereas the impedance detuning is inversely proportional to the energy. Consequently, at 315 GeV, our measurements are free from any space charge contribution and should therefore reflect the detuning due to the impedance only. We shall therefore try to estimate this space charge component and check whether it agrees with our measurements at 26 GeV.

5.1 Direct space charge detuning

The evaluation of this contribution follows from a relation derived in Ref. [2], namely:

$$\langle \Delta Q^{V}_{sc} \rangle = - \frac{72\ R\ \varepsilon_o^*\ \hat{\imath}}{E_o/e\ \gamma^2\ \varepsilon_V} \qquad (9)$$

where $\hat{\imath} = \frac{3}{8} \frac{Nec}{\sigma_s}$ and $\varepsilon_o^* = \frac{\sigma_V}{(\sigma_V + \sigma_H)}$,

$$\text{accordingly } \langle \Delta Q^{H}_{sc} \rangle = \langle \Delta Q^{V}_{sc} \rangle \cdot \frac{\sigma_V}{\sigma_H} \qquad (10)$$

The corresponding results are presented in Fig. 6. One immediately observes that the space charge component alone is larger than the total detuning measured. This illustrates clearly that the space charge, if considered at all, should not be accounted completely. However, to estimate its contribution, it is possible to consider a superposition of the two effects and write:

$$|\Delta Q^{V}_{TOT}| = |\ \Delta Q^{V}(\text{impedance})| + A\ |\ \Delta Q^{V}_{sc}|$$

$$|\Delta Q^{H}_{TOT}| = |\ \Delta Q^{H}(\text{impedance})| - A\ |\ \Delta Q^{H}_{sc}| \qquad (11)$$

where the constant A has been introduced as scaling factor. It is now possible to evaluate A and check the validity of the model with the following procedure:

a) Assume the 315 GeV vertical impedance is correct and scale it to 26 GeV.

b) Evaluate A from (11) in the vertical plane.

c) Insert A in the equation for the horizontal plane.

d) Calculate the corresponding horizontal impedance.

This yields:

$$Z^{H}_{T} = -14.2\ M\Omega/m \text{ with } A = 0.17 \qquad (12)$$

which is about 15% lower than the value measured at 315 GeV.

Remembering that the impedance at 315 GeV should still be slightly lowered for nonlinear effects (octupoles) which are known to be non-negligible in the SPS, one therefore experimentally obtains:

$$Z^{V} < 27\ M\Omega/m$$

which has to be compared with the fit obtained from the simulation, namely,

$$Z_T^V = 23\ M\Omega/m$$

These two results are felt to be in fair agreement.

6. Dynamical simulation along the cycle vs. experiments

Because of the good agreement obtained so far between simulation and experiment, it was decided to simulate the dynamical behaviour of the bunch along the SPS cycle, and estimate what improvements could be expected, as far as the thresholds for instabilities are concerned.

Although the nominal intensity of the LEP injection complex corresponds in the SPS to 8 bunches of 10^{10} particles each, the CPS is capable of producing single bunches of up to 5.10^{10} particles. This allows one to measure instability thresholds over a wide range of parameters at injection . By modifying the partition numbers and the Rf voltage in the CPS, it is possible to inject into the SPS bunches with different length and energy spread. The cases which have been most often used are shown below:

	Case 1	Case 2	Case 3	(13)
$\sigma_{E/E}$	$0.6\ 10^{-3}$	$1.0\ 10^{-3}$	$1.0\ 10^{-3}$	
σ_S	16 cm	16 cm	22.5 cm	

With $\sigma_{E/E} = 10^{-3}$ it is even possible, by making use of the low frequency RF system of the CPS, to increase σ_S up to 40 cm. The transverse emittances at injection are $\sigma^2/\beta = 7.10^{-8}$ rad.m in the horizontal plane and 10^{-7} rad.m in the vertical plane. For the purpose of our comparison, we concentrated our efforts on the study of Case 3.

The important parameters of the SPS acceleration cycle are displayed in Table 3, including the theoretical bunch length equilibrium value $(\sigma_S)_o$.

				SIMULATION		
t (ms)	E (GeV)	τ_E (s)	$(\sigma_s)_o$ (cm)	σ_s (cm)	transverse threshold (10^{10})	calculated longitudinal threshold (10^{10})
200	3.57	4.24	1.48	22.5	1.6	1.73
216	3.59	4.17	1,44	19.5	1.6	1.85
250	3.83	3.44	1.46	18.6	1.6	1.70
283	4.49	2.13	1.55	17.1	1.5	1.53
316	5.80	0.99	1.74	15.0	1.73	1.79
350	7.60	0.44	2.04	12.3	1.73	2.00
383	10.0	0.19	2.59	9.9	1.73	2.18
416	12.8	0.092	3.22	8.1	1.73	2.14
450	15.9	0.048	3.73	6.9	1.73	1.95
483	18.0	0.033	4.30	5.0	1.90	1.8

Table 3 Main parameters during the SPS cycle.

As can be seen from Table 3, the damping times at injection are so long, that leptons do in fact behave like protons at low energy. The beam dimensions are essentially governed by the acceleration process and it is only at higher energies that the synchrotron radiation becomes dominant so that the beam size is finally determined by the equilibrium between damping and excitation by synchrotron radiation. As far as the thresholds are concerned, one benefits from the increased dimensions along almost the whole cycle, but this advantage disappears around 18 GeV. This behaviour is well borne out by the simulation, where one observes that the steady decrease of the bunch length tends to counteract the natural tendency of the thresholds for collective instabilities to increase with energy (see Table 3).

For this set of simulations, the coupling impedance assumed was:

$$(R/Q)_T = 12.5\ M\Omega/m$$

$$Z/n = 6.4\ \Omega \qquad (14)$$

$$Q = 6.0 \text{ and } fr = 1.35\ GHz$$

One should note, that in this case the selected value of (R/Q) is smaller than that quoted in (2).

The reason can be explained as follows:

When simulating above the threshold, the losses are faster than any other effect. We therefore expect that only the impedance of the machine matters. However, when simulating below this threshold (as in the present case), other stabilizing effects not included in the simulation (like octupoles) have to be accounted for by reducing the shunt impedance.

The energy spread, the bunch length and the RF voltage as a function of the cycle time are plotted in Fig. 7. When compared to experimental observations, these simulation results do exhibit three interesting features, namely:

1) When the bunch is injected above the threshold for longitudinal instability, a fast increase of the energy spread occurs (see Fig. 7). Actually, the same behaviour is also observed experimentally, as can be seen from Fig. 8 which shows the evolution of the energy spread measured along the cycle.

2) Simulation results and analytical estimations predict that the thresholds for both longitudinal and transverse instabilities are very close from each other all along the cycle, and almost constant (see Table 3). Experimentally, one observes that: at higher energies, when the bunch length decreases, these intense bunches may become unstable. However, the consequences are very different depending on which threshold is crossed first. If the transverse instability is dominant, a large fraction of the beam is lost (Fig. 9a). If the longitudinal microwave instability starts first, the result is an increase of the bunch length, which pushes the transverse threshold to higher values, and no loss occurs (Fig. 9b). In our SPS experiments, 4 bunches were simultaneously accelerated. Only one of them (the first one) was used to pilot the RF phase loop. As a consequence, this bunch was probably injected and captured in a

more efficient way than its followers. At any rate, it systematically suffered from a microwave instability during the ramp, and was transmitted without important losses (Fig. 9b). The other bunches, which did not show any longitudinal instability suffered important losses while high frequency signals could be detected on a vertical monitor (Fig. 9a).

3) Under the conditions defined for this experiment, it was possible to accelerate about 2.2 10^{10} particles up to 18 GeV in the first bunch, provided the RF phase loop was active on this bunch. Without this RF phase loop the bunch intensity was limited around 1.8 10^{10} particles. Remembering that the effect of the RF phase loop is not part of the simulation, this last result fairly agrees with the simulated thresholds given in Table 3.

7. Conclusions

Experimental observations of the transverse mode coupling instability and the longitudinal microwave instability of lepton bunches in the SPS were used in a simulation program to fit a broad band resonator model as a description of the machine coupling impedance. The simulation outcome is in fair agreement with measurements performed previously with protons.

With this impedance model, it is then possible to simulate the dynamical behaviour of the bunch along the whole SPS cycle and thus try to predict the increased thresholds one could expect by varying the injection conditions. Here again, the predicted thresholds are in reasonable agreement with the experimental ones. It therefore clearly demonstrates that a broad band resonator is an adequate model for the representation of the SPS impedance. It is felt that this agreement is related to the fact that one has to deal with relatively long bunches and also that the SPS impedance is composed of many different contributions which are spread out over the whole machine. Another very interesting comparison between simulation and experiments will become available very soon with the experimental data collected in LEP. This next step will basically differ from the present one in the sense that the bunches are short and that the LEP impedance is known to be dominated by both the RF cavities and the vacuum chamber bellows.

References

[1] D. Brandt, LEP Note 512 (1984)

[2] L. Vos, CERN SPS/86-21 (1986)

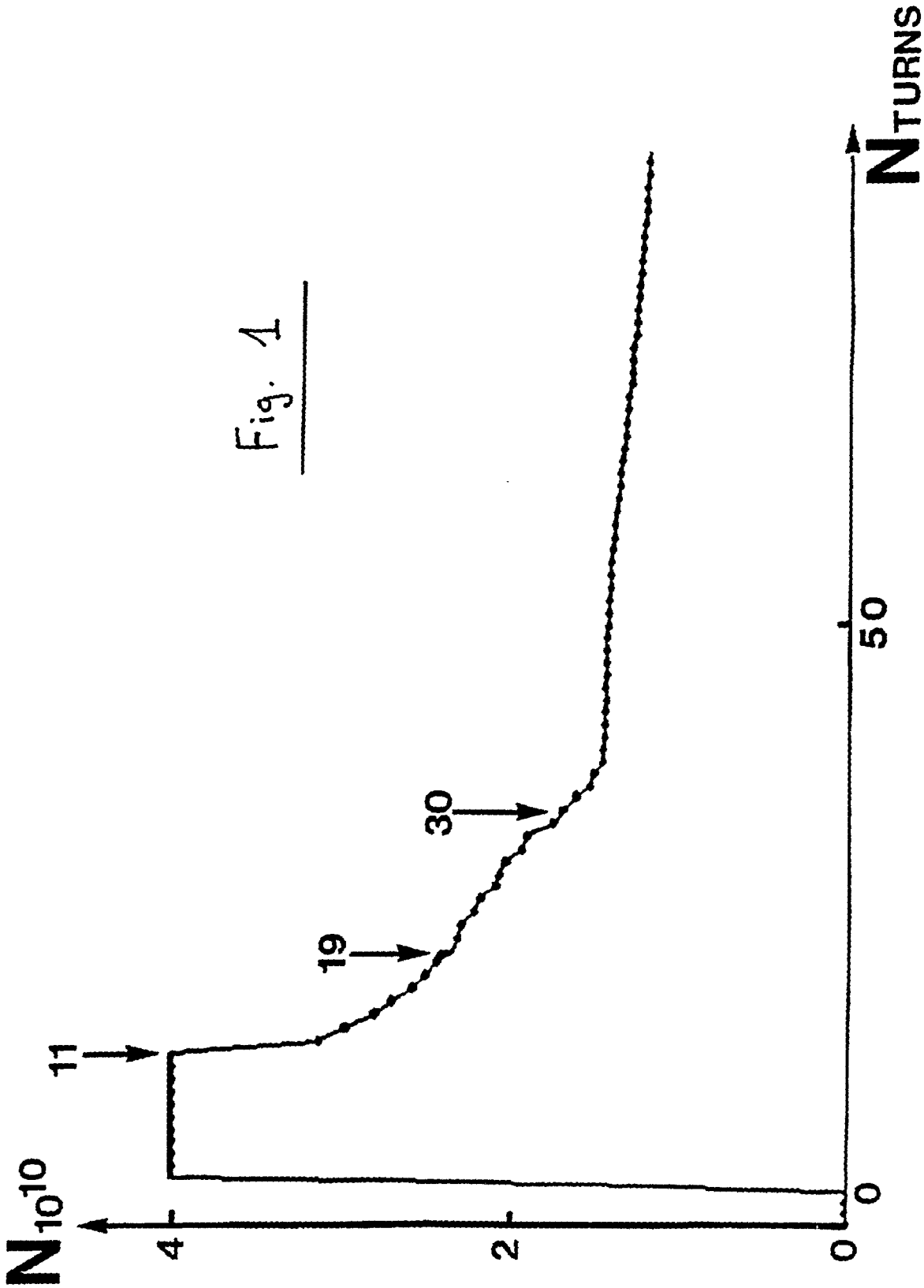

Fig. 1

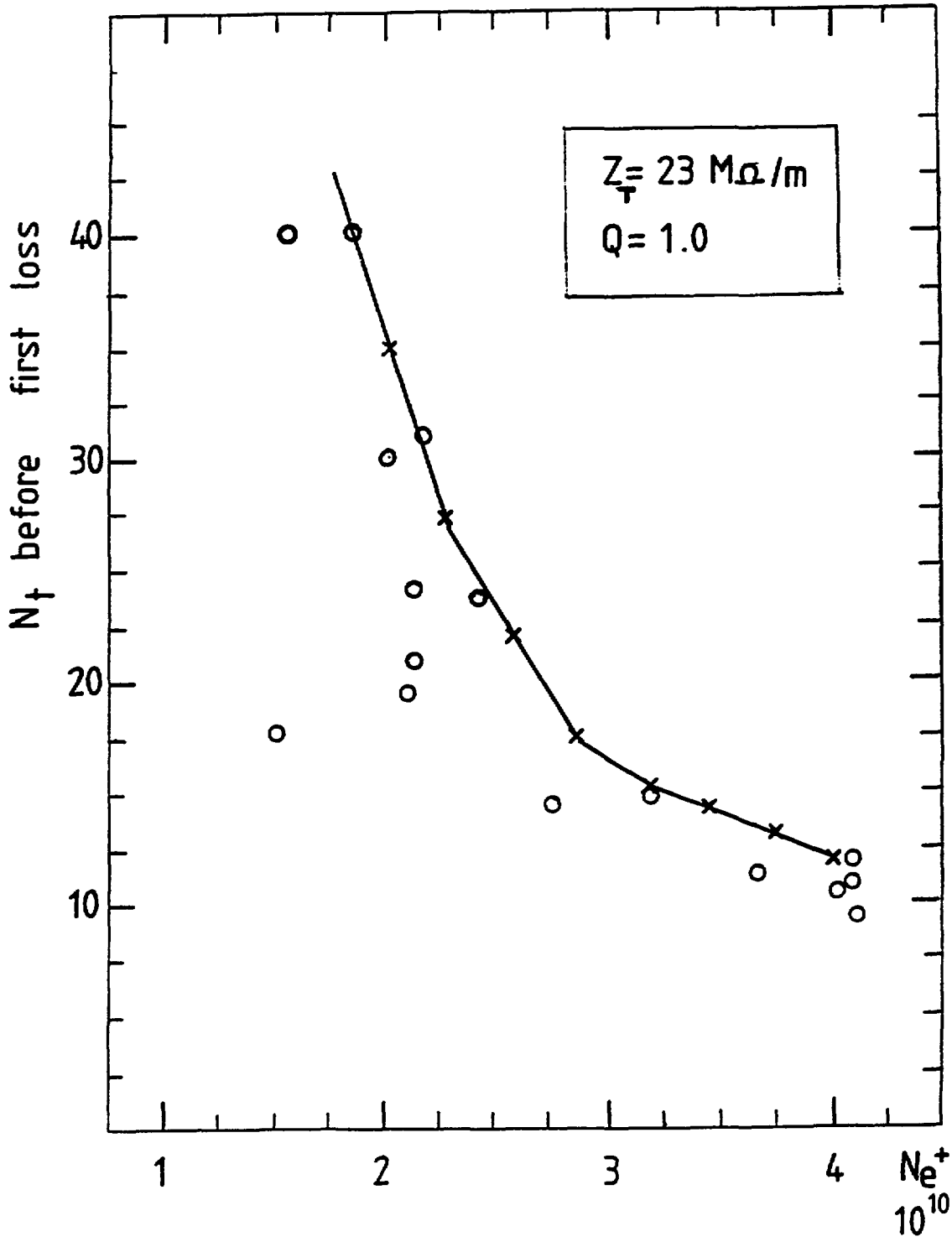

Fig. 2

$Z_T = 17\ M\Omega m^{-1}$ $Q_T = 6.0$ $f_r = 1.35\ GHz$

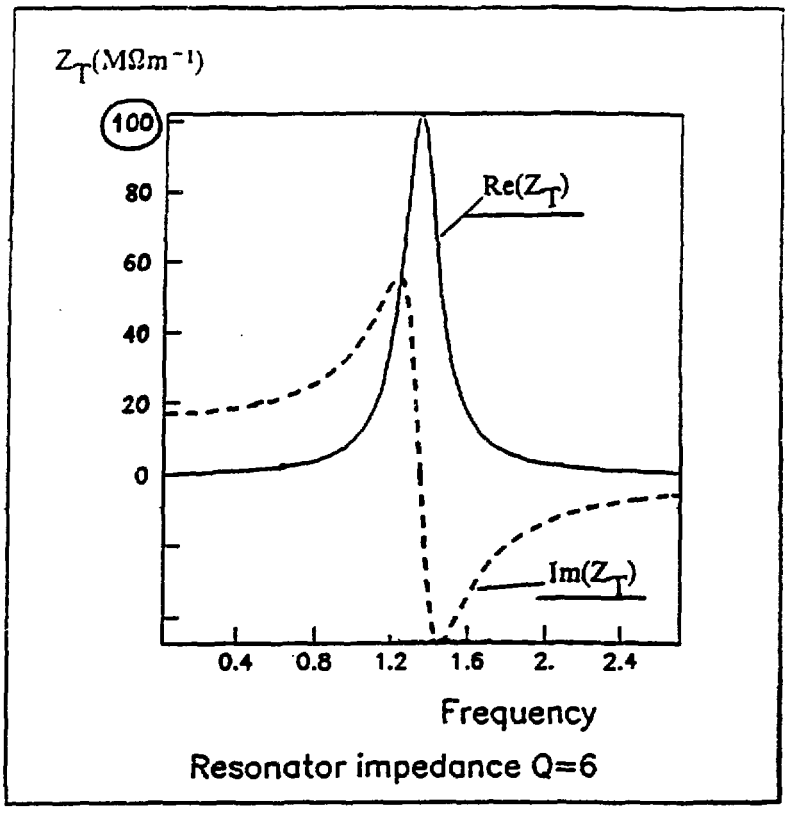

Fig. 3

$Z_T = 23\ M\Omega m^{-1}$ $Q_T = 1.0$ $f_r = 1.35\ GHz$

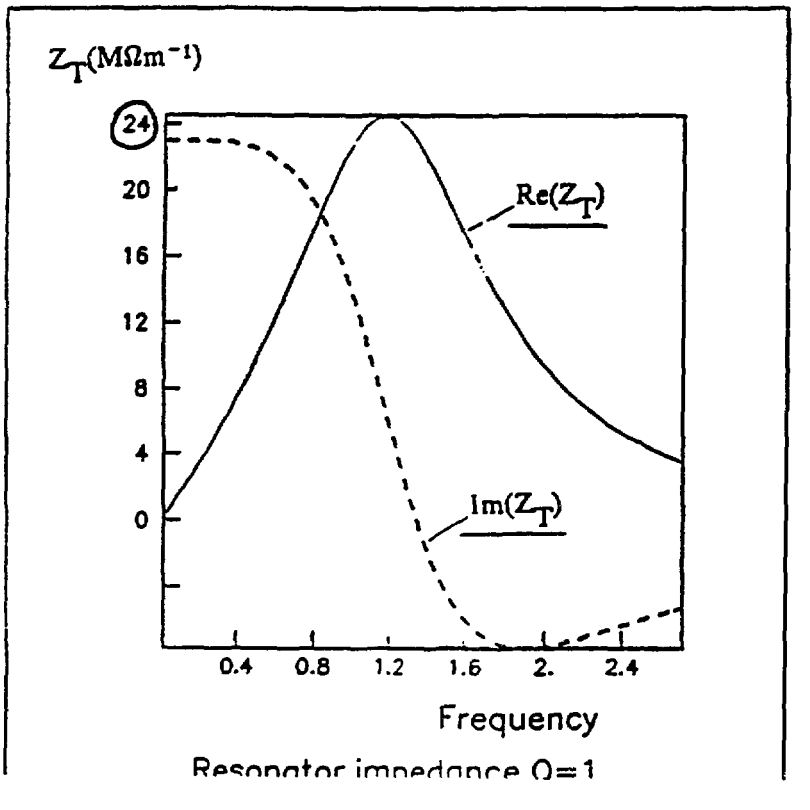

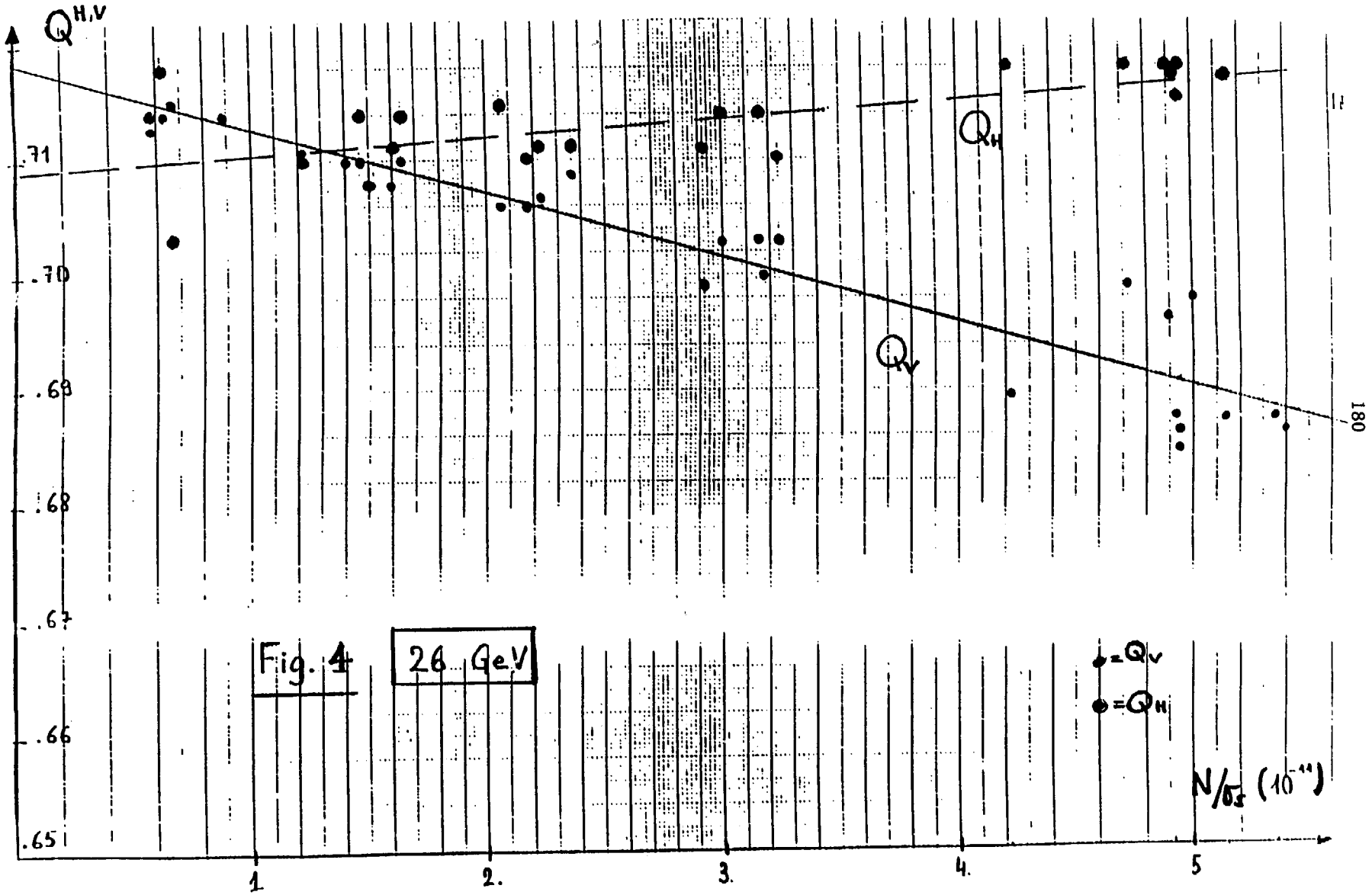

Fig. 4 — 26 GeV

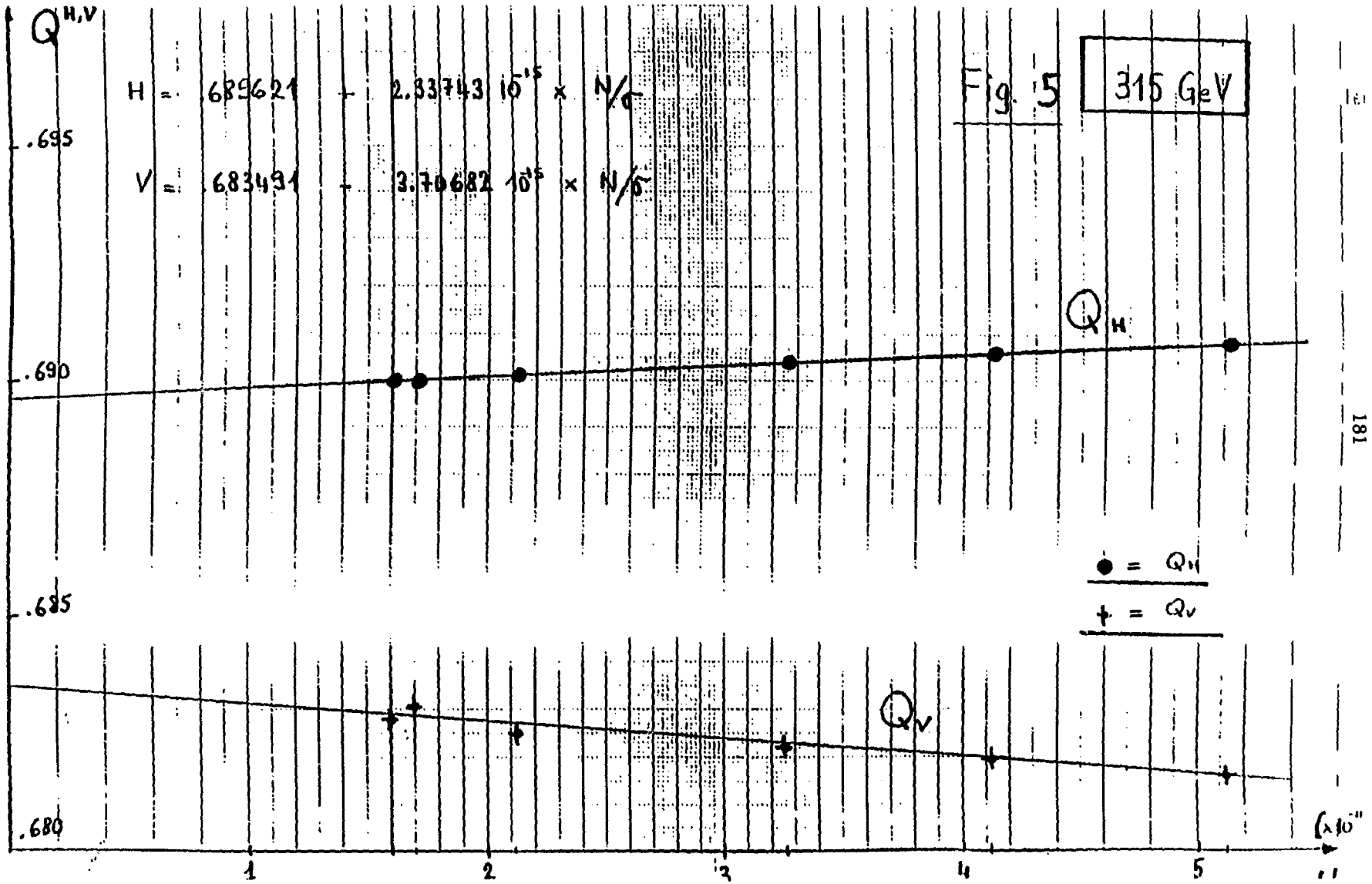
$Q^{H,V}$
H = 689621 + 2.33743 10^{-5} × N/c
V = 683491 + 3.70682 10^{-5} × N/c
Fig. 5
315 GeV
.695
.690
.685
.680
Q_H
Q_V
● = Q_H
+ = Q_V
1
2
3
4
5
(×10")
181

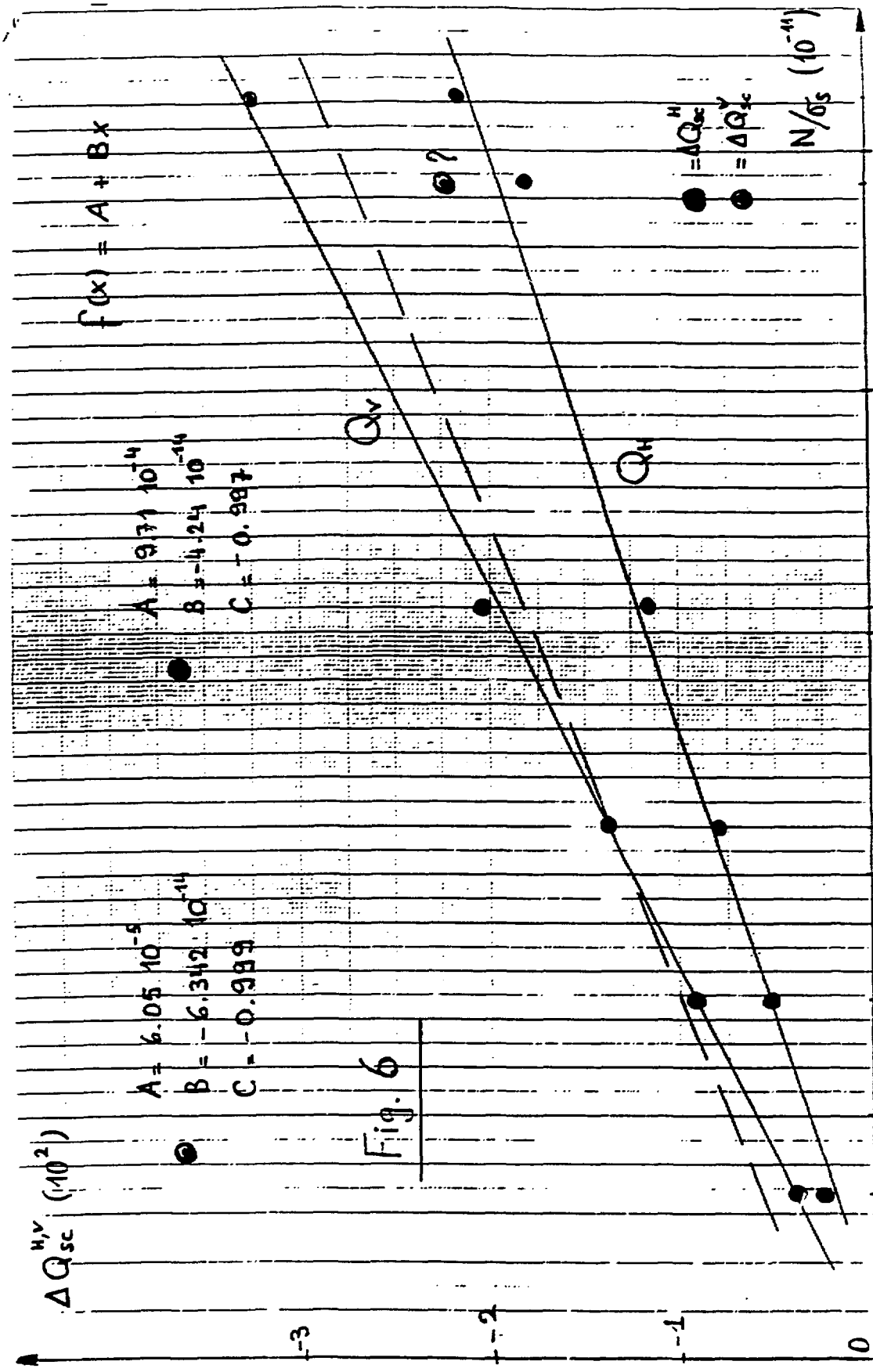
f(x) = A + Bx
A = 9.71 10^-4
B = -4.24 10^-14
C = -0.997
A = 6.05 10^-5
B = -6.342 10^-14
C = -0.999
Qv
QH
= ΔQsc^H
= ΔQsc^V
N/σs (10^-11)
ΔQsc^H,V (10^-2)
-3
-2
-1
0
1
2
3
4
5

Fig. 6

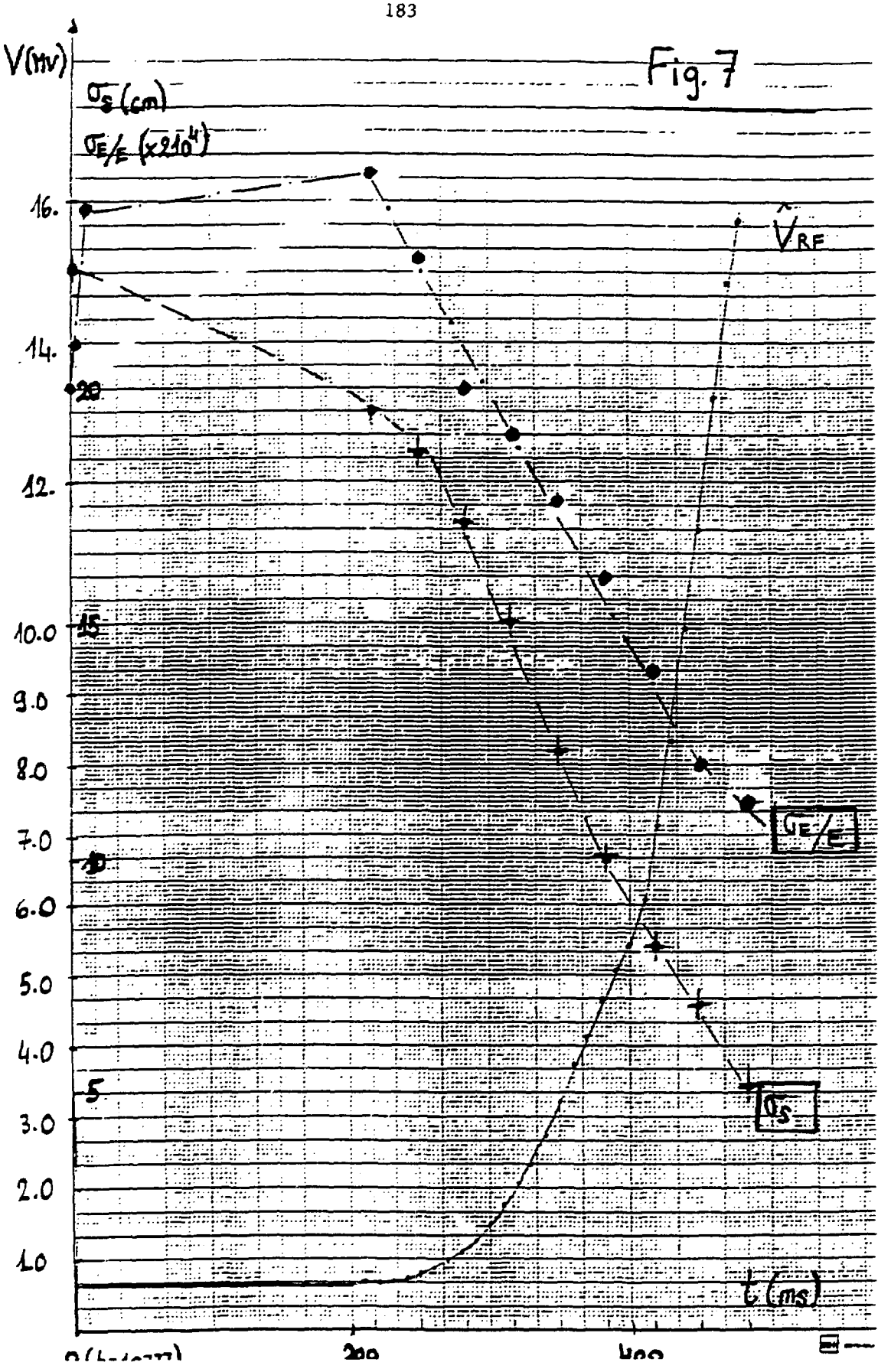
V(MV)
Fig. 7
σs (cm)
σE/E (x2 10⁻⁴)
16.
14.
12.
10.0
9.0
8.0
7.0
6.0
5.0
4.0
3.0
2.0
1.0
20
15
10
5
V̂RF
σE/E
σs
t (ms)
200
400

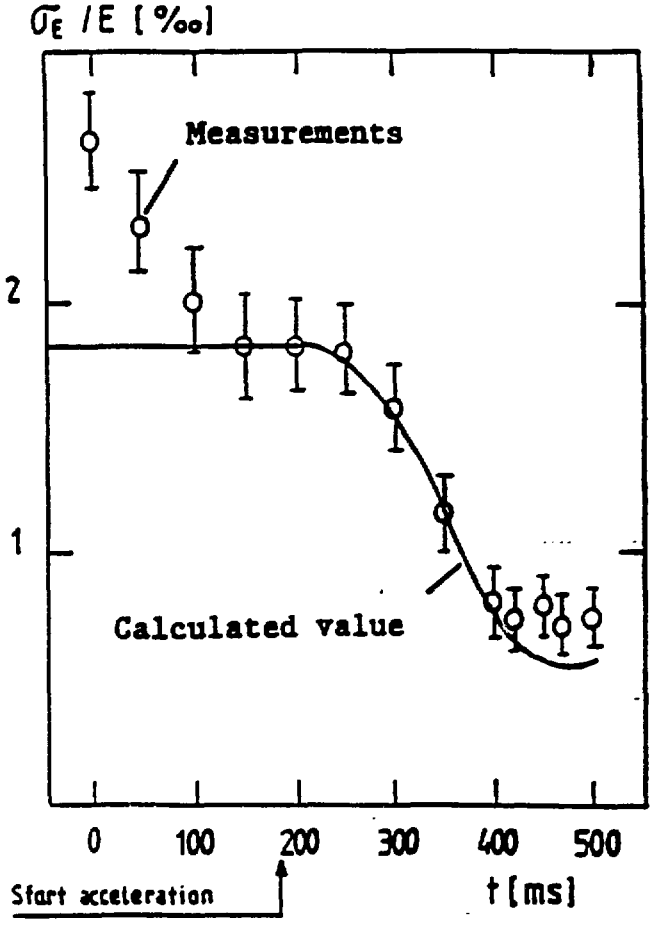

Fig. 8

Energy spread during the cycle

Fig. 9

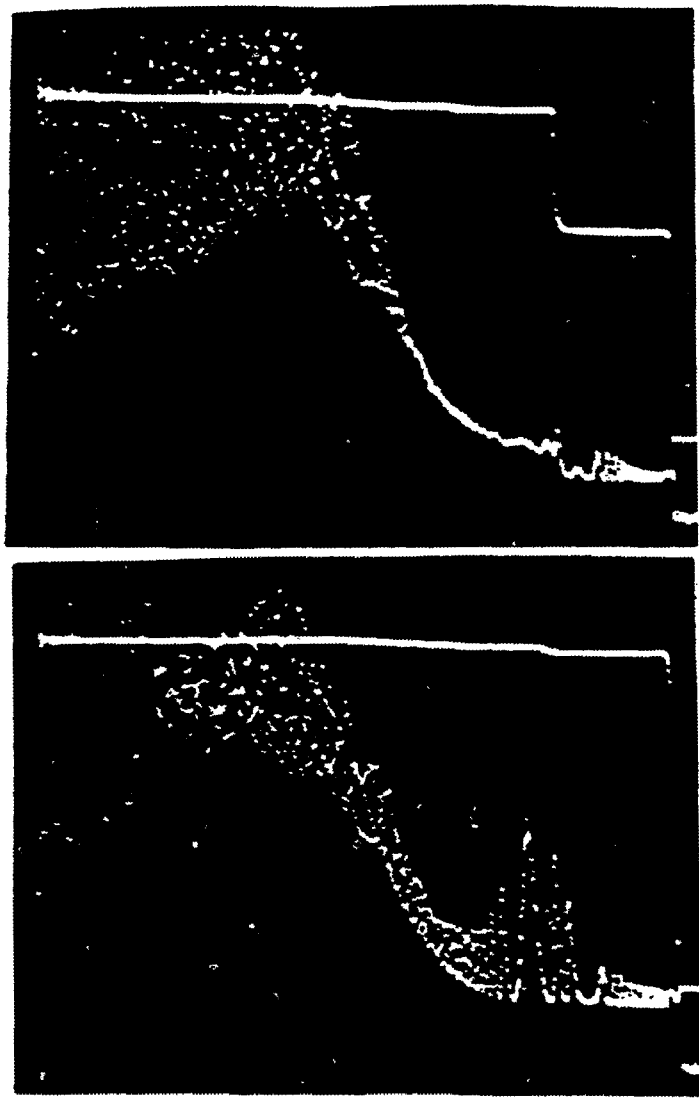

a)

RF Loop OFF

bunch intensity

bunch length

b)

RF Loop ON

H scale :
50 ms/div

Bunch Lengthening in the SLC Damping Rings*

Karl L. F. Bane

Stanford Linear Accelerator Center
Stanford University, Stanford, Callifornia 94309

Argonne National Laboratory
Advanced Photon Source
Impedance and Bunch Instability Workshop
October 31 - November 1, 1989

---

*Work supported by Department of Energy contract DE-AC03-76SF00515.

TABLE OF CONTENTS

1. INTRODUCTION

A high level of current dependent bunch lengthening has been observed on the North damping ring of the Stanford Linear Collider (SLC).[1] At currents of 3×10^{10} this behavior does not appear to degrade the machine's performance significantly. However, at the higher currents that are envisioned for the future one fears that its performance could be greatly degraded due to the phenomenon of bunch lengthening. This was the motivation for the work described in this paper.

In Chapter 2 we calculate the longitudinal impedance of the damping ring vacuum chamber. More specifically, in this chapter we find the response function of the ring to a short Gaussian bunch, which we call the Green function wake. In addition, we try to estimate the relative importance of the different vacuum chamber objects, in order to see how we might reduce the ring impedance. Chapter 3 describes bunch length measurements performed on the North damping ring. In Chapter 4, we use the Green function wake, discussed above, to compute the bunch lengthening. Then we compare these results with those obtained from the measurements. In addition, in this chapter we calculate the current dependence of the tune distribution. Note that each of these chapters is based on work already described in a published report: Chapter 2 in "The Calculated Longitudinal Impedance of the SLC Damping Rings" by K. Bane, Ref. (2), Chapter 3 in "Bunch Lengthening in the SLC Damping Ring" by L. Rivken *et al.*, Ref. (1), and Chapter 4 in "Bunch Lengthening Calculations for the SLC Damping Rings" by K. Bane and R. Ruth, Ref. (3). The only completely new work is the tune calculations.

2. THE CALCULATED LONGITUDINAL IMPEDANCE

2.1 Introduction

The SLC damping ring vacuum chamber contains many small discontinuities—such as shallow steps, transitions, masks, and bellows—as well as larger objects like the beam position monitors and the rf cavities. In this chapter we study the relative importance of the various objects to the total ring impedance. In addition,

we obtain a Green function that will be used in a later chapter for bunch length calculations.

In this paper we are interested only in the single bunch effects of the vacuum chamber impedance. The true vacuum chamber impedance is normally very complicated, containing many resonances and other structure, and covers a wide frequency range. A single bunch, however, only probes the impedance after it has been smoothed by the bunch spectrum, the so-called "broad-band impedance." The time domain correspondent to this impedance is the short range wakefield.

In this paper, we choose to work in the time domain, and all our results are based on wakefield computations. Consider an infinitely long tube which at some position is momentarily interrupted by a cavity, an obstruction, or other change in cross-section. Now consider a bunch of electrons (or positrons) passing at the speed of light c parallel to the axis of the pipe, from minus to plus infinity. The longitudinal wakefield $W(t)$, then, is defined as the total voltage—divided by the charge in the bunch—gained by a test particle that has followed the same path, also at velocity c, but at relative position ct. We will use the convention that a more negative value of time t is more toward the front of the bunch. In most of the cases that we consider the structure geometry is cylindrically symmetric, and we use T. Weiland's computer program TBCI[4] to calculate the wakefield. Note that by limiting our structures to those with equal beam pipes we force the system's potential energy at the beginning of the calculation to be the same as at the end.

2.2 Types of Impedances

2.2.1 Introduction

A vacuum chamber object in a storage ring can be described as inductive, resistive, or capacitive, depending upon whether it tends to cause bunch lengthening, bunch shortening, or does not affect the bunch length. We can discern which of these catagories applies to an object from the shape of the voltage that it induces. We can further speak of a vacuum chamber object as being a good—or

ideal—inductor, resisitor, or capacitor if its induced voltage is related to the driving current in a manner analogous to that found in the corresponding simple circuit element. It is important to note, however, that in either case the applicability of the terms inductive, resistive, or capacitive depends not only on the shape of the object itself, but also on the length of the exciting bunch. As the bunch length changes different parts of the object's impedance become emphasized. Normally, vacuum chamber objects appear more inductive to longer bunches, more capacitive to shorter bunches.

2.2.2 Inductive Objects

If the effective slope of the induced voltage opposes the slope of the rf wave then the object is inductive, and it will tend to lengthen the bunch. We denote as good inductors objects for which the induced voltage can be approximated by $V_{ind} = -L\,dI/dt$ with the constant L the inductance and I the bunch current. We note that this model, in detail, is unphysical: it predicts that the beam loses no energy passing by the object. If the induced voltage of a vacuum chamber object is well approximated by the above relation, it means that the beam sees primarily the low frequency part of the object's impedance; and that in this region the impedance is purely imaginary, and linear with a slope of $-L$. Note that if an object is a good inductor at a certain bunch length, it will continue to be so at longer bunch lengths.

It is often easy to see whether or not an object is a good inductor for a Gaussian bunch with length σ. Normally, inductive objects tend to be small discontinuities. Now suppose we have a small obstruction in a tube of radius a. If the bunch length obeys the relation $\sigma \gtrsim a/2$ then little of its power spectrum ($\lesssim 9\%$) is above the tube cut-off frequency. When the beam passes by the obstruction it will therefore leave little energy behind, since the tube will not support free waves below its cut-off. The head of the beam will lose energy to the discontinuity, but the tail will reabsorb most of it, resulting in an inductive wakefield. In the SLC damping rings there are many small discontinuities on tubes of radius 11 mm (or less) which,

according to the above criterion, are good inductors for bunch lengths down to 5.5 mm. Note that since only for the tails of the beam's spectrum—at frequencies above the tube cut-off—is the real part of the impedance nonzero, the higher mode loss that we do find in inductors decreases exponentially fast as the bunch length is increased.

Objects that can be considered good inductors for bunch lengths normally found in storage rings are shallow transitions, shallow cavities, bellows, masks, or bumps in the vacuum chamber walls. We shall see that the SLC damping ring contains many such objects, which therefore define the character of its impedance. As an example of a good inductor Fig. 1(b) displays the shape of a QD bellows of the SLC damping rings. The wakefield of a 6 mm Gaussian beam passing by this object, as calculated by TBCI, is shown in Fig. 1(a). The beam shape is represented by the dotted curve, with the front to the left. Note that in our convention the slope of the applied rf must be negative for machines operating above transition.

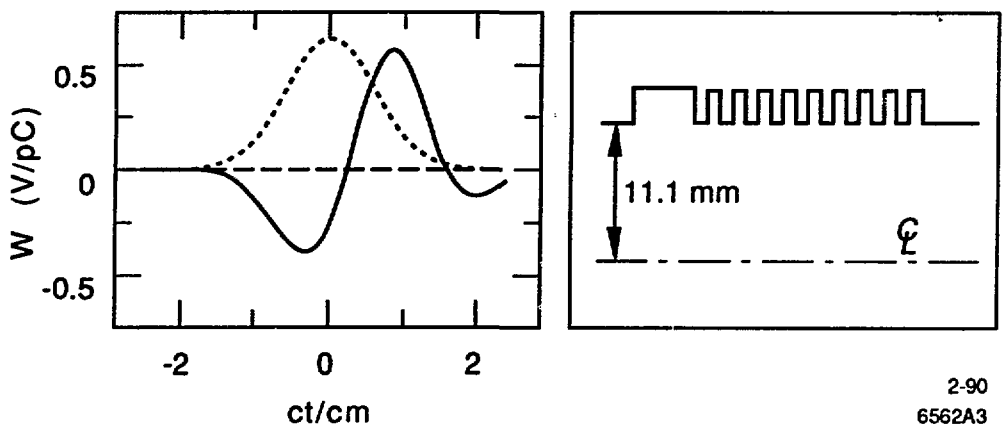

Fig. 1. An inductive example: the wakefield of a 6 mm Gaussian bunch passing by the QD bellows of the SLC damping ring.

2.2.3 Resistive Objects

If the effective slope of the induced voltage is almost zero then the object is resistive, and it has little effect on bunch lengthening. We denote as good resistors

objects for which the induced voltage ca be approximated by $V_{ind} = -IR$, with the constant R the resistance. We note that this model is also not strictly physical: since these beams are assumed to be moving at the speed of light, the induced voltage must lag, even if by a slight amount, behind the driving current. Note that for good resistors the loss factor—the total higher mode loss divided by the bunch charge—is approximated by $k = R/(2\sqrt{\pi}\sigma)$. Examples of good resistive elements found in storage rings are deep cavities, such as the rf cavities, for bunches that are not short compared to the beam tubes. As resistive example Fig. 2(a) shows the wakefield left by a 6 mm Gaussian bunch passing by one of the two 2-cell rf cavities of the SLC damping rings [Fig. 2(b) displays the shape of one cell].

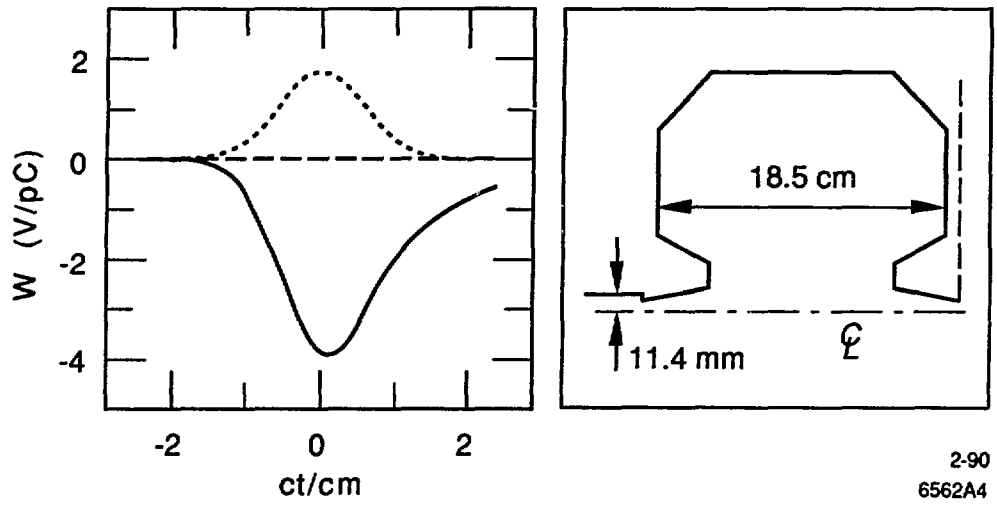

Fig. 2. A resistive example: the wakefield of a 6 mm Gaussian bunch passing by one of the rf cavities of the SLC damping ring.

2.2.4 Capacitive Objects

Finally, if the effective slope of the induced voltage enhances the rf slope then the object is capacitive, and it will tend to shorten the bunch. We denote as good capacitors objects for which the induced voltage is approximately proportional to the integral of the current, with constant of proportionality $-1/C$, and C the

capacitance. This model is strictly unphysical in that it predicts that the energy loss of a bunch depends only on the total charge of the beam, and not on the peak current. This type, of the three types of objects, is probably the least commonly encountered in storage rings. Reference (5) describes a capacitive device, the so-called "SPEAR capacitor," that was installed in a ring for the specific purpose of shortening the bunch. The wakefield of very short bunches in deep cavities falls somewhere between that of a pure resistor and a pure capacitor. The rf cavity of Fig. 2 can be considered slightly capacitive in that the average slope of the induced voltage is slightly negative. However, there are no very capacitive objects in the SLC damping rings. But to give an example of a fairly good capacitor, we show in Fig. 3(a) the wakefield of a 6 mm Gaussian bunch passing by the cavity of Fig. 3(b).

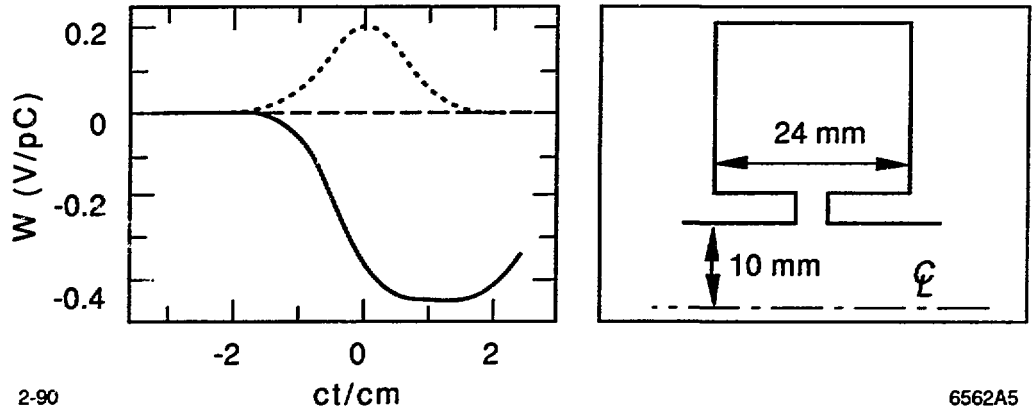

Fig. 3. A capacitive example: the wakefield of a 6 mm Gaussian bunch passing by the structure shown at right.

2.3 The Effective Inductance

The loss factor k is often used to estimate the contribution of an object to the ring impedance. This parameter gives the higher mode losses of the object but says little about its contribution to bunch lengthening. Alternatively, we can say that it is a measure of the real, not the imaginary, part of the impedance. As a

figure of merit that is a complement to the loss factor, and that is a measure of the imaginary part of the impedance, we will use the effective inductance ℓ.

Recall that the loss factor is given by the average value of the wakefield along the bunch

$$k = -\int_{-\infty}^{\infty} W(t)\lambda(t)\,dt = \int_{-\infty}^{\infty} \left[\int_{0}^{\infty} W_\delta(t')\lambda(t-t')\,dt'\right] \lambda(t)\,dt \quad , \tag{1}$$

with λ the longitudinal charge distribution and W_δ the Green function (or delta function) wake. The Green function, in turn, is given by the inverse Fourier transform of the impedance Z:

$$W_\delta(t) = \frac{1}{2\pi}\int_{-\infty}^{\infty} Z(\omega)e^{-i\omega t}\,d\omega \quad , \tag{2}$$

with ω the frequency. Therefore, the loss factor can also be written in terms of the impedance as

$$k = \frac{1}{\pi}\int_{0}^{\infty} X(\omega)|\tilde{\lambda}(\omega)|^2\,d\omega \quad , \tag{3}$$

with $\tilde{\lambda}$ the Fourier transform of the charge distribution and X the real part of Z. Thus k gives the real part of the impedance averaged over the square of the bunch spectrum.

Let us define the effective inductance ℓ by the following operation: We compute the wakefield for a Gaussian bunch and then perform a least squares fit to

$$W(t) = -\ell\frac{d\lambda(t)}{dt} \quad . \tag{4}$$

Therefore ℓ can be written in terms of the impedance as

$$\ell = -\int_{0}^{\infty} Y(\omega)|\tilde{\lambda}(\omega)|^2\omega\,d\omega \Big/ \int_{0}^{\infty} |\tilde{\lambda}(\omega)|^2\omega^2\,d\omega \quad , \tag{5}$$

with Y the imaginary part of Z. We see that ℓ—up to a bunch length factor—is the product of $Y\omega$ averaged over the square of the bunch spectrum. For a pure inductance, $Z = -i\omega L$, we see that ℓ reduces to L. For a Gaussian beam Eq. (5) becomes

$$\ell = -\frac{4\sigma^3}{\sqrt{\pi}} \int_0^\infty Y(\omega) e^{-\omega^2\sigma^2} \omega \, d\omega \quad . \tag{6}$$

Note that, as in Ref. (5), we might alternatively have chosen as figure of merit the bunch length times the average slope of the wake:

$$\alpha = \sigma \int_{-\infty}^{\infty} W'(t)\lambda(t)\, dt = 2\sigma \int_0^\infty Y(\omega)|\tilde{\lambda}(\omega)|^2 \omega \, d\omega \quad . \tag{7}$$

We see that α—up to a bunch length factor—is the same as ℓ. As a fine point, we also note that in the results to be presented a Gaussian weighting factor has been included in the least squares calculations that determine ℓ. Therefore, instead of by Eq. (6), ℓ will be given by

$$\ell = -\frac{3}{2}\sqrt{\frac{3}{\pi}} \int_0^\infty Y(\omega) e^{-3\omega^2\sigma^2/4} \omega \, d\omega \quad . \tag{8}$$

2.4 Some Simple Inductors

Let us consider the simple discontinuities of Fig. 4. To a Gaussian bunch sufficiently long (*i.e.*, one with length σ greater than half the tube radius) they will appear as good inductors. For each of the three models we have performed parametric studies to find its inductance. To obtain a data point, we first computed the wakefield of a reasonably long Gaussian bunch passing by the structure in question, using TBCI. Then, we performed a least squares fit to Eq. (4), weighted by the Gaussian bunch shape, in order to obtain the effective inductance ℓ. And finally we found the limiting value of ℓ, as σ becomes large, which we take as the inductance L of the object.

In order to reduce our work we computed the wakefield in the following manner: We first performed a TBCI calculation for a short Gaussian bunch of length σ_1, calculating the wakefield to a long distance behind the driving bunch. Given this wakefield W_1, we then obtained the wakefield for longer bunches, with length σ, by performing the following integration[6]:

$$W(t) = \frac{1}{\sqrt{2\pi}\sigma_t} \int_{-\infty}^{\infty} W_1(t') \exp\left[-\frac{(t-t')^2}{2\sigma_t^2}\right] dt' \qquad (\sigma > \sigma_1) \quad , \tag{9}$$

with $\sigma_t^2 = \sigma^2 - \sigma_1^2$. In this way, for any given structure, one TBCI calculation provides the wakefield for Gaussians over a wide range of bunch lengths.

We began our studies with the small cavity, shown in Fig. 4(a). It is interesting to note that the numerical results we obtained for it can be well approximated by a simple application of Faraday's Law. According to Faraday's Law the voltage induced across the gap depends on the time rate of change of the magnetic flux φ_m in the cavity. If we approximate φ_m by the product of the beam's unperturbed magnetic field at the cavity times the cavity cross-sectional area, we obtain the inductance[7]

$$L = \varphi_m / I = \frac{Z_0}{2\pi c} \frac{g\Delta}{a} \qquad (\Delta/a \text{ small}) \quad . \tag{10}$$

with I the beam current and $Z_0 = 377\ \Omega$. The inductance of a bellows—which is just a sequence of small cavities—can be approximated by the above result multiplied by the number of convolutions. Next we studied the shallow iris [see Fig. 4(c)]. The numerical results agree well with

$$L = \frac{Z_0}{\pi c} \frac{\Delta^2}{b} \qquad (\Delta/b \text{ small}, g/b \text{ small}) \quad . \tag{11}$$

It appears that for the shallow iris the effective distance from the corner over which the magnetic flux changes with time is on the order of Δ.

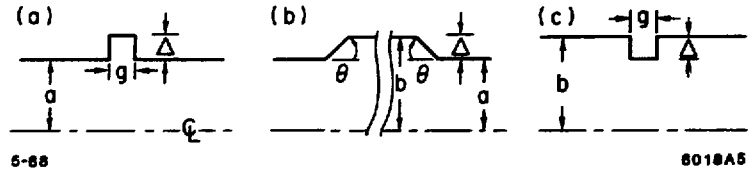

Fig. 4. Some simple vacuum chamber elements: (a) a small cavity, (b) a symmetric pair of shallow transitions, and (c) a shallow iris.

Finally we considered a pair of symmetric, shallow transitions [Fig. 4 (b)]. Our simulation results—if the transitions are separated by a distance at least on the order of b—can be approximated by

$$L = \frac{3Z_0}{2\pi c}\frac{a\Delta^2}{b^2}\left(\frac{2\theta}{\pi}\right)^{1/2} \qquad (\Delta/b \text{ small}, \; g/b \gtrsim 1, \; \theta \leq \pi/2) \quad . \tag{12}$$

Note that this equation approximates the numerical results well even for $\Delta/b \sim 0.5$. We see from Eq. (12) that when $\theta < \pi/2$ the inductance of a transition can be reduced, though only very slowly, by changing the transition angle. However, if we break up a transition into n smaller steps, that are separated by a sufficient distance, we can gain by the factor n. Note that Eq. (12) with $\theta = \pi/2$ must also apply to the iris of Fig. 4(c) when $g/b \gtrsim 1$.

For the example transition with parameters $a = 10$ mm and $\Delta/b = 1/6$ we demonstrate, in Fig. 5, the validity of the angular dependence of Eq. (12). The plotting symbols signify the computed results, the dotted curve the approximation Eq. (12). More specifically, the plotted values give the effective inductance ℓ computed for a 16 mm Gaussian bunch; when the bunch length was doubled the results remained essentially unchanged. We see that within its limits of validity Eq. (12) agrees very well with the computations. Note that, over the entire range of data points, the results of Fig. 5 vary roughly as $\sqrt{\tan(\theta/2)}$.

Finally we point out that the formulas of this section may also be used to estimate the imaginary part of the transverse impedance $Y_\perp$ at the origin for these

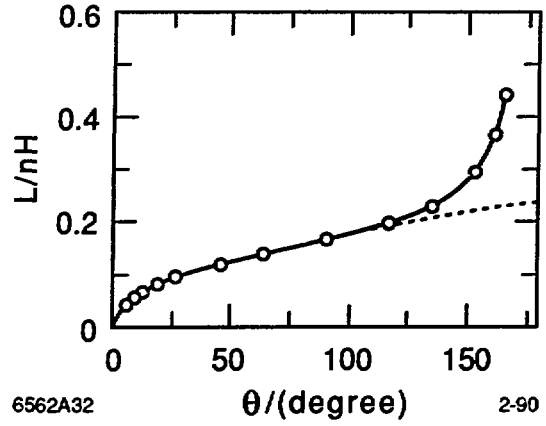

Fig. 5. The θ dependence of L for a symmetric pair of shallow transitions when $a = 10$ mm and $\Delta/b = 1/6$. The dotted curve gives the analytic approximation, Eq. (12).

structures. Using a well-known formula[8] for estimating the transverse from the longitudinal impedance of a cylindrically symmetric structure, with tube radius a, we find near the origin

$$Y_\perp \approx \frac{2c}{a^2}\ell \quad . \tag{13}$$

2.5 The Damping Ring Vacuum Chamber

The damping ring vacuum chamber is divided into 8 girders (see Fig. 6). Of these girders 2, 3, 6 and 7 are almost identical. They each contain 4 1/2 FODO cells, with the quadrupole vacuum chambers—which are cylindrically symmetric—separated by the roughly square bend vacuum chambers (see Fig. 7). Girders 5 and 8, in addition to half a FODO cell on each end, contain kickers, septa, rf cavities and other vacuum chamber elements not found in the rest of the ring.

The vacuum chamber of the FODO cells can be divided into two groups of objects, each of which is repeated 20 times in the ring. One group, which we will call a "QD vacuum chamber segment" is centered on a defocusing quadrupole vacuum chamber, with each end at the middle of the neighboring bend chamber.

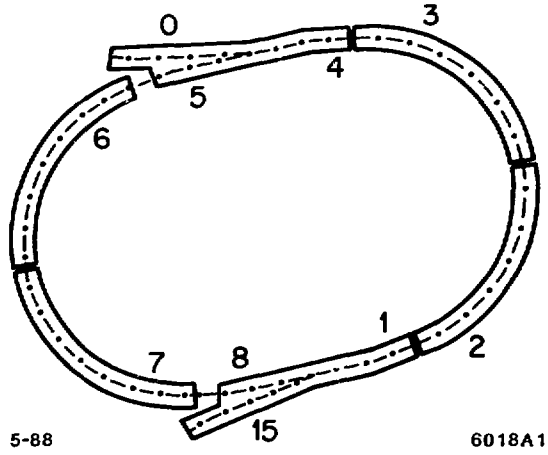

Fig. 6. The girders of the SLC north damping ring.

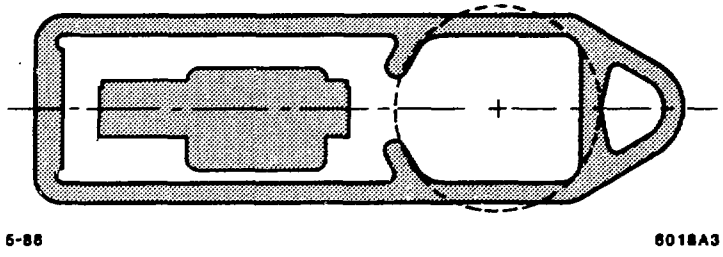

Fig. 7. The cross-section of the bend chamber. The dashed circle shows the size of a quad chamber.

The "QF vacuum chamber segment" is similar, though centered on a focusing quadrupole. The vertical profile of these segments is sketched in Fig. 8, with the ends truncated. Nonsymmetric portions are shown dashed. The figures are drawn to scale. The total length of each segment is about 60 cm; the half-length of the bend chamber is 15 cm.

A QD segment (see the top sketch) begins with the roughly square bend chamber (1), which is connected by a tapered transition (2) to the cylindrically symmetric defocusing quadrupole (QD) chamber. The QD chamber contains a 1 inch beam position monitor (1″ BPM) (3), a QD bellows (4), a serf gasket (5), and a QD mask (6). Finally there is another transition (7) into the next bend (8). The

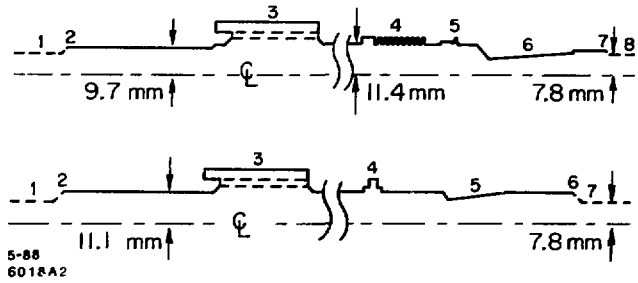

Fig. 8. The vertical profile of a QD segment (top) and a QF segment (bottom). The noncylindrically symmetric portions are drawn with dashes.

ends of a QF segment are similar (see the bottom of Fig. 8). The cylindrically symmetric QF chamber, however, contains a 1″ BPM (3), a flex joint (4), and a QF mask (5).

Ring Girders 5 and 8 include two kickers, two septa, a two cell rf cavity, two 1″ to 2″ transitions, four 2″ BPM's, four 1.4″ BPM's, an optical monitor and a dielectric gap.

2.6 The Impedance of Individual Vacuum Chamber Elements

2.6.1 The Inductive Elements

In order to estimate the relative importance for bunch lengthening of the different objects found in the SLC damping rings we divided the vacuum chamber into a number of recognizable pieces. Then, for each piece we computed the wakefield of a Gaussian bunch with length $\sigma = 6$ mm using TBCI. This length was taken as typical for the damping rings. Then finally we obtained ℓ by performing a least squares fit, as described earlier. Note that dividing a stretch of several vacuum chamber objects into its parts does not affect the answer so long as $\sigma \gtrsim a/2$, with a the tube radius, and so long as neighboring pieces are separated by at least $2a$. With typically $a = 11$ mm the former condition is normally met. The latter condition, unfortunately, cannot always be met. Therefore, the results we present

only approximately give the relative importance of the various vacuum chamber objects.

Unfortunately, many of the vacuum chamber objects are not cylindrically symmetric. Whenever possible, we took a suitable cylindrically symmetric (2-D) model to represent the noncylindrically symmetric (3-D) object in the calculations. In some cases it was evident how one might go about this. For example, the geometry of the ion pump slots, a 3-D object, can partially be seen in Fig. 7. We see that each slot can be approximated by a simple, shallow transition, whose outer radius is defined by the pump housing, and which fills only 10% of the azimuth. For the slots, we computed the wakefield for a cylindrically symmetric version of the shallow transition using TBCI, and then multiplied the results by a filling factor of 0.1. The beam position monitors (BPM's), with their noncylindrically symmetric electrodes, were treated in a similar manner. In other cases, it was not so evident what the right 2-D model should be. For example, the QD and QF transitions are transitions from an approximately square to a round vacuum chamber tube. For such objects, we obtained insight into how best to model them by applying the computer program T3,[9] the 3-D counterpart of TBCI, to a simple 3-D approximation to the real structure.

Table 1 gives the results for the elements that are inductive to a 6 mm Gaussian bunch. Figure 9 shows the geometry used for (a) the QD bellows, (b) the QD mask, (c) the QD transitions, and (d) the ion pump slots. The factor in Column 3 is an azimuthal filling factor used to account for the contribution of noncylindrically symmetric objects. Column 4 gives the total number of these objects in the ring. We see that the total effective inductance of the ring is approximately 50 nH, spread over many objects. Not included in the table are the septa, each of which is a complicated obstruction in a 25 mm ID tube. Using the computer program T3 on a simple 3D model we find that the septum has an inductive and resistive component. We estimate that $\ell \approx 2$ nH for each septum.

Table 1. The inductive vacuum chamber elements.

Single Element Inductance		Contribution in Ring		
Type	L/(nH)	Factor	Number	L/(nH)
QD bellows	0.62	1.0	20	12.5
QD & QF masks	0.47	1.0	20	9.5
QD & QF trans.	0.52	0.9	20	9.3
Ion pump slots	1.32	0.1	40	5.3
Kicker bellows	2.03	1.0	2	4.1
Flex joint	0.18	1.0	20	3.6
1″ BPM trans.	0.10	0.8	40	3.3
Other				2.4
		Total		50.0

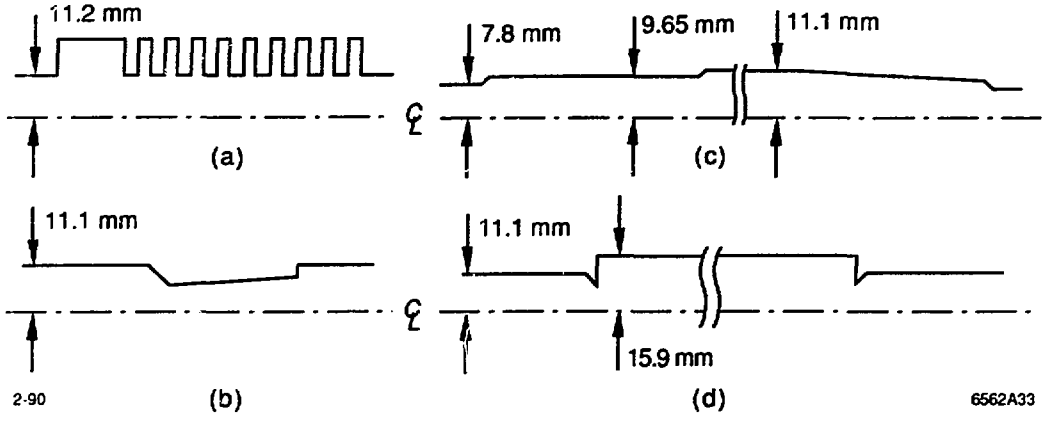

Fig. 9. The geometries used to calculate ℓ for: (a) the QD bellows, (b) the QD mask, (c) the QD transition, and (d) the pump slots.

Since the inductance of the ring is spread over so many objects it would take more than a small modification to reduce it significantly. Recently sleeves were installed to shield the QD bellows from the beam. From the table we would estimate that the ring inductance would therefore be reduced by 25%. However, since the bellows are close to the QD mask (see Fig. 8) there is coupling between these two objects. By performing the calculation for the entire QD segment taken

as one piece, once with and once without the bellows, we estimate the bellows contribution to the ring inductance to be more like 15%.

2.6.2 The Resistive Elements

There are objects in the ring that are resistive, most important of which are the two 2-cell rf cavities. At a bunch length of 6 mm the rf cavities contribute 5.8 V/pC to the ring loss factor k. We can speak of them having an effective resistance of 411 Ω. At this bunch length the forty 1″ BPM cavities are also resisitive with a total k of 3.2 V/pC. However, these small cavities become less resistive at longer bunch lengths. Other objects that are resistive at this bunch length, but contribute little to the ring loss are two 2″ BPM's, two 1.4″ BPM's, two kicker gaps, an optical monitor, the ion pump holes and a dielectric gap.

How can we compare the contribution of the inductive and the resistive vacuum chamber components to the longitudinal instability? In instability analysis the impedance enters as the quantity $|Z(n)/n|$, with $n = \omega/\omega_0$ and ω_0 the revolution frequency. For the damping rings $\omega_0 = 5.4 \times 10^7$ s^{-1}. Therefore, for the inductive elements the effective inductance of 50 nH corresponds to an effective $|Z/n|$ of 2.6 Ω. For resistive elements let us consider only the rf cavities. If for the cavities we take as typical frequency $\omega = 1/\sigma$ we find that an effective resistance of 411 Ω corresponds to an effective $|Z/n|$ of 0.44 Ω. According to this rough estimate the inductors contribute 6 times as much to the $|Z/n|$ of the ring as the cavities. If we want to bring the contribution of the inductors down to that of the rf cavities we would clearly need to rebuild the entire vacuum chamber.

2.7 The Green Function Computation

We will need a Green function wake for the damping rings in order to perform bunch length calculations. However, it suffices if we can find the wakefield of a bunch that is very short compared to the natural bunch length in the ring, and that has been calculated out to a sufficient distance behind the driving bunch. Ideally we would like to compute the wake for one whole turn around the ring in

one long computer run, with the beam moving from one element to the next just as it does in the real machine. Then all interference effects between neighboring elements, even at frequencies above cut-off, are properly accounted for. However, due to the limitations in computer time and memory available to us we need to make compromises.

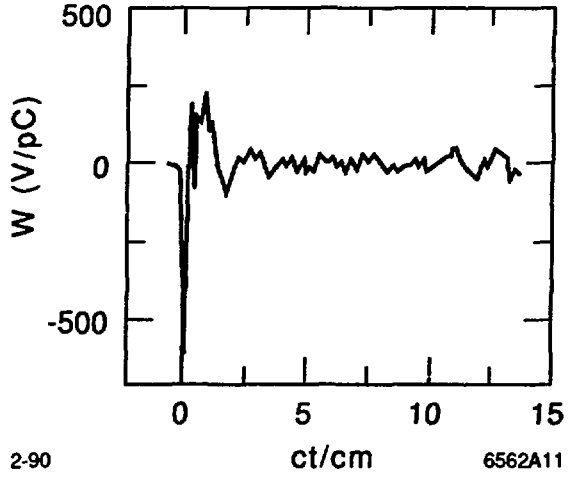

Fig. 10. The longitudinal wakefield of a 1 mm Gaussian bunch in the SLC damping ring.

For our Green function we first calculated the wakefield of a 1 mm Gaussian bunch, out to 15 cm behind the bunch, for the various damping ring vacuum chamber objects. The only exception is for the rf cavities, where a 2.7 mm bunch was used, due to limitations in the computer memory available to us. As best as possible we wanted to properly include the interference effects of neighboring objects. To this end we calculated the wakefields of the entire QD and QF segments each in one piece. To account for the noncylindrical symmetry of the BPM electrodes we performed the calculation for each segment twice—once with and once without cylindrically symmetric electrodes—and then added the two results in the ratio 8:2, according to the azimuthal filling factor of the real electrodes. However, the calculations of the pump slots, as well as of the remaining objects found in girders 5 and 8, were all done in separate computations. Objects that were not included

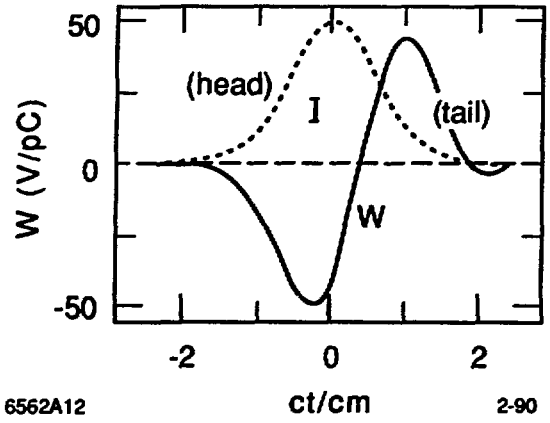

Fig. 11. The longitudinal wakefield of a 6 mm Gaussian bunch in the SLC damping ring. The current distribution is also shown.

in the calculations are the septa, the ion pump holes, the optical monitor, and the dielectric gap.

The sum of all the computations, which we take to represent the wakefield of a 1 mm Gaussian bunch in the SLC damping rings, is shown in Fig. 10. We note that most of the response occurs within the first 2 cm behind the driving bunch. By performing the integral of Eq. (9) we can find the wakefield of any Gaussian bunch that is longer than 1 mm. Figure 11 shows the results that are obtained for a 6 mm Gaussian bunch. At this length the ring is clearly very inductive.

In the same manner we have obtained the wakefields of Gaussian bunches with different lengths. From these wakefields we have found the loss factor k and the effective inductance ℓ of the ring as functions of bunch length. These results are shown in Fig. 12. The dotted curve gives the contribution to the loss factor of the rf cavities alone. We see that both k and ℓ reach asymptotic values at long bunch lengths. In addition, we see that the loss factor of the entire ring drops in an exponential fashion with increasing σ, while the loss of the rf cavities drops only very slowly.

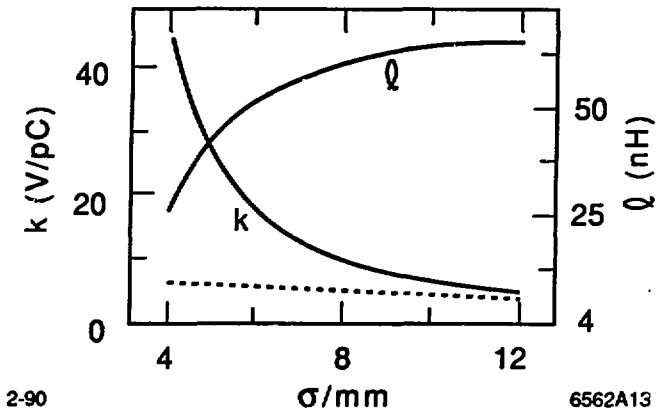

Fig. 12. The loss factor k and the effective inductance ℓ of the damping ring as function of bunch length. The dotted curve gives the loss contribution of the rf cavities alone.

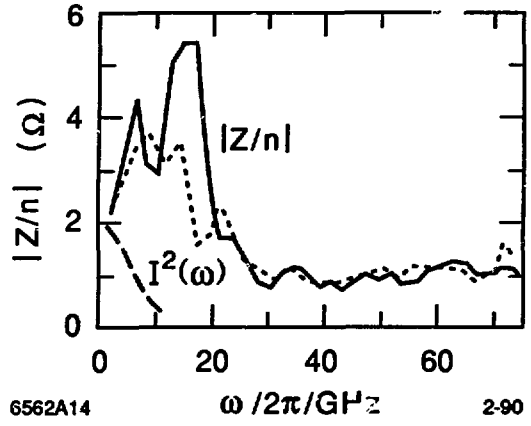

Fig. 13. The impedance $|Z/n|$ of the damping ring. The dots give what remains when the QD bellows (with their antechambers) are perfectly shielded. The power spectrum of a 6 mm Gaussian bunch is also shown.

By taking the Fast Fourier Transform of the 1 mm wake we can obtain the impedance. In Fig. 13 we plot the quantity $|Z/n|$ (remember $\omega_0 = 5.4 \times 10^7\ s^{-1}$). We see a large broad peak at 16 GHz, with a peak value of 5.5 Ω and Q of 2; it is due mostly to the bellows. A smaller resonance, at 6.5 GHz, with a peak value 4.4 Ω, and a Q of about 1, is due to the BPM cavities. (We note, however, that the results

for this resonance may be very inaccurate, due to the very approximate manner in which we included the BPM electrodes.) In Fig. 13 we also see that $|Z/n|$ obtains a constant value at high frequencies, an effect that is due to numerical noise. When we repeat the calculation of the 1 mm wake, but this time leaving out the QD bellows, and then take the Fourier transform, we obtain the results shown by the dots in Fig. 13. These results are meant to represent the damping ring with the QD bellows shielded, as has recently been done. We note a substantial reduction in the impedance beyond 10 GHz. Although we do not expect this modification to have a great effect on the bunch length it may still have a significant effect on the instability threshold.

From the 1 mm wake we contructed the Green function wake W_δ in the following manner: we first changed its sign and then modified the front of the function so that it is 0 for $t < 0$. This modification yields a Green function that is causal. This Green function will later be used to calculate the wakes for bunch shapes that are long compared to 1 mm and that are rather smooth. We therefore expect the results not to be very sensitive to the details of the modification just mentioned, provided that the changes are localized near $t = 0$ and that the area under the curve remains unchanged. For our calculations we have chosen to reflect the leading tail to the back, and then to add it to the existing wake. The leading part of the Green function wake is shown in Fig. 14. The dots give the negative of the 1 mm wake.

3. BUNCH LENGTHENING MEASUREMENTS

3.1 Introduction

Under normal SLC operations the beam, after leaving the damping ring, is shortened by about a factor of 10 in the Ring-to-Linac (RTL) transfer line before entering the linac proper. The bunch shortening is the result of a phase space rotation. It is accomplished by an rf section, which induces an energy variation that is correlated with longitudinal position, followed by a beam line with nonzero

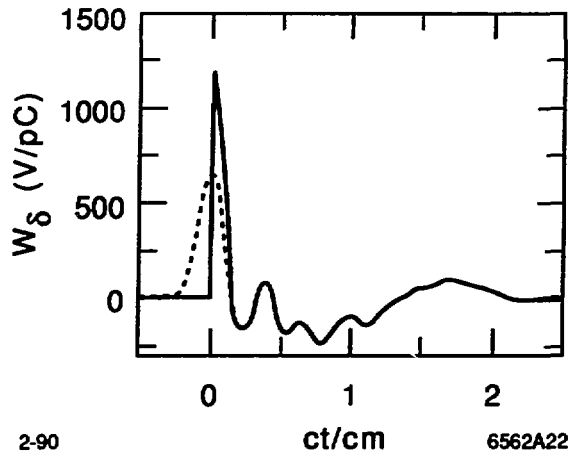

Fig. 14. The Green function wake for the SLC damping rings.

momentum compaction. Using this hardware and, in addition, a phosphor screen and video camera, we are able to measure the longitudinal charge distribution of individual damping ring pulses, of pulses having an rms length on the order of 5 mm. Although the measurements to be discussed contain some fluctuations due to screen imperfections, we expect that with a better, newly installed screen we can now measure the longitudinal intensity accurately to a resolution of 0.1 mm[10] for a bunch with a length of 5 to 10 mm.

Using the same hardware but with the compressor rf off, and with a modified optics, we can measure the bunch's energy distribution as function of current. In particular, this measurement allows us to find the threshold current for turbulence. We also discuss, in this chapter, measurements of the current dependence of the beam's synchronous phase and of the longitudinal quadrupole tune.

3.2 Measuring the Longitudinal Charge Distribution

3.2.1 Introduction

The hardware, as it is configured for bunch length measurements, is shown in Fig. 15. The setup is essentially the same as during normal operations. However, at a downstream position of high horizontal dispersion a phosphor screen is inserted in

the path of the beam. An off-axis camera can then capture the image, the intensity of which can—in turn—be digitized over a grid and sent to a computer. If we can assume that the response of the screen to charge intensity and the response of the camera to light intensity are linear, then the horizontal distribution measured in this way will be correlated to the longitudinal charge distribution in the ring.

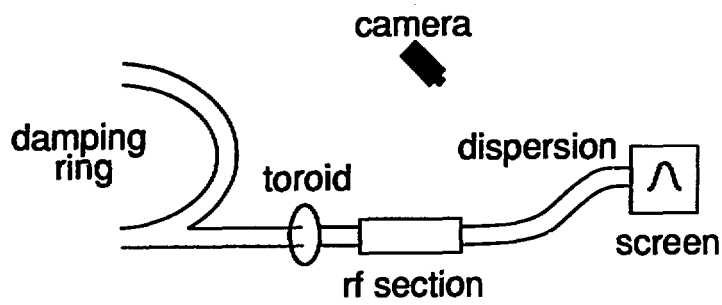

Fig. 15. Layout of the apparatus used in the bunch length and energy spread measurements.

Now let us assume for the following discussion that (i) the longitudinal distribution does not reach past the crests of the rf wave, (ii) the induced energy spread is large compared to the beam's initial energy spread and compared to the wake-field induced energy variation, and (iii) the dispersive part of the beam size ($\eta^2\delta^2$) dominates the emittance part ($\beta\epsilon$). For the measurements about to be presented all these conditions were met. Given these assumptions, the connection between longitudinal position t within the bunch and transverse position x on the screen is

$$x - x_0 = \kappa \sin k_{rf}(ct - z_0) \quad , \tag{14}$$

with x_0 the screen position that corresponds to the zero of the rf the sine wave z_0, and k_{rf} the rf wave number. The parameter $\kappa = \eta e V_c/E$, with η the dispersion

at the screen, V_c the peak compressor voltage, and E the beam energy. The longitudinal charge distribution is given by

$$\lambda = c\lambda_x \left|\frac{dx}{dz}\right| = c\lambda_x k_{rf}\sqrt{\kappa^2 - (x - x_0)^2} \quad . \tag{15}$$

Equations (14) and (15) allow us to obtain the beam distribution $\lambda(t)$ given the measured distribution $\lambda_x(x)$.

Note that in the SLC the compressor wave length is 10.5 cm and the beam energy $E = 1.153$ GeV. For the bunch length measurements we took $V_c \approx 33$ MV.

3.2.2 Results

We began the measurements by finding κ and x_0. Taking a low current beam we varied the rf phase and measured the excursion limits of the spot: the half distance between these two points gave us κ. Thus the dispersion and the compressor voltage do not need to be known explicitly. For our data $\kappa = 18.25$ mm; thus a 1 mm distance near x_0 on the screen corresponded to a 1.1 mm longitudinal distance within the bunch. Then measuring the spot with the compressor rf off gave us x_0. We then turned the compressor back on and adjusted the phase so the low current spot was again at x_0. With this setup we measured and stored the distributions over a range of currents, at a ring rf voltage $V = 0.8$ MV. For each measurement a toroid reading, giving us the current, was also taken.

As an example, Fig. 16 gives the measured distribution λ_x for a bunch population $N = 2.9 \times 10^{10}$ after it has been transformed to λ (as described above). The vertical axis is $y = eN\lambda Z_0/(\dot{V}_{rf}\sigma_0)$, with $Z_0 = 377\ \Omega$ and σ_0 the natural bunch length ($c\sigma_0 = 5$ mm at this ring voltage); the horizontal axis is t/σ_0. We note that the distribution is broad and it is not symmetric: the rising edge is steeper than the falling edge. The corresponding centroid shift is a measure of the higher mode losses. For the moment, however, we should take the position $t = 0$ on the plot as arbitrary since the beam's position on the screen drifted over the duration of the measurements, apparently due to phase drift of the ring rf. (We will present

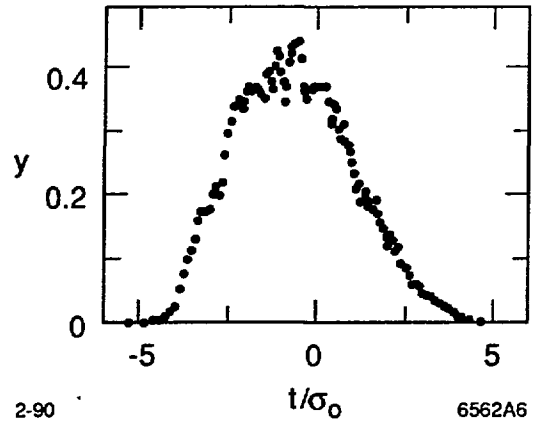

Fig. 16. The measured bunch shape for $N = 2.9 \times 10^{10}$ when $V_{rf} = 0.8$ MV.

more accurate measurements of the centroid shift below.) As in this example all the measured distributions are quite smooth, except in the vicinity of their peaks. We believe the fluctuations that we do see in the data are due to imperfections in the screen. Recently a new screen with a more uniform phosphor layer has been installed in the RTL. We expect, therefore, that future measurements will result in smoother distribution curves.

We present the rms widths of the distributions, times 2.355, as function of current in Fig. 17(c) (the full circles). On the same frame we plot the full-width-at-half-maximum (the open circles). For a Gaussian distribution these two quantities should be equal. That the open circles lie above the closed ones at higher currents implies that these distributions are more bulbous than a Gaussian. Note that there is very little scatter in the data.

We mentioned earlier that the current values of each measurement were based on toroid readings. However, we could alternatively have taken the areas under the distribution curves as the measure of current, since these areas are also proportional to the charge. In fact, with the areas one obtains a current reading for the same pulse that is being measured, whereas with the toroids one never knows to which pulse the reading corresponds. In any case, the pulse-to-pulse current variation

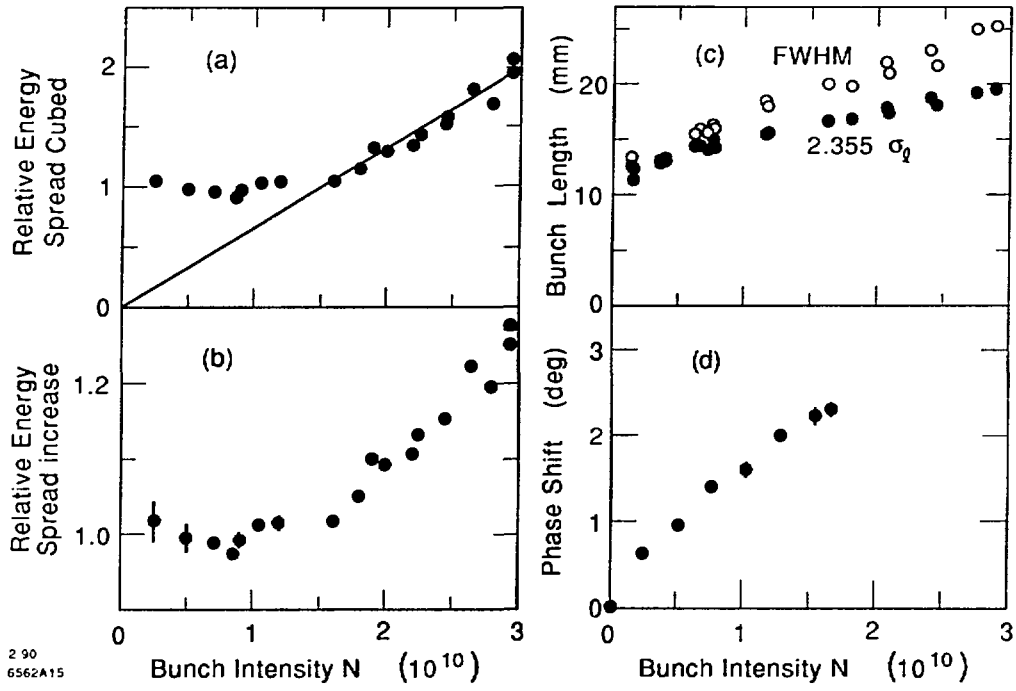

Fig. 17. Measurement results: (a) the relative energy spread cubed, (b) the relative rms energy spread, (c) the bunch length, and (d) the synchronous phase shift as function of current. The ring voltage $V_{rf} = 0.8$ MV.

was small during the course of our measurements. We found that the correlation of the areas of the distributions with the toroid readings was extremely good. This suggests that, despite the local fluctuations that we saw in the distribution curves, the overall response of the hardware to intensity was essentially linear. When we plot the bunch length as function of distribution area rather than as function of toroid reading the data follows a smoother curve.

3.3 Other Measurements

3.3.1 Energy Spread Measurement

The beam's energy spread was measured in a fashion similar to its bunch length. For this measurement we turned off the compressor, used another screen, and modified the RTL optics to give an increased dispersion function at the screen.

In this configuration increases in the beam's intrinsic energy spread translate into an increased spot size on the screen. This measurement is difficult since at high currents the small, intense spot will tend to damage the screen.

The energy spread measurements yielded distributions that all appeared to be Gaussians. Figure 18 shows the measured distribution when $N = 3 \times 10^{10}$, with a Gaussian curve superimposed on the data. The rms energy spread as function of current is displayed in Fig. 17(b). We see that the data is rather flat up to about $N = 1.5 \times 10^{10}$, at which point it begins to rise. We will take this value as the threshold current N_{th}. By plotting the energy spread cubed as function of current [see Fig. 17(a)] we see that above threshold the data agrees well with

$$\sigma_\epsilon = \sigma_{\epsilon_0} \left(\frac{N}{N_{th}} \right)^{1/3} \qquad (N > N_{th}) \quad , \tag{16}$$

with σ_{ϵ_0} the initial energy spread. As we shall see in the next chapter, we expect the energy spread to behave in this way for a ring with an inductive impedance, such as the damping ring.

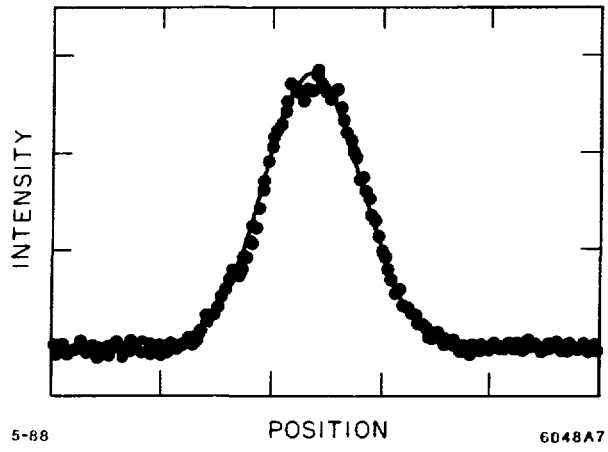

Fig. 18. The measured energy spectrum for $N = 3 \times 10^{10}$ when $V_{rf} =$ 0.8 MV.

3.3.2 Measurement of the Synchronous Phase

The measurement of the synchronous phase complements the bunch length measurement. The bunch length measurement probes the imaginary part of the broad band impedance, while the synchronous phase measurement probes the real part, giving also the higher mode losses. We began the measurement by first storing a high current beam in the ring. Then, we gradually scraped away beam while we continually monitored the beam's phase using a vector voltmeter and a chart recorder. At the same time the circulating current, which we could continually read from a current monitor in the ring, was marked at frequent intervals on the chart. For more details of the measurement technique see Ref. (11).

The measured phase shift as function of current is shown in Fig. 17(d). The plot gives the average of several traces of the chart recorder, all of which agreed quite well with one another. The data grows linearly at low current, and more slowly as the current increases. This is the kind of behavior we would expect since, as we have seen above, as the damping ring current increases the bunch length also increases, and we know that the higher mode losses depend inversely on bunch length. Note that the total shift at $N = 1.5 \times 10^{10}$ is only 2.3 degrees. This size of shift corresponds to a higher mode loss of 32 keV and a loss factor $k = 13$ V/pC.

3.3.3 Synchrotron Tune Shift Measurement

Measuring the current dependence of the coherent oscillation frequencies is another way of probing the broad band impedance of the ring. Sometimes this coherent shift is also taken as a measure of the incoherent tune shift with current. In this measurement we excited quadrupole mode oscillations by amplitude modulating the rf gap voltage, and then measured the response from a beam position monitor. In Fig. 19 both the measured dipole and half the quadrupole frequencies are displayed over a range of currents. We see that the quadrupole frequency initially decreases but then appears to level off near $N = 5 \times 10^9$. The maximum reduction is 3 to 4%. From the plot, we also see the dipole frequency, which should remain flat, rise slightly with current.

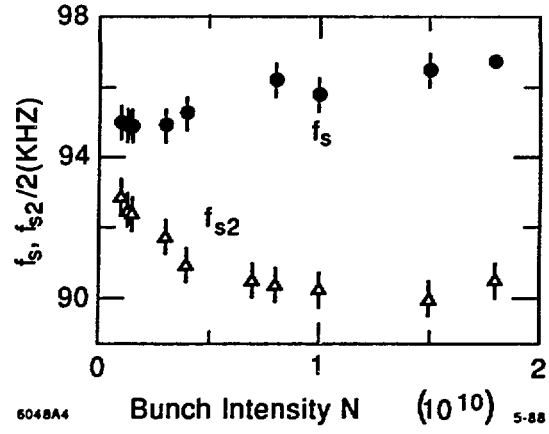

Fig. 19. The longitudinal dipole and half the quadrupole oscillation frequency as function of current.

3.4 Measurements Since the Addition of Bellows Sleeves

The bellows mentioned previously, in Chapter 2, are inner bellows, which are themselves surrounded by a set of outer bellows. Since the inner bellows are very inductive we normally expect a bunch to leave almost no energy behind after its passage. If, however, there is not a complete contact between the inner bellows and the vacuum chamber walls, then the beam can deposit energy in the cavity between the two bellows. We believe this to be the case for some of the QD bellows. During very high current operation it was observed that some of these bellows became very hot, in at least one instance resulting in a puncture of the outer bellows and a loss of vacuum. Largely to guard against more of this type of damage, and partly to reduce the bunch lengthening, sliding shields were placed within all the QD bellows in the North damping ring. This modification will be repeated in the South ring soon.

Since the introduction of the bellows shields in the North ring more bunch lengthening measurements were performed.[12] We found that the current dependence of the bunch length did not change significantly from the earlier measurements, at least up to currents of 2.8×10^{10}. We also repeated the energy spread

measurements. As mentioned before this measurement can be difficult. For currents greater than 1.5×10^{10} the beam, if left on the screen more than a moment, tended to damage it. Although we are not so confident in this new data, it appears that the turbulent threshold of the ring, at $V_{rf} = 0.8$ MV, has risen from 1.5 to about 1.9×10^{10} since the introduction of the bellows sleeves. We hope to repeat this measurement, and obtain better data, soon.

4. BUNCH LENGTHENING CALCULATIONS

4.1 Introduction

Once we know the Green function wake we can calculate the bunch shape as function of current. All our bunch length calculations are based on the theory of potential well distortion, as formulated by J. Haïssinski.[13] This method has been applied to a pillbox impedance,[14,15] to an rf cavity impedance,[16,17] and to a broad band resonator impedance,[18] to find the steady state shape of a beam in a storage ring. Given the potential well, we can also calculate the amplitude dependence of the tune within the well. E. Keil has performed this calculation for a pillbox impedance.[15]

We begin this chapter by reviewing potential well theory and describing the calculation of the incoherent tune. We follow by describing our method for extending the calculations into the turbulent regime. Then, in order to illustrate different types of behavior, we give the bunch shapes and the tune distributions for a purely inductive, resistive, and capacitive impedance. Finally, we repeat the calculations using the Green function for the damping rings, and compare the results with the measurements.

4.2 Potential Well Distortion[13]

The steady-state phase space distribution in a storage ring $\psi(\epsilon, t)$ is given by the Hamiltonian of the system H:

$$\psi(\epsilon, t) = e^{-H(\epsilon,t)} \quad . \tag{17}$$

For electron machines below the threshold current for turbulence the Hamiltonian is—up to an arbitrary constant—given by

$$H(\epsilon,t) = -\frac{\epsilon^2}{2\sigma_\epsilon^2} - \frac{t^2}{2\sigma_0^2} + \frac{1}{\dot{V}_{rf}\sigma_0^2}\int_0^t V_{ind}(t')\,dt' \quad , \tag{18}$$

with σ_ϵ the energy spread, σ_0 the natural bunch length, $\dot{V}_{rf}$ the slope of the rf voltage at the position of the bunch (we assume the applied rf wave is linear) and V_{ind} the transient induced voltage. In Eq. (18) a smaller value of t signifies an earlier point in time, while $t = 0$ designates the synchronous point for a low current beam.

The induced voltage V_{ind} is given by

$$V_{ind}(t) = -\int_0^\infty W_\delta(t')I(t-t')\,dt' = -\int_0^\infty S(t')\dot{I}(t-t')\,dt' \quad , \tag{19}$$

with $W_\delta(t)$ the longitudinal Green function wakefield, I the current [note: $I = eN\lambda$], and $S(t)$—known as the step function response—the indefinite integral of $W_\delta(t)$. By taking the phase space distribution and integrating out the energy dependence we find the longitudinal charge distribution. Then, by multiplying by the total charge Q [$Q = eN$] we obtain the current:

$$I(t) = K\exp\left(-\frac{t^2}{2\sigma_0^2} + \frac{1}{\dot{V}_{rf}\sigma_0^2}\int_0^\infty S(t')I(t-t')\,dt'\right) \quad , \tag{20}$$

with K a normalization constant. Note that $I(t)$, the unknown, is on both sides of Eq. (20). However, note also that at time t the integral on the right depends only on the current at more negative (earlier) times. Therefore, we can solve for $I(t)$ numerically by beginning far in front of the beam (say at $t = -5\sigma_0$), where we assume the induced voltage is zero, and then proceeding, in small time steps, to the back of the bunch. And then finally, if the area under the newly computed

curve does not equal Q we adjust K, and iterate the whole procedure until it does. Taking the derivative of both sides of Eq. (20) yields an alternative form of it:

$$\frac{\dot{I}}{I} = -\frac{t}{\sigma_0^2} + \frac{V_{ind}}{\dot{V}_{rf}\sigma_0^2} \quad . \tag{21}$$

This form of the problem is more convenient when V_{ind} is given explicitly in terms of I, as is the case for the simple inductive, resistive, and capacitive models that we consider later. Of particular interest to us will be the rms length, the full-width-at-half-maximum, and the centroid shift of the current distribution. The ratio of the first two quantities is a measure of the similarity of the distribution to a Gaussian. Due to energy conservation the third quantity, when multiplied by $-\dot{V}_{rf}$, gives the higher mode losses.

In what follows all distances will be given in terms of σ_0. Thus the independent variable becomes $x = t/\sigma_0$. We will also normalize voltages to $\dot{V}_{rf}\sigma_0$: the induced voltage becomes $v_{ind} = V_{ind}/(\dot{V}_{rf}\sigma_0)$, and the total voltage $v = v_{ind} - x$.

4.3 The Incoherent Synchrotron Tune

Once we know the current shape, we also know the shape of the potential well. For convenience let us choose the bottom of the well to be at zero energy. Then the potential energy is simply given by $u = -\ln(I/\hat{I})$ with $\hat{I}$ the peak of the distribution. Given the shape of the potential well we can numerically solve for the incoherent synchrotron tune.

The equation of motion for a test particle moving in the well is

$$\frac{d^2x}{d\tau^2} - 4\pi^2 v(x) = 0 \quad , \tag{22}$$

with τ the time in units of the low current synchrotron period and v the total voltage. If the test particle has the initial conditions $x = \hat{x}$ and $x' = 0$ then its period of oscillation is given by

$$\mathcal{T} = \frac{1}{\sqrt{2}\pi} \int_{\hat{x}}^{x_c} \frac{dx'}{\sqrt{u(\hat{x}) - u(x')}} \quad . \tag{23}$$

The integration is performed over half a cycle: beginning at $\hat{x}$, we move down the potential well and up the other side until we reach the position x_c for which $u(x_c) = u(\hat{x})$. Note that when $v_{ind} = 0$ $[u(x) = x^2/2]$ then $\mathcal{T} = 1$. The relative incoherent tune ν is simply given by $1/\mathcal{T}$. Note that from Eq. (23) we can find the tune either as function of $\hat{x}$ or as function of energy $h = u(\hat{x})$.

If we know the tune as function of h, then we can also calculate the tune distribution:

$$\lambda_\nu = \sum_{h(\nu)} \frac{\lambda_h}{|d\nu/dh|} = \sum_{h(\nu)} \frac{e^{-h}}{|d\nu/dh|} \quad . \tag{24}$$

The sum in Eq. (24) is there to indicate that if more than one value of h corresponds to a certain value of ν we need to sum the contribution from each correspondence. This will happen when there is an interior extremum of $\nu(h)$. It will also happen when $\nu(h)$ has more than one branch, as will occur when there is a relative maximum in the potential well curve. Note also that Eq. (24) implies that wherever $d\nu/dh = 0$ the distribution is infinite.

4.4 Some Simple Impedance Models

Over a frequency interval the impedance of vacuum chamber elements can often be characterized by a simple electrical circuit element—an inductor, a resistor, or a capacitor. We study in this section the potential well distortion when the whole ring can be characterized by these simple models.

4.4.1 An Inductive Impedance

For a purely inductive impedance the induced voltage is given by $V_{ind} = -L\,dI/dt$, with the constant L the inductance. Bunch lengthening has been observed in many storage rings, and we expect it to be due to an inductive impedance. In the case of the SLC damping rings we have seen that the impedance is dominated by the many inductive vacuum chamber elements. We, therefore, expect the general features of the bunch shape to be given by this model. Note that Haïssinski has presented numerically calculated bunch shapes for this model in Ref. (13).

For a purely inductive impedance Eq. (21) can be written as

$$y' = -\frac{xy}{1+y} \quad , \tag{25}$$

with prime denoting the derivative with respect to $x = t/\sigma_0$. The normalized current is given by $y = LI/(\dot{V}\sigma_0^2)$; the normalized charge Γ (the complete integral of y) equals $LQ/(\dot{V}\sigma_0^3)$. The normalized induced voltage $v_{ind} \equiv V_{ind}/(\dot{V}_{rf}\sigma_0) = -y'$.

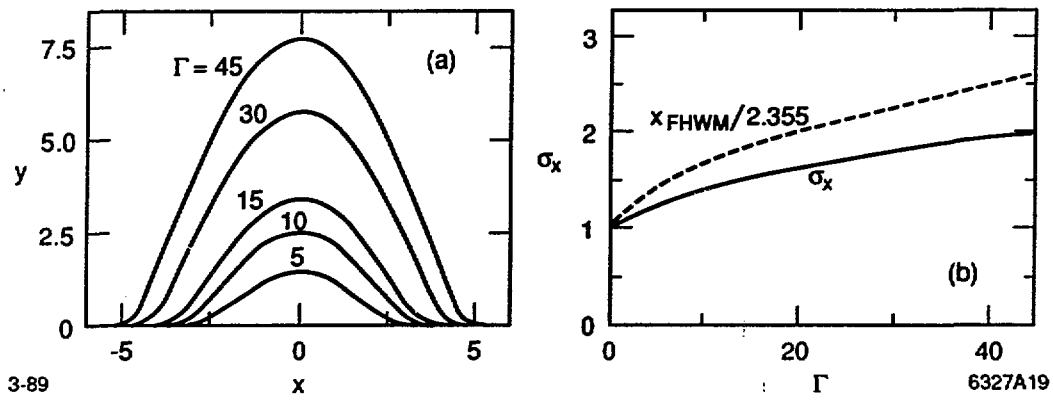

Fig. 20. An inductive impedance: (a) the bunch shape for several values of bunch population and (b) the bunch length variation as a function of current.

The numerical solution of Eq. (25), for several values of Γ, is shown in Fig. 20(a). Note that the charge distribution for a perfect inductor is symmetric about $x = 0$ (since there are no losses) and is more bulbous than a Gaussian distribution. From Eq. (25) it is apparent that the solution is parabolic wherever $y \gg 1$. In Fig. 20(b) we display σ_x and $x_{FWHM}/2.355$ (the dashes) as functions of Γ. Note that for large currents σ_x varies roughly as $\Gamma^{1/3}$. If we apply the inductive model to the SLC damping rings, taking $L = 50$ nH, then an intensity of $\Gamma = 7.5$ corresponds to $N = 1.5 \times 10^{10}$ at $V_{rf} = 0.8$ MV. At this current we see from Fig. 20(b) that $\sigma_x = 1.33$ and $x_{FWHM} = 3.69$. We shall see, in a future section, that these values

approximate the results of the more detailed calculations, calculations that use the Green function wake.

Consider a current of $\Gamma = 7.5$ in an inductive machine. Now suppose a test particle is initially at rest at position $x = \hat{x}$ in the potential well. Figure 21(b) then displays the tune ν as function of $\hat{x}$. Only half of the curve is shown; since the well is symmetric about the origin $\nu(\hat{x}) = \nu(-\hat{x})$. We see that the tune decreases monotonically as $\hat{x}$ approaches zero, and that it is very much depressed at the bottom of the well, to about 60% of its nominal value. On the same plot ν as function of energy $h = u(\hat{x})$ is also shown. We note that the slope of the tune is nonzero for $h = 0$, *i.e.*, at the bottom of the well. In Fig. 21(a) we give the tune distribution λ_ν. [It is plotted sideways so that its connection with $\nu(\hat{x})$ and $\nu(h)$ is easier to see.] We note that the peak of the distribution is at the tune minimum, that the tune at the peak is greatly depressed, and that the distribution is broad.

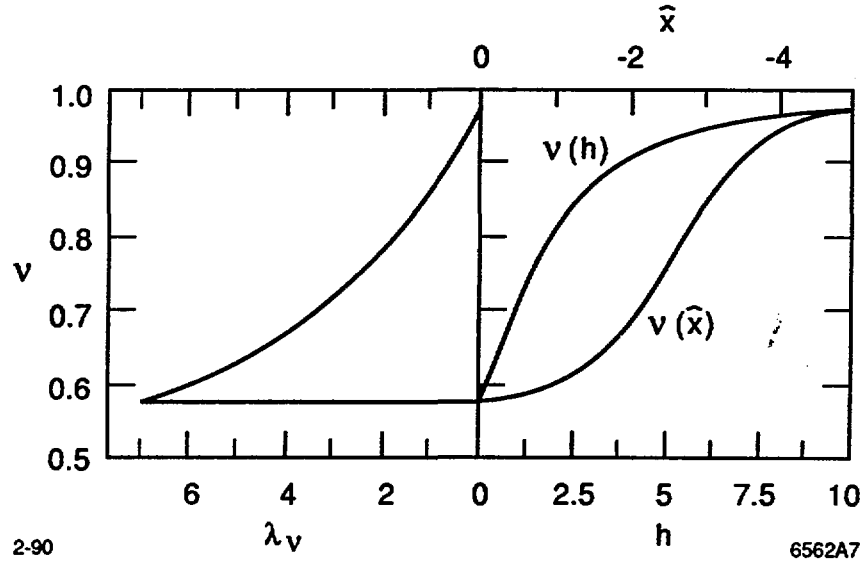

Fig. 21. (a) The tune distribution and (b) the dependence of tune on $\hat{x}$ and h when $\Gamma = 7.5$ for an inductive impedance.

Let us use the following notation: let ν_x denote the tune above the fraction of the beam given by x. Thus $\nu_{.50}$ gives the median value of the tune. Then Fig. 22

displays as functions of current the tune at the peak of the tune distribution ν_0, as well as $\nu_{.25}$, $\nu_{.50}$, $\nu_{.75}$, and $\nu_{.95}$. We see that ν_0 drops most quickly at the low end of the current scale, and levels off at the high end. Note that for $\Gamma > 0.5$ the curve for ν_0 in Fig. 22 can be approximated by $1-0.15(1+\ln\Gamma)$. We can estimate the low amplitude tune shift $\Delta\nu_0$ at low currents by assuming the bunch remains Gaussian and that $-y''(0)$ is small compared to 1. Then $\Delta\nu_0 \approx y''(0)/2 \approx -\Gamma/(2\sqrt{2\pi}) \approx -0.2\Gamma$. The quantity $1-0.2\Gamma$ is given by the dotted curve in Fig. 22. We note that it only approximates ν_0 for very low currents. At $\Gamma = 0.5$ it already deviates from the exact calculation by 30%. For the damping ring this current corresponds to a bunch population of only 10^9.

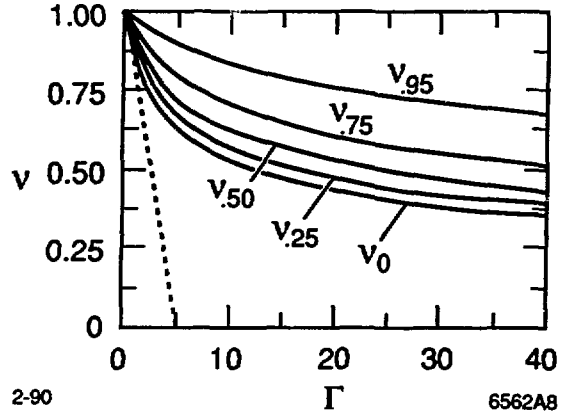

Fig. 22. The current dependence of the characterizing parameters of the tune distribution ν_0, $\nu_{.25}$, $\nu_{.50}$, $\nu_{.75}$, and $\nu_{.95}$, for an inductive impedance.

4.4.2 A Resistive Impedance

For an ideal resistive impedance the induced voltage can be written as $V_{ind} = -IR$, with the constant R the resistance. This model is applicable to electron rings that don't have many inductive elements, and whose impedance is dominated by the rf and other large cavities. In storage rings where the builders have been very careful to avoid transitions and bellows we would expect the impedance to be resistive.

For an ideal resistive impedance Eq. (21) becomes

$$y' = -(x+y)y \quad , \tag{26}$$

with $y = RI/(\dot{V}\sigma_0)$ and $\Gamma = RQ/(\dot{V}\sigma_0^2)$. Note that $v_{ind} = -y$. The analytic solution to Eq. (26) was found by A. Ruggiero[19]:

$$y = \sqrt{\frac{2}{\pi}} \frac{e^{-x^2/2}}{\coth(\Gamma/2) + \mathrm{erf}(x/\sqrt{2})} \quad , \tag{27}$$

with $\mathrm{erf}(x)$ the error function.

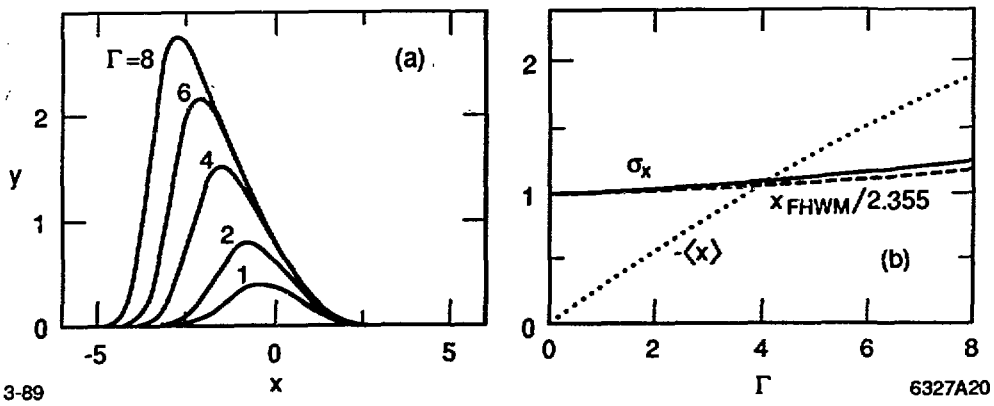

Fig. 23. A resistive impedance: (a) the bunch shape for several values of total charge and (b) the change of bunch length and centroid position (dots) with current.

The solution, Eq. (27), for several values of current is displayed in Fig. 23(a). As Γ is increased the bunch tilts forward (up the rf wave) by an ever increasing amount, in order to compensate for the increased higher mode losses. Figure 23(b) gives σ_x and $x_{FWHM}/2.355$ (the dashes). We see that the bunch length increases only very slowly in a resistive machine. The dots give the centroid shift $\langle x \rangle$ of the bunch. It can be approximated by $\langle x \rangle = -\Gamma/(2\sqrt{\pi})$, which is the centroid shift assuming that the bunch shape does not change with Γ.

Suppose we could remove all the impedance of the SLC damping rings except that of the rf cavities. As we saw before, we could approximate what was left by a resistive impedance with $R = 411\ \Omega$. A bunch population of 5×10^{10} in this ideal machine, when $V_{rf} = 0.8$ MV, corresponds to $\Gamma = 3.4$. For this current Fig. 24(b) displays the tune as function of the maximum extent of oscillation $\hat{x}$, for $\hat{x}$ more negative than the position of the bottom of the potential well. We see that for both low and very high amplitude oscillations the tune is not changed. For amplitudes in between these two extremes, however, the tune is depressed, but by a very small amount. Also shown on the plot is the tune as function of energy $\nu(h)$.

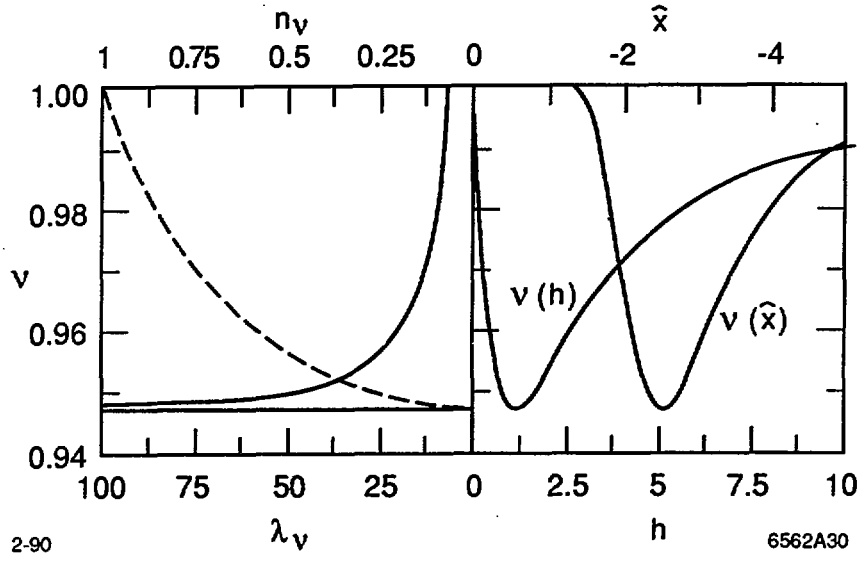

Fig. 24. (a) The tune distribution and its integral (dashes) and (b) the dependence of tune on $\hat{x}$ and h when $\Gamma = 3.4$ for a resistive impedance.

In Fig. 24(a) we show the tune distribution λ_ν. Note that there is an infinite spike at the lowest tune value. The dashed curve in the figure gives the integral of the tune distribution n_ν. We note that 50% of the particles have tunes in the lowest 20% of the tune range. In Fig. 25 we give as function of current the parameter ν_0, $\nu_{.25}$, $\nu_{.50}$, $\nu_{.75}$, and $\nu_{.95}$ that charactrize the tune distribution.

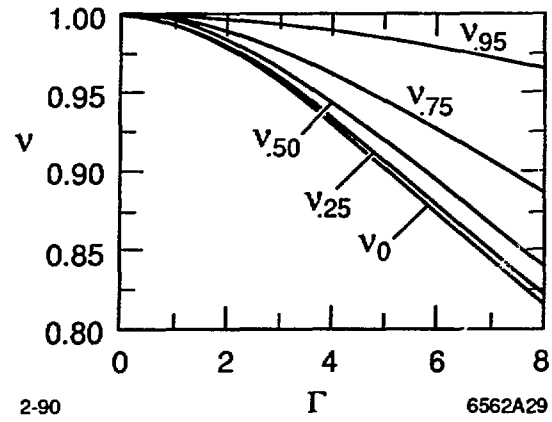

Fig. 25. The current dependence of ν_0, $\nu_{.25}$, $\nu_{.50}$, $\nu_{.75}$, and $\nu_{.95}$ for a resistive impedance.

4.4.3 A Capacitive Impedance

For an ideal capacitive impedance the induced voltage is proportional to the integral of the current, with constant of proportionality $-1/C$, and C the capacitance. Deep cavities, such as the rf cavities, are slightly capacitive at normal bunch lengths, and become more capacitive for very short bunches. Of the three simple models the capacitive is probably the least applicable to the types of impedances one finds in storage rings. We note that bunch shortening has not been observed in storage rings, except possibly at low currents in SPEAR, when the ring had many rf cavities.[20]

For a purely capacitive impedance Eq. (21) becomes

$$y' = -y[x + \int_{-\infty}^{x} y(x')\,dx'] \quad , \tag{28}$$

with $y = I/(\dot{V}_{rf}C)$ and $\Gamma = Q/(\dot{V}_{rf}\sigma_0 C)$. The solution to Eq. (28) closely approximates a Gaussian that has been shortened and shifted. Since the energy stored in a capacitor is $Q^2/2C$, the centroid shift is given by $\langle x \rangle = -\Gamma/2$. Figure 26 shows the bunch length dependence on Γ. By substituting a Gaussian into Eq. (28) we

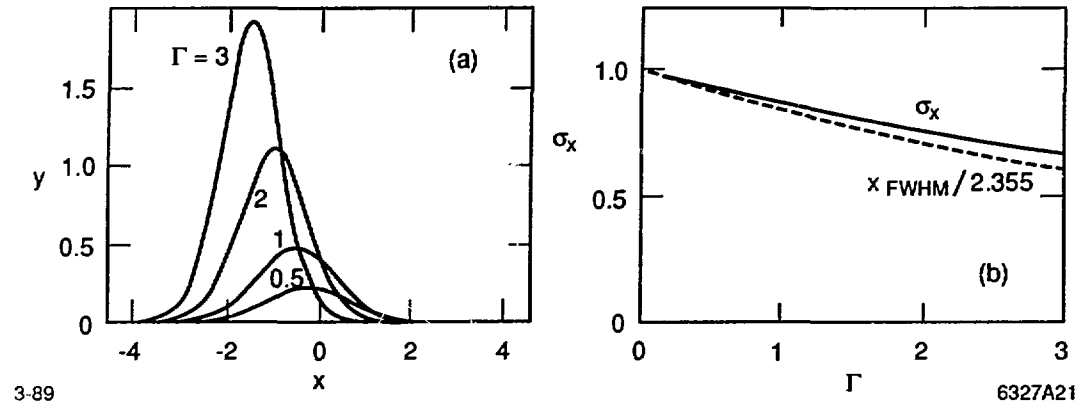

Fig. 26. (a) The bunch shape for various currents and (b) bunch shortening as a function of current, for a capacitive impedance.

can arrive at an analytical approximation of the bunch shortening, which for small current becomes $\sigma_x \approx 1 - \Gamma/\sqrt{8\pi}$.

In a capacitive machine the bunch becomes shorter and the tune of all the particles will rise. As was the case for the inductive machine the tune as function of energy is monotonic. The low amplitude particles have the highest tune. Their tune shift can be approximated by $\Delta\nu \approx 1/\sigma_x \approx \Gamma/\sqrt{8\pi} \approx 0.2\Gamma$.

4.5 The Turbulent Regime

4.5.1 Calculations Beyond Threshold

Beyond some threshold current the energy spread begins to increase, and we enter what is known as the turbulent regime. At the moment, there is, unfortunately, still no reliable calculation of the behavior of short bunches in this regime. However, for a formalism that at least in theory can be used to solve the problem see, for example, J. M. Wang and C. Pellegrini.[21]

In the case of SLC damping rings, however, we will use a simpler method. We believe that the instability that we find in the damping rings is a fast instability of the microwave type, and we expect the potential well approach to calculating the bunch shape still to be applicable. As threshold current we take the value

given by the measurements. To find the bunch shape beyond this current we (i) scale the energy spread according to the Boussard criterion (see below), and then (ii) perform the normal potential well calculation but replacing σ_0 in Eq. (20) by $\sigma_0' = \sigma_0 \sigma_\epsilon / \sigma_{\epsilon_0}$, with σ_{ϵ_0} the nominal energy spread. Implicit in our method is the assumption that the energy distribution remains Gaussian.

4.5.2 The Boussard Criterion

The Boussard criterion is often used to estimate the threshold for instability. Boussard[22] conjectured that the longitudinal instability in a bunched beam is due to a coasting-beam-like instability within the bunch. Then in estimating the threshold for instability one might use the coasting beam threshold[23] but replacing I by $\hat{I}$ the peak current. The issue of the applicability of a coasting beam instability criterion to a bunched beam was studied in detail by J. M. Wang and C. Pellegrini.[21] They found that one obtains a coasting-beam-like instability condition provided that: (i) the impedance is broad band relative to the bunch spectrum, (ii) the growth rate is much greater than the synchrotron frequency, and (iii) the instability occurs at wavelengths much shorter than the bunch length.

Their threshold condition looks like a coasting beam threshold condition[21]:

$$\frac{e\hat{I}|Z(n)/n|}{2\pi\alpha E\sigma_\epsilon^2} \leq 1 \quad , \tag{29}$$

with Z the broad band (or smoothed) impedance and $n = \omega_1/\omega_0$, with ω_1 a representative frequency sampled by the bunch spectrum and ω_0 the revolution frequency; with α the momentum compaction factor and E the beam energy. Equation (29) is a stability condition, *i.e.*, a condition for no fast blow-up. In our calculations we will take as threshold the measured value, and use Eq. (29) solely for scaling the energy spread in the turbulent regime.

In Eq. (29) both $\hat{I}$ and Z/n in general depend on bunch length which, in turn, depends on the energy spread. Consider, for example, a very resistive impedance where $Z = R$ the resistance. As typical frequency $n\omega_0$ we might take the inverse

bunch length. Then since $\hat{I}$ is also proportional to the inverse bunch length we find that Eq. (29) implies that, above turbulence, $\sigma_\epsilon \sim N^{1/2}$, with N the bunch population, for a resistive machine. On the other hand, for a very inductive machine, such as the SLC damping rings, $|Z/n|$ is approximately constant. If we substitute the peak current for a Gaussian beam in Eq. (29), and note that the bunch length is proportional to the energy spread, we see that, above threshold,

$$\sigma_\epsilon = \sigma_{\epsilon_0} \left(\frac{N}{N_{th}} \right)^{1/3} \qquad (N > N_{th}) \quad , \tag{30}$$

with N_{th} the threshold current. This is the scaling we will use for calculating the damping ring bunch shapes in the turbulent regime.

We make two observations: (1) This scaling is roughly supported by the measurement results discussed in Chapter 3. (2) For an inductive machine the bunch length increases with current due to potential well distortion, and thus the growth of the peak current with current is somewhat reduced. To be more consistent we could have included this fact in determining the scaling of energy spread with current. For the purely inductive impedance discussed earlier we find that the peak current increases approximately as $N^{0.8}$, rather than as simply N, due to potential well distortion. Thus, for the damping rings we would expect σ_ϵ to vary as $N^{0.27}$ rather than as $N^{1/3}$ above threshold. And this modification, in turn, would result in a slight reduction in the calculated bunch lengths at the higher currents. For the results to be presented, however, the difference would not be significant.

4.5.3 Another Threshold Criterion

P. B. Wilson[24] has suggested that one threshold criterion might be that the slope of the total voltage v' becomes zero (or equivalently $u'' = 0$) somewhere within the bunch. This criterion has also been studied by G. Besnier,[18] who has used it to predict turbulent bunch lengthening for ESRF, the European light source. It is easy to show that if we assume a purely inductive impedance, and we also assume that the bunch shape remains Gaussian, then Wilson's criterion is equivalent to

the Boussard criterion. We can also show that this condition can never be met for the models of a purely inductive, resistive, or capacitive impedance. For it to be met requires some high frequency structure in the impedance curve (as is the case, for example, for the broad band resonator model with a high frequency resonance). Note that if Wilson's conjecture ($u'' = 0$) is met at the bottom of the potential well, then the tune becomes zero for small amplitudes. If, however, $u'' = 0$ is first met at another position within the bunch, as we will see in our potential well calculations using the damping ring Green function, then the physical significance of the conjecture is not so clear.

Wilson's conjecture suggests another, more stringent threshold condition with a simple physical interpretation. Consider as threshold criterion that there be a relative maximum in the potential well shape, *i.e.*, $u' = 0$, $u'' < 0$, somewhere within the bunch. If this condition is met then there will be two stable fixed points within the bunch and one unstable fixed point at the position of the maximum. Consequently, a subset of bunch particles will oscillate about a relative minimum of the potential well, rather than about the absolute minimum. Note that this is a more stringent condition than Wilson's and will tend to be met at higher currents than his condition. Finally, we should stress that both these threshold criteria are merely conjectures. Their validities need to be demonstrated in a self consistent manner.

4.6 Bunch Lengthening in the SLC Damping Rings

4.6.1 The Bunch Shape

Using our pseudo-Green function (see Fig. 14) in the potential well equation, Eq. (20), we have calculated bunch shapes for many values of current, for a ring voltage $V_{rf} = 0.8$ MV. Figure 27(a) displays the rms length σ_x and $x_{FWHM}/2.355$, and Fig. 27(b) gives the centroid shift $\langle x \rangle$ of the calculated distributions as functions of current. Length dimensions are again given in units of σ_0 (at this rf voltage $c\sigma_0 = 4.95$ mm). In Chapter 3 we saw that the measured threshold at this rf voltage was $N_{th} = 1.5 \times 10^{10}$. Taking this as our threshold, we extended the po-

tential well calculations into the turbulent regime by simply scaling the parameter σ_0 as $(N/N_{th})^{1/3}$, as was discussed earlier. (The turbulent regime is indicated by the dashed lines in the figure.) Superimposed on the curves are the measurement results presented in Chapter 3.

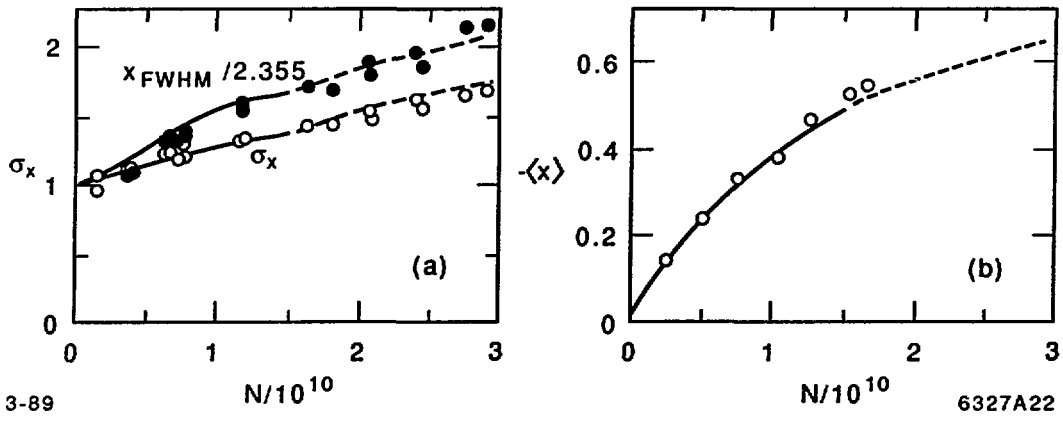

Fig. 27. (a) Bunch lengthening and (b) the centroid shift calculated for the SLC damping rings at $V_{rf} = 0.8$ MV. The symbols indicate the measurement results.

As we saw for the simple inductive model the current distributions calculated for the damping rings are more bulbous than a Gaussian. At $N = 1.5 \times 10^{10}$, we see that $\sigma_x = 1.38$ and and $x_{FWHM} = 3.93$. These values compare well with those obtained assuming a purely inductive machine with $L = 50$ nH, for which we found $\sigma_x = 1.33$ and and $x_{FWHM} = 3.69$. The turbulent threshold is seen as a slight kink in the curves. Beyond this point σ_x varies roughly as $N^{1/3}$. We see that at $N = 3 \times 10^{10}$ the rms bunch length is increased by 70%. From Fig. 27(b) we see that the calculations give a significant amount of higher mode losses. At $N = 1.5 \times 10^{10}$ the centroid shift $\langle x \rangle = -0.5$ is equivalent to a higher mode loss of 30 keV; at 3×10^{10} the loss is 38 keV. For both the bunch length and the centroid shift the calculations agree well with the measurements.

In Fig. 28 we present the bunch shapes for bunch populations of $N = 0.7$, 1.2, 2.1, and 2.9×10^{10}. The abscissas give $x = t/\sigma_0$, the ordinates are $y = IZ_0/(\dot{V}\sigma_0)$

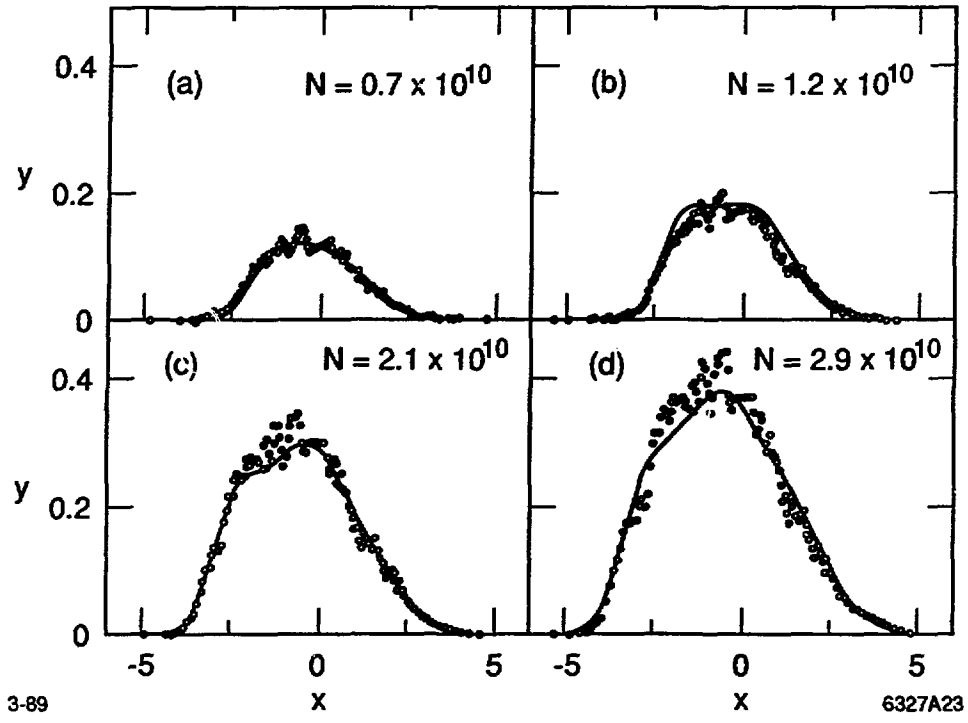

Fig. 28. The calculated damping ring bunch shapes for several current values, when $V_{rf} = 0.8$ MV. Superimposed on the curves are the measurement results.

with $Z_0 = 377\ \Omega$. Superimposed on the curves are the digitized measurement results. The fluctuations in the data (especially at the peaks) are due to nonuniformity in the response of the screen. Considering that there are no fit parameters, the agreement between the data and the calculations is very good. Finally, in Fig. 29 we show the induced voltage v_{ind} and the total voltage v calculated for these same four currents.

4.6.2 The Incoherent Tune

For the following calculations let us consider the current $N = 1.5 \times 10^{10}$ at $V_{rf} = 0.8$ MV in the damping rings. Suppose we begin a test particle at rest at position $x = \hat{x}$ in the distorted potential well. Then subsequent oscillations

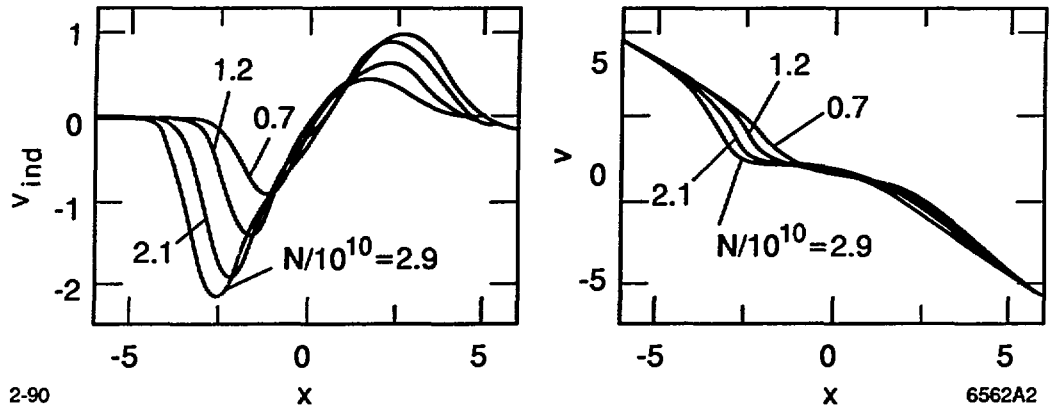

Fig. 29. (a) The induced voltage v_{ind} and (b) the total voltage $v = v_{ind} - x$ when $N = 0.7$, 1.2, 2.1, and 2.9×10^{10} and $V_{rf} = 0.8$ MV.

within the well are shown in Fig. 30(b), for the cases $\hat{x} = -2, -1, 0, 1$, and 2. The horizontal axis is the time in units of the nominal synchrotron period. We see quite a variation in oscillation period. The potential well itself is shown in Fig. 30(a); the dashes give the well of the rf alone. Note that $u = 0$, the bottom of the well, is at $x = -0.24$. Note also that the bottom of the well is not just broadened and that there is an inflection point ($u'' = 0$) away from the bottom.

For the same current we display, in Fig. 31(b), $\nu(\hat{x})$, for $\hat{x}$ more negative than the position of the bottom of the well. We see that, as with a simple inductive impedance, there is a great tune depression within the bunch. We also note that, as with a simple resistive impedance, the curve has a minimum within the distribution; at the minimum $\nu = 0.18$. In the same frame we display $\nu(h)$. [Although h values up to 10 were included in the calculation, we only show the very beginning of the h range, in order that the dip in $\nu(h)$, near $h = 0.1$, can be seen.] At $h = 0$ the tune is 0.66. In Fig. 31(a) we show the tune distribution. We see that it is broad, centered about $\nu = 0.7$ with a full-width-at-half-maximum of 0.24. Also visible in the plot is a spike, at $\nu = 0.18$, containing very few particle.

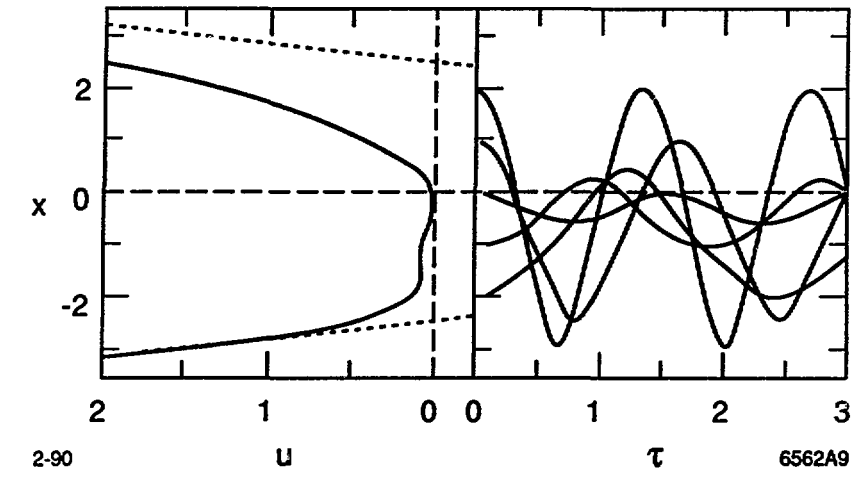

Fig. 30. (a) The potential well and (b) five oscillations within the well when $N = 1.5 \times 10^{10}$ and $V_{rf} = 0.8$ MV.

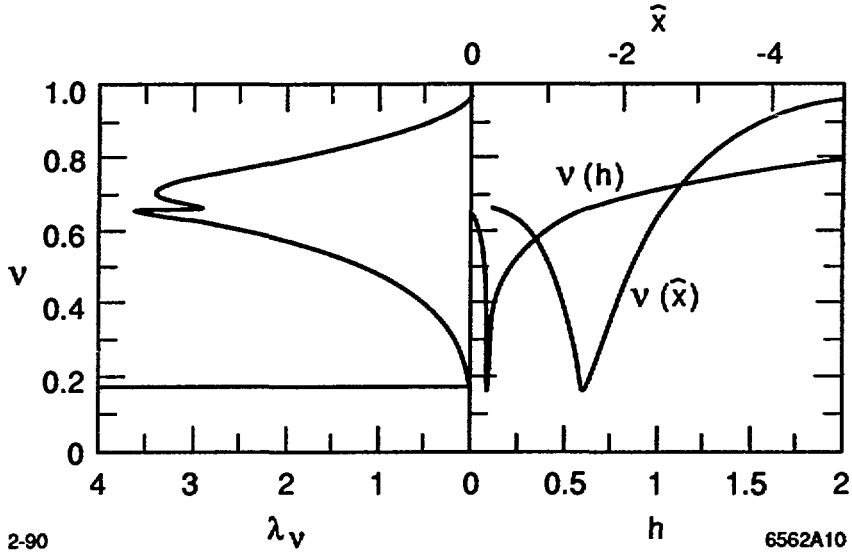

Fig. 31. (a) The tune distribution and (b) the dependence of tune on $\hat{x}$ and h when $N = 1.5 \times 10^{10}$ and $V_{rf} = 0.8$ MV.

In Fig. 32 we characterize the current dependence of the tune distribution by five parameters: $\nu_{.05}$, $\nu_{.25}$, $\nu_{.50}$, $\nu_{.75}$, and $\nu_{.95}$ which signify, respectively, the tune above the first 5%, 25%, 50%, 75%, and 95% of the particles. The region

with dashed curves is the turbulent regime. We see that the tune spread is quite large beyond 5×10^9. If we look, for the moment, at the the curve representing the median tune $\nu_{.50}$, we note that it drops most quickly at the beginning of the range, for currents up to 5×10^9 and then begins to level off. This general behavior was observed for the quadrupole tune measurements discussed in Chapter 3. In absolute terms, however, the 25% shift shown here at 5×10^9 does not agree with the 3 to 4% shift given by the measurements. We believe that this discrepancy signifies that the connection between the coherent quadrupole tune and the incoherent tune of a machine with a broad tune distribution is not so simple.

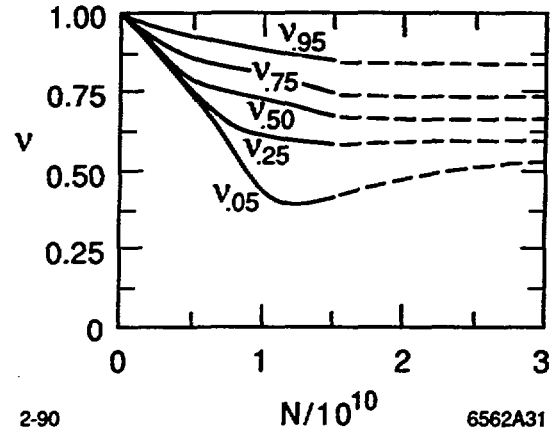

Fig. 32. The current dependence of $\nu_{.05}$, $\nu_{.25}$, $\nu_{.50}$, $\nu_{.75}$, and $\nu_{.95}$ as calculated for the damping rings when $V_{rf} = 0.8$ MV.

5. CONCLUSIONS

The study of bunch lengthening in the SLC damping rings, described in this paper, can be divided into three parts: the impedance calculations, the bunch length measurements, and the bunch length calculations.

In the paper's first part we described the vacuum chamber geometry of the damping rings. We introduced a figure of merit for bunch lengthening, the effective inductance ℓ. We found that the ring impedance is dominated by many small,

inductive discontinuities—such as bellows, shallow transition, and masks. There are so many objects that contribute to the total inductance, that if we want to reduce bunch lengthening, we basically need to rebuild the entire vacuum chamber. We ended this part of the paper by computing the wakefield of a very short bunch passing through the entire damping ring, a function that can be used as Green function for the bunch length calculations.

In the paper's second part we described measurements of energy spread, synchronous phase shift, and longitudinal quadrupole tune shift with current that were performed on the SLC North damping ring. We saw that by taking advantage of the unique hardware features found in the SLC it is possible to measure the bunch shape of individual damping ring pulses to good resolution. We found a large amount of bunch lengthening at higher currents; at an rf voltage of $V_{rf} = 0.8$ MV and bunch population $N = 3 \times 10^{10}$ the rms bunch length was doubled. From energy spread measurements we found the threshold current—at the same rf voltage—was 1.5×10^{10}.

In the paper's final part we described bunch length calculations that are based on the theory of potential well distortion. We saw, for example, that an inductive machine has lots of bunch lengthening, a resisitive machine little. We saw that in an inductive machine the incoherent tune shift and the tune spread are both large, in a resistive machine they are small. In this chapter we also described a method of extending the potential well calculations into the turbulent regime, once the threshold current for turbulence is known. Then taking the measured threshold value, and using the Green function discussed above, we calulated bunch shapes as function of current. When these shapes were compared with the measured shapes we found excellent agreement. Then finally we computed the tune distribution we expect for the damping rings. As for a purely inductive impedance at higher currents we found the tunes depressed, with the average tune shift large and the tune spread broad.

ACKNOWLEDGMENTS

Credit for the measurements described in Chapter 3 goes to the SLC Damping Rings Commissioning Group, of which the author was but one member. Also, aside from the tune shift calculations, Chapter 4 is based on work that was done with R. Ruth. In addition, the author has profited from discussions with R. Ruth, M. Sands, R. Warnock, T. Weiland, and P. B. Wilson.

REFERENCES

1. L. Rivkin *et al.,* Proc. of the 1st European Particle Acc. Conf., Rome, 1988, p. 634.
2. K. Bane, Proc. of the 1st European Particle Acc. Conf., Rome, 1988, p. 637.
3. K. Bane and R. Ruth, Proc. of the 1989 IEEE Particle Acc. Conf., Chicago, 1989, p. 789.
4. T. Weiland, DESY **82**–015 (1982) and *Nucl. Inst. Meth.* **212**, 13 (1983).
5. K. Bane *et al.,* Proc. of the 1st European Particle Acc. Conf., Rome, 1988, p. 878.
6. K. Bane, in *Physics of High Energy Particle Accelerators,* AIP Conf. Proc. No. 153 (Am. Inst. of Physics, New York, 1987), p. 978.
7. E. Keil and B. Zotter, *Particle Accelerators* **3**, 11 (1972).
8. F. Sacherer, CERN Report 77–13, 198 (1977).
9. R. Klatt and T. Weiland, 1986 Linear Accelerator Conference Proceedings, SLAC, p. 282.
10. M. Ross, private communication.
11. L. Rivken *et al., IEEE Trans. Nucl. Sci.* **NS–32**, No. 5, 2628 (1985).
12. K. Bane, L. Rivken, and R. Ruth, measurements taken on Nov. 1988 (not published).
13. J. Haïssinski, *Il Nuovo Cimento* **18B**, No. 1, 72 (1973).
14. A. Papiernik, M. Chatard-Moulin, and B. Jecko, Proc. of the 9th Int. Conf. on High-Energy Acc., SLAC, 1974, p. 375.
15. E. Keil, PEP Note 126, SLAC (1975).
16. K. Bane and P. B. Wilson *et al., IEEE Trans. Nucl. Sci.* **NS–24**, 1485 (1977).

17. K. Nakajima *et al.*, Proc. of the 1st European Particle Acc. Conf., Rome, 1988, p. 570.

18. G. Besnier, "Etude de la Stabilité d'un Paquet Intense dans l'Anneau ESRF: Effets Longitudinaux," Laboratoire Théorie des Systèmes Physiques, Université de Rennes I (1987).

19. A. Ruggiero *et al., IEEE Trans. Nucl. Sci.* **NS–24**, No. 3, 1205 (1977).

20. P. B. Wilson *et al., IEEE Trans. Nucl. Sci.* **NS–24**, No. 3, 1211 (1977).

21. J. M. Wang and C. Pellegrini, Proc. of the 11th Int. Conf. on High-Energy Acc., CERN, 1980, p. 554.

22. D. Boussard, CERN LABII/RF/INT/75–2 (1975).

23. V. K. Neil and A. N. Sessler, *Rev. Sci. Instr.*, **36**, 429 (1965).

24. P. B. Wilson, private communication.

Status of Impedance Measurements for the SPring-8 Storage Ring

T. Yoshiyuke and S.H. Be

RIKEN-JAERI

Synchrotron Radiation Facility Design Team

Argonne National Laboratory
Advanced Photon Source
Impedance and Bunch Instability Workshop
October 31 - November 1, 1989

Abstract

The coupling impedance of vacuum chamber components is estimated for the SPring-8 storage ring. Three different approaches are discussed; analytical calculation, numerical simulation, and measurement. The simulation shows that the contribution to the impedance is mainly attributed to RF cavities, bellows, flanges, and transitions to ID chambers. Loss parameters of an RF cavity are also measured by using the coaxial wire method.

Motivation of impedance estimate

Before a quantitative estimation of the impedance, we must get a reasonable idea on how much it can be allowed. The allowable impedance |Z/n| is , in a classical stability criterion, described by

$$\left|\frac{Z}{n}\right| \leq \frac{\alpha E}{e I_P}\left(\frac{\Delta E}{E}\right)^2 \quad ,$$

where α is the momentum compaction factor, E the total particle energy, $\Delta E/E$ the FWHM of relative energy distribution, and I_P the peak current defined by

$$I_P = I_{AV}\frac{2\pi R}{3 M \sigma_l} \quad .$$

I_{AV} is the average current in M bunches, σ_l the rms bunch length, and $2\pi R$ the circumference of the ring. n is the ratio of storage ring circumference to the wavelength of perturbation traveling around the bunch. For our storage ring; E = 8 GeV, $\alpha = 1.5 \times 10^{-4}$, $\Delta E/E = 3 \times 10^{-3}$, $I_{AV} = 100$ mA, $2\pi R = 1{,}436$ m, M = 1000, and $\sigma_l = 3.2$ mm, therefore $|Z/n| < 0.7\ \Omega$. This quantity is relatively small compared with the other rings, indicating that the impedance problem is more serious in our ring.

Estimate of Impedance

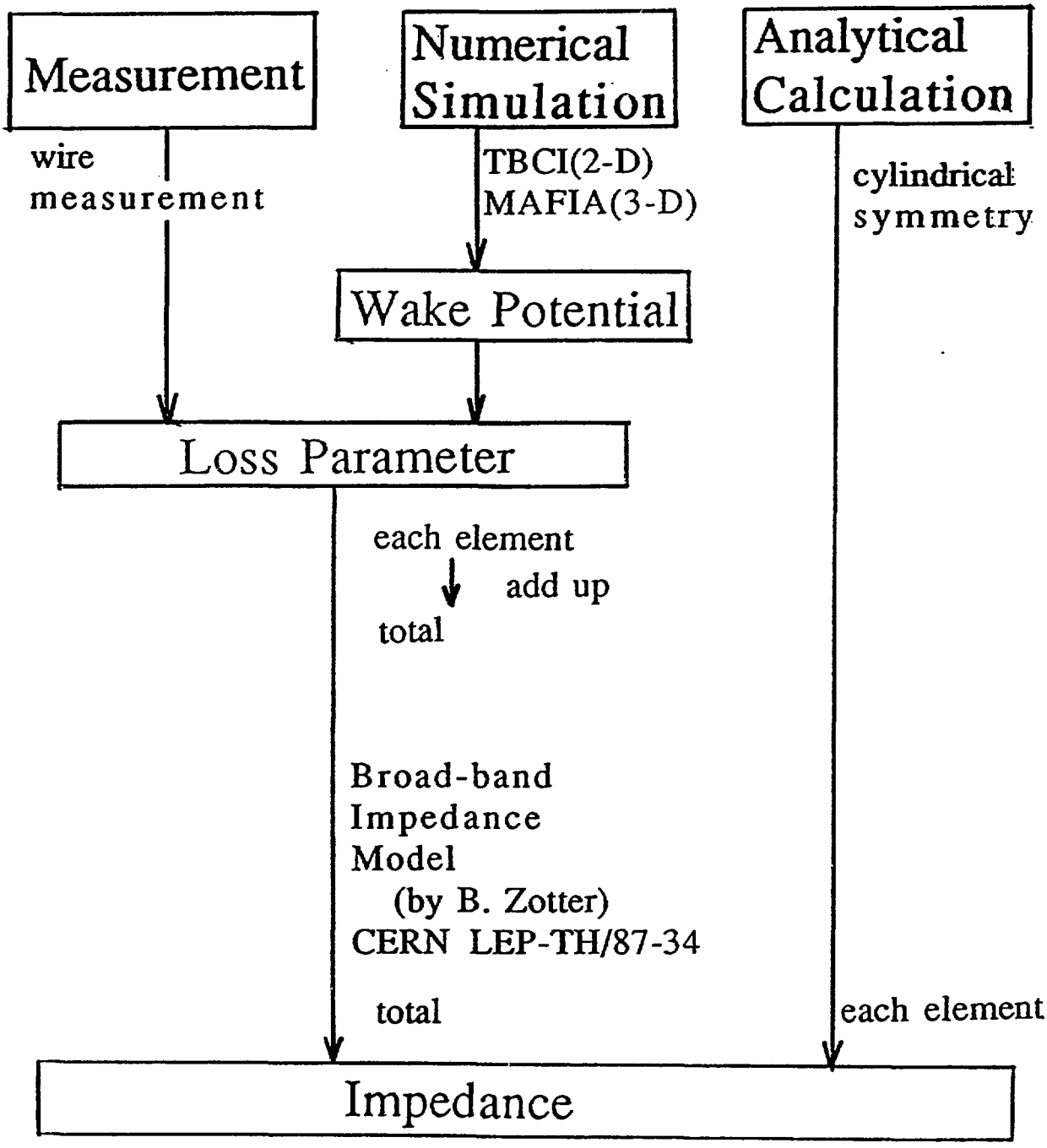

Fig. Flow diagram for estimation of impedance.

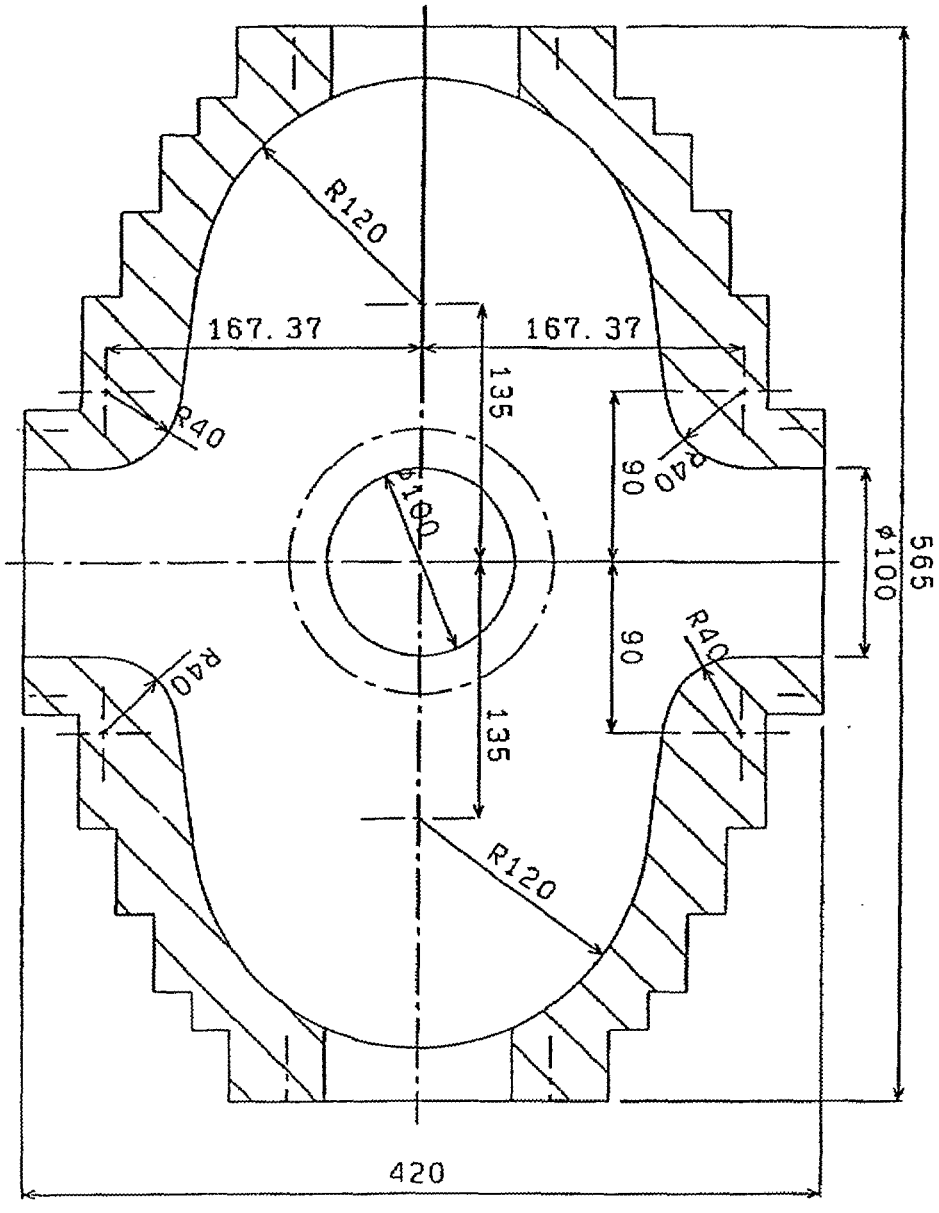

Fig. Single-cell cavity without nose cones, which is under design as a low HOM-impedance cavity for our storage ring.

We calculate loss parameters of this type of cavity by using TBCI.

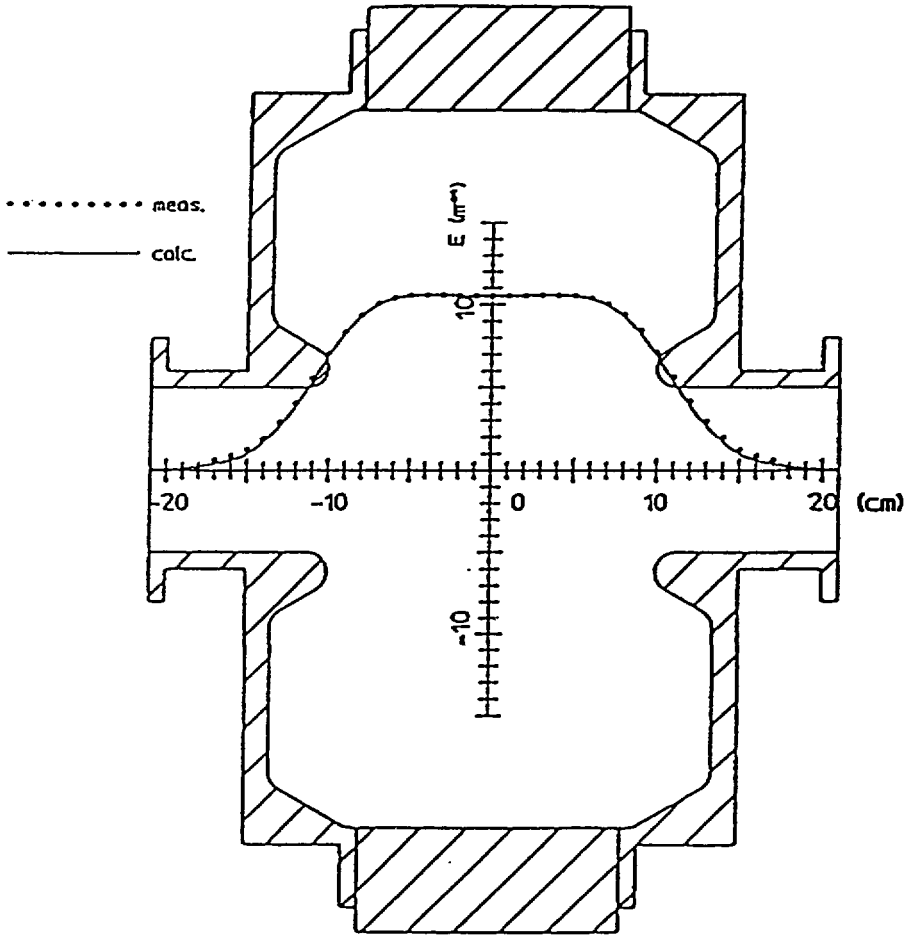

TM010 mode

Fig. Single-cell cavity with nose cones.

We calculate loss parameters of this type of cavity by using TBCI to compare with the cavity without nose cones.

We also measure loss parameters of this type of cavity.

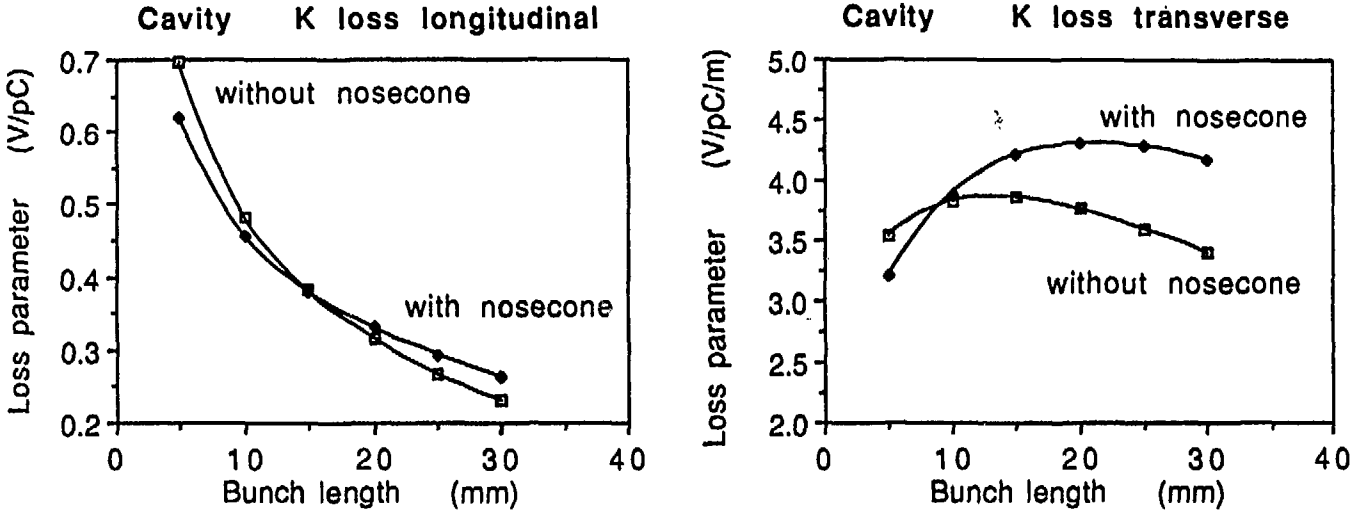

Fig. Loss parameters for cavities both with and without nose cones; (a) longitudinal case, (b) transverse case.

The HOM impedances which exert a harmful effect on a beam are suppressed in the cavity without nose cones, but other HOM impedances seem to become larger than we expected, especially above cut-off frequency.

Calculation geometry

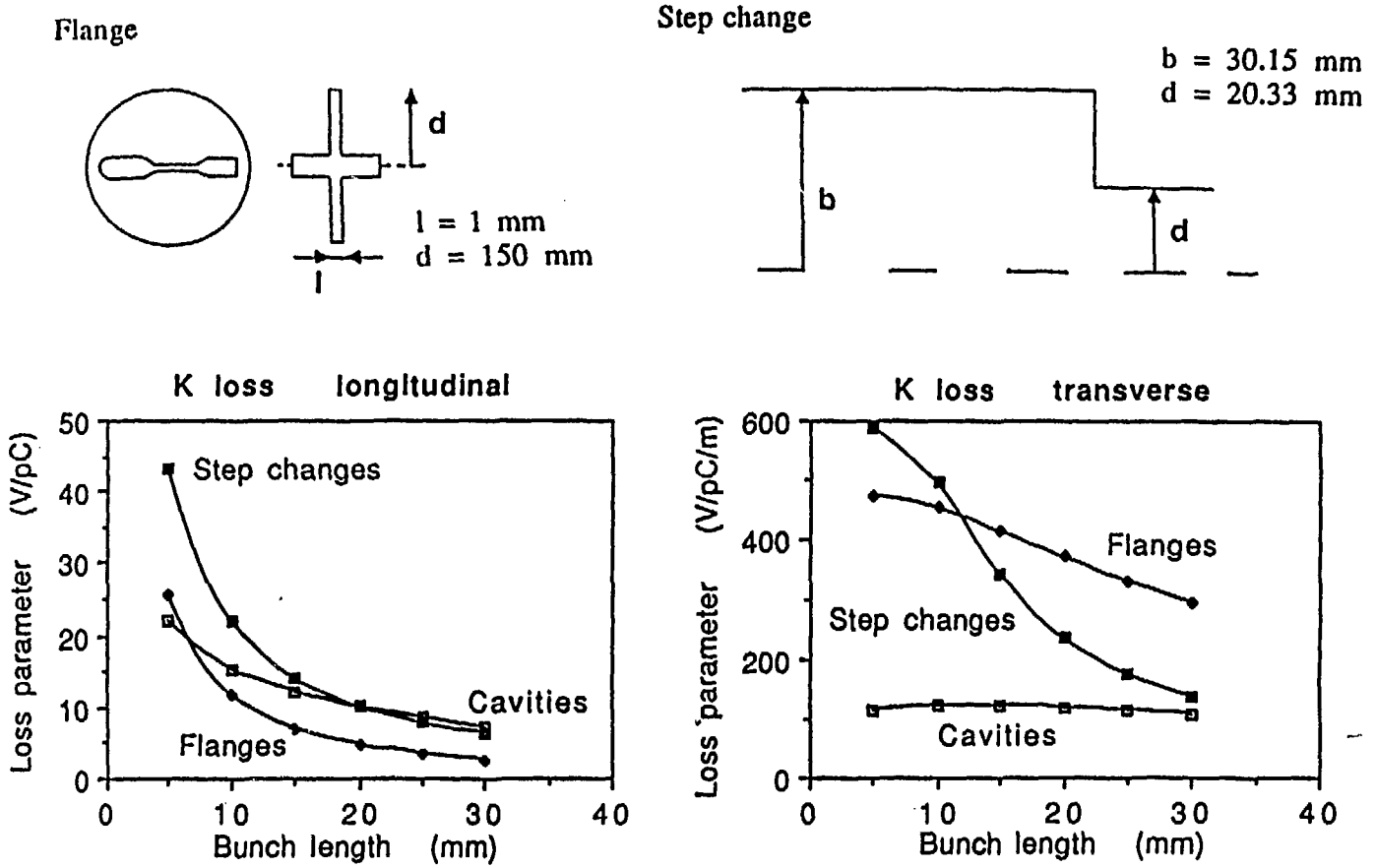

Fig. Total loss parameters of the whole ring for typical components; (a) longitudinal case, (b) transverse case.

Cavities x 32
Flanges x 912
Step changes x 96

It turns out that, in a longitudinal case, step changes give a large effect on the impedance, and the step changes and flanges do in a transverse case. As far as the step changes are concerned, however, as the transitions to ID chambers consists of tapered parts, the loss parameters are, in fact, reduced further. Bellows themselves have large effect on the impedance, but the loss parameters are steeply

Method

coaxial wire technique, in the time domain.
(PEP-95; M. Sands, J. Rees)

the comparison between the pulses transmitted through the vacuum chamber to be tested and the reference chamber gives the wake potential:

$$W_{//} = 2 Z_0 \left(i_0(t) - i_m(t) \right)$$

and longitudinal loss parameter:

$$k_{//} = \frac{2 Z_0 \int i_0(t) \left(i_0(t) - i_m(t) \right) dt}{\left[\int i_0(t)\, dt \right]^2}$$

where Z0 is the characteristic impedance of the reference line.

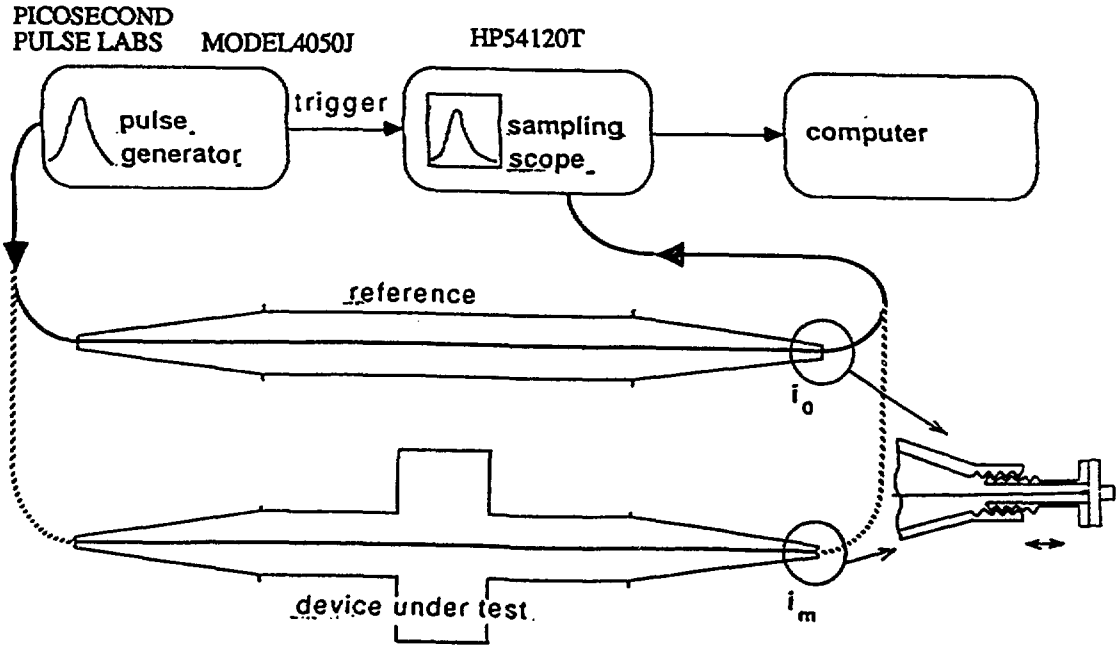

Fig. Set-up for the measurement of the loss parameter.

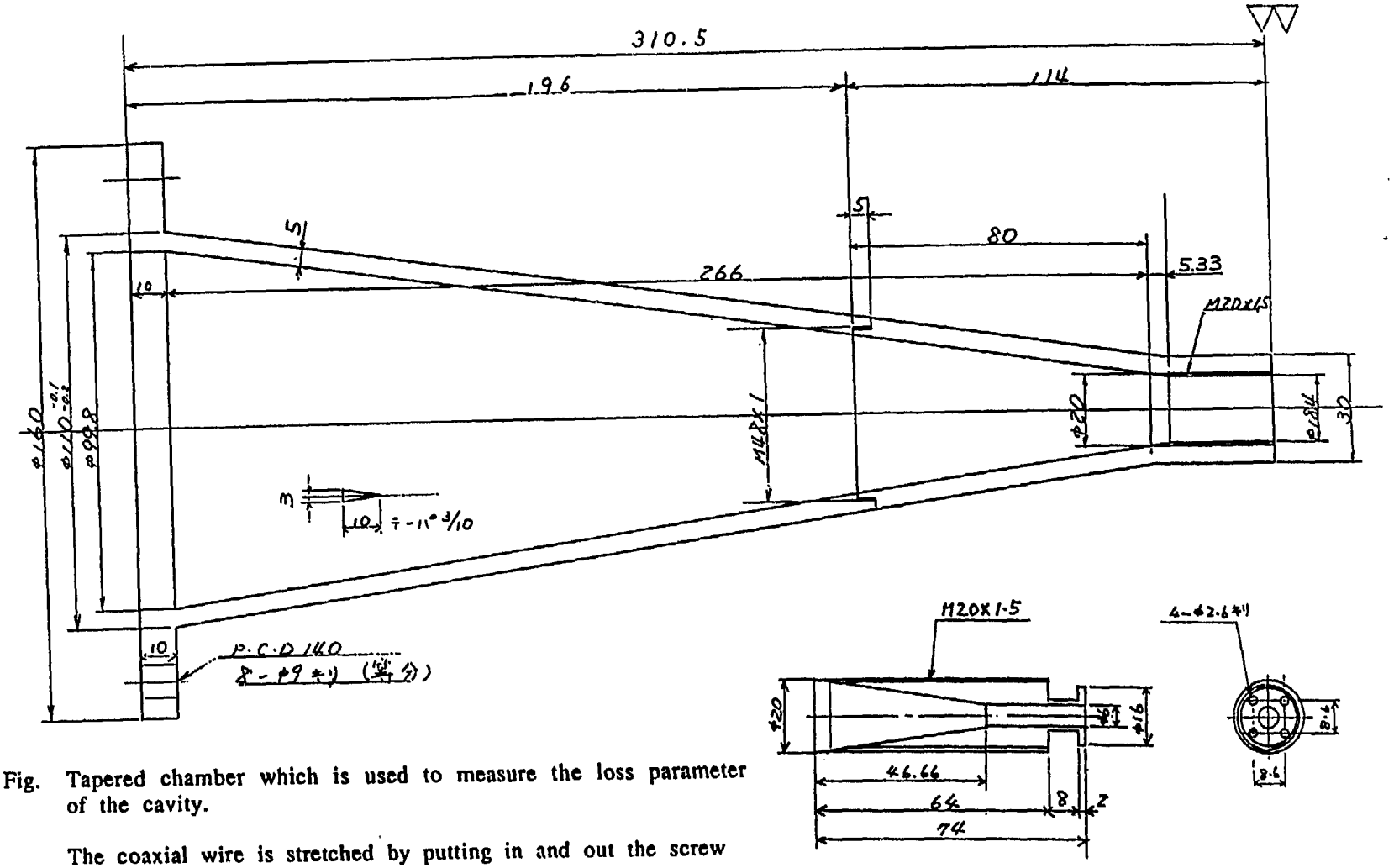

Fig. Tapered chamber which is used to measure the loss parameter of the cavity.

The coaxial wire is stretched by putting in and out the screw cutting connector at the narrow end.

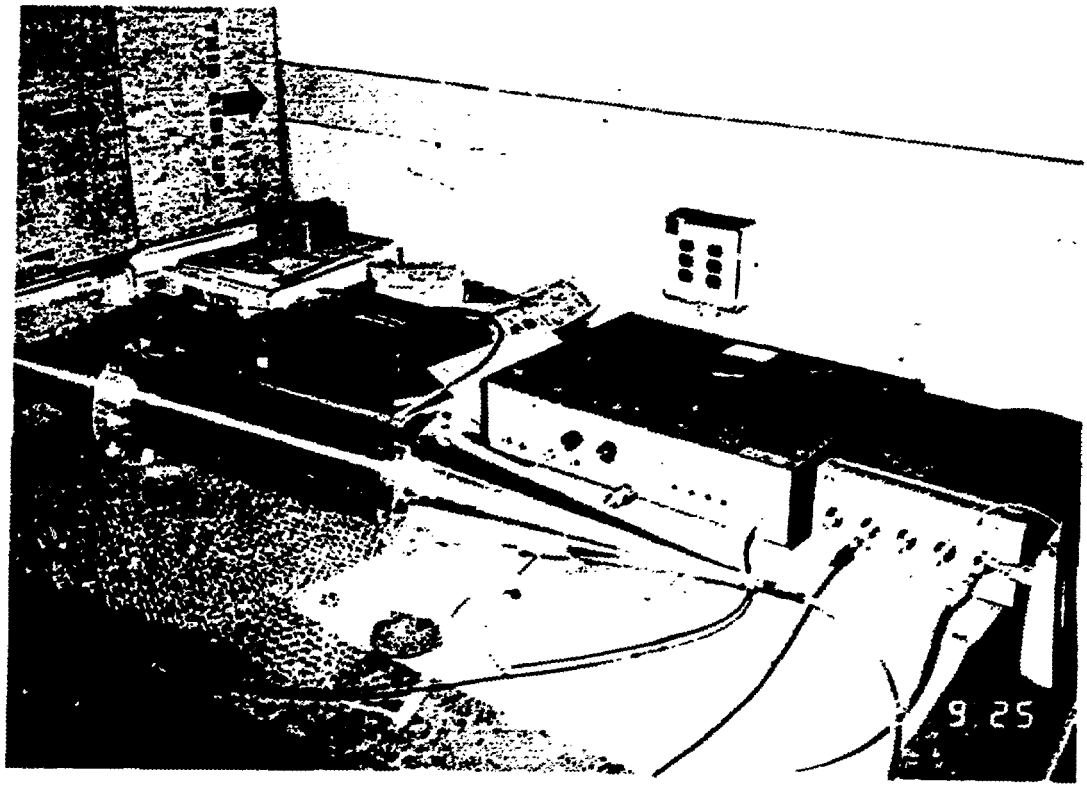

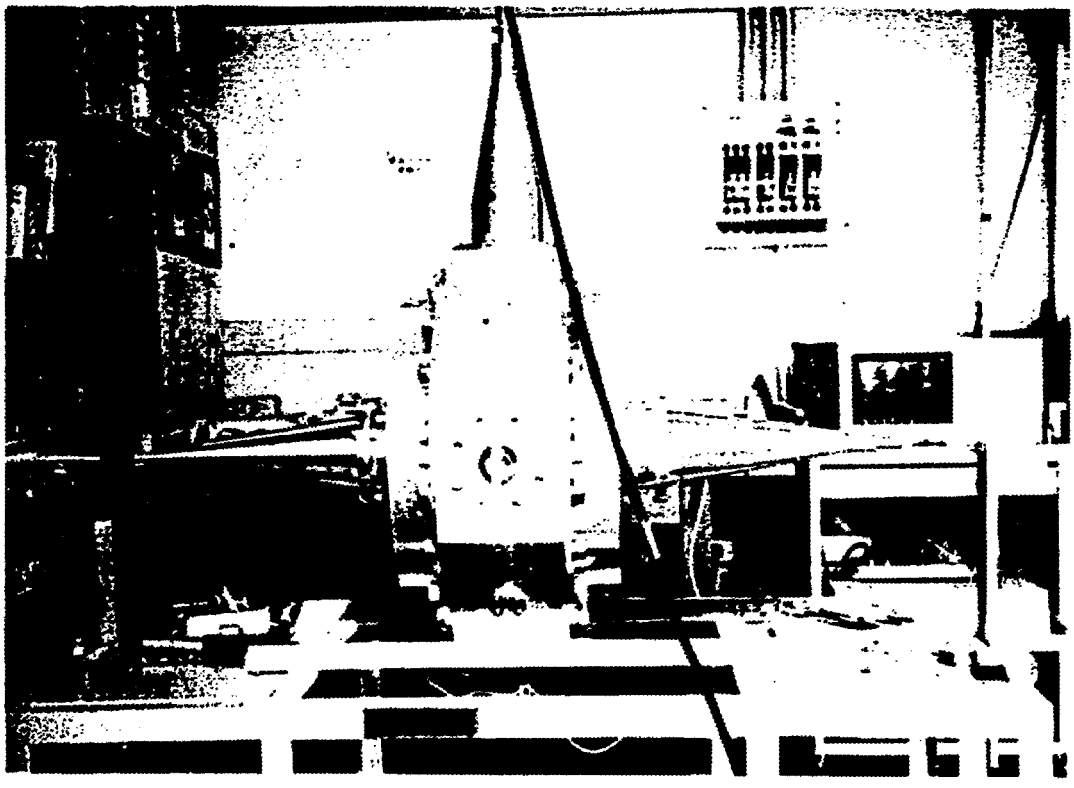

Fig. Photo of the experimental equipment: upper one is the reference chamber, lower one is the single-cell cavity with nose cones under experiment.

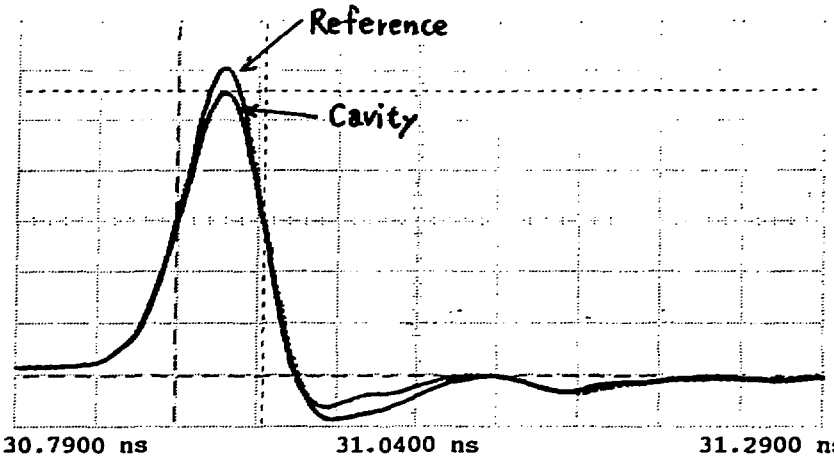

FWHM ~50 ps

■Ch. 2 = 400.0 mVolts/div
Timebase = 50.0 ps/div
■Memory 3 = 400.0 mVolts/div
■Timebase = 50.0 ps/div
■Ch. 2 Parameters
■Rise Time = 52.0 ps
■+ Width = 55.2 ps
■Preshoot = 14.44 %

Offset = 1.200 Volts
Delay = 30.7900 ns
Offset = 1.200 Volts
Delay = 30.7910 ns
P-P Volts = 2.5750 Volts
Fall Time = 30.8 ps
Overshoot = 0.000 %

(a)

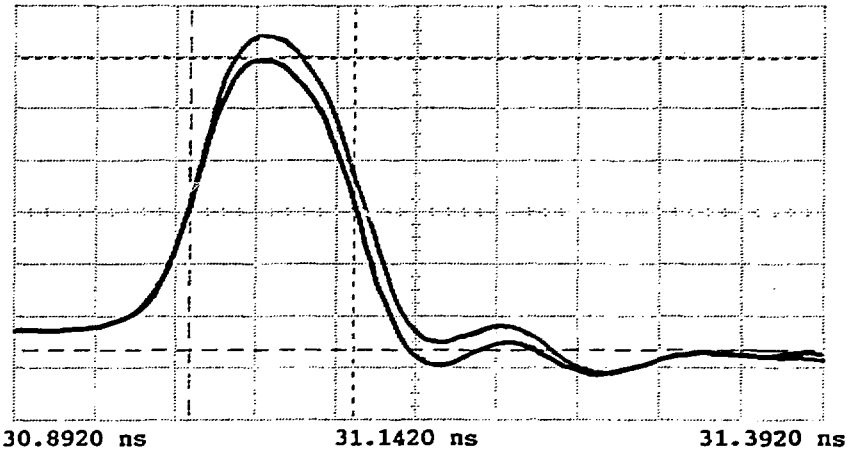

FWHM ~100 ps

■Ch. 2 = 1.000 Volts/div
Timebase = 50.0 ps/div
■Ch. 2 Parameters
■Rise Time = 69.0 ps
■+ Width = 102.0 ps
■Preshoot = 8.333 %

Offset = 2.320 Volts
Delay = 30.8920 ns
P-P Volts = 6.0937 Volts
Fall Time = 56.6 ps
Overshoot = 0.000 %

(b)

Fig. Recorded output pulses from both the reference chamber, $I_0(t)$, and the RF cavity, $i_m(t)$.
(a) FWHM : ~50 ps, (b) FWHM : ~100 ps,

The 50 ps pulse looks like a Gaussian pulse, but other pulses don't.

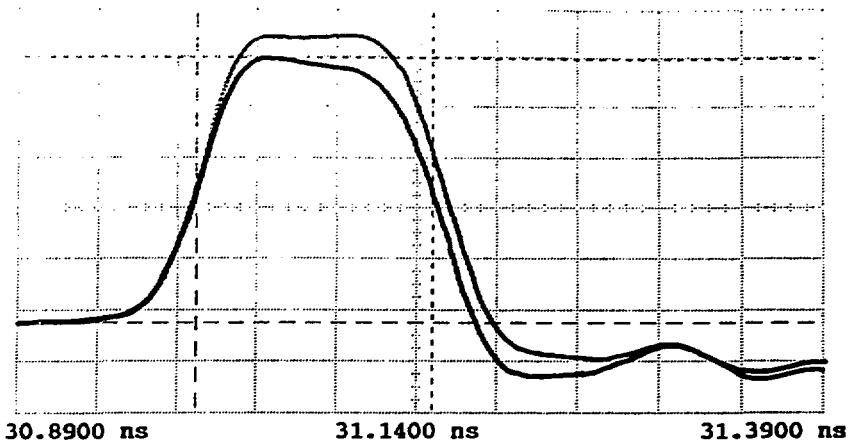

Ch. 2 = 1.000 Volts/div
Timebase = 50.0 ps/div
Ch. 2 Parameters
Rise Time = 52.6 ps
+ Width = 147.2 ps
Preshoot = 19.76 %

Offset = 2.320 Volts
Delay = 30.8900 ns
P-P Volts = 6.2500 Volts
Fall Time = 54.8 ps
Overshoot = 0.000 %

(c)

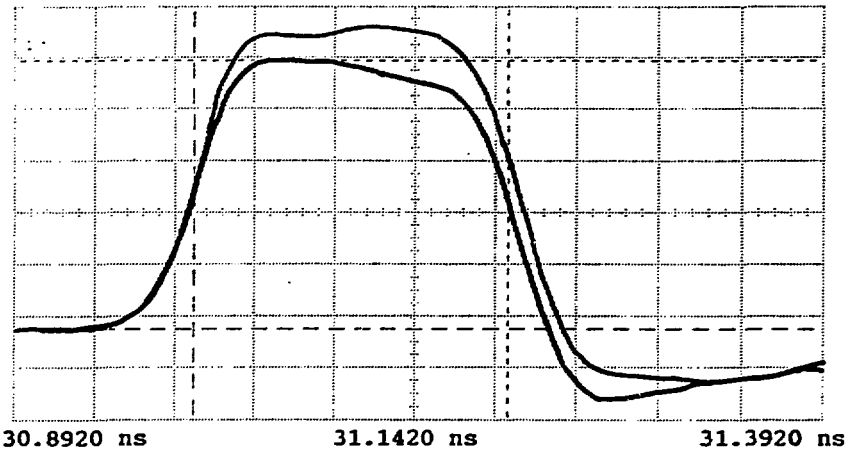

Ch. 2 = 1.000 Volts/div
Timebase = 50.0 ps/div
Memory 4 = 1.000 Volts/div
Timebase = 50.0 ps/div
Ch. 2 Parameters
Rise Time = 53.2 ps
+ Width = 195.4 ps
Preshoot = 26.50 %

Offset = 2.320 Volts
Delay = 30.8920 ns
Offset = 2.320 Volts
Delay = 30.8930 ns
P-P Volts = 6.5937 Volts
Fall Time = 61.4 ps
Overshoot = 602.4 m%

(d)

Fig. Recorded output pulses from both the reference chamber, $I_0(t)$, and the RF cavity, $i_m(t)$.
(c) FWHM : ~150 ps, (d) FWHM : ~200 ps,

The 150 ps and 200 ps pulses are rather close upon square pulses.

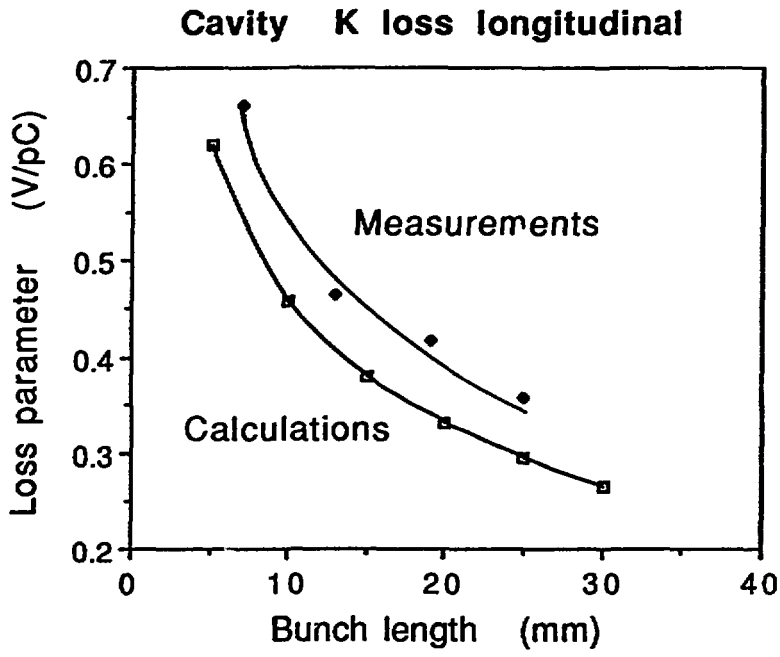

Fig. Loss parameters of the RF cavity for measurements and numerical simulations.

The measured data seem to be overestimated somewhat, but the measurements and calculations show the same distribution properties. Overestimation is considered to be due to that the generated pulse had no perfect Gaussian distribution and the coaxial line in a tapered chamber didn't match well with a 50 Ω and connectors.

Upcoming plan for measurements of impedance

1) Impedance comparison between racetrack type chamber and antechamber type

   The step change-induced impedance is also measured.

2) Comparison of impedances for bellows between the RF contact and RF slide finger

3) Impedance of the flange with gaps of various sizes

4) Impedance of the cavity without nose cones

5) Crotch etc.

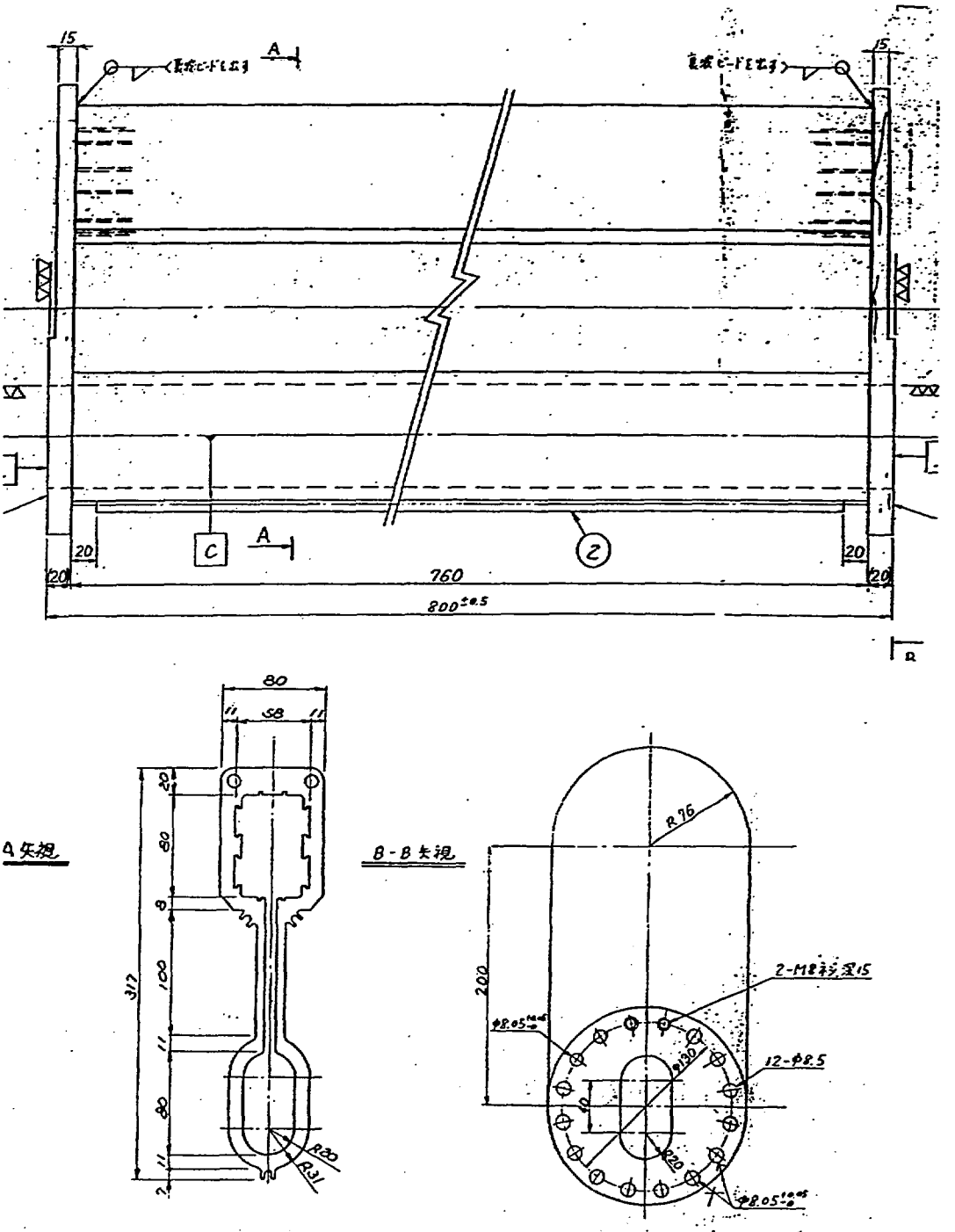

Comparison between rapid transition and smooth one

Fig. Straight chamber with a slot-isolated antechamber to measure the loss parameter.

Next we measure loss parameters of this chamber.
We compare the loss parameters between rapid transition and smooth one at the part of the slot to antechamber.

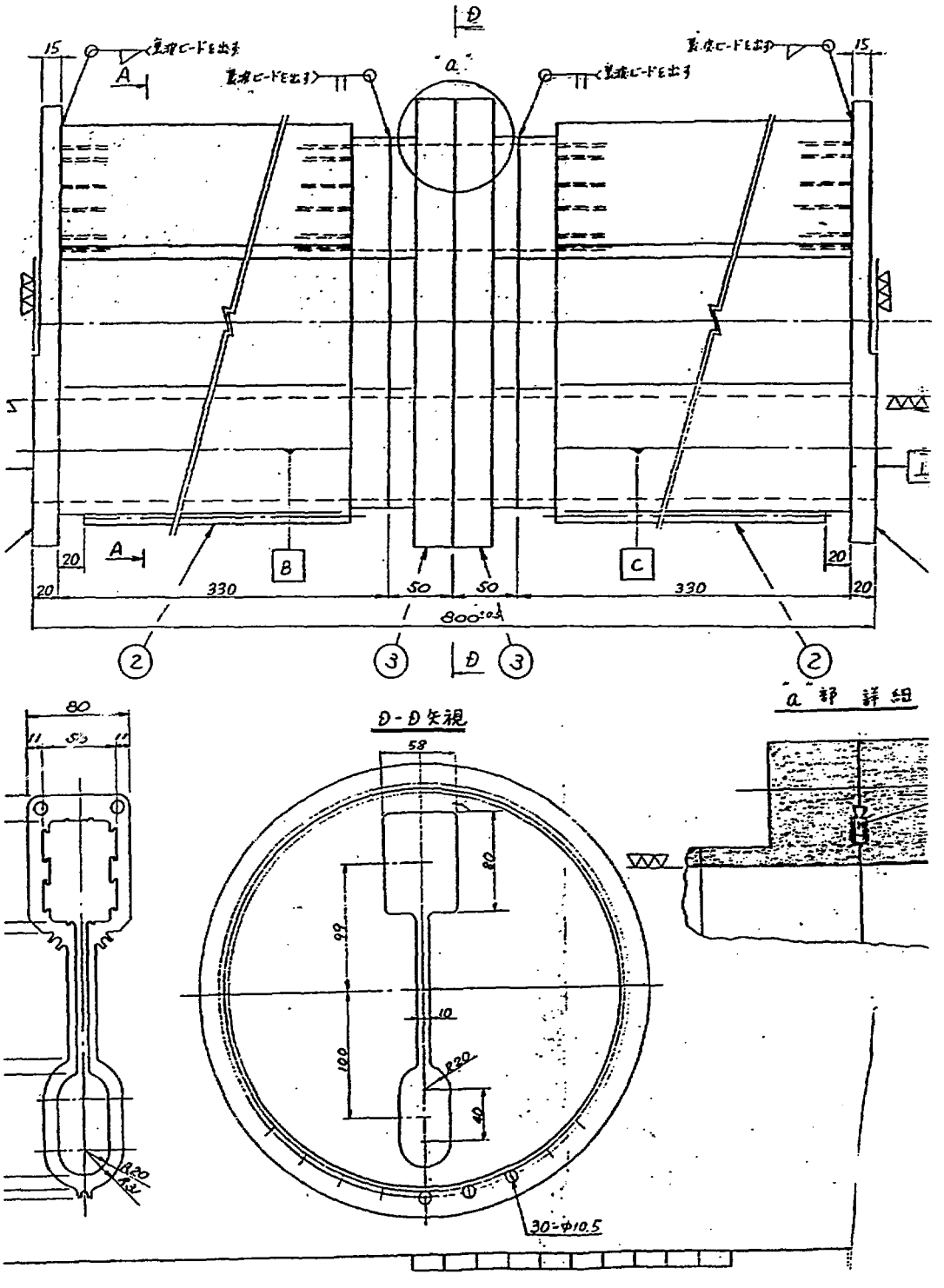

Fig. Chamber with a Conflat flange to measure the loss parameter.

We can change the gap size by inserting various sicknesses of gaskets.

Next we measure loss parameters of this flange.

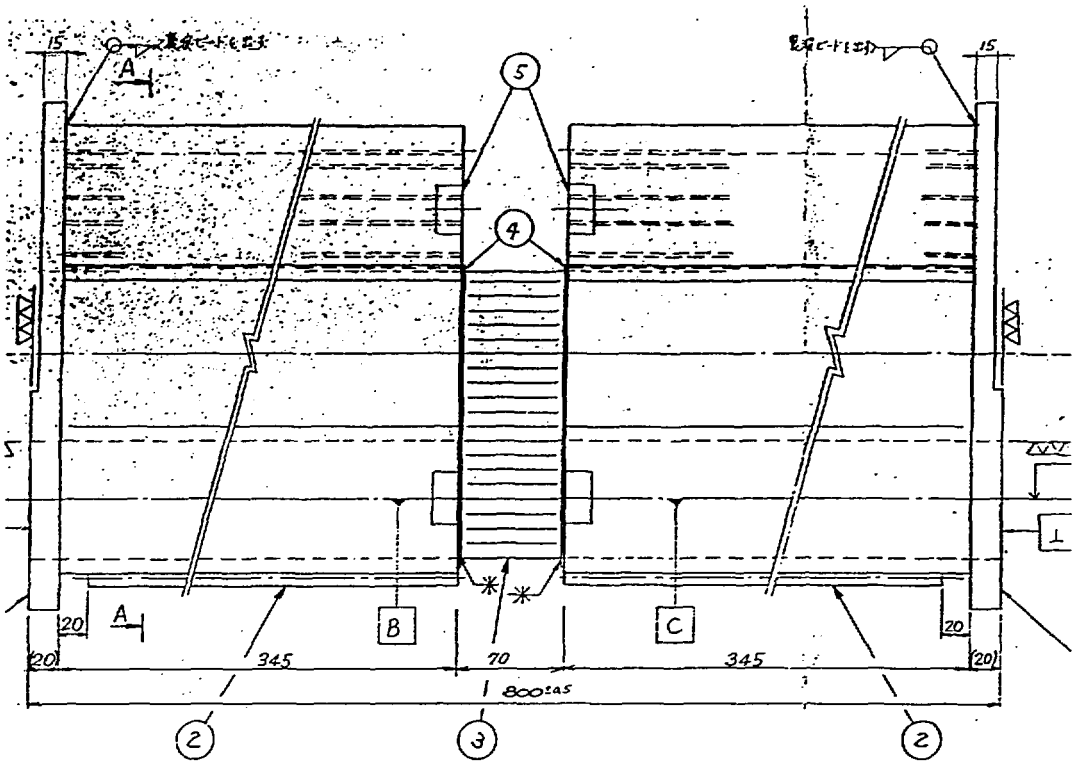

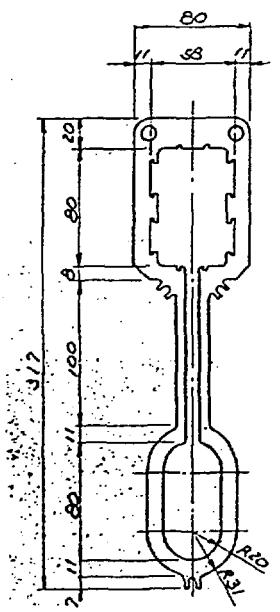

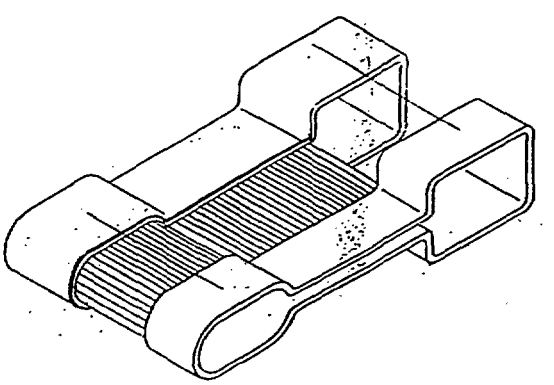

Comparison between RF contact and RF Fingers

Fig. Chamber with an RF contact to measure the loss parameter.

Next we measure loss parameters of this RF contact and compare with conventional RF slide fingers.

Appendix

This paper is contributed to
the 7th Symposium on Accelerator
Science and Technology
(Dec. 1989, Osaka, Japan)

ESTIMATION OF THE COUPLING IMPEDANCE FOR THE SPring-8 STORAGE RING

T. Yoshiyuki, T. Kusaka, M. Hara, and S. H. Be
RIKEN-JAERI Synchrotron Radiation Facility Design Team
2-28-8 Honkomagome, Bunkyo-ku, Tokyo 113, Japan

Abstract

The coupling impedance of vacuum chamber components is estimated for the SPring-8 storage ring. Three different approaches are discussed; analytical calculation, numerical simulation, and measurement. The results turn out that the contribution to the impedance is mainly attributed to RF cavities, bellows, flanges, and transitions to ID chambers.

Introduction

The SPring-8 storage ring is under design to be a low emittance synchrotron-radiation ring covering even the hard x-ray domain. High brilliance, which is implied by the low emittance, is related to large stored beam current in the ring. The beam current is, however, limited by the coherent instabilities of bunched beam. The important ingredients to evaluate the instabilities are a longitudinal coupling impedance Z/n, and a transverse impedance $Z_\perp$, the latter of which is usually correlated to the former. The storage ring consists of a large variety of structures which contribute to the impedance: vacuum chambers, bellows, gaps between flanges, step changes, box-like objects, vacuum ports, slits of RF contacts, RF cavities, and so on. Charged particles passing through the above components induce electromagnetic fields that act back on the beam, which results in energy losses and instabilities. The impedance is usually employed to describe the interaction of the beam with the environment. In order to estimate the effect on the beam more precisely, a detailed impedance analysis is carried out. In this report, we analyze the contribution of several vacuum components to the impedance, and suggest the way to minimize the energy losses.

Motivation of impedance estimate

Before a quantitative estimation of the impedance, we must get a reasonable idea on how much it can be allowed. The allowable impedance $|Z/n|$ is , in a classical stability criterion,[1] described by

$$\left|\frac{Z}{n}\right| \le \frac{\alpha E}{e I_p}\left(\frac{\Delta E}{E}\right)^2 , \qquad (1)$$

where α is the momentum compaction factor, E the total particle energy, $\Delta E/E$ the FWHM of relative energy distribution, and I_p the peak current defined by

$$I_p = I_{AV}\frac{2\pi R}{3 M \sigma_l} . \qquad (2)$$

I_{AV} is the average current in M bunches, σ_l the rms bunch length, and $2\pi R$ the circumference of the ring. n is the ratio of storage ring circumference to the wavelength of perturbation traveling around the bunch. For our storage ring; E = 8 GeV, $\alpha = 1.5 \times 10^{-4}$, $\Delta E/E = 3 \times 10^{-3}$, I_{AV} = 100 mA, $2\pi R$ = 1,436 m, M = 1000, and σ_l = 3.2 mm, therefore $|Z/n| < 0.7\ \Omega$. This quantity is relatively small compared with the other rings,[2] indicating that the impedance problem is more serious in our ring.

Method of impedance estimate

Since an exact analysis of the impedance of a storage ring is impossible, some different approaches have been developed to estimate this quantity;

- analytical calculations for several simple geometries,
- numerical simulations of electromagnetic fields in some elements of the vacuum chamber, and
- impedance measurements for test components.

We can obtain the contribution of several simple geometries to the longitudinal impedance analytically, assuming a cylindrical symmetry.[2] Naturally, it is followed that most of the vacuum components can not be evaluated in this way owing to their complicated geometries.

The electromagnetic field, which is created by a bunch circulating through a given section of the vacuum chamber, can be computed numerically by means of TBCI[3] and MAFIA.[4] Either TBCI or MAFIA computes wake potentials as a function of delay with respect to the head of bunch, together with the loss parameters, when a Gaussian-distributed rigid bunch is traveling in structures. The results of numerical computations can be used for the longitudinal and transverse broad-band impedances, $Z_{//}(\omega)$ and $Z_\perp(\omega)$, respectively, which are given by

$$Z_{//}(\omega) = R_S \frac{1+jQ\left(\frac{\omega_r}{\omega}-\frac{\omega}{\omega_r}\right)}{1+Q^2\left(\frac{\omega_r}{\omega}-\frac{\omega}{\omega_r}\right)^2} \qquad Z_\perp(\omega) = R_{S\perp}\frac{\omega_r}{\omega}\frac{1+jQ\left(\frac{\omega_r}{\omega}-\frac{\omega}{\omega_r}\right)}{1+Q^2\left(\frac{\omega_r}{\omega}-\frac{\omega}{\omega_r}\right)^2} , \qquad (3)$$

where R_S is the shunt impedance, Q the quality factor, and f_r the resonant frequency ($= \omega_r/2\pi$). The loss parameters of different contributions are computed as a function of σ_l, and summed for all the vacuum elements. The derivation of impedance is based on the fact that the loss parameter is proportional to the integral over the real part of impedance, according to

$$k_{//}(\sigma_l) = \frac{1}{\pi}\int_0^\infty \mathrm{Re}[Z_{//}(\omega)]\cdot\exp\cdot\left(\frac{\omega\sigma_l}{c}\right)^2\cdot d\omega . \qquad (4)$$

Therefore, the parameters of a broad-band impedance (f_r, Q, R_S) can be fitted to match a computed loss-parameter curve.[5]

On the other hand, the loss parameter can be measured for each element of the vacuum chamber by a coaxial wire method as discussed later. In principle every geometry can be measured in this method, but it is impossible to measure the loss parameters for all the kinds of elements of the storage ring. Practically, the loss parameters of most of the elements are acquired using both methods: numerical simulations and measurements.

Profile of vacuum chamber elements

The vacuum chamber is designed in a racetrack geometry of 8 cm wide and 4 cm high with a slot-isolated antechamber in which NEG strips are installed for pumping. Figure 1(a) shows the H-field lines for the first TM mode at a frequency of 4.3 GHz. Figure 1(b) also indicates deep penetration of electromagnetic

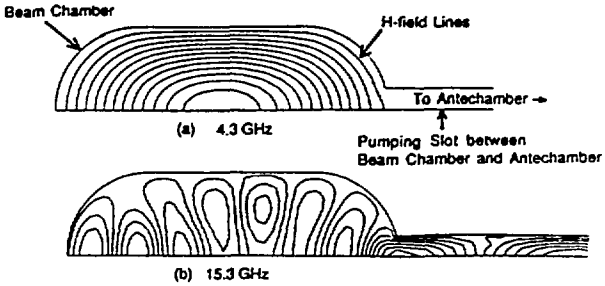

Fig. 1 Calculation of the H-fields lines for the vacuum chamber; (a) the first TM mode, 4.3 GHz, (b) higher-order mode, 15.3 GHz.

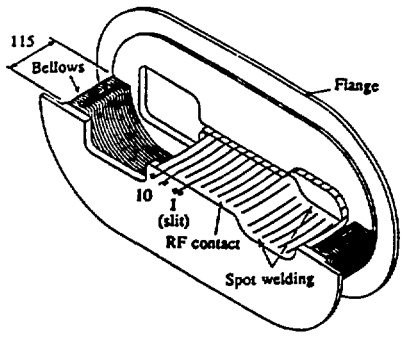

Fig. 2 RF contact by which the bellows are screened on the vacuum chamber.

fields into the pumping slot at frequencies above 15 GHz. A distortion of the H-field lines is remarkable compared with the beam chamber without antechamber. In case of a short bunch below 5 mm in length, as the modes above 15 GHz have a large contribution to the loss parameter according to Eq. (4), it may be that the slot has significant effects.

The RF contact screens the bellows to reduce the energy losses, and keep the electric contact between the chambers, as shown in Fig. 2. The numerous long and narrow slits absorb the shrinkage of bellows at baking, and make between the RF contact and bellows evacuated.

We adopt the Conflat flanges for our ring. The outer diameter gets over 350 mm in case of the connection between vacuum chambers. The gap between conventional Conflat flanges comes even to a few mm with a gasket inserted, but a special flange is designed so as to reduce the gap below 0.5 mm for a less impedance.

There is a radius discontinuity between the normal and insertion-device (ID) chamber. In fact, a tapered transition is used in place of a step change between different chambers. Nevertheless, the calculation was carried out assuming the step changes in the aspect of safety.

Calculation results

Analytical calculation

We have estimated the impedances of the various kinds of elements analytically: free space, space charge, resistive wall, bellows, flanges, pick-up electrodes, step changes, and slits and holes. Table 1 shows the impedances of typical elements. This preliminary study suggests that the bellows must be securely screened and RF contacts are effective to screen them. It also shows that transitions to ID chambers and flanges must be improved to achieve the design goal.

Table 1 Preliminary study of the impedance for analytical calculations

Impedance source	Number	|Z/n| (Ω)
Free space	—	0.2 (f = 10 GHz)
Space charge	—	4×10^{-6}
Resistive wall	—	0.1 (f = 100 MHz)
		0.01 (f = 3.8 GHz)
Bellows		
(without RF contact)	336	9.0
(with RF contact)	336	3.9×10^{-6}
Flanges (1 mm gap)	912	0.39
Step changes	96	0.26
Pick-up electrodes	432	0.05
Vacuum pump holes	~300	0.005

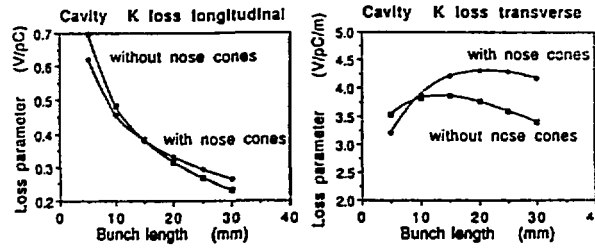

Fig. 3 Loss parameters for cavities both with and without nose cones; (a) longitudinal case, (b) transverse case.

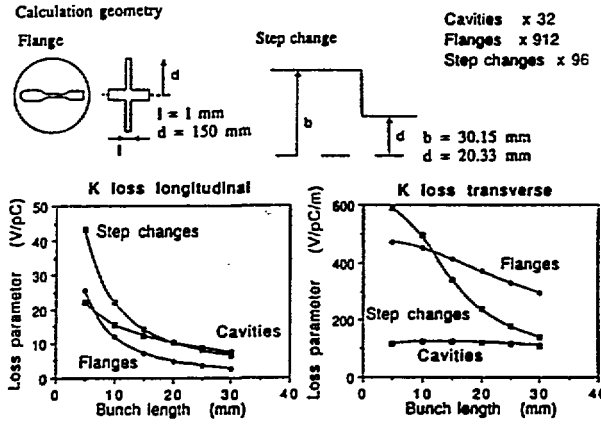

Fig. 4 Total loss parameters of the whole ring for typical components; (a) longitudinal case, (b) transverse case.

Numerical simulation

A 2D code, TBCI, is used to calculate the loss parameters, assuming again cylindrical symmetry. The simulation was carried out for longitudinal (monopole fields) and transverse impedance (dipole fields) independently, and applied to RF cavities, bellows, flanges, and transitions to ID chambers.

As far as RF cavities are concerned, the calculation has been done for the single-cell cavities both with nose cones, which have been already studied, and without nose cones, which are under design[6] as a low impedance cavity for our ring. The loss parameters for both cases are plotted in Fig. 3 as a function of bunch length. We expected the loss parameters of the cavity without nose cones to be lower than those of the cavity with nose cones for every bunch length, but the loss parameters become reversed for short bunch lengths. The HOM impedances which have a harmful effect on the beam are suppressed in the cavity without nose cones as in Ref. 6, but the other HOM impedances seem to get larger than we expected, especially over cut-off frequency. In either case, it turns out that the contribution from the RF cavities to the loss parameter are inevitable.

Figure 4 shows the total loss parameters of the whole ring, considering only the elements which have large contributions to the impedance. The bellows themselves have large loss parameters, because the number is large (N = 336) and the shape looks like a pill-box type of cavity. On the other hand, once they are screened adequately by the RF contacts, the loss parameters are decreased tremendously even not to be plotted in Fig. 4. It turns out that in longitudinal case step changes have a large effect on the impedance, and step changes and flanges do in transverse one. However, as far as step changes are concerned, the loss parameters are, in fact, reduced further as the transitions to ID chambers get tapered. In case of flanges, the real loss parameters can be also reduced

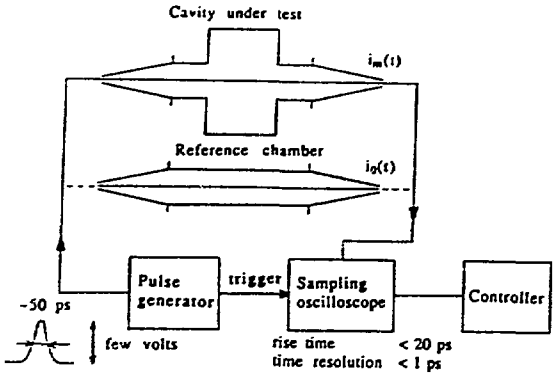

Fig. 5 Set-up for the measurement of the loss parameter.

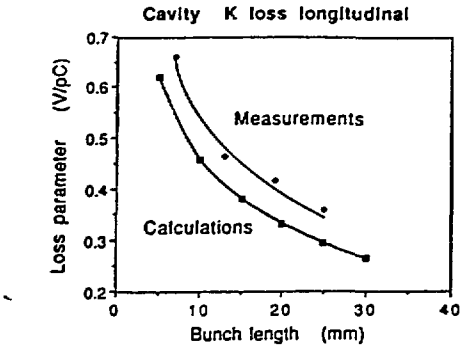

Fig. 7 Loss parameters of the RF cavity for measurements and numerical simulations.

at the rate of reduction of the gap, but they are still larger than those of the cavities in transverse case. The impedance needs to be decreased more.

In the next step, we calculate the loss parameters of the asymmetric geometries using the 3D code MAFIA. But as a 3D simulations have limitations such as the number of meshes, minimum bunch length, and computational time, there is some room for improvement.

Measurement of loss parameter

The coaxial wire method which has been described by Sands and Rees[7] is a widely-spread tool for bench measurements of beam coupling impedance. By the introduction of a thin wire into the chamber components under test, a surface current distribution on the inner surface of the beam pipe can be obtained, which corresponds approximately to the current distribution produced by a passing bunch. When this image-current distribution has been perturbed by a discontinuity, a reaction on the wire takes place similar to that of a perturbed wake field on the bunch.

A measurement set-up is shown in Fig. 5. A nearly Gaussian pulse is generated with 50 ps of the minimum pulse width by a pulse generator. It travels through either the reference chamber with a thin wire at the axis of beam, or a component under test of the same mechanical length. Both signals, reference signal $i_0(t)$ and object signal $i_m(t)$, are recorded sequentially, and stored in a sampling oscilloscope which has time resolution below 1 ps. The data acquired into the oscilloscope are sent to a controller and then the longitudinal loss parameter $k_{\parallel}(\sigma_l)$ is calculated by

$$k_{\parallel}(\sigma_l)=2Z_0\int i_0(t)(i_0(t)-i_m(t))\,dt \Big/\left[\int i_0(t)\,dt\right]^2 , \qquad (5)$$

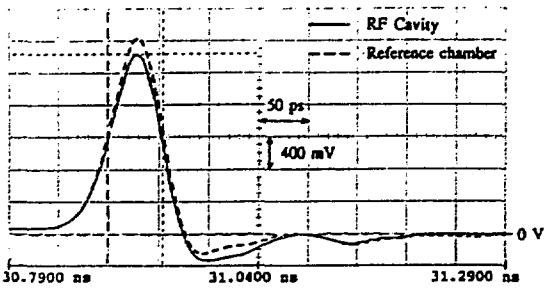

Fig. 6 Recorded output pulses $I_0(t)$ for the reference pipe and $I_m(t)$ for the RF cavity.

where Z_0 is the characteristic impedance of the coaxial line formed by the reference chamber with wire and σ_l the length of the Gaussian pulse. Figure 6 shows the recorded output pulses from both the reference chamber and an RF cavity with nose cones. The measured loss parameters are plotted in Fig. 7 together with the calculated results by TBCI. They were obtained for four pulse widths; about 50, 100, 150, and 200 ps. The measurement data look somewhat overestimated, but both measurement and calculation show the same distribution property. The causes of overestimation are considered such that the generated pulse didn't have a perfect Gaussian distribution and the coaxial line in the tapered chamber didn't match well with the 50 Ω cable and connectors.

Measurement method has its drawbacks: the first is the measurement precision and the second is that the objects are limited in number. In the next step, we improve the measurement precision and then measure the loss parameters of a vacuum chamber with antechamber, a Conflat flange, and RF contact.

Conclusion

The impedances of vacuum chamber components turns out to be serious problem in our storage ring. A special attention has to be paid on the design of each component in order to achieve the designed performance. The most critical elements have been found to be transitions to ID chambers, flanges, and RF cavities. However, the transitions to ID chambers are, in fact, tapered smoothly and the impedance gets small. On the other hand, the impedance of bellows can be reduced sufficiently by screening them with RF contacts.

We have estimated the impedance in three ways: analytical calculation, numerical simulation, and measurement. The analytical calculation is only preliminary and limited to simple geometries. The numerical simulation and measurement also have many limitations. We need to estimate almost all the vacuum components of the storage ring by using three ways. From now on, we have to advance the calculation efficiency and have a plan to employ a 3D code, MAFIA. We also have to improve the measurement precision and estimate the other vacuum components: a crotch, gate valve, and so on.

References

1. E. Keil and W. Schnell, CERN-ISR-TH-RF/69-48, 1969.
2. A. G. Ruggiero, BNL Informal Report, Aug. 1979.
3. T. Weiland, Nucl. Inst. Meth. 212, 1983.
4. R. Klatt, et al., Proceeding of the 1986 Linear Accelerator Conference, SLAC, 1986.
5. B. Zotter, CERN LEP-TH/87-34, 1987.
6. T. Kusaka, et al., presented at this symposium.
7. M. Sands and J. Rees, SLAC-report PEP-95, 1974.

Conclusion

The impedances of vacuum chamber components turns out to be serious problem in our storage ring. A special attention has to be paid on the design of each component in order to achieve the designed performance. The most critical elements have been found to be transitions to ID chambers, flanges, and RF cavities. However, the transitions to ID chambers are, in fact, tapered smoothly and the impedance gets small. On the other hand, the impedance of bellows can be reduced sufficiently by screening them with RF contacts.

We have estimated the impedance in three ways: analytical calculation, numerical simulation, and measurement. The analytical calculation is only preliminary and limited to simple geometries. The numerical simulation and measurement also have many limitations. We need to estimate almost all the vacuum components of the storage ring by using three ways. From now on, we have to advance the calculation efficiency and have a plan to employ a 3D code, MAFIA. We also have to improve the measurement precision and estimate the other vacuum components: a crotch, gate valve, and so on.

Summary of the APS Workshop on
(1) Bunch Lengthening and Instabilities
(2) Computation of Bunch Length
(3) Impedances and Wakes

B. Zotter

CERN

Argonne National Laboratory
Advanced Photon Source
Impedance and Bunch Instability Workshop
October 31 - November 1, 1989

Summary of the APS Workshop on (1) Bunch Lengthening and Instabilities (2) Computation of Bunch Length (3) Impedances and Wakes

B.Zotter

9 January 1990

1 Single Bunch Effects

While the title of the workshop changed several times, the interest of the organizers was clearly centered on single bunch effects, which are feared to limit the performance of the Advanced Photon Source (APS) which is in construction at the Argonne National Laboratory. The present state of calculations of impedances and their effect on bunch lengthening and beam stability in the APS were reported by W. Chou and H. Bizek. A certain number of problems with existing computer programs were enumerated, some of which could be resolved in the following days. E.g. a strong discrepancy was found in bunch length - and hence transverse stability - when either the wake potential or a $Q = 1$ broad-band resonator were used in the simulation program SIMTRAC. However, the results did agree when all 3 parameters of the resonator were matched, yielding an extremely low Q value: then the bunch length - and the threshold for transverse mode coupling instability - were as small as with the wake potential computations. Convergence difficulties in the wake potential computation for chambers with long tapers could be traced to an unfavorable ratio of spatial to temporal steps. However, the changes required in the relevant programs appear somewhat more difficult to apply.

There exist a number of approaches to calculate single bunch effects, some of which will be discussed below. For brevity, we shall omit references to well-known computer programs, as most of these have already been referred to in the individual presentations. Similarly, references to talks at this workshop will be limited to the names of the authors in the text.

1.1 Wake function

The wake function (i.e. the wake potential of a delta function pulse) can be used as a Green function for arbitrary particle distributions. It is particularly useful for the simulation of

(super) particle motion including wall effects (e.g. SIMTRAC, HERSIM etc.), where the bunch shape is not known a priori and changes with time.

The main problem with the wake function is the fact that it cannot be calculated exactly for realistic structures. Analytic expressions exist only for (closed) pillboxes, uniform tubes and similar over-simplified geometries.

Numerical computation of wake potentials with time-domain codes like TBCI, ABCI, MAFIA etc. is limited in principle to finite bunch lengths, e.g. the mesh size has to be less than one quarter of the standard deviation of a Gaussian bunch. One thus needs very fine meshes in order to obtain the important short-range part of the wake correctly. However, small mesh sizes lead rapidly to excessive computer space requirements and to extremely long computation times. For tubes with long tapers, W.Chou reported that longitudinal wakes depended on mesh size, and even several days of computing were not sufficient to yield convergence. Discrepancies of wakes computed with existing 2-D and 3-D codes were mentioned by him and W.Ng, who is working on a new finite element code permitting variable mesh sizes.

Adding the leading part of the wake function of a finite bunch to the trailing one (i.e. conserving the area under the curve) is an often used approximation. However, it is far from unique and may give completely incorrect results for the wake at very short distances.

1.2 Impedances

The wake function is the Fourier transform of the (wall) impedance, and may also be obtained from the frequencies and loss factors of the resonances of a structure. These can be computed by computer codes for the frequency domain (e.g. SUPERFISH, URMEL etc. for single obstacles; KN7C, TRANSVRS etc. for periodic ones). The wake function then can be found by a simple summation

$$w(\tau) = -2 \sum_n k_n \cos \omega_n \tau. \qquad (1)$$

Clearly, one would need a very large number of resonances to obtain the short-range wake correctly, which requirement again leads to excessive demands on computer time and space.

Replacement of the high-frequency tail of the impedance by an analytic estimate like the "optical resonator model"[1] has yielded quite good results in the past, but again relies on a number of arbitrary assumptions which may break down in specific geometries.

A novel method to compute impedances of single, rotationally symmetric obstacles with infinite side tubes was described by R. Gluckstern[2]. It is based on the solution of an integral equation, and yields a wide variety of results in a rather compact fashion. E.g. it shows the transition of the asymptotic frequency dependence of the impedance of a single obstacle ($\omega^{-1/2}$) to that of periodic ones ($\omega^{-3/2}$), and yields criteria for the validity of these expressions. Another application of the method was to coaxial wire measurement of the impedance, where the presence of the wire is often suspected to change the results as reported by L. Farvarque.

1.3 De-convolution of impedances

In principle, the Fourier transform of the wake potential of a finite bunch (sometimes called an "effective impedance") could be used to compute the wall impedance by "de-convolution"

$$Z(\omega) = \frac{Z_{eff}(\omega, \sigma)}{\tilde{\lambda}(\omega, \sigma)} \tag{2}$$

where $\tilde{\lambda}$ is the Fourier transform of the bunch distribution. However, this technique leads to insurmountable numerical difficulties. This can easily be seen e.g. for a Gaussian bunch, where the effective impedance has to be multiplied with the inverse of the Fourier transform of a Gaussian distribution, i.e. with $\exp(+\omega^2\sigma^2/2)$. This factor becomes exponentially large for frequencies higher than $1/\sigma$ where, on the other hand, the effective impedance is nearly zero. This excessive weighting of the (effective) impedance where it is very small (and hence rather noisy) leads to completely unusable results for the high-frequency impedance and for short-range wakes.

1.4 Gaussian wakes

One method mentioned in this workshop[3] circumvents all of these problems by expressing the wake potential of a Gaussian (standard deviation σ_1) by that of a Gaussian with smaller standard deviation ($\sigma_2 < \sigma_1$)

$$W_{\sigma_1}(\tau) = \frac{1}{\sqrt{2\pi}\sigma_1} \int_{-\infty}^{\infty} W_{\sigma_2}(t) \exp\left[-\frac{(\tau - t)^2}{2(\sigma_1^2 - \sigma_2^2)}\right] dt \tag{3}$$

Thus one avoid the wake function altogether, and use the wake potential of a short Gaussian bunch like a Green function. However, the method appears to be limited to the computation of wake potentials of Gaussian bunches.

Shortly after the workshop, a generalization of this method to arbitrary distributions has been developed[4], which is based on an expansion into a series of Hermite polynomials (also called "Gram-Charlier" series). It could be shown that the products of Hermite polynomials and a Gaussian have the same property as a Gaussian alone, i.e. they can be expressed as convolutions of similar functions with smaller standard deviations. This technique may be used to compute wake potentials of arbitrary distributions inside a simulation program. However, applying this procedure at every turn might still slow down the simulation unduly. Therefore it may be preferable to use it only once for the generation of pre-calculated tables which can be read by the code using fast interpolation techniques.

2 Model Impedances

2.1 Broad-Band Resonator

A broad-band (BB) impedance corresponds to a short-range wake and is thus generally sufficient for the calculation of effects of single bunches. In particular, the BB resonator model has been used widely in the past for its simplicity: it contains only 3 parameters

(resonant frequency ω_r, shunt impedance R_s, and quality factor Q to describe the (complex) impedance function over all frequencies. Its Green function has the simple, analytic form of a damped oscillation. Many integrals and infinite sums, which appear in the theory of instabilities, can be evaluated analytically.

However, there are limitations to the applicability of this model, in particular at high frequencies where the real part falls off too quickly

$$Re\ (Z_{BB}) \sim \omega^{-2} \tag{4}$$

while the correct behavior is expected to be $\omega^{-1/2}$ for single obstacles, and $\omega^{-3/2}$ for periodic structures. This incorrect asymptotic behavior may lead to wrong answers for very short bunches.

For such bunches, the determination of the parameters of the resonator impedance may cause problems in the longitudinal direction (m=0 mode). In the transverse direction (m=1 mode), matching of the loss factors of long bunches yields in general quite good results for the ratio R_s/Q[5].

In the longitudinal direction, however, this technique fails since the wake depends on both the shunt impedance and the quality factor individually, not only on their ratio. Straight forward fitting of the loss factors may lead to extremely small quality factors, which furthermore depend on the bunch lengths used[6]. It has therefore been proposed to obtain the broad-band resonator parameters by fitting directly to the wake potential. However, also these results depend on the bunch lengths considered.

In order to alleviate these problems, we make here the following proposal:

Alter existing simulation programs to permit variation of the broad-band resonator parameters in accordance with the instantaneous bunch length. The latter is calculated in some program options anyhow, if not its calculation can be added easily, without unduly slowing down the execution. The corresponding BB parameters may be stored in a precalculated table which can be read and interpolated by the program.

2.2 Improved Model Impedances

It is possible to construct model impedances which have the expected asymptotic frequency dependence and are only slightly more complicated than the BB resonator. A number of such models have been described recently[7], which tend either towards $\omega^{-1/2}$ or towards $\omega^{-3/2}$ at high frequencies, while their low frequency behavior is proportional to ω^2 as for the BB resonator. The corresponding wake functions can still be expressed analytically, and are eith· · exponentials divided by a square-root exp $y/\sqrt{y}$, or "complementary error functions" of square-root argument erfc($\sqrt{y}$) (y is a quantity proportional to the distance behind the particle). Both these models contain 3 free parameters which may be adjusted to fit wake potentials or loss factors over a given range of bunch lengths. The application of these model impedances to analytical work and/or to simulation appears quite straightforward, but has not been attempted yet to our knowledge.

A second set of model impedances is described in the same report: in addition to the asymptotic high-frequency dependence, also the low-frequency behavior is improved.

For lossless structures, the real part of the impedance should remain zero up to the first resonant frequency (usually related to the largest transverse dimensions). While the expressions for both the real and imaginary part of these model impedances remain rather simple, the corresponding wake functions become too complicated for analytical work.

3 Bunch Lengthening

Over the past 25 years, at least as many theories of bunch lengthening in particle accelerators and storage rings have been published. Also computer simulation has a long history since the early 60's. We list here an incomplete selection in Table I. While many of these theories gave good agreement with observations in some machines, none of them seems to be valid over the whole parameter range. One of these theories[8], based on the inclusion of negative mode numbers, was described by Y. Chin.

In recent large electron storage rings (e.g.PEP, PETRA, CESR) with short bunches (i.e. with standard deviation smaller than vacuum chamber diameter), observed bunch lengthening is often less than calculated. For longer bunches, such as electrons in the CERN SPS, the agreement with theory - but in particular with simulation - is much better as reported by D. Brandt. Bunch lengthening in the SLC damping rings could finally be explained satisfactorily by careful calculation of even the smallest obstacles in the vacuum chamber wall, as shown by K. Bane. First measurements of bunch lengthening and calculations of impedances in LEP required some tricky corrections as reported by D. Brandt and B. Zotter. Comparisons with the expected bunch lengthening obtained with the code BBI were presented.

4 Conclusions

Computation of wake potentials in rotationally symmetric structures with existing mesh programs may be rather time consuming, but usually the results converge for fine enough mesh sizes. However, for tubes with long tapers, even several days of computing were not enough to give convergence. For unsymmetric structures the situation is worse: 3-dimensional codes with even larger space and time requirements have to be used, and the results often differ significantly from those obtained with 2-D codes.

The wake potentials may be used to approximate impedances and wake functions required to simulate the evolution of bunch length and other parameters of single bunches in accelerators and storage rings. Existing simulation programs can give quite good results, but may need some adaptation to the particular machine studied.

Quite satisfactory results can often be obtained with simplified model impedances, even if they fail in extreme cases. In particular, we propose to alter existing simulation programs to permit variation of broad-band resonator parameters. We summarize this situation with the provocative slogan: "The BB resonator is dead - long live the BB resonator!"

References

[1] D. Brandt, B. Zotter, Report CERN/ISR-TH/82-13 (1982)

[2] R. Gluckstern, to be published in Physical Review D

[3] K. Bane et al., AIP Conf.Proc. 127, p.875 (1985)

[4] T. Wang, B. Zotter, Report CERN/LEP-TH/89-75 (1989)

[5] B. Zotter, Report CERN/LEP-TH/87-34 (1987)

[6] L. Farvarque, A. Ropert, ESRF Impedance Workshop 1988

[7] A. Hofmann, B. Zotter, Report CERN/LEP-TH/88-51 (1988)

[8] T. Suzuki, Y. Chin, K. Satoh, KEK Preprint 82-26 (1982)

Table I

Bunch Lengthening Theories		
Author	*Year*	*Subject*
C. Pellegrini, A. Sessler	68	Potential well
K. Robinson	69	Potential well
A. Piwinski	72	power losses
J. Haissinski	73	Integral Equation
M. Chatard-Moulin et al	73	Pillbox wake
D. Boussard	75	Localized impedance
P. Channel, A. Sessler	76	Turbulence
E. Messerschmid, M. Month	76	Vlasov Equation
A. Chao, J. Gareyte	76	Waterbag
F. Sacherer	77	Mode-coupling
P. Wilson	77	"HP-35" model
A. Hofmann, J. Maidment	78	Combined model
B. Zotter	81	Potential well - BB
Y. Chin, K. Yokoya	82	Overshoot
R. Meller	84	Thermodynamic model
R. Channel	85	Waterwaves
K. Hirata	87	Mapping approach
G. Besnier	88	Absence of mode-coupling

Bunch Lengthening Simulation		
Author	*Year*	*Subject*
R. Dory	63	Overshoot
A. Renieri	75	Capacitive wake
K. Bane, P.Wilson	79	Computed wakes
T. Weiland	81	PETRA
D. Brandt	82	LEP
R. Siemann	83	SPEAR
V. Nys	85	Hermite polynomials
S. Myers	86	reactive feedback
T. Wang	89	multiple RF